

<https://doi.org/10.15388/vu.thesis.491>

<https://orcid.org/0000-0001-7120-739X>

VILNIUS UNIVERSITY

CENTER FOR PHYSICAL SCIENCES AND TECHNOLOGY

Raman Novikau

# Evaluation of the Adsorption Properties of Composite Materials for Caesium, Cobalt, and Europium

**DOCTORAL DISSERTATION**

Natural Sciences,  
Chemistry (N 003)

VILNIUS 2023

The dissertation was prepared between 2019 and 2023 at the Center for Physical Sciences and Technology.

**Academic supervisor – Dr. Galina Lujanienė** (Center for Physical Sciences and Technology, Natural sciences, Chemistry, N 003).

This doctoral dissertation will be defended in a public meeting of the Dissertation Defence Panel:

**Chairman – Dr. Evaldas Maceika** (Center for Physical Sciences and Technology, Natural Sciences, Physics, N 002).

**Members:**

**Prof. Dr. Jurgis Barkauskas** (Vilnius University, Natural Sciences, Chemistry, N 003).

**Prof. Dr. Linas Kliučininkas** (Kaunas University of Technology, Technological Sciences, Environmental Engineering, T 004).

**Dr. Jixin Qiao** (Technical University of Denmark, Natural Sciences, Chemistry, N 003).

**Dr. Arūnas Gudelis** (Center for Physical Sciences and Technology, Natural Sciences, Physics, N 002).

The dissertation shall be defended at a public meeting of the Dissertation Defence Panel at 10 a.m. on 22<sup>nd</sup> September 2023 in meeting room D401 of the Center for Physical Sciences and Technology.

Address: Saulėtekio av. 3, D401, Vilnius, Lithuania.

Tel. +37052649211; e-mail: office@ftmc.lt

The text of this dissertation can be accessed at the libraries of Center for Physical Sciences and Technology and Vilnius University, as well as on the website of Vilnius University: [www.vu.lt/lt/naujienos/ivykiu-kalendorius](http://www.vu.lt/lt/naujienos/ivykiu-kalendorius)

<https://doi.org/10.15388/vu.thesis.491>

<https://orcid.org/0000-0001-7120-739X>

VILNIAUS UNIVERSITETAS

FIZINIŲ IR TECHNOLOGIJOS MOKSLŲ CENTRAS

Raman Novikau

# Kompozicinių medžiagų adsorbicinių savybių ceziui, kobaltui ir europiui vertinimas

**DAKTARO DISERTACIJA**

Gamtos mokslai,

Chemija (N 003)

VILNIUS 2023

Disertacija rengta 2019–2023 metais Fizinių ir technologijos mokslų centre.

**Mokslinė vadovė – dr. Galina Lujanienė** (Fizinių ir technologijos mokslų centras, gamtos mokslai, chemija, N 003).

Gynimo taryba:

**Pirmininkas – dr. Evaldas Maceika** (Fizinių ir technologijos mokslų centras, gamtos mokslai, fizika, N 002).

**Nariai:**

**prof. dr. Jurgis Barkauskas** (Vilniaus universitetas, gamtos mokslai, chemija, N 003).

**prof. dr. Linas Kliučininkas** (Kauno technologijos universitetas, technologijos mokslai, aplinkos inžinerija, T 004).

**dr. Jixin Qiao** (Danijos technikos universitetas, gamtos mokslai, chemija, N 003).

**dr. Arūnas Gudelis** (Fizinių ir technologijos mokslų centras, gamtos mokslai, fizika, N 002).

Disertacija ginama viešame Gynimo tarybos posėdyje 2023 m. rugsėjo mėn. 22 d. 10:00 val. Fizinių ir technologijos mokslų centro D401 auditorijoje.

Adresas: Saulėtekio al. 3, D401, Vilnius, Lietuva.

Tel. +37052649211; el. paštas [office@ftmc.lt](mailto:office@ftmc.lt)

Disertaciją galima peržiūrėti Fizinių ir technologijos mokslų centro bei Vilniaus universiteto bibliotekose ir VU interneto svetainėje adresu: [www.vu.lt/lt/naujienos/ivykiu-kalendorius](http://www.vu.lt/lt/naujienos/ivykiu-kalendorius)

## CONTENTS

ABBREVIATIONS.....	8
INTRODUCTION.....	9
THE MAIN AIM AND TASKS .....	12
NOVELTY .....	13
DEFENSIVE STATEMENTS .....	13
CONTRIBUTION OF THE AUTHOR .....	13
LIST OF PUBLICATIONS.....	14
LIST OF CONFERENCES .....	14
1. LITERATURE REVIEW .....	16
1.1. Radionuclides .....	16
1.2. Anthropogenic sources of caesium, cobalt, and europium.....	20
1.3. Adsorbents: characteristics and adsorption studies .....	22
1.3.1. Characteristics of adsorbents .....	23
1.3.1.1. Phyllosilicates and zeolites.....	23
1.3.1.2. Chitosan.....	26
1.3.1.3. Graphene oxide.....	28
1.3.1.4. Prussian blue, magnetite, and maghemite .....	30
1.3.2. Adsorption studies .....	32
1.3.2.1. Adsorption of caesium.....	33
1.3.2.2. Adsorption of cobalt.....	38
1.3.2.3. Adsorption of europium .....	40
1.4. Adaptive neuro-fuzzy inference system .....	45
2. MATERIALS AND METHODS .....	47
2.1. Preparation of composites .....	47
2.1.1. Preparation of muscovite mica clay-graphene oxide-maghemite-magnetite composite.....	47
2.1.2. Preparation of Prussian blue-graphene oxide and magnetite- Prussian blue-graphene oxide composites.....	48

2.1.3. Preparation of chitosan-mineral composites.....	49
2.2. Characterisation.....	50
2.3. Batch experiments .....	51
2.4. Adsorption isotherms, kinetics, and thermodynamics.....	53
2.5. ANFIS development.....	55
3. RESULTS AND DISCUSSION .....	59
3.1. Material characterisation .....	59
3.1.1. XRD .....	59
3.1.2. ATR-FTIR and FTIR.....	62
3.1.3. Raman spectroscopy.....	70
3.1.4. XPS.....	71
3.1.5. Mössbauer spectroscopy.....	79
3.1.6. SEM and TEM.....	81
3.2. Primary adsorption studies for MSMC-GO-MGH-MG composites and for original components.....	83
3.3. Adsorption studies.....	84
3.3.1. Effect of initial concentration.....	84
3.3.2. Effect of pH.....	87
3.3.3. Effect of contact time .....	89
3.3.4. Effect of the mass of the adsorbent and thermodynamic study ..	90
3.4. Adsorption isotherms and kinetics .....	91
3.5. The suggested adsorption mechanism.....	102
3.6. ANFIS .....	106
CONCLUSIONS.....	118
SANTRAUKA .....	120
ĮVADAS.....	120
PAGRINDINIS TIKSLAS IR UŽDAVINIAI .....	123
NAUJUMAS .....	124
GINAMIEJI TEIGINIAI.....	124
AUTORIAUS INDĖLIS .....	124

4. EKSPERMENTO METODIKA.....	125
4.1. Kompozitų paruošimas.....	125
4.1.1. Muskovito žėručio molio-grafeno oksido-magemito-magnetito kompozito paruošimas.....	125
4.1.2. Berlyno mėlio-grafeno oksido ir magnetito-Berlyno mėlio-grafeno oksido kompozitų paruošimas.....	125
4.1.3. Chitozano-mineralų kompozitų paruošimas.....	126
4.2. Apibūdinimas .....	126
4.3. Sorbcijos eksperimentai .....	126
4.4. Adsorbcijos izotermos, kinetika ir termodinamika .....	128
4.5. ANFIS taikymas .....	128
5. TYRIMO REZULTATAI IR JŲ APTARIMAS .....	129
5.1. Medžiagos apibūdinimas.....	129
5.1.1. XRD .....	129
5.1.2. ATR-FTIR ir FTIR.....	129
5.1.3. Ramano spektroskopija .....	130
5.1.4. XPS.....	130
5.1.5. Mösbauerio spektroskopija.....	131
5.1.6. SEM ir TEM.....	131
5.2. MSMC-GO-MGH-MG kompozitų ir originalių komponentų pirminės adsorbcijos tyrimai .....	132
5.3. Adsorbcijos tyrimai, izotermos, kinetika ir siūlomas adsorbcijos mechanizmas .....	132
5.4. ANFIS .....	137
IŠVADOS.....	138
REFERENCES .....	140
CURRICULUM VITAE .....	168
ACKNOWLEDGMENTS/PADĖKA .....	169

## ABBREVIATIONS

ANFIS – adaptive neuro-fuzzy inference system  
ATR – attenuated total reflectance  
CS – chitosan  
CS-MSMC – chitosan-muscovite mica clay  
CS-MSMC-GLUT – chitosan-muscovite mica clay-glutaraldehyde  
CS-MSMC-ECH – chitosan-muscovite mica clay-epichlorohydrin  
CS-MSMC-STP – chitosan-muscovite mica clay-sodium tripolyphosphate  
CS-Mt-GLY – chitosan-montmorillonite-glycerol  
CS-Zeo – chitosan-zeolite  
ECH – epichlorohydrin  
FTIR – Fourier transform infrared spectroscopy  
GLUT – glutaraldehyde  
GLY – glycerol  
GO – graphene oxide  
M – magnetite  
MPBGO – magnetite-Prussian blue-graphene oxide  
MSMC – muscovite mica clay  
Mt – montmorillonite  
MGH-MG – maghemite-magnetite  
MSMC-GO-MGH-MG – muscovite mica clay-graphene oxide-maghemite-magnetite  
PB – Prussian blue  
PBGO – Prussian blue-graphene oxide  
SEM – scanning electron microscope  
TEM – transmission electron microscope  
STP – sodium tripolyphosphate  
XPS – X-ray photoelectron spectroscopy  
XRD – X-ray diffraction  
Zeo – zeolite  
ZSM-5 – zeolite Socony Mobil-5



## INTRODUCTION

Human-caused disasters such as the Chornobyl and Fukushima-Daiichi nuclear power plants and nuclear weapons testing have led to environmental pollution with anthropogenic radionuclides (RN). In addition, the potential risks related to the release of anthropogenic RN may currently arise from an increase in the amount of radioactive waste due to the active use of nuclear energy and the existence of problems related to disposal, e.g. of high-level radioactive waste. The active use of nuclear energy as a green energy source, especially in the face of energy crises, is due to the fact that in most cases it is more competitive than, for example, solar and wind energy (Jalali-Rad et al. 2004; Zhang et al. 2019; Masoudi et al. 2019; Zhidkin et al. 2020; Liu et al. 2022; Nian et al. 2022; Tong et al. 2023). Among RN, some of the most common pollutants are  $^{137}\text{Cs}$ ,  $^{60}\text{Co}$ ,  $^{152}\text{Eu}$ , and  $^{154}\text{Eu}$ .  $^{137}\text{Cs}$  is produced by the nuclear fission of uranium.  $^{60}\text{Co}$  is produced when metal structures of nuclear reactors are irradiated with neutron radiation.  $^{152}\text{Eu}$  and  $^{154}\text{Eu}$  are formed from  $^{151}\text{Eu}$  and  $^{153}\text{Eu}$  by neutron absorption. The half-lives for  $^{137}\text{Cs}$ ,  $^{60}\text{Co}$ ,  $^{152}\text{Eu}$ , and  $^{154}\text{Eu}$  are 30.17, 5.27, 13.5, and 8.6 years, respectively. These RN are among the toxic pollutants that are also carcinogenic (IAEA 1963; Directive 1966; Carter et al. 1993; Jalali-Rad et al. 2004; Peterson et al. 2007; Fazal-ur-Rehman and Akram 2017; Vanhoudt et al. 2018; Garty et al. 2020; Wang et al. 2022; Tong et al. 2023; Xiong et al. 2023). The result of anthropogenic saturation of the non-radioactive forms of cobalt and europium in the environment is their active use in industry. For example, cobalt is used in the electronics, mining, alloy, catalyst, pigment, planting, and steel industries, while europium is mainly used in the electronics industry, e.g. in fluorescent lamps, light-emitting diodes, portable wireless devices, smartphones, optical fibres, and flat panel displays. As for non-radioactive caesium, its commercial use is limited due to its high reactivity and is mainly used as a getter for residual gas impurities in vacuum tubes, caesium iodide and fluoride in scintillation counters (ATSDR 2004; Rim et al. 2013; Liang et al. 2014; Ramos et al. 2016; Rzetala 2016; Yang et al. 2016c; Henriques et al. 2021; Montes de Oca-Palma et al. 2021). Unlike the radioactive forms of caesium, cobalt, and europium, the non-radioactive forms are less toxic, but their overexposure has negative environmental and human health impacts (Domingo 1989; ATSDR 2004, 2023; Ramos et al. 2016; Leyssens et al. 2017; Henriques et al. 2021).

Various removal methods such as ion exchange, adsorption, solvent extraction, coagulation, reverse osmosis, and electrodeposition are used to protect the environment from the effects of contamination by RN and metals

(Ca and Cox 2004; Bruggeman and Maes 2010; Newsome et al. 2015; Yu et al. 2019). Furthermore, adsorption has proven to be the most promising method for the removal of RN and metals due to its high efficiency, low cost, and simplicity (Li et al. 2014; Yang et al. 2016b; Wang et al. 2020).

Currently, more and more emphasis is being placed on obtaining highly efficient, environmentally friendly adsorbents that are based on natural materials due to their low toxicity. These materials include, for example, silicate minerals (bentonite, montmorillonite, vermiculite, illite, muscovite, biotite, zeolites, phlogopite, etc.), alginate, and chitosan (Macht et al. 2011; Uddin 2017; Ohkubo et al. 2018; Hong et al. 2019; Brix et al. 2019; Falyouna et al. 2020; Wu et al. 2020; Liu et al. 2021, 2023; Sutirman et al. 2021; Biswas et al. 2021; Gendy et al. 2021; Latrille and Bildstein 2022; Novikau and Lujaniene 2022; Ewis et al. 2022). Also in high demand are low-cost materials such as magnetite, maghemite, ferrites, Prussian blue, and nanomaterials that are several atomic layers thick, such as polymer nanosheets, graphene oxide, layered double hydroxides, etc., due to their highly reactive regions and large specific surface area (Yong et al. 2014; Modi et al. 2015; Jang et al. 2015; Liu et al. 2021, 2023; Novikau and Lujaniene 2022; Wani et al. 2022; Wang et al. 2023). Silicate minerals, chitosan, magnetite, maghemite, Prussian blue, and graphene oxide are promising adsorbents for RN and metals. They are often modified, combined with each other or with other potential adsorbents to increase the efficiency of use and minimise the number of drawbacks of these materials (Romanchuk et al. 2013; Jang et al. 2015; Jang and Lee 2016, 2018; Thakur et al. 2016; Xu et al. 2016, 2019; Kuzenkova et al. 2020; Boulanger et al. 2020, 2022; Biswas et al. 2021; Abukhadra et al. 2021).

The available studies on the adsorption of caesium ions were carried out with the following adsorbents: Biotite (Mukai et al. 2018), ammonium-pillared montmorillonite- $\text{Fe}_3\text{O}_4$  composite (Zheng et al. 2017), magnetic Prussian blue (Yang et al. 2016a), muscovite (Cornell 1993; McKinley et al. 2004; Kwong-Moses et al. 2020), magnetic Prussian blue core/shell nanoparticles (Chang et al. 2016), rayon fibres coated with chitosan and immobilised with Prussian blue (Dechojarassri et al. 2017), iron-based zeolite nanoparticles (Eljamal et al. 2019), Prussian blue analogues anchored on 3D reduced graphene oxide aerogel (Huo et al. 2021), nanostructured chitosan/molecular sieve-4A (Goyal et al. 2020), fibrous chitosan modified with metal hexacyanoferrates (Zhuang et al. 2022), magnetic Prussian blue/graphene oxide (Yang et al. 2014), montmorillonite-Prussian blue hybrid (Alamudy and Cho 2018), magnetic zeolite (Falyouna et al. 2020), chitosan-coated porous vermiculite with low expansion (Zhang et al. 2021), and magnetic bentonite-chitosan (Wang et al. 2019).

Cobalt ions on: Graphene oxide-magnetite (Tayyebi et al. 2015), magnetic chitosan/activated carbon@UiO-66 (Motaghi et al. 2022), maleic acid grafted chitosan (Zhuang et al. 2018), magnetic cyanoethyl chitosan beads (Zhang et al. 2020c), magnetic graphene oxide/chitosan (Zhuang and Wang 2019), chitosan (Khan et al. 2022), and chitosan-montmorillonite (Wang et al. 2014).

Europium ions (note: in adsorption studies they are used as a homologue of the trivalent actinides (Shao et al. 2009; Kapnisti et al. 2018; Zheng et al. 2020)) on: Muscovite (Pan et al. 2017; Wu et al. 2021), magnetic amidoxime-functionalised MCM-41 (Liu et al. 2022), phlogopite (Wu et al. 2021), granite (Li et al. 2019), sodium dodecyl sulphate-modified molybdenum disulphide (Wang et al. 2020), magnetite decorated graphene oxide (Li et al. 2014), NKF-6 zeolite (Khan et al. 2021), zeolite Socony Mobil-5 (Shao et al. 2009), magnetite nanoparticles (Carvalho et al. 2016), titanate nanorings (Zheng et al. 2020), synthetic maghemite (Xu et al. 2016), chitosan (Cadogan et al. 2014), and *Saccharomyces cerevisiae* immobilised in glutaraldehyde cross-linked chitosan (Arunraj et al. 2019).

Although a large number of studies have been carried out on the adsorption of Cs(I), Co(II), and Eu(III) on various adsorbents, no work has been found for the adsorption of Cs(I) and Co(II) on MSMC-GO-MGH-MG composite. For Cs(I), Co(II), and Eu(III) on CS-MSMC, CS-MSMC-GLUT, CS-MSMC-ECH, CS-MSMC-STP, CS-Mt-GLY, and CS-Zeo composites. In addition, the available analogues of these composites, such as chitosan-montmorillonite/bentonite/kaolinite, show good adsorption capacity and efficiency for various dyes and heavy metals (Biswas et al. 2021), and in a recent work by Esmaeili and Tamjidi (2020), the resulting montmorillonite-graphene oxide-magnetite composite showed high efficiency in removing hexavalent chromium compared to original montmorillonite and magnetite-montmorillonite. Although there is already work on the adsorption of caesium on magnetic Prussian blue and magnetic Prussian blue graphene oxide, this work provides information on the use of new approaches in the synthesis of these composites to increase their adsorption capacity.

Currently, machine learning is actively used in adsorption studies. It allows the prediction of adsorption capacity or efficiency of adsorbents as a function of different conditions (pH, contact time, initial concentration, etc.), which in turn is useful in the subsequent design of experiments, saving time, and reagent consumption. The most commonly used modelling methods are response surface methodology, artificial neural network, neural general regression network, and adaptive neuro-fuzzy inference system, of which ANFIS gives the best prediction result. ANFIS is a powerful tool for

describing non-linear changes in complex systems, such as adsorbent-adsorbate, and is a multi-level network whose principle is to construct a set of fuzzy if-then rules and to create stipulated input-output pairs. ANFIS combines artificial neural network approaches and fuzzy logic (Amiri et al. 2013; Rezaei et al. 2017; Mendoza-Castillo et al. 2018; Dolatabadi et al. 2018; Souza et al. 2018; Sadeghizadeh et al. 2019; Foroutan et al. 2020; Khomeyrani et al. 2021; Onu et al. 2021). Previously, ANFIS has been used for the following systems: tropical soils-Cu(II)/Cd(II)/Pb(II) (Agbaogun et al. 2022), functionalised bentonite-Pb(II)/As(V) (Lingamdinne et al. 2023), ostrich bone ash-Pb(II) (Amiri et al. 2013), X and Y faujasite zeolites-methane (Rezaei et al. 2017), activated carbon-Ni(II) (Souza et al. 2018), hydroxyapatite/chitosan-Pb(II) (Sadeghizadeh et al. 2019), chitosan/clay/Fe<sub>3</sub>O<sub>4</sub>-Cr(VI) (Foroutan et al. 2020), and Nteje clay-eriochrome black-T (Onu et al. 2021). However, no work was found on the application of ANFIS for the systems MSMC-GO-MGH-MG-Cs(I)/Co(II), chitosan-mineral-Cs(I)/Co(II)/Eu(III), PBGO-Cs(I), and MPBGO-Cs(I).

## THE MAIN AIM AND TASKS

The aim of this work is to evaluate the adsorption properties of muscovite mica clay-graphene oxide-maghemite-magnetite composite for caesium and cobalt ions, of Prussian blue-graphene oxide and magnetite-Prussian blue-graphene oxide composites for caesium, and of chitosan-mineral composites for caesium, cobalt, and europium. In addition, to develop the ANFIS model using the experimental datasets obtained. To achieve the aims of the study, the following tasks were formulated:

1. To synthesise MSMC-GO-MGH-MG, PBGO, MPBGO, CS-MSMC, CS-MSMC-GLUT, CS-MSMC-ECH, CS-MSMC-STP, CS-Mt-GLY, and CS-Zeo composites.
2. To characterise the resulting composites.
3. To investigate ion adsorption on composites in batch experiments.
4. To analyse the adsorption behaviour of ions on composites using adsorption isotherms, kinetics, and thermodynamics.
5. To investigate the mechanism of ion adsorption on composites.
6. To train and test the ANFIS model to predict the adsorption capacity of composites.

## NOVELTY

As far as is currently known, the composite MSMC-GO-MGH-MG was first used in the adsorption studies for caesium and cobalt, while CS-MSMC, CS-MSMC-GLUT, CS-MSMC-ECH, CS-MSMC-STP, CS-Mt-GLY, and CS-Zeo composites were used for caesium, cobalt, and europium. New approaches for the synthesis of PBGO and MPBGO composites as caesium adsorbents were developed and used. Furthermore, the ANFIS model was created and applied for the first time to the systems MSMC-GO-MGH-MG-Cs(I)/Co(II), PBGO-Cs(I), MPBGO-Cs(I), and chitosan-mineral-Cs(I)/Co(II)/Eu(III).

## DEFENSIVE STATEMENTS

1. The composite MSMC-GO-MGH-MG has a sufficiently high adsorption capacity for Cs(I) and Co(II). The suggested mechanism for the adsorption of Cs(I) and Co(II) is ion exchange, complexation, and electrostatic attraction.

2. The composites PBGO 2.1, PBGO 2.2, and MPBGO 3.2 adsorb Cs(I) better than MPBGO 2.3. The suggested mechanism for Cs(I) adsorption is complexation, ion exchange, and ion trapping.

3. Among the chitosan-mineral composites, the composites CS-MSMC, CS-MSMC-ECH, and CS-Mt-GLY have the highest adsorption capacity for Cs(I) and Co(II), while the composite CS-Zeo has the highest adsorption capacity for Eu(III).

4. ANFIS has good performance and generalisation ability to predict the adsorption capacity of composites.

## CONTRIBUTION OF THE AUTHOR

The author of the work synthesised MSMC-GO-MGH-MG composites, planned and conducted studies on the adsorption of caesium and cobalt in batch experiments. Participated in the synthesis of chitosan-mineral composites and the subsequent adsorption studies. Participated in the analysis and interpretation of the results, designed graphical illustrations, wrote manuscripts, and presented the results at scientific conferences.

## LIST OF PUBLICATIONS

1. **Novikau R**, Lujanienė G (2022) Adsorption behaviour of pollutants: Heavy metals, radionuclides, organic pollutants, on clays and their minerals (raw, modified and treated): A review. *J Environ Manage* 309:114685.

<https://doi.org/10.1016/J.JENVMAN.2022.114685>

2. **Novikau R**, Lujanienė G, Pakštas V, et al (2022) Adsorption of caesium and cobalt ions on the muscovite mica clay-graphene oxide- $\gamma$ -Fe<sub>2</sub>O<sub>3</sub>-Fe<sub>3</sub>O<sub>4</sub> composite. *Environ Sci Pollut Res* 29:74933–74950.

<https://doi.org/10.1007/s11356-022-21078-0>

3. Lujanienė G, **Novikau R**, Leščinskytė A, et al (2023) Prussian blue composites for Cs adsorption – modification of the method and modelling of the adsorption processes. *J Radioanal Nucl Chem* 332:1033–1045.

<https://doi.org/10.1007/s10967-022-08660-z>

## OTHER PUBLICATIONS

4. Lujanienė G, **Novikau R**, Joel EF, et al (2022) Preparation of Graphene Oxide-Maghemite-Chitosan Composites for the Adsorption of Europium Ions from Aqueous Solutions. *Molecules* 27:8035.

<https://doi.org/10.3390/molecules27228035>

## LIST OF CONFERENCES

1. **Raman Novikau**, Galina Lujanienė, Vidas Pakštas, Martynas Talaikis, Audrius Drabavičius, Arnas Naujokaitis, DEVELOPMENT OF NANOCOMPOSITES BASED ON CLAY, GRAPHENE OXIDE AND MAGNETITE/MAGHEMITE, 64<sup>th</sup> International Conference for Students of Physics and Natural Sciences „Open Readings 2021“, 16–19<sup>th</sup> of March, 2021, Vilnius, Lithuania, poster.

2. **Raman Novikau**, Galina Lujanienė, Vidas Pakštas, Martynas Talaikis, Audrius Drabavičius, Arnas Naujokaitis, Sergej Šemčuk, ADSORPTION OF CESIUM AND COBALT ONTO NANOCOMPOSITE BASED ON CLAY, GRAPHENE OXIDE AND MAGNETITE/MAGHEMITE, 16<sup>th</sup> international conference of Lithuanian society of chemistry, 24 September 2021, Vilnius, Lithuania, poster.

3. **Raman Novikau**, Galina Lujanienė, Vidas Pakštas, Martynas Talaikis, Audrius Drabavičius, Arnas Naujokaitis, Sergej Šemčuk, ADSORPTION BEHAVIOR OF CS<sup>+</sup> AND CO<sup>2+</sup> ON CLAY-GRAPHENE OXIDE-MAGNETITE/MAGHEMITE COMPOSITE, 3rd ICSTR Athens -

International Conference on Science & Technology Research, 8<sup>th</sup> of October 2021, Athens, Greece, poster.

4. **Raman Novikau**, Galina Lujanienė, Vidas Pakštas, Martynas Talaikis, Audrius Drabavičius, Arnas Naujokaitis, Sergej Šemčuk, STUDY OF CESIUM AND COBALT ADSORPTION BY NANOCOMPOSITE BASED ON CLAY, GRAPHENE OXIDE AND MAGNETITE/MAGHEMITE, Conference of Doctoral Students and Young Researchers FizTech2021, 20–21<sup>th</sup> October 2021, Vilnius, Lithuania, oral presentation.

5. **Raman Novikau**, and Galina Lujanienė, ADSORPTION MECHANISM OF CAESIUM AND COBALT ON MUSCOVITE MICA CLAY-GRAPHENE OXIDE- $\gamma$ -Fe<sub>2</sub>O<sub>3</sub>/Fe<sub>3</sub>O<sub>4</sub> COMPOSITE, 65<sup>th</sup> International Conference for Students of Physics and Natural Sciences „Open Readings 2022“, 15–18<sup>th</sup> March, 2022, Vilnius, Lithuania, poster.

6. Galina Lujanienė, **Raman Novikau**, Agnė Leščinskytė, Karolina Karalevičiūtė, Sergej Šemčuk, Kęstutis Mažeika, Vidas Pakštas, Saulius Tumėnas, Beata Šilobritienė, A comparison of Prussian blue-graphene oxide and chitosan-clay based nano-composites for the pre-concentration of radiocesium from seawater. 6<sup>th</sup> - International Nuclear Chemistry Congress. Programme and Abstracts Book, 29<sup>th</sup> August – 2nd September, 2022, Lanzhou, China, p. 145–146, poster.

7. **Raman Novikau**, Galina Lujanienė, Vidas Pakštas, Martynas Talaikis, Vitalija Jasulaitienė, Audrius Drabavičius, Arnas Naujokaitis, Investigation of the adsorption behaviour of Cs(I) and Co(II) on the muscovite mica clay/graphene oxide/ $\gamma$ -Fe<sub>2</sub>O<sub>3</sub>-Fe<sub>3</sub>O<sub>4</sub> composite, 12<sup>th</sup> Conference of Doctoral Students and Young Researchers FizTech2022, 19–20<sup>th</sup> October, 2022, Vilnius, Lithuania, oral presentation.

# 1. LITERATURE REVIEW

## 1.1. Radionuclides

Radionuclides are radioactive isotopes of chemical elements with varying mass numbers, some of which occur naturally in the environment, while others are the result of anthropogenic activities. Each radionuclide emits radiation at its own specific rate, which is measured by the half-life, i.e. the time it takes for half the atoms of a radioactive substance to decay. Based on this parameter, radionuclides are divided into short-lived and long-lived with half-lives of less than and more than 10 days, respectively. According to toxicity, and in particular according to the original classification, radionuclides are divided into three categories – highly toxic, medium toxic (Upper Sub-Group A and Lower Sub-Group B), and low toxic (IAEA 1963). According to a more recent classification (Carter et al. 1993), radionuclides are divided into four groups, with the toxicity of radionuclides decreasing from the first to the fourth group (Table 1). This classification is based on the annual limit on intake (ALI) and the specific activity. The ALI is the derived limit for the amount of radioactive material that an adult worker inhales or ingests in a year.

**Table 1.** Classification of the toxicity of radionuclides based on ALI and specific activity by Carter et al. (1993).

<b>Group 1</b>
<sup>225</sup> Ac, <sup>226</sup> Ac, <sup>227</sup> Ac, <sup>241</sup> Am, <sup>242m</sup> Am, <sup>247</sup> Bk, <sup>249</sup> Bk, <sup>113</sup> Cd, <sup>113m</sup> Cd, <sup>144</sup> Ce, <sup>246</sup> Cf, <sup>248</sup> Cf, <sup>249</sup> Cf, <sup>250</sup> Cf, <sup>251</sup> Cf, <sup>252</sup> Cf, <sup>253</sup> Cf, <sup>254</sup> Cf, <sup>240</sup> Cm, <sup>242</sup> Cm, <sup>243</sup> Cm, <sup>244</sup> Cm, <sup>246</sup> Cm, <sup>250</sup> Cm, <sup>253</sup> Es, <sup>254</sup> Es, <sup>254m</sup> Es, <sup>252</sup> Fm, <sup>253</sup> Fm, <sup>257</sup> Fm, <sup>148</sup> Gd, <sup>178m</sup> Hf, <sup>115</sup> In, <sup>258</sup> Md, <sup>194</sup> Os, <sup>228</sup> Pa, <sup>230</sup> Pa, <sup>232</sup> Pa, <sup>210</sup> Pb, <sup>210</sup> Po, <sup>236</sup> Pu, <sup>238</sup> Pu, <sup>24</sup> Pu, <sup>223</sup> Ra, <sup>224</sup> Ra, <sup>225</sup> Ra, <sup>228</sup> Ra, <sup>106</sup> Ru, <sup>90</sup> Sr, <sup>90</sup> Sr+ <sup>90</sup> Y, <sup>227</sup> Th, <sup>228</sup> Th, <sup>229</sup> Th, <sup>44</sup> Ti, <sup>230</sup> U, <sup>232</sup> U.
<b>Group 2</b>
<sup>224</sup> Ac, <sup>228</sup> Ac, <sup>105</sup> Ag, <sup>106m</sup> Ag, <sup>108m</sup> Ag, <sup>110m</sup> Ag, <sup>111</sup> Ag, <sup>242</sup> Am, <sup>243</sup> Am, <sup>244</sup> Am, <sup>72</sup> As, <sup>73</sup> As, <sup>74</sup> As, <sup>76</sup> As, <sup>211</sup> At, <sup>195</sup> Au, <sup>198</sup> Au, <sup>198m</sup> Au, <sup>128</sup> Ba, <sup>133</sup> Ba, <sup>140</sup> Ba, <sup>205</sup> Bi, <sup>206</sup> Bi, <sup>207</sup> Bi, <sup>210</sup> Bi, <sup>212</sup> Bi, <sup>213</sup> Bi, <sup>214</sup> Bi, <sup>245</sup> Bk, <sup>250</sup> Bk, <sup>45</sup> Ca, <sup>47</sup> Ca, <sup>109</sup> Cd, <sup>115</sup> Cd, <sup>115m</sup> Cd, <sup>134</sup> Ce, <sup>139</sup> Ce, <sup>141</sup> Ce, <sup>143</sup> Ce, <sup>244</sup> Cf, <sup>238</sup> Cm, <sup>241</sup> Cm, <sup>245</sup> Cm, <sup>248</sup> Cm, <sup>56</sup> Co, <sup>57</sup> Co, <sup>58</sup> Co, <sup>60</sup> Co, <sup>134</sup> Cs, <sup>136</sup> Cs, <sup>137</sup> Cs, <sup>166</sup> Dy, <sup>172</sup> Er, <sup>251</sup> Es, <sup>146</sup> Eu, <sup>148</sup> Eu, <sup>150</sup> Eu, <sup>152</sup> Eu, <sup>154</sup> Eu, <sup>155</sup> Eu, <sup>156</sup> Eu, <sup>59</sup> Fe, <sup>254</sup> Fm, <sup>255</sup> Fm, <sup>222</sup> Fr, <sup>223</sup> Fr, <sup>146</sup> Gd, <sup>151</sup> Gd, <sup>153</sup> Gd, <sup>68</sup> Ge, <sup>69</sup> Ge, <sup>172</sup> Hf, <sup>175</sup> Hf, <sup>179m</sup> Hf, <sup>181</sup> Hf, <sup>194</sup> Hg, <sup>203</sup> Hg, <sup>166</sup> Ho, <sup>166m</sup> Ho, <sup>124</sup> I, <sup>125</sup> I, <sup>126</sup> I, <sup>130</sup> I, <sup>131</sup> I, <sup>133</sup> I, <sup>114m</sup> In, <sup>190</sup> Ir, <sup>192</sup> Ir, <sup>192m</sup> Ir, <sup>194</sup> Ir, <sup>194m</sup> Ir, <sup>140</sup> La, <sup>171</sup> Lu, <sup>172</sup> Lu, <sup>173</sup> Lu, <sup>174</sup> Lu, <sup>174m</sup> Lu, <sup>177m</sup> Lu, <sup>257</sup> Md, <sup>28</sup> Mg, <sup>52</sup> Mn, <sup>54</sup> Mn, <sup>93</sup> Mo, <sup>99</sup> Mo, <sup>22</sup> Na, <sup>93m</sup> Nb, <sup>95</sup> Nb, <sup>96</sup> Nb, <sup>147</sup> Nd, <sup>56</sup> Ni, <sup>66</sup> Ni, <sup>236</sup> Np, <sup>236m</sup> Np, <sup>238</sup> Np, <sup>185</sup> Os, <sup>191</sup> Os, <sup>32</sup> P, <sup>227</sup> Pa, <sup>231</sup> Pa, <sup>233</sup> Pa, <sup>211</sup> Pb, <sup>212</sup> Pb, <sup>214</sup> Pb, <sup>100</sup> Pd, <sup>143</sup> Pm, <sup>144</sup> Pm, <sup>145</sup> Pm, <sup>146</sup> Pm, <sup>147</sup> Pm, <sup>148</sup> Pm, <sup>148m</sup> Pm, <sup>149</sup> Pm, <sup>142</sup> Pr, <sup>143</sup> Pr, <sup>234</sup> Pu, <sup>239</sup> Pu, <sup>240</sup> Pu, <sup>242</sup> Pu, <sup>246</sup> Pu, <sup>226</sup> Ra, <sup>226+d</sup> Ra, <sup>83</sup> Rb, <sup>84</sup> Rb, <sup>86</sup> Rb, <sup>87</sup> Rb, <sup>101</sup> Rh, <sup>102</sup> Rh, <sup>102m</sup> Rh, <sup>182m</sup> Rh, <sup>184</sup> Rh,



184mRh, 186Rh, 103Ru, 120mSb, 122Sb, 124Sb, 125Sb, 126Sb, 127Sb, 44mSc, 46Sc, 48Sc, 75Se, 32Si, 145Sm, 113Sn, 117mSn, 119mSn, 123Sn, 125Sn, 82Sr, 85Sr, 89Sr, 179Ta, 182Ta, 183Ta, 149Tb, 156Tb, 158Tb, 160Tb, 161Tb, 95mTc, 97mTc, 121mTe, 123mTe, 125mTe, 127mTe, 129mTe, 131mTe, 132Te, 226Th, 230Th, 234Th, 167Tm, 170Tm, 171Tm, 172Tm, 233U, 234U, 237U, 48V, 188W, 88Y, 90Y, 91Y, 166Yb, 169Yb, 65Zn, 72Zn, 88Zr, 95Zr, 97Zr.
<b>Group 3</b>
102Ag, 103Ag, 104Ag, 104mAg, 106Ag, 112Ag, 115Ag, 238Am, 239Am, 240Am, 244mAm, 245Am, 246Am, 246mAm, 69As, 70As, 71As, 77As, 78As, 207At, 193Au, 194Au, 199Au, 200Au, 200mAu, 126Ba, 131Ba, 133mBa, 135mBa, 139Ba, 141Ba, 142Ba, 10Be, 7Be, 200Bi, 201Bi, 202Bi, 203Bi, 246Bk, 74mBr, 80mBr, 74Br, 75Br, 76Br, 77Br, 80Br, 82Br, 83Br, 84Br, 14C, 104Cd, 107Cd, 117Cd, 117mCd, 135Ce, 137Ce, 137mCe, 38Cl, 39Cl, 247Cm, 249Cm, 58mCo, 62mCo, 55Co, 61Co, 48Cr, 49Cr, 51Cr, 125Cs, 127Cs, 129Cs, 130Cs, 131Cs, 132Cs, 134mCs, 138Cs, 60Cu, 61Cu, 64Cu, 67Cu, 155Dy, 157Dy, 159Dy, 165Dy, 161Er, 169Er, 171Er, 250Es, 145Eu, 149Eu, 152mEu, 157Eu, 158Eu, 18F, 52Fe, 55Fe, 60Fe, 65Ga, 66Ga, 67Ga, 68Ga, 70Ga, 72Ga, 73Ga, 145Gd, 147Gd, 149Gd, 159Gd, 66Ge, 67Ge, 71Ge, 75Ge, 77Ge, 78Ge, 3H, 170Hf, 173Hf, 177mHf, 180mHf, 182mHf, 183Hf, 184Hf, 193Hg, 193mHg, 195Hg, 195mHg, 197Hg, 197mHg, 199mHg, 155Ho, 167Ho, 120I, 120mI, 121I, 123I, 128I, 132I, 132mI, 134I, 135I, 109In, 110In, 110mIn, 111In, 113mIn, 115mIn, 116mIn, 117In, 117mIn, 119mIn, 182Ir, 184Ir, 185Ir, 186Ir, 187Ir, 188Ir, 189Ir, 190mIr, 195Ir, 195mIr, 42K, 43K, 44K, 45K, 131La, 132La, 135La, 141La, 142La, 143La, 169Lu, 170Lu, 176mLu, 177Lu, 178Lu, 178mLu, 179Lu, 52mMn, 51Mn, 56Mn, 101Mo, 90Mo, 93mMo, 24Na, 89Nb, 89mNb, 90Nb, 94Nb, 95mNb, 97Nb, 98Nb, 136Nd, 138Nd, 139mNd, 149Nd, 151Nd, 57Ni, 63Ni, 65Ni, 232Np, 234Np, 235Np, 237Np, 239Np, 240Np, 181Os, 182Os, 191mOs, 193Os, 33P, 234Pa, 195mPb, 198Pb, 199Pb, 200Pb, 201Pb, 202mPb, 203Pb, 209Pb, 101Pd, 103Pd, 109Pd, 141Pm, 150Pm, 151Pm, 203Po, 205Po, 207Po, 137Pr, 138mPr, 139Pr, 142mPr, 144Pr, 145Pr, 147Pr, 186Pt, 188Pt, 189Pt, 191Pt, 193mPt, 195mPt, 197Pt, 197mPt, 199Pt, 200Pt, 237Pu, 243Pu, 245Pu, 227Ra, 82mRb, 79Rb, 81Rb, 88Rb, 89Rb, 100Rh, 101mRh, 105Rh, 106mRh, 181Rh, 182Rh, 188Rh, 188mRh, 189Rh, 99Rh, 99mRh, 105Ru, 94Ru, 97Ru, 35S, 116mSb, 118mSb, 119Sb, 126mSb, 128mSb, 129Sb, 130Sb, 131Sb, 43Sc, 44Sc, 47Sc, 49Sc, 73mSe, 70Se, 73Se, 81mSe, 83Se, 31Si, 141Sm, 141mSm, 142Sm, 151Sm, 153Sm, 156Sm, 110Sn, 121Sn, 121mSn, 123mSn, 127Sn, 128Sn, 80Sr, 81Sr, 83Sr, 87mSr, 91Sr, 92Sr, 172Ta, 173Ta, 174Ta, 175Ta, 176Ta, 177Ta, 178Ta, 180mTa, 185Ta, 147Tb, 150Tb, 151Tb, 153Tb, 154Tb, 155Tb, 156mTb, 157Tb, 104Tc, 93Tc, 93mTc, 94Tc, 94mTc, 95Tc, 96Tc, 99mTc, 116Te, 121Te, 123Te, 127Te, 129Te, 131Te, 133Te, 133mTe, 134Te, 231Th, 45Ti, 194mTl, 195Tl, 197Tl, 198Tl, 198mTl, 199Tl, 200Tl, 201Tl, 202Tl, 204Tl, 166Tm, 173Tm, 231U, 236U, 239U, 240U, 47V, 49V, 176W, 177W, 178W, 181W, 185W, 187W, 86Y, 86mY, 87Y, 90mY, 91mY, 92Y, 93Y, 94Y, 95Y, 175Yb, 177Yb, 178Yb, 62Zn, 63Zn, 69Zn, 69mZn, 71mZn, 86Zr, 89Zr.
<b>Group 4</b>
126A, 237Am, 41Ar, 201Au, 131mBa, 210mBi, 11C, 41Ca, 36Cl, 60mCo, 135Cs, 135mCs, 165Er, 152Gd, 182Hf, 157Ho, 159Ho, 161Ho, 162Ho, 162mHo, 164Ho, 164mHo, 129I, 112In, 40K, 74Kr, 76Kr, 77Kr, 81mKr, 83mKr, 85Kr, 85mKr, 87Kr, 88Kr, 137La, 138La, 176Lu, 53Mn, 88Nb, 139Nd, 141Nd, 59Ni, 233Np, 180Os, 189mOs, 202Pb, 205Pb, 107Pd, 203mPo, 136Pr, 193Pt, 235Pu, 244Pu, 81mRb, 103mRh, 107Rh, 177Rh, 178Rh, 186mRh, 187Rh, 115Sb, 116Sb,

$^{117}\text{Sb}$ , $^{120}\text{Sb}$ , $^{124\text{m}}\text{Sb}$ , $^{128}\text{Sb}$ , $^{79}\text{Se}$ , $^{81}\text{Se}$ , $^{146}\text{Sm}$ , $^{147}\text{Sm}$ , $^{155}\text{Sm}$ , $^{111}\text{Sn}$ , $^{126}\text{Sn}$ , $^{85\text{m}}\text{Sr}$ , $^{180}\text{Ta}$ , $^{182\text{m}}\text{Ta}$ , $^{186}\text{Ta}$ , $^{101}\text{Tc}$ , $^{96\text{m}}\text{Tc}$ , $^{97}\text{Tc}$ , $^{98}\text{Tc}$ , $^{99}\text{Tc}$ , $^{\text{Nat}}\text{Th}$ , $^{\text{Ore}}\text{Th}$ , $^{232}\text{Th}$ , $^{194}\text{Tl}$ , $^{162}\text{Tm}$ , $^{175}\text{Tm}$ , $^{\text{Nat}}\text{U}$ , $^{\text{Ore}}\text{U}$ , $^{235}\text{U}$ , $^{238}\text{U}$ , $^{179}\text{W}$ , $^{131\text{m}}\text{Xe}$ , $^{133}\text{Xe}$ , $^{133\text{m}}\text{Xe}$ , $^{135}\text{Xe}$ , $^{135\text{m}}\text{Xe}$ , $^{162}\text{Yb}$ , $^{167}\text{Yb}$ , $^{93}\text{Zr}$ .
---

Consider some of the most common pollutants among radionuclides:  $^{137}\text{Cs}$ ,  $^{60}\text{Co}$ , and  $^{152, 154}\text{Eu}$ . The isotopes listed are the most common radioactive forms of these elements, which are also active in the medical, commercial, and military fields.

*Caesium-137* is produced by nuclear fission and is also a by-product in nuclear reactors and nuclear weapons testing. It emits gamma radiation and decays into stable barium-137,  $^{137}\text{Cs}$  has a half-life of 30.17 years (Alexander 2015). It is used in small quantities, e.g. to calibrate a Geiger-Muller counter, and in large quantities in devices for radiation therapy of oncological diseases. Environmental contamination with  $^{137}\text{Cs}$  occurs in accidents at nuclear power plant reactors and in nuclear fallout, but only in ground-based nuclear explosions (Yamamoto et al. 1985; IAEA 2006; Buddemeier and Dillon 2009; Yasunari et al. 2011). In the environment, it binds with chlorides to form a crystalline powder, which is why it easily spreads through the air and dissolves in water. In addition,  $^{137}\text{Cs}$  binds strongly to soil and concrete, but does not penetrate deeply underground. When it falls out of the atmosphere,  $^{137}\text{Cs}$  concentrates in lichens. Higher plants and fungi growing on soils contaminated with it take up and accumulate  $^{137}\text{Cs}$ , whereupon it enters the food chain (Hove et al. 1990; Sawidis et al. 1990; Ahman and Ahman 1994; Hoshi et al. 1994; Zibold et al. 2001).

*Cobalt-60* is a by-product of nuclear reactors and is formed by the action of neutron radiation on reactor metal structures such as steel rods. It is also obtained on an industrial scale by neutron activation of stable cobalt. Like  $^{137}\text{Cs}$ , it is a source of gamma radiation with a half-life of 5.27 years, decaying into the stable isotope nickel-60 (McHaffie et al. 2012; Alexander 2015). Used in levelling devices, thickness gauges, and radiotherapy equipment (Meredith and Massey 1977; EPA 2022a). It is mainly found in nuclear waste, wastewater near nuclear power plants, and spent nuclear fuel reprocessing plants. Unlike  $^{137}\text{Cs}$ , its mobility in the environment and uptake by plants is moderate. The transfer of  $^{60}\text{Co}$  through the food chain is limited and the higher up the food chain an organism is, the lower its concentration coefficient (Adam et al. 2010).

*Europium-152* and *-154* are products of nuclear fission and are produced from  $^{151}\text{Eu}$  and  $^{153}\text{Eu}$  by the absorption of neutrons. Another way to obtain radioisotopes of europium is chain absorption in Sm.  $^{152}\text{Eu}$  and  $^{154}\text{Eu}$  decay by

beta-emission into unstable  $^{152}\text{Gd}$  and stable  $^{154}\text{Gd}$ , respectively. The half-lives are 13.5 and 8.6 for  $^{152}\text{Eu}$  and  $^{154}\text{Eu}$ , respectively (IAEA 1998; Bolsunovsky et al. 2017). The use of europium radioisotopes is limited and mainly serves as a reference standard for the calibration of gamma-ray spectrometers (Iwahara et al. 2009; Ravindra et al. 2022). The radioisotopes  $^{152}\text{Eu}$  and  $^{154}\text{Eu}$  can be found in nuclear reactor structures exposed to neutron radiation, such as bioshield concrete, graphite core, and control rods, because they contain the isotopes that precede them (IAEA 1998). These radioisotopes may also be present in spent fuel reprocessing facilities in addition to nuclear reactor structures (Niese and Gleisberg 1996). In addition,  $^{154}\text{Eu}$  is also produced during the production of medical-grade  $^{153}\text{Sm}$  in a high-flux nuclear reactor (Van De Voorde et al. 2018). Traces of  $^{152}\text{Eu}$  and  $^{154}\text{Eu}$  are present in soil around the globe from radioactive fallout (Peterson et al. 2007; Hu et al. 2010). In addition, their content is observed in water near nuclear reactors. (Linnik et al. 2006; Bolsunovsky et al. 2017). Europium radioisotopes tend to be among the most immobile in the environment (Peterson et al. 2007). Plants growing in an area contaminated with  $^{152}\text{Eu}$  and  $^{154}\text{Eu}$  accumulate them mainly in the root system, as noted by the authors of Kropatcheva et al. (2012), who also found that the most contaminated parts of the root system are the root hairs. Furthermore, the authors of Zhdanova et al. (2003) found that  $^{152}\text{Eu}$  is more actively absorbed and accumulated in micromycetes than  $^{137}\text{Cs}$ .

*Effects of  $^{137}\text{Cs}$ ,  $^{60}\text{Co}$ ,  $^{152}\text{Eu}$ , and  $^{154}\text{Eu}$  on human health.* A risk to humans may arise from both external and internal exposure to  $^{137}\text{Cs}$ ,  $^{60}\text{Co}$ ,  $^{152}\text{Eu}$ , and  $^{154}\text{Eu}$ , as they are a source of gamma radiation. External exposure leads to an increased risk of oncological diseases and, in the case of exposure to large amounts of these radionuclides, burns, acute radiation sickness and even death. When these radionuclides enter the body, mainly through the digestive tract, they accumulate in organs and tissues and are subsequently exposed to gamma radiation, increasing the risk of developing cancer.  $^{137}\text{Cs}$ , for example, mainly distributes in soft tissues and especially in muscle tissue. In the case of  $^{60}\text{Co}$ ,  $^{152}\text{Eu}$ , and  $^{154}\text{Eu}$ , most is excreted in the faeces, while a small part is absorbed into the bloodstream and distributed in the liver and kidneys, and is also absorbed in bone tissue – characteristic of  $^{60}\text{Co}$  or is found on the surface of bones – characteristic of  $^{152}\text{Eu}$  and  $^{154}\text{Eu}$  (Peterson et al. 2007; EPA 2022a, b).

## 1.2. Anthropogenic sources of caesium, cobalt, and europium

The main anthropogenic sources of  $^{137}\text{Cs}$  pollution are nuclear weapons testing, nuclear reactors, and reprocessing plants. During nuclear weapons testing, a total of  $\sim 948$  PBq (petabecquerel) of  $^{137}\text{Cs}$  were released. One of the largest accidents, which occurred on 26 April 1986 at the fourth unit of the Chernobyl nuclear power plant in Ukraine, released  $\sim 70$  PBq of  $^{137}\text{Cs}$ . Currently, forest fires in the exclusion zone are a potential source of secondary releases of  $^{137}\text{Cs}$  into the atmosphere. In April 2020, the total radioactivity of  $^{137}\text{Cs}$  emissions due to a large fire in the Chernobyl zone was 574 GBq (gigabecquerel) according to modelling. The accident at the Fukushima Daiichi nuclear power plant (11 March 2011; Fukushima Prefecture, Japan) resulted in the release of  $\sim 17$  PBq of  $^{137}\text{Cs}$ . For many years, spent fuel reprocessing plants have discharged their waste directly into rivers, seas, and oceans. For example, between 1949 and 1956, the Mayak Production Association (Chelyabinsk-65, now Ozersk, Chelyabinsk area, Russia) discharged  $1.3 \times 10^4$  TBq (terabecquerel) of  $^{137}\text{Cs}$  into the Techa River, which flows into the Kara Sea via the Ob River. Another body of water on the territory of the Mayak complex that was used as a dump is a small ( $0.5 \text{ km}^2$ ) marshy lake – Lake Karachai, where waste with a radioactivity of  $4.4 \times 10^6$  TBq (of which  $3.6 \times 10^6$  TBq of  $^{137}\text{Cs}$ ) accumulated from 1951 to 1993. From the 1960s, Lake Karachai began to dry up, contaminating an area of  $1800 \text{ km}^2$  with 12 GBq (gigabecquerel)  $^{137}\text{Cs}/\text{km}^2$ . At Sellafield (UK), the annual release of  $^{137}\text{Cs}$  from the reprocessing plant between 1974 and 1978 was 4000 TBq. In total,  $\sim 42$  PBq of  $^{137}\text{Cs}$  were released from reprocessing plants worldwide (Cochran et al. 1989; UNSCEAR 1993, 2000, 2013; Christensen et al. 1997; Solodov et al. 1998; Smith et al. 2003; Balonov et al. 2006, 2007; Novikov et al. 2006; Kobayashi et al. 2013; Talerko et al. 2021). In addition, consider some other sources of  $^{137}\text{Cs}$ . As a result of the Kyshtym disaster (29 September 1957), an area of  $20000 \text{ km}^2$  was contaminated with radioactivity of  $7.4 \times 10^5$  TBq, of which  $\sim 0.04\%$  was  $^{137}\text{Cs}$  (Christensen et al. 1997; Hu et al. 2010; IAEA 2011). In September 1987 (Brazil), a series of tamperings with a teletherapy unit (contained 51 TBq of  $^{137}\text{Cs}$ ) left in an abandoned hospital resulted in contamination of  $\sim 1 \text{ km}^2$  area (Hu et al. 2010). More recently, on 30 January 2023, Australian Mining (2023a) reported the loss of a radioactive  $^{137}\text{Cs}$  capsule (19 GBq) in Western Australia. However, as early as 2 February 2023, it was reported that the capsule had been found and the loss had no serious consequences (Australian Mining 2023b). Anthropogenic sources of non-radioactive forms of caesium in the environment include coal-fired power plants, waste incinerators, and the mining, milling and processing of pollucite

ore. For example, caesium has been found in the effluent of a coal-fired power plant and in fly ash from municipal incinerators at concentrations of 10.8 and 6.11 mg/m<sup>3</sup> (milligramme per cubic metre), respectively (ATSDR 2004).

Anthropogenic sources of <sup>60</sup>Co are nuclear weapons testing, reprocessing plants, and nuclear reactors. For example, 0.037 TBq of <sup>60</sup>Co was released into the air from the Hanford Site (USA) between 1944 and 1972. Underground nuclear weapons testing in French Polynesia resulted in the release of 560 TBq of <sup>60</sup>Co (Hu et al. 2010). <sup>60</sup>Co particles whose activity reached 46400 Bq/particle (becquerel per particle) were found in the Yenisei River. These particles may have resulted from corrosion of the primary coolant system of a nuclear reactor (the reactor is located on the territory of the Mining-and-Chemical Combine (MCC) of Rosatom (Russia)) (Bolsunovsky et al. 2017). In addition, equipment containing radioactive <sup>60</sup>Co sources in industrial and medical applications can be potential sources of <sup>60</sup>Co environmental contamination (UNSCEAR 2008). For example, in December 1983, the destruction of a radioactive source (16.7 TBq of <sup>60</sup>Co) from a teletherapy facility (Juarez, Mexico) by dismantling it for resale on metal resulted in severe contamination (Hu et al. 2010). The main anthropogenic sources of stable forms of cobalt in the atmosphere are fossil fuel combustion and sewage sludge, mining and processing of cobalt-containing ores, emissions from vehicle exhaust, processing of cobalt-containing alloys, smoking, phosphate fertilisers, and industries that use or process cobalt compounds. According to ATSDR (2023), global atmospheric emissions of cobalt from anthropogenic sources are ~4400 tonnes/year. Cobalt enters the hydrosphere from anthropogenic sources such as mining and processing of cobalt-containing ores, wastewater from paint/pigment and battery factories, process water, and effluent from coal gasification. Additional source of cobalt in water and soil is atmospheric deposition. In addition, an increase in the cobalt content of the soil can be caused by the following anthropogenic activities: Application of cobalt-containing sludge or phosphate fertiliser to soil, mining and processing of cobalt-containing ores, and disposal of cobalt-containing waste (ATSDR 2023).

Anthropogenic sources of <sup>152</sup>, <sup>154</sup>Eu mainly include nuclear weapons testing. For example, tests at the Nevada Test Site (USA) released a total of 3690 TBq of <sup>152</sup>, <sup>154</sup>Eu and tests in French Polynesia released a total of ~202 TBq of <sup>152</sup>, <sup>154</sup>Eu (Peterson et al. 2007; Hu et al. 2010). In addition, <sup>152</sup>, <sup>154</sup>Eu particles have been detected as a result of MCC activities in the Yenisei River, with <sup>152</sup>Eu activity predominating at up to 315 Bq/particle (Bolsunovsky et al. 2017). The main anthropogenic sources of non-radioactive forms of europium are fertilisers, mining, industrial dust, and vehicle exhaust (Li et al. 2022). For

example, in areas where rare earths are mined (Baotou, China), europium concentrations have reached 96.9  $\mu\text{g/L}$  (micrograms per litre) and 98.6  $\mu\text{g/L}$  in the Sidaosha River (Wei et al. 2013; Liang et al. 2014). Europium accumulation has been found in freshwater and marine fish and in the human body via drinking water, food, air, and therapeutic and diagnostic agents (Zaichick et al. 2011; Yang et al. 2016c).

### 1.3. Adsorbents: characteristics and adsorption studies

Numerous studies on the adsorption of caesium, cobalt, and europium have shown that materials such as phyllosilicates, zeolites, chitosan, graphene oxide, Prussian blue, magnetite, and maghemite can be promising adsorbents for radionuclides and metals. These materials are used in original, modified, and composite forms. It is useful to combine them with each other or with other potential adsorbents, as the resulting composites have a higher adsorption capacity than the original materials due to the synergistic effect. In addition, some disadvantages of these materials can be minimised in the composite composition. For example, the combination of phyllosilicates with graphene oxide enables the minimisation of the disadvantages of graphene oxide such as aggregation, accumulation in the water medium, and high toxicity. The use of magnetic particles (magnetite/maghemite) with phyllosilicates, graphene oxide, Prussian blue, and graphene oxide-Prussian blue composites reduces the likelihood of colloid formation of these materials during magnetic separation, thus preventing incomplete separation (Jolivet et al. 2004; Omar et al. 2009; Yuan et al. 2009; Chen et al. 2011; Cho et al. 2012; Sun et al. 2013; Gui et al. 2014; Li et al. 2014; Vincent et al. 2015; Ma et al. 2015; Tayyebi et al. 2015; Jang et al. 2015; Hastuti et al. 2016; Thakur et al. 2016; Jang and Lee 2016, 2018; Makarchuk et al. 2016; Qiu et al. 2016; Tran et al. 2017; Hu et al. 2017; Kryuchkova and Fakhrullin 2018; Liu et al. 2018b; Taher et al. 2018; Falyouna et al. 2020; Tripathy and Hota 2020; Wei et al. 2020; Hoor et al. 2020; Yu et al. 2021; Saheed et al. 2021; Biswas et al. 2021; Zhao et al. 2021; Abukhadra et al. 2021; Yang et al. 2022; Abdelmonem et al. 2023). Moreover, the use of these materials as adsorbents has the advantage of being widely available (phyllosilicates and zeolites), environmentally friendly (phyllosilicates, zeolites, and chitosan), and inexpensive (graphene oxide, Prussian blue, magnetite, and maghemite) (Macht et al. 2011; Yong et al. 2014; Modi et al. 2015; Jang et al. 2015; Uddin 2017; Ohkubo et al. 2018; Hong et al. 2019; Brix et al. 2019; Falyouna et al. 2020; Wu et al. 2020; Liu et al. 2021, 2023; Biswas et al. 2021; Gendy et al. 2021; Latrille and Bildstein 2022; Novikau and Lujanienė 2022; Ewis et al. 2022; Wani et al. 2022; Wang

et al. 2023). Additionally, some composites based on these materials, such as montmorillonite-Prussian blue (Alamudy and Cho 2018) and magnetic Prussian blue/graphene oxide encapsulated in calcium alginate microbeads (Yang et al. 2014) with adsorption capacities for caesium of ~57 and ~43 mg/g (milligramme per gramme), respectively, as well as magnetic chitosan/activated carbon@UiO-66 (Motaghi et al. 2022) and chitosan-montmorillonite (Wang et al. 2014) with adsorption capacities for cobalt of ~44 and 150 mg/g, respectively, are not inferior and in some cases exceed the adsorption capacity of a commercial adsorbent – Lewatit® S100 (cation exchange resin), with adsorption capacities for caesium and cobalt of ~60 mg/g (El-Naggar et al. 2014). Furthermore, montmorillonite-Prussian blue and magnetic Prussian blue/graphene oxide encapsulated in calcium alginate microbeads composites are not inferior, and in some cases exceed the adsorption capacity of composites based on commercial caesium-selective adsorbent (ammonium molybdophosphate (AMP)) – AMP/alumina, AMP/zirconium phosphate, AMP/silica, SM-AMP20, AMP/silica gel, and CMC-AMP, whose adsorption capacity for caesium ranges from 7.7–65.4 mg/g (Yang et al. 2014; Alamudy and Cho 2018; Zhang et al. 2020e).

### 1.3.1. Characteristics of adsorbents

#### 1.3.1.1. Phyllosilicates and zeolites

Phyllosilicates have a layered structure with tetrahedral and octahedral sheets. The tetrahedral sheet consists of a cation ( $\text{Si}^{4+}/\text{Al}^{3+}/\text{Fe}^{3+}$ ) coordinated with four oxygen atoms. The tetrahedral sheets are connected by the basal oxygen atoms and form a two-dimensional hexagonal mesh pattern. The octahedral sheet consists of a cation ( $\text{Al}^{3+}/\text{Fe}^{3+}/\text{Mg}^{2+}/\text{Fe}^{2+}$ ) coordinated with six oxygen atoms and connected to neighbouring octahedral sheets through sharing edges, creating a hexagonal or pseudo-hexagonal symmetry. Furthermore, depending on the position of the octahedron OH, a distinction is made between cis-oriented octahedra (along one edge) and trans-oriented octahedra (along the diagonal). Depending on the ratio of tetrahedral and octahedral sheets, phyllosilicates are divided into two types – 1:1 and 2:1, respectively. The layered structure of 1:1 type phyllosilicates consists of a tetrahedral and an octahedral sheet, e.g. kaolinite, serpentine, and halloysite, while in the 2:1 type an octahedral sheet is embedded between two tetrahedral sheets, e.g. montmorillonite, bentonite, muscovite, vermiculite, and illite. Furthermore, in the 1:1 structure, the unit cell comprises six octahedral sites (four cis-oriented octahedra and two trans-oriented octahedra) and four

tetrahedral sites. In the 2:1 structure, on the other hand, the unit cell comprises six octahedral sites and eight tetrahedral sites. Structures in which all six octahedral sites are occupied are called trioctahedral, while those in which only four of the six octahedral sites are occupied are called dioctahedral (Brigatti et al. 2013). Phyllosilicates of the 2:1 type have a permanent negative charge due to isomorphous substitutions in the layers, e.g. the substitution of  $\text{Si}^{4+}$  by  $\text{Al}^{3+}$  in a tetrahedral sheet or of  $\text{Al}^{3+}$  by  $\text{Mg}^{2+}$  in an octahedral sheet, which is balanced by cationic counterions in the interlayer space. However, pyrophyllite and talc – 2:1 phyllosilicates are electrically neutral. Phyllosilicates of the 1:1 type, are also electrically neutral. Phyllosilicates are considered effective adsorbents because the counterions can be replaced by inorganic or organic cationic pollutants (Bhattacharyya and Gupta 2008; Brigatti et al. 2013; Zhu et al. 2016). Furthermore, phyllosilicates are widely available and have low toxicity (Novikau and Lujanienė 2022).

Consider some phyllosilicates presented in this work – montmorillonite and muscovite. Montmorillonite (clay mineral) (Fig. 1a), which belongs to the smectite group, is a dioctahedral 2:1 phyllosilicate. It has an interlayer space between the triple-sheet-layer, in which cations are located. Muscovite (Fig. 1b) is a true dioctahedral 2:1 micas with an interlayer space filled with potassium cations. It should be noted that montmorillonite is a swelling clay mineral with an expanding interlayer space, making the interlayer sites available for adsorption of cations from the medium, whereas muscovite is a non-swelling mineral with a non-expanding interlayer space and its interlayer sites (IS) are inaccessible. Primarily planar sites (PS) are available for adsorption. In addition, muscovite has a frayed edge site (FES), which is a highly selective site for caesium ions.

Zeolites (Fig. 1c) are a group of natural and synthetic hydrated aluminosilicates with microporous frameworks that have a three-dimensional network of tetrahedral ( $\text{Si}/\text{AlO}_4$ ). The microporous frameworks of zeolites contain a large number of cations (e.g.  $\text{Na}^+$ ,  $\text{K}^+$ ,  $\text{Ca}^{2+}$ ,  $\text{Mg}^{2+}$ ), which are only weakly bound and can be easily replaced by other cations from the medium, which determines the use of zeolites as adsorbents. The zeolite Socony Mobil-5 presented in this work is a synthetic zeolite in which the ratio of silica is greater than that of alumina and the pore diameter is 5 Å (medium pore zeolite) (Li et al. 2011; Brigatti et al. 2013; Fan et al. 2014; Farrokhpay et al. 2016; Widayat and Annisa 2017; Hong et al. 2019; Massaro et al. 2020; Wu et al. 2020, 2021).



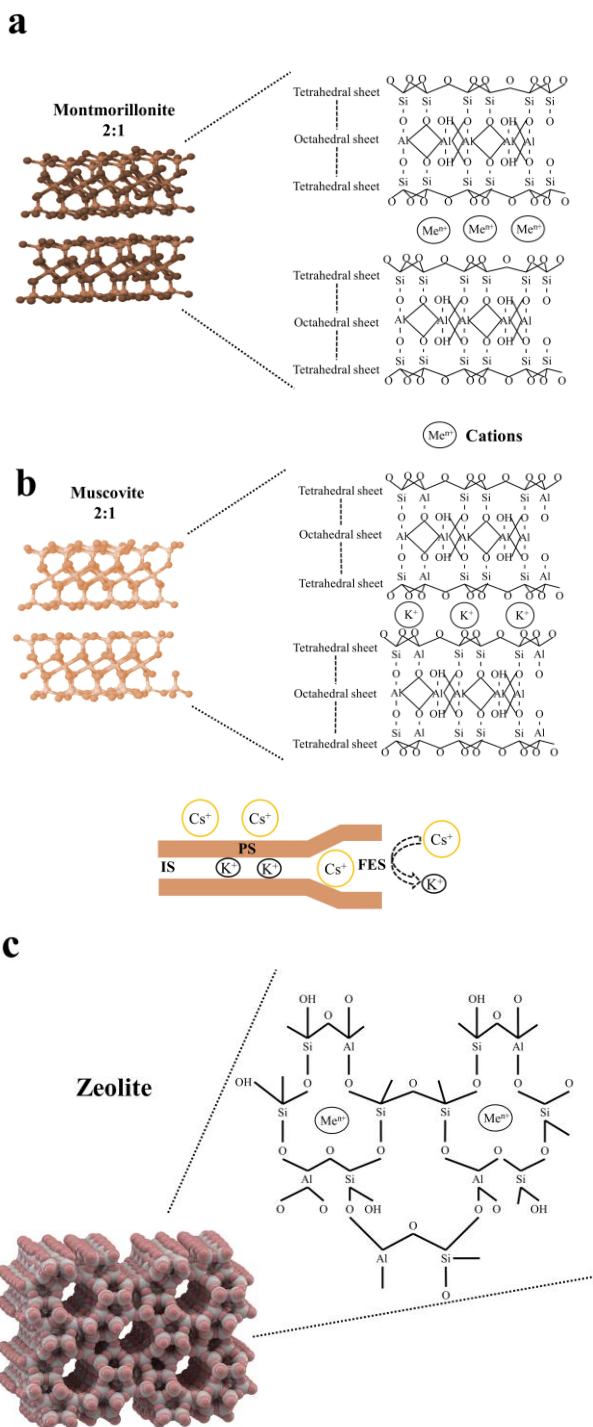


**Fig. 1.** Structure of montmorillonite (a), muscovite (b), and zeolite (c).

### 1.3.1.2. Chitosan

Chitosan (Fig. 2) is a biopolymer produced mainly by the thermochemical deacetylation of chitin (an aminated polysaccharide, the main component of the exoskeleton of arthropods), which hydrolyses the acetamide groups to form acetate ions and amino groups. The amino groups of chitosan can be ionised and become cationic in an acidic medium, which in turn contributes to the dissolution of chitosan in that medium. In the solid state, chitosan is a highly ordered crystallite. Overall, two crystalline polymorphs are distinguished – “tendon chitosan” and “annealed polymorph”. The first is the most common and is a hydrated form, the second is an anhydrous crystalline form. A huge number of properties are attributed to chitosan: Biocompatibility, biodegradability, biological activity (antibacterial, antiviral, antifungal activity, and various effects, e.g. hypocholesterolaemic effect, transfection of genetic material, stimulation of wound healing, etc.), adsorption capacity, structural capacity (can form capsules, particles, films, fibres, gels alone or in combination with other polymers – organic and inorganic compounds in the composite composition), etc. These properties of chitosan depend on two important characteristics: the degree of acetylation and the molecular weight (Lizardi-Mendoza et al. 2016; Biswas et al. 2021).

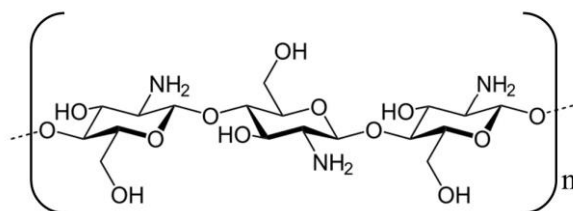


**Fig. 2.** Structure of chitosan.

The use of chitosan as an adsorbent is associated with its biocompatibility, biodegradability, structural capacity, and its content of a large number of  $\text{-NH}_2$  and  $\text{-OH}$  groups. However, due to its ability to dissolve in an acidic medium, its use as an adsorbent under these conditions is limited. Therefore, to increase the stability of chitosan in an acidic medium, it is often modified by cross-linking. There are ionic cross-linking agents (linked to form ionic bonds) and covalent cross-linking agents (linked to form covalent bonds). The most common covalent cross-linking agents are glutaraldehyde and epichlorohydrin. Cross-linking with glutaraldehyde occurs when the aldehyde groups react with the amino groups of the chitosan to form Schiff's bases. In the case of epichlorohydrin, cross-linking occurs via the hydroxyl groups of the chitosan and involves the breaking of the epoxide ring of the

compound and a condensation reaction. A commonly used ionic cross-linking agent is sodium tripolyphosphate, which cross-links chitosan via amino groups, whereby the interaction between chitosan and the cross-linking agent is based on electrostatic attraction (Fig. 3). Furthermore, chitosan cross-linked with a covalent cross-linking agent is more stable in an acidic medium than with an ionic cross-linking agent. The disadvantage of using cross-linking agents is that in some cases they reduce the adsorption capacity of chitosan, especially when its amino groups are used for cross-linking, e.g. when glutaraldehyde and sodium tripolyphosphate are used. In contrast, the use of cross-linkers to cross-link the hydroxyl groups of chitosan, such as epichlorohydrin, can increase the adsorption capacity (Hastuti et al. 2016; Józwiak et al. 2017; Yu et al. 2021; Biswas et al. 2021).

Glycerol is used to improve parameters of chitosan such as thermal stability, hydrophilicity, and flexibility by reducing intermolecular forces along the polymer chains. It is actively used as a plasticiser because it is a renewable material that is environmentally friendly, inexpensive, and has low toxicity. The interaction of glycerol with chitosan occurs through the formation of hydrogen bonds between the –OH groups of glycerol and –OH/–NH<sub>2</sub> groups of chitosan. In addition, glycerol improves the intercalation of chitosan chains into clay layers (Priyadarshi et al. 2018; Kusmono and Abdurrahim 2019; Smith et al. 2021). Although glycerol restricts some of the amino and hydroxyl groups of chitosan, it can increase the adsorption capacity of the adsorbent when optimally loaded, as found, for example, in the work of Ekrayem et al. (2021) on the removal of Pb(II) by chitosan/polyester cross-linked spheres derived from chitosan and glycerol-based polyester.

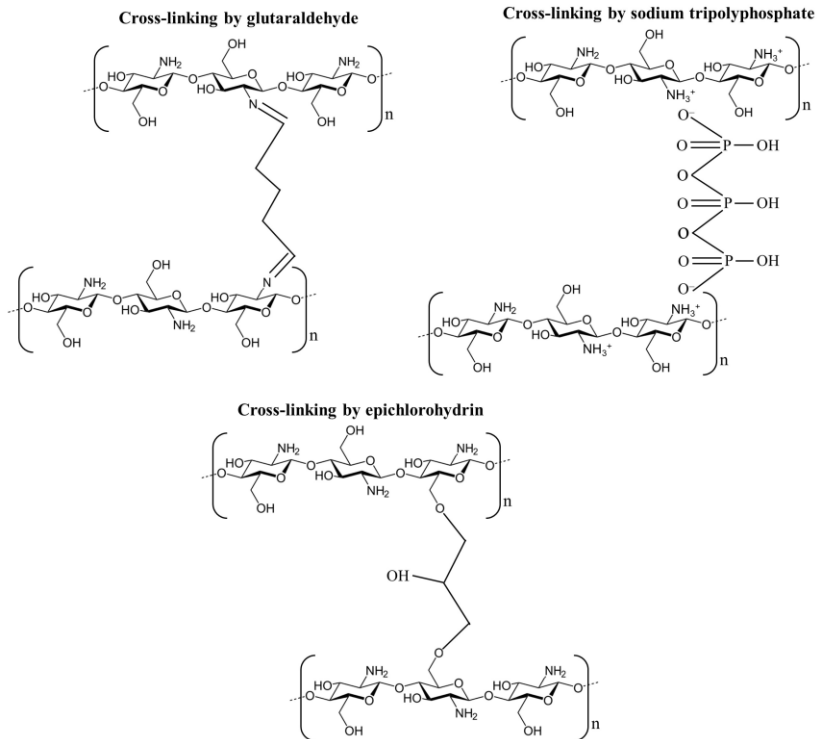


**Fig. 3.** Cross-linking of chitosan by glutaraldehyde, epichlorohydrin, and sodium tripolyphosphate.

### 1.3.1.3. Graphene oxide

Graphene oxide, a two-dimensional material, is a derivative of graphite formed by treatment with strong oxidising agents. The structure and properties of graphene oxide depend on the synthesis method and oxidation state (Lu et al. 2019; Brisebois and Sijaj 2020). The most popular synthesis method was proposed by Williams Hummers JR and Richard Offeman in 1958 (Hummers and Offeman 1958), according to which graphite was mixed with concentrated sulphuric acid, then oxidising agents such as sodium nitrate and potassium permanganate were added, and in the final phase reducing agents and agents that stop the reaction – hydrogen peroxide. However, the graphene oxide obtained by this method has many defects, for example, holes, irregular shapes, wrinkles, and the presence of impurities (traces of sulphur and nitrogen). The second popular method for the synthesis of graphene oxide, proposed by the Tour group in 2010 (Marcano et al. 2010), is an improved Hummers method. In this method, sodium nitrate was no longer used, the graphite was treated with a mixture of acids ( $H_2SO_4$  and  $H_3PO_4$ ) and the amount of potassium permanganate added as an oxidant was increased. The

graphene oxide obtained by the Tour method had a higher degree of oxidation and a more regular structure with fewer defects. The structure of graphene oxide (Fig. 4) obtained by oxidative chemical exfoliation of graphite with potassium permanganate is well described by the most popular model proposed by Lerf–Klinowski in late 1990 (Brisebois and Sijaj 2020). According to this model, graphene oxide contains domains with aliphatic six-membered rings and aromatic domains with unoxidised benzene rings, with the size of the domains depending on the degree of oxidation. The graphene oxide sheet is a partially folded carbon network consisting of double bonds, epoxide groups, and aromatic compounds. The oxygen-containing functional groups are located above and below the level of the carbon network and form layers of oxygen atoms with different concentrations. Among the oxygen-containing functional groups (epoxy, hydroxyl, carboxyl, and carbonyl groups), the epoxy and hydroxyl groups form the majority. Furthermore, graphene oxide forms stable colloids in water due to the presence of hydrophilic groups on the surface (Brisebois and Sijaj 2020).

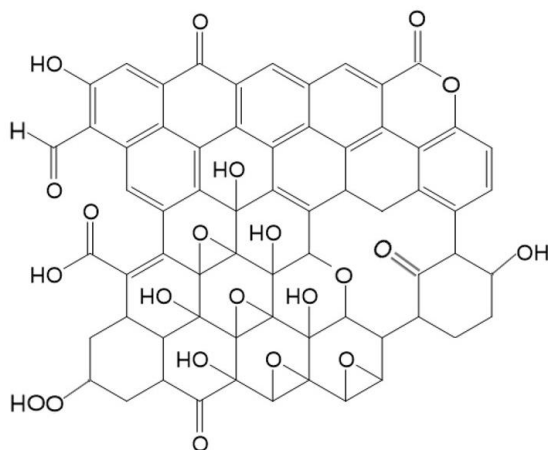


**Fig. 4.** Graphene oxide structure according to Lerf–Klinowski.

Graphene oxide is a promising adsorbent for many pollutants, including radionuclides (Lu et al. 2019; Ajala et al. 2022), because it has a large specific surface area (up to 2630 m<sup>2</sup>/g (square metre per gramme), depending on the synthesis method) (Montes-Navajas et al. 2013; Zhang et al. 2020d) and its oxygen-containing functional groups are potential adsorption sites.

### 1.3.1.4. Prussian blue, magnetite, and maghemite

Prussian blue (iron(III) hexacyanoferrate(II)) is a dark blue synthetic pigment with a face-centred cubic lattice structure containing Fe(II) octahedral centres attached to six cyanide ligands whose terminal N-donors are associated with Fe(III). There are two chemical formulae for Prussian blue –  $\text{Fe}_4[\text{Fe}(\text{CN})_6]_3 \cdot x\text{H}_2\text{O}$  (Fig. 5a) and  $\text{KFe}[\text{Fe}(\text{CN})_6] \cdot x\text{H}_2\text{O}$  (Fig. 5b). The first refers to “insoluble” Prussian blue, the second to “soluble”. “Insoluble” Prussian blue is obtained in the presence of an excess of ferrous ferrocyanide salts, “soluble” in the presence of an excess of potassium ferrocyanide or by mixing potassium ferrocyanide and iron(III) salts in a molar ratio of 1:1. Both forms are completely insoluble in water and their names are related to the ability of Prussian blue to remain in water as a colloidal suspension (Lin et al. 2008; Ishizaki et al. 2013; Doumic et al. 2016; Nguyen et al. 2021).

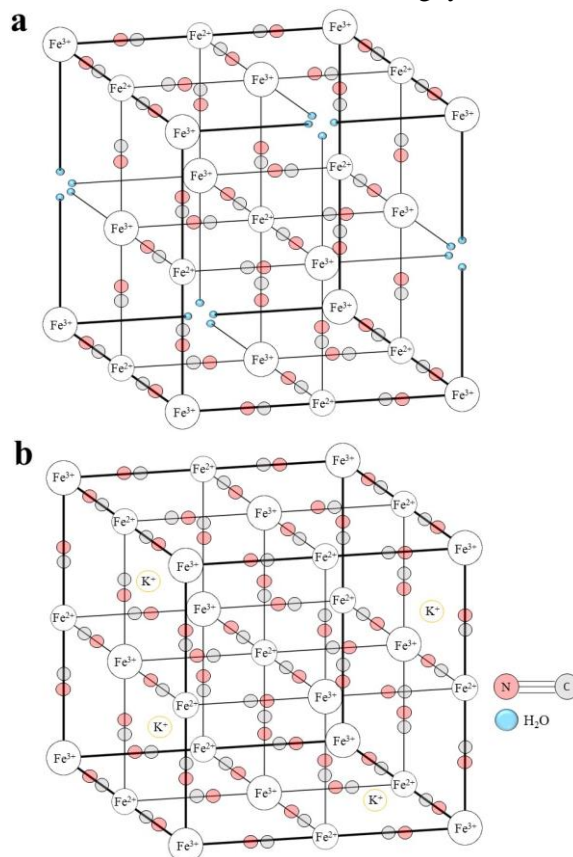


**Fig. 5.** Structures of “insoluble” (a) and “soluble” (b) forms of Prussian blue.

Magnetite ( $\text{Fe}_3\text{O}_4$ ) (Fig. 6) is ferromagnetic and has a cubic spinel structure with densely packed oxygen ions and iron cations occupying interstitial sites. The interstices form two sites – A (with tetrahedral oxygen coordination) and B (with octahedral oxygen coordination). The sites A and B form two magnetic sublattices and the spins in sublattice A are coupled antiparallel to the spins of sublattice B. Furthermore, the iron cations are unevenly distributed on these sites: Fe(III) in the A sites and Fe(III) and Fe(II) in the B sites. The structural formula of magnetite can be expressed as follows:  $[\text{Fe}^{3+}]_A [\text{Fe}^{3+}; \text{Fe}^{2+}]_B \text{O}^{2-}_4$ . Magnetite occurs naturally and is quite commonly obtained under laboratory conditions by the co-precipitation of Fe(II) and Fe(III) salts using ammonium hydroxide as a precipitant (Petcharoen and Sirivat 2012; Moskowitz et al. 2015; Dubey and Kain 2018).

Maghemite ( $\gamma\text{-Fe}_2\text{O}_3$ ) (Fig. 6) has a cubic, inverse spinel crystal structure and ferrimagnetic properties similar to magnetite. The difference, however, is that it has a defective lattice in which 1/9 of the Fe positions are vacant, and the structural formula has the following form:  $[\text{Fe}^{3+}]_A [\text{Fe}^{3+}; \text{Vacancy}]_B \text{O}^{2-}_3$ . Maghemite forms from magnetite by weathering or oxidation at low temperatures (Lee et al. 2004; Maxbauer et al. 2016).

The use of Prussian blue as an adsorbent is due to its crystal structure and the presence of space within it, which is involved in adsorption processes. In addition, Prussian blue is a highly selective and effective adsorbent for caesium, the adsorption of which takes place by chemisorption (Ishizaki et al. 2013; Alamudy and Cho 2018; Takahashi et al. 2018; Nguyen et al. 2021). The use of magnetite and maghemite is mainly related to their magnetic properties, due to which they can be separated from the solution by magnetic separation after adsorption, thus avoiding secondary contamination. In addition, these materials are not expensive. Moreover, due to these properties, these magnetic particles are often used as adsorbents in composite materials (Obeid et al. 2013; Foerstendorf et al. 2014; Liu et al. 2015; Carvalho et al. 2016; Chang et al. 2016; Xu et al. 2016; Wang et al. 2019; Zhuang and Wang 2019; Zhang et al. 2020b; Lujanienė et al. 2022).

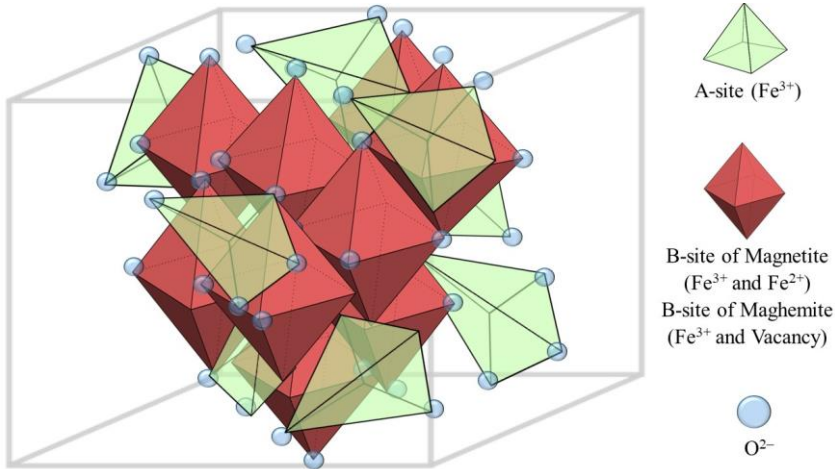


**Fig. 6.** Magnetite and maghemite structure.

### 1.3.2. Adsorption studies

In the following subsections consider some studies on the adsorption of caesium ions on: Ammonium-pillared montmorillonite- $\text{Fe}_3\text{O}_4$  composite (Zheng et al. 2017), montmorillonite-Prussian blue hybrid (Alamudy and Cho 2018), iron-based zeolite nanoparticles (Eljamal et al. 2019), magnetic zeolite (Falyouna et al. 2020), muscovite (Cornell 1993; McKinley et al. 2004; Kwong-Moses et al. 2020), magnetic prussian blue/graphene oxide (Yang et al. 2014), magnetic Prussian blue (Yang et al. 2016a), nanostructured chitosan/molecular sieve-4A (Goyal et al. 2020), fibrous chitosan modified with metal hexacyanoferrates (Zhuang et al. 2022), and chitosan-coated porous vermiculite with low expansion (Zhang et al. 2021).

Cobalt ions on: Graphene oxide-magnetite (Tayyebi et al. 2015), magnetic graphene oxide/chitosan (Zhuang and Wang 2019), magnetic cyanoethyl chitosan beads (Zhang et al. 2020c), magnetic chitosan/activated carbon@UiO-66 (Motaghi et al. 2022), chitosan-montmorillonite (Wang et al. 2014), and chitosan (Khan et al. 2022).

Europium ions on: Magnetite decorated graphene oxide (Li et al. 2014), magnetic amidoxime-functionalised MCM-41 (Liu et al. 2022), magnetite nanoparticles (Carvalho et al. 2016), synthetic maghemite (Xu et al. 2016), *Saccharomyces cerevisiae* immobilised in glutaraldehyde cross-linked chitosan (Arunraj et al. 2019), chitosan (Cadogan et al. 2014), muscovite (Wu et al. 2021), and zeolite Socony Mobil-5 (Shao et al. 2009).



### 1.3.2.1. Adsorption of caesium

Zheng et al. (2017) found that the adsorption capacity of a composite (with an average particle size of 7.338  $\mu\text{m}$  (micrometre)) based on ammonium-pillared montmorillonite and magnetic nanoparticles ( $\text{Fe}_3\text{O}_4$ ) increases with an increase in the initial concentration of caesium ions. The maximum experimental adsorption capacity of the composite was  $\sim 27$  mg/g at an initial concentration of  $\text{Cs(I)}=40$  mg/L (milligramme per litre), a pH of 6.7, a temperature of 25  $^\circ\text{C}$ , a contact time of 2 h (hours), and an adsorbent dosage of 0.5 g/L (gramme per litre). It is noteworthy that under these conditions the adsorption capacity of the original montmorillonite was  $\sim 32$  mg/g, while that of the original magnetite was  $\sim 2.5$  mg/g. Moreover, in the concentration range of caesium ions from 5 to 25 mg/L, the adsorption capacity of the composite exceeds that of the original components, and after 25 mg/L it is only slightly worse than that of the original montmorillonite, but clearly exceeds that of the magnetite. The experimental data on the effect of initial concentration is well described by the Freundlich isotherm. The influence of contact time showed that montmorillonite, magnetite, and the composite reached an equilibrium state within 1 h. The resulting kinetic data are well described by a pseudo-second-order kinetic model. The effect of adsorbent dosage showed that the adsorption capacity of the composite and its original components decreased with increasing dosage from 0.1 to 0.9 g/L. With increasing temperature, the adsorption capacity on magnetite increased, indicating an endothermic adsorption process in contrast to montmorillonite, while the adsorption capacity on the composite practically did not change. The influence of pH showed that the adsorption capacity of composite, montmorillonite, and magnetite increased with increasing pH, and reached a maximum at pH=11, which is associated with a decrease in the  $\text{H}_3\text{O}^+$  content in the solution. Above a pH of 11, the adsorption capacity decreases. In this case, the authors explain this by an increase in the  $\text{Na}^+$  content, which competes with  $\text{Cs}^+$  for adsorption sites. The test on the influence of the competing ions ( $\text{Na}^+$ ,  $\text{K}^+$ ,  $\text{Mg}^{2+}$ , and  $\text{Ca}^{2+}$ ) in the medium showed that the adsorption capacity of the composite and its original components decreases in the following order:  $\text{Ca}^{2+} > \text{Mg}^{2+} > \text{K}^+ > \text{Na}^+$ . The authors also found that the mechanism of  $\text{Cs(I)}$  adsorption on the composite consists of the exchange of  $\text{NH}_4^+$  ions (predominantly) and the coordination of hydroxyl groups on the surface. The results on the reuse of the composite showed that the caesium removal efficiency was not less than 60% for four cycles of use – in the case of using HCl as the regeneration agent, which showed a better result in regeneration compared to NaCl and NaOH. Moreover, the adsorbent was

tested in different types of water (seawater, river water, drinking water, and deionised water) and the caesium removal efficiency was not less than 80% except for seawater.

Alamudy and Cho (2018) presented the results of a study on caesium adsorption on montmorillonite (surface area:  $242.15 \pm 8.8 \text{ m}^2/\text{g}$ , pore volume:  $0.3670 \pm 0.0149 \text{ cm}^3/\text{g}$  (cubic centimetre per gramme)) and on montmorillonite-Prussian blue hybrids obtained by different methods – the montmorillonite-Prussian blue ferric to cyanide (MMT-PBFC; surface area:  $259.26 \pm 14.6 \text{ m}^2/\text{g}$ , pore volume:  $0.3201 \pm 0.0161 \text{ cm}^3/\text{g}$ ) and montmorillonite-Prussian blue cyanide to ferric (MMT-PBCF; surface area:  $259.08 \pm 12.1 \text{ m}^2/\text{g}$ , pore volume:  $0.3411 \pm 0.0201 \text{ cm}^3/\text{g}$ ). The adsorption of caesium ions on montmorillonite and hybrids based on it rapidly reaches equilibrium within 30 min (minutes), which was established under the following conditions: Initial concentration of caesium ions of 200 mg/L, adsorbent dosage of 2 g/L, pH of 6.5–7, and room temperature. The resulting kinetic data are well fitted with a pseudo-second-order kinetic model. The experimental data on the effect of the initial concentration of caesium ions obtained at an initial concentration of 20–250 mg/L, an adsorbent dosage of 2 g/L, a pH of 6.5–7, room temperature, and a contact time of 2 h can be better described with the Langmuir isotherm than with the Freundlich isotherm. The maximum theoretical adsorption capacities were 37.31, 57.47, and 52.63 mg/g for montmorillonite, MMT-PBFC, and MMT-PBCF, respectively. In addition, the hybrids showed high selectivity for caesium ions compared to the original montmorillonite in the presence of competing ions ( $\text{Na}^+$ ,  $\text{K}^+$ ,  $\text{Mg}^{2+}$ , and  $\text{Ca}^{2+}$ ). The authors also reported that the predominant adsorption mechanism on the hybrids is ion exchange, ion trapping, and electrostatic interaction.

Eljamal et al. (2019) found that the adsorption of caesium on nanoscale zero-valent iron-zeolite (nZVI-Z) and nano-Fe/Cu-zeolite (nFe/Cu-Z) composites increases with increasing pH in the range of 3–12, reaching a maximum at pH of 6. In an acidic and strongly alkaline medium, the adsorption capacity of the composites was low. As the authors explain, in the first case this is due to a high content of  $\text{H}^+$  cations competing with  $\text{Cs}^+$  for adsorption sites and the dissolution of iron nanoparticles, and in the second case it is due to the formation of Fe-(oxy)hydroxide layers on the active sites of the composites, which inhibit the adsorption of caesium ions. The results on the effect of contact time (5–120 min) and initial concentration (50–20 mg/L) showed that with an increase in both parameters, the adsorption capacity of the composites increased. The equilibrium state was reached for nFe/Cu-Z and nZVI-Z after 20 and 30 min, respectively, and did not depend on the initial concentration and pH. Furthermore, an increase in the dosage of

adsorbents was accompanied by an increase in adsorption efficiency. In addition, the adsorption efficiency of caesium ions was higher with nFe/Cu-Z than with nZVI-Z. The process of adsorption of caesium on the composites was endothermic and spontaneous. The obtained experimental data are well described by the pseudo-second-order kinetic model and the isotherms of Langmuir and Freundlich. Another paper by these authors (Falyouna et al. 2020) reported that a magnetic zeolite composite (Ze/Fe<sup>0</sup>) is more suitable than nZVI (Fe<sup>0</sup>), Cu/Fe<sup>0</sup>, Ni/Fe<sup>0</sup>, Ag/Fe<sup>0</sup>, Ze/Fe<sup>0</sup>-Cu, Ze/Fe<sup>0</sup>-Ni, and Ze/Fe<sup>0</sup>-Ag for the treatment of caesium-contaminated water in a laboratory-scale continuous treatment system. In addition, the study showed that the optimum mass ratio of magnetite and zeolite in the composite is 1:1, that temperature and pH have no significant effect on adsorption, and that the optimum dosage of adsorbent is 5 g/L. The experimental data are well described by the pseudo-second-order kinetic model and the Freundlich isotherm. Moreover, the zeolite in the composite functions mainly as an adsorbent, while the magnetite function is associated with the removal of the composite from water by magnetic separation. The magnetic zeolite composite obtained by physically mixing these components was found to be more effective in removing caesium (95.11%) than the same composite obtained chemically (61.25%).

It is known that muscovite, with a cation exchange capacity of 5.2 meq/100 g (milliequivalents per 100 gramme) and a specific surface area of 11 m<sup>2</sup>/g, is a highly selective adsorbent for caesium ions, like illite, because it has a frayed edge site. Unlike illite, these cation exchange sites are slowly accessible to caesium, which isolates it more effectively. In addition, the K<sub>d</sub> value (distribution coefficient) of muscovite decreases slightly when the pH increases from 5 to 9. Furthermore, the adsorption of caesium on muscovite in a medium with competing divalent cations (they compete more strongly for adsorption sites with caesium) is lower than with monovalent cations (Cornell 1993; McKinley et al. 2004; Kwong-Moses et al. 2020).

Yang et al. (2014) tested nanocomposites of magnetic Prussian blue and magnetic Prussian blue/graphene oxide encapsulated in calcium alginate microbeads (PFM and PFGM) in batch experiments. The test results showed that these nanocomposites adsorb caesium ions quite stably in the pH range of 4–8. However, under strongly acidic and alkaline conditions, the adsorption capacity decreases as dissolution and decomposes of the Prussian blue occur, respectively. The initial caesium ion concentration tests were conducted under the following conditions: Initial concentration of 25–150 ppm (parts per million), adsorbent mass of 0.05 g, pH of 7, contact time of 24 h, and room temperature. The experimental data obtained were analysed using the Langmuir and Freundlich models, with the Langmuir model being more

suitable for describing the data. The obtained values of the maximum theoretical adsorption capacity for the PFM and PFGM nanocomposites were 40.766 and 43.516 mg/g, respectively. From the results of the contact time tests, the equilibrium state for the nanocomposites is reached after ~10 h. Thermodynamic studies in turn showed that with increasing temperature, the adsorption of caesium on both nanocomposites increased, from which it follows that the adsorption is endothermic. The authors also found that the presence of competing ions in the medium, such as  $\text{Na}^+$ ,  $\text{K}^+$ ,  $\text{Mg}^{2+}$ , and  $\text{Ca}^{2+}$ , did not affect the binding of caesium (at its excess) with the nanocomposites. As for the adsorption mechanism, the authors suggest that it is a combination of chemisorption (cation exchange) and physisorption (ion trapping). In addition, PFM and PFGM nanocomposites were used to purify caesium-contaminated soils through water. The results showed that the efficiency of removal of caesium from soil by PFM and PFGM averaged 74.36 and 79.33%, respectively.

The use of Prussian blue-functionalised magnetic nanoclusters to remove  $^{137}\text{Cs}$  was reported by Yang et al. (2016a). According to the results of the study, the removal efficiency of  $^{137}\text{Cs}$  by the composite averaged 99.34% and the decontamination factor (DF) averaged 199. The activity of  $^{137}\text{Cs}$  decreased from 39.64 to 0.21 Bq/g on average. In addition, the presence of competing cations in the medium (with a concentration of 3000 ppm) decreased the efficiency of  $^{137}\text{Cs}$  removal in the following order:  $\text{Mg}^{2+}$ ,  $\text{Ca}^{2+}$ ,  $\text{Na}^+$ , and  $\text{K}^+$ . However, the average radioactive caesium removal efficiency was 99.45%. In addition, the mean DF value was 195, a high value indicating that this composite can be used to remediate  $^{137}\text{Cs}$ -contaminated aqueous systems and to remove radiocaesium from nuclear wastewater.

Goyal et al. (2020), the results of a study on Cs(I) adsorption on nanostructured chitosan/molecular sieve 4A hybrid (surface area: 77.07  $\text{m}^2/\text{g}$ , average pore size: 16.43 nm (nanometer), and pore volume: 0.316  $\text{cm}^3/\text{g}$ ) are presented. It was found that with an increase in pH from 3 to 7, the removal of caesium ions from solution by the hybrid increased from 53.92 to 90.87%, but decreased to ~70% after pH of 7. In addition, the surface charge of the adsorbent is negative at  $\text{pH} > 3.3$ , which favours the adsorption of caesium ions due to electrostatic attraction. With an increase in the initial concentration of caesium from 10 to 30 mg/L, the adsorption capacity of the adsorbent decreases while the adsorption efficiency increases. The maximum experimental adsorption capacity and efficiency of the adsorbent were ~25 mg/g and ~95% at initial caesium concentration of 10 and 30 mg/L, respectively. The data obtained from the experiments as a function of initial concentration are in good agreement with the Freundlich model. The

nanostructured chitosan/molecular sieve 4A hybrid adsorbed Cs(I) rather rapidly, so that the efficiency of Cs(I) removal was more than 80% within 40 min, and the adsorbent reached an equilibrium state after 40 min. The data from the kinetic studies are well described by the pseudo-second-order kinetic model. When the dosage of the adsorbent was increased from 0.1 to 2 g/L, the adsorption capacity of the adsorbent decreased from ~30 to ~5 mg/g, respectively. While the adsorption efficiency increased from ~30 to ~90% in the range of adsorbent dosage from 0.1 to 1 g/L and then up to 2 g/L, the caesium removal efficiency remained stable at ~90%. As the authors explain, this is due to the congregation of adsorbent particles. Thermodynamic studies have shown that the process of adsorption of Cs(I) on the nanostructured chitosan/molecular sieve 4A hybrid is exothermic and spontaneous. The presence of competing ions ( $Mg^{2+}$ ,  $Ca^{2+}$ ,  $Na^+$ , and  $K^+$ ) in the medium decreased the efficiency of  $Cs^+$  removal, while  $K^+$  significantly decreased the adsorption of caesium (less than 60%), compared to other cations where the efficiency of caesium removal ranged from ~75 to ~90%. Furthermore, the authors suggest that the mechanism of adsorption is ion exchange and ionic interactions. Repeated use of the adsorbent showed that it removed caesium in a sufficiently stable manner over five cycles, with a removal efficiency of ~90%.

The results of an adsorption study carried out with adsorbents consisting of Cu, Co, and Ni hexacyanoferrates (CuHCF, CoHCF, and NiHCF) modified fibrous chitosan (CuHCF/chitosan fibres (surface area: 19.3 m<sup>2</sup>/g, average pore size: 1.9 nm), CoHCF/chitosan fibres (surface area: 29.4 m<sup>2</sup>/g, average pore size: 1.9 nm), NiHCF/chitosan fibres (surface area: 18.2 m<sup>2</sup>/g, average pore size: 1.9 nm)) were presented by Zhuang et al. (2022). It was found that the adsorbents reached an equilibrium state within 90 min in the contact time range of 0 to 360 min. Moreover, the kinetic data are well fitted with a pseudo-second-order kinetic model. The Sips model is well suited to describe the experimental data on the effects of initial concentrations of caesium ions obtained in the range of caesium concentrations of 20–300 mg/L and adsorbents mass of 10 mg. The calculated values of maximum adsorption capacity for CuHCF/chitosan fibres, CoHCF/chitosan fibres, and NiHCF/chitosan fibres were 25.9, 16.8, and 18.2 mg/g, respectively. Furthermore, the CuHCF/chitosan fibres were shown to remove caesium ions very efficiently (over 82%) from simulated seawater and tap water. The mechanism of caesium adsorption on these adsorbents involves ion exchange and electrostatic attraction.

The results of the study presented by Zhang et al. (2021) show that the adsorption capacity of chitosan coated-porous low expansion vermiculite

increases from 0.033 to 0.707 mmol/g (millimol per gramme) when the initial concentration of caesium ions is increased from 0.5 to 12 mmol/L (millimol per litre). The adsorption efficiency, on the other hand, decreases from 98.63 to 54.45%. As the pH of the solution increases, the adsorption capacity and efficiency increase and reach their maximum at a pH of 8, then decrease to a pH of 10. The increase in adsorption capacity and efficiency in the pH range of 2–8 is due to the fact that as the pH increases, the content of competing ions, such as  $H^+$ , decreases and the negative charge of the adsorbent surface increases, whereby the resulting electrostatic attraction between the adsorbent and adsorbate has a favourable effect on adsorption. The decrease in adsorption capacity and efficiency at  $pH > 8$  is due to the binding of  $Cs^+$  to the surrounding  $OH^-$  and the destruction of the silicate structure of vermiculite under strongly alkaline conditions. It should also be noted that as the ionic strength increases, the adsorption capacity and efficiency of the adsorbent decreases. The influence of contact time showed that the adsorbent reaches the equilibrium state within ~10 min. Moreover, the experimental data agree well with the Langmuir isotherm and the pseudo-second-order kinetic model. The results of a study on the removal of the radioactive form of caesium ( $^{137}Cs$ ) using chitosan coated-porous low expansion vermiculite showed that the radioactivity of the supernatant decreased from 90 to 0 Bq within 4 h. The adsorbent proved to be quite effective when reused, with removal of Cs(I) being no less than 96.03% in five cycles.

#### 1.3.2.2. Adsorption of cobalt

A study on the adsorption of Co(II) on graphene oxide-magnetite was conducted by Tayyebi et al. (2015). In their work, they report the results of a series of tests: Influence of initial cobalt ion concentration, temperature, contact time, pH, and ionic strength. Consider the main points of this work. The test, carried out in the range of initial Co(II) concentration from 1 to 70 ppm, showed that the composite was saturated at a loading of 0.56 meq/g (milliequivalents per gramme) Co(II). The data obtained fitted the Langmuir isotherm better than the Freundlich isotherm, and the calculated maximum adsorption capacity was 18.9 mg/g at 25 °C. A thermodynamic study was also carried out as part of this test, according to which the adsorption capacity of the composite increases with increasing temperature. From the thermodynamic parameters obtained, it appears that the adsorption process is endothermic and spontaneous. The tests on the effect of contact time were carried out in a range from 1 to 24 h, with an initial cobalt concentration of 50 ppm and a pH of 6.5. It was found that the equilibrium state on the composite

was reached in 3 h, and the data obtained agreed well with the pseudo-second-order kinetic model. The results on the effect of pH showed that the cobalt removal efficiency was ~20% up to a pH of 5. After a pH of 5 and up to 10, the adsorption efficiency increased from 20 to 100%. The increase in adsorption efficiency after a pH of 5 is due to the fact that the content of competing  $H^+$  in the solution decreases and, moreover, at a pH of 5 the charge on the composite surface becomes negative, which has a favourable effect on the adsorption of cobalt. Furthermore, the adsorption of cobalt on the composite is independent of ionic strength and the adsorption process is controlled by the inner-sphere complexation. The presence of competing ions in the medium resulted in a decrease in adsorption efficiency at  $pH < 8$ , in the following order:  $K^+$ ,  $Na^+$ , and  $Li^+$ .

Authors Zhuang and Wang (2019) found that the adsorption of cobalt on graphene oxide/chitosan was quite stable in the pH range of 5–9 and the adsorption capacity was ~9 mg/g. Kinetic studies showed that the composite reached saturation within 160 min, and the experimental data are well fitted with a pseudo-second-order kinetic model. The results of the adsorption isotherms also show that the Langmuir model describes the experimental data better than the Freundlich and Temkin models. The calculated value of the maximum adsorption capacity for this composite is 9.92 mg/g. Thermodynamic studies have shown that the adsorption of cobalt on the composite was endothermic and spontaneous.

Zhang et al. (2020c) showed in a pH effect test that the adsorption capacity of magnetic cyanoethyl chitosan beads towards cobalt ions slightly increases in the pH range of 5–8, as the adsorbent becomes more negatively charged with increasing pH. An increase in adsorption capacity of the adsorbent also occurs when the initial concentration of cobalt is increased in the range of 10–600 mg/L, while the adsorbent reaches saturation at 600 mg/L and the adsorption capacity at this initial concentration is ~17 mg/g. These data were fitted using the Langmuir, Freundlich, and Temkin models, with the Langmuir model fitting the data better. The calculated value for the maximum adsorption capacity was 17.92 mg/g. Kinetic studies showed that equilibrium on the adsorbent is reached in 120 min, and the pseudo-second-order kinetic model fits the obtained data well. According to the thermodynamic studies, the adsorption process was endothermic and spontaneous. The authors also found that the adsorption of the adsorbate on the adsorbent occurs by chemisorption, where the  $-CN$  and  $-NH_2$  groups are responsible for the adsorption of cobalt, with the  $-CN$  groups of the adsorbent occupying a dominant position.

Motaghi et al. (2022) present the results of adsorption isotherms and kinetics for magnetic chitosan/activated carbon@UiO-66, according to which the Langmuir model and the pseudo-second-order kinetic model are well suited to describe the experimental data. The calculated maximum adsorption capacity for magnetic chitosan/activated carbon@UiO-66 for cobalt ions was 44.5 mg/g. The thermodynamic study in turn showed that the adsorption of cobalt on the adsorbent is endothermic and spontaneous. The adsorption mechanism is complex and combines chemical and physical adsorption: electrostatic forces, hydrogen bonding,  $\pi$ - $\pi$ , and  $n$ - $\pi$  interactions. In addition, a test was carried out to reuse the adsorbent. The results showed that the adsorbent was sufficiently stable in removing cobalt ions when used five times. At the same time, the adsorption efficiency was not less than 80%. The results of the tests of the adsorbent in different types of water (distilled water, tap water, mineral water, lake water, and river water) showed that the efficiency of removal of cobalt ions ranged from  $91.23 \pm 4.53$  to  $97.89 \pm 2.21\%$ .

Wang et al. (2014) found that the chitosan-montmorillonite composite with a mass ratio of 0.25 (chitosan:montmorillonite) reached an equilibrium state for 12 h when adsorbing cobalt, and the adsorption capacity was 150 mg/g at this time. The results of kinetics, isotherms, and thermodynamics show that the experimental data agree well with the Temkin model and the pseudo-second-order kinetic model and that the adsorption of cobalt ions on the composite is endothermic, spontaneous, and irreversible. The predominant mechanism of adsorption is chemisorption, as Co(II) forms complexes with –OH and –NH<sub>2</sub> groups of the adsorbent.

In their work, Khan et al. (2022) investigated the use of Co(II)/glutaraldehyde cross-linked chitosan as a photocatalyst for the photodegradation of methyl violet dye. As part of the study, it was found that the adsorption capacity of cross-linked chitosan increased with an increase in cobalt ion concentration from 6.37 to 144 ppm, and at 144 ppm the maximum experimental adsorption capacity of chitosan was 289.82 mg/g. Furthermore, in this work, the adsorption equilibrium data were analysed using the Langmuir and Freundlich models. The Freundlich model fits the experimental data better than the Langmuir model.

### 1.3.2.3. Adsorption of europium

Li et al. (2014) present the results of a study on the adsorption of europium ions on magnetite decorated graphene oxide. It was found that with an increase in pH from 2 to 8, the europium removal efficiency increased from ~18.2 to 90.1%, and at a pH > 8, the adsorption efficiency remained at a high



level (~95.1%). The increase in europium adsorption with increasing pH is related to an increase in the content of deprotonated centres, which are more accessible to retain Eu(III) and surface complexation between  $\text{Eu}^{3+}$ ,  $\text{Eu}(\text{OH})^{2+}$ ,  $\text{Eu}(\text{OH})_2^+$  and composite. Furthermore, adsorption of europium ions on the composite occurs by inner-sphere surface complexation, as shown by the results of the influence of ionic strength in the pH range 3.5–8.5. The results of the kinetic studies show that the equilibrium state on the composite is reached within 5 h, and the pseudo-second-order kinetic model agrees well with the experimental data. The results on the influence of humic acid (HA) and fulvic acid (FA) show that HA and FA increase the adsorption of europium ions at low pH values, while they decrease at high values. The authors explain this as follows: At low pH, negatively charged HA and FA are adsorbed onto the positively charged surface of the composite due to electrostatic attraction, making the adsorbent more negatively charged, which has a favourable effect on the adsorption of europium. At high pH values, the surface of the adsorbent is negatively charged and due to electrostatic repulsion, the negatively charged HA and FA cannot be adsorbed. As a result, a large amount of HA and FA remain in the solution, which in turn form strong complexes with Eu(III), which significantly reduces the adsorption of the adsorbate on the adsorbent. With regard to the reuse of the composite and the tests in the model and actual wastewater, it was found that the adsorption efficiency decreased slightly from 50.5 to 47.1% over six cycles of use. The Eu(III) removal efficiency in the model and actual wastewater was ~55 and ~40%, respectively.

Liu et al. (2022) studied the adsorption of Eu(III) on magnetic amidoxime-functionalised MCM-41 (surface area:  $19 \text{ m}^2/\text{g}$ , total pore volume:  $0.06 \text{ cm}^3/\text{g}$ , and average pore diameter: 11.8 nm). They found that the adsorption capacity of the composite increases with increasing pH and reaches its maximum at pH of 8 (~20 mg/g). In the pH range of 2–5, europium is only weakly adsorbed, while it increases strongly at a pH>5. This can be attributed to electrostatic attraction, as the charge of the composite takes on a negative charge after a pH of 5. At a pH>7, the removal of europium occurs through the co-precipitation of  $\text{Eu}(\text{OH})_3$  on the surface. The equilibrium state on the composite is reached in ~2 h, and the kinetic data can be well described by the pseudo-second-order model. The equilibrium of the adsorption data is well described by the Langmuir model, and the calculated maximum adsorption capacity was 26.46 mg/g. According to the thermodynamic studies, the adsorption of europium on the composite was endothermic and spontaneous. The results on the influence of coexisting ions showed that this composite has a low affinity for europium. Reusing the adsorbent three times resulted in a

slight decrease in its adsorption capacity, and the use of HCl as a regenerant was more effective than NaHCO<sub>3</sub> and ethylenediaminetetraacetic acid. The predominant adsorption mechanism is chemisorption, and amino, hydroxyl, phenol, and amidoxime groups on the surface of the composite are responsible for europium adsorption.

The authors of Carvalho et al. (2016) studied the adsorption of Eu(III) on Fe<sub>3</sub>O<sub>4</sub> (surface area: 26.9 m<sup>2</sup>/g, pore volume: 0.066 cm<sup>3</sup>/g), Fe<sub>3</sub>O<sub>4</sub>@SiO<sub>2</sub> (surface area: 50.9 m<sup>2</sup>/g, pore volume: 0.129 cm<sup>3</sup>/g), Fe<sub>3</sub>O<sub>4</sub>@SiO<sub>2</sub>/3-aminopropyltrimethoxysilane (APMS) (surface area: 42.2 m<sup>2</sup>/g, pore volume: 0.076 cm<sup>3</sup>/g), and Fe<sub>3</sub>O<sub>4</sub>@SiO<sub>2</sub>/dithiocarbamate (DTC) (surface area: 77.2 m<sup>2</sup>/g, pore volume: 0.137 cm<sup>3</sup>/g). It was found that among the magnetite nanoparticles presented, Fe<sub>3</sub>O<sub>4</sub>@SiO<sub>2</sub> and Fe<sub>3</sub>O<sub>4</sub>@SiO<sub>2</sub>/APMS exhibited the highest adsorption capacity for europium ions, with maximum adsorption capacity of 37.9 and 32.6 mg/g, respectively. With increasing pH, the adsorption of Eu(III) on magnetite nanoparticles increases and reaches a maximum at pH of 10. The removal efficiency at this pH was more than 90%. The equilibrium state on the adsorbents was reached in 4 h, except for Fe<sub>3</sub>O<sub>4</sub>@SiO<sub>2</sub>/DTC where it was reached in 2 h. Furthermore, the pseudo-second-order model is well suited to describe the kinetic data.

The authors of Xu et al. (2016) found that the efficiency of europium removal by synthetic maghemite was low in the pH range of 2–4, then increased sharply in the pH range of 4–8 and reached a maximum at pH>8, where the adsorption efficiency was ~100%. The low percentage of europium removal at pH<4 is related to the electrostatic repulsion between the positively charged surfaces of the adsorbent and the adsorbate, while at pH>4 the surface charge of maghemite becomes negative and the resulting electrostatic attraction is favourable for the adsorption of europium ions. Increasing the ionic strength over a wide pH range from 2 to 10 decreases the efficiency of Eu(III) removal, while at a pH of 10 the ionic strength has no effect on adsorption. It follows that adsorption of europium ions on maghemite occurs by ion exchange or outer-sphere surface complexation. Furthermore, according to the results of X-ray photoelectron spectroscopy, the oxygen-containing groups of maghemite are responsible for the adsorption of europium. Furthermore, in the contact time range of 0 to 1440 min, the equilibrium state on maghemite was reached within ~120 min. The obtained data on the kinetics and equilibrium of adsorption can be well explained by the pseudo-second-order model and Freundlich model, respectively. According to the thermodynamic studies, the adsorption process is endothermic and spontaneous. When the adsorbent is reused for five cycles,

the adsorption capacity decreases from 33.47 (for the first cycle) to 27.69 mg/g (for the fifth cycle).

Arunraj et al. (2019) found that the adsorption efficiency of *Saccharomyces cerevisiae* immobilised in glutaraldehyde cross-linked chitosan increased in the pH range from 2 to 8 and reached its maximum at pH of 5 (~100%) and then remained at a constant level. The low efficiency of europium removal in the pH range of 2–5 is due to the protonation of the functional groups of the adsorbent, which acquire a positive charge, resulting in electrostatic repulsion between the adsorbent and the adsorbate. The high adsorption in the pH range of 5–6, although the adsorbent only acquires a negative surface charge at a pH>5.58, is related to ion exchange mechanisms. A high percentage of removal at pH of 6–8 is related to the electrostatic interaction between the deprotonated functional groups of the adsorbent and the europium ions. The adsorption efficiency increased with increasing dosage of the adsorbent and reached a maximum at 6 g/L, where the percentage of removal was ~100%. With an increase in the initial Eu(III) concentration from 20 to 200 mg/L and contact time from 5 to 60 min, the adsorption capacity of the composite increased, and the Freundlich and pseudo-second-order models described the experimental data well. Moreover, a state of equilibrium was reached on the adsorbent within 60 min. According to the thermodynamics results, the adsorption of Eu(III) on *Saccharomyces cerevisiae* immobilised in glutaraldehyde cross-linked chitosan was endothermic and spontaneous. The adsorption efficiency of the adsorbent from the first to the fourth application cycle was 94.8, 93.5, 90.2, and 87.3%, respectively. Potassium thiocyanate was used as a regenerant. In a medium containing samarium, erbium, lanthanum, and cerium, the selectivity of the adsorbent for europium was 98%. The adsorption mechanism involves physisorption and chemisorption, and the following functional groups OH, NH<sub>2</sub>, C=N, and COOH of the composite are responsible for the adsorption.

The authors of Cadogan et al. (2014) reported that the adsorption of europium ions on chitosan increased sharply from a pH of 2 to a pH of 3. After a pH of 3, adsorption was stable and the adsorption capacity was ~25 mg/g. The increase in adsorption capacity with an increase in pH is associated with an increase in deprotonated adsorption sites. Increasing the mass of the adsorbent from 10 to 100 mg increased the adsorption efficiency (from 7.21 to 98.1%) but decreased the adsorption capacity. In the contact time range of 5–120 min, the adsorbent reached equilibrium in 60 min, and the maximum adsorption capacity in this time range was 24.9 mg/g. The adsorption of europium on chitosan follows the pseudo-second-order kinetic model. The adsorption capacity of chitosan increases from 23 to 142 mg/g in direct

proportion to the increase in the initial concentration of Eu(III) from 10 to 100 mg/L. Furthermore, the Langmuir model fits these experimental data better than the Freundlich and Temkin models. The calculated value for the maximum adsorption capacity was 114.9 mg/g.

The results of a study on the adsorption of Eu(III) on muscovite (cation exchange capacity: 4.01 meq/100 g) were presented by Wu et al. (2021). It was found that the adsorption of Eu(III) at pH<5 was consistently low (~35%) and controlled, according to the ionic strength results, by ion exchange and/or outer-sphere complexation. In the pH range of 5–7, the removal efficiency increases rapidly (from 35 to 99%) due to an increase in the negative charge of the muscovite and the formation of inner-sphere complexes (according to the ionic strength results) on the surface of the muscovite. After pH>7, the percentage removal was consistently high at 99%. Moreover, no precipitation of Eu(III) was observed at pH of 8.4. Competing ions such as K<sup>+</sup>, Cs<sup>+</sup>, and Ca<sup>2+</sup> inhibit the adsorption of Eu(III) more than Na<sup>+</sup> in the pH range of 2–7. However, at a pH>7, there was no significant effect and the removal efficiency was ~99%. According to the X-ray diffraction analysis, the structure of muscovite remained practically unchanged after adsorption of europium, indicating that adsorption occurs mainly at planar sites. Fulvic acid in the presence of Na<sup>+</sup> or Cs<sup>+</sup> in the medium increased the adsorption of europium from ~5% to ~60% in the pH range of 2–6, and then, after a pH of 6, the removal rate decreased to less than 5% at a pH of 11. Moreover, according to the sequential extraction results, muscovite has a low affinity for Eu(III), compared to another member of the mica family – phlogopite.

Shao et al. (2009) found that the adsorption of europium in NaClO<sub>4</sub> solution (0.01 mol/L (moles per litre)) on ZSM-5 increased from ~3 to ~90% when the pH increased from ~2 to ~5, and above a pH of 5, europium adsorption was consistently high. In NaClO<sub>4</sub> solution (0.1 mol/L), the percentage removal increased from ~3 to ~90% in the pH range of 2–9. Furthermore, the authors note that no precipitation of Eu(OH)<sub>3</sub> was found at a pH of ~8.5 and that ion exchange processes predominate at low pH, while surface complexation processes predominate at neutral or alkaline pH. The adsorption of Eu(III) on ZSM-5 at pH of 3.62 is well described by the Langmuir model and at pH of 4.85 by the Freundlich model. The calculated value for the maximum adsorption capacity of the adsorbent was  $\sim 1.59 \times 10^{-5}$  mol/g (mole per gramme) at a pH of 3.62. Furthermore, the presence of humic acid increases the adsorption of europium on ZSM-5.

#### 1.4. Adaptive neuro-fuzzy inference system

The adaptive neuro-fuzzy inference system is a multi-level neural network based on the fuzzy if-then rule to produce stipulated input-output pairs. ANFIS emerged from a combination of artificial neural network approaches and fuzzy logic. The role of the artificial neural network in ANFIS is to control the adaptability of the system, while the fuzzy logic improves the accuracy and reliability of the system (Jang 1992; Dolatabadi et al. 2018; Sadeghizadeh et al. 2019; Foroutan et al. 2020). ANFIS is a powerful tool for forecasting, mapping, and modelling. It is used to describe non-linear changes in complex systems, such as adsorbent-adsorbate, where the behaviour of the adsorbate on the adsorbent is non-linear and depends on a number of factors (pH, temperature, contact time, initial adsorbate concentration, and adsorbent dosage) (Amiri et al. 2013; Rezaei et al. 2017; Souza et al. 2018; Khomeyrani et al. 2021; Onu et al. 2021).

ANFIS training is mainly performed on ~70% of the datasets, while ~30% are used for testing, the results of which in turn provide an independent assessment of the generalisation ability of the network. It should also be noted that data are randomly selected prior to input into the network and in some cases normalised from 0 to 1 to reduce the influence of higher magnitude factors on the ANFIS and ensure error-free analysis of the system (Amiri et al. 2013; Rezaei et al. 2017; Mendoza-Castillo et al. 2018; Dolatabadi et al. 2018; Souza et al. 2018; Foroutan et al. 2020; Onu et al. 2021). Moreover, the number of input parameters used (adsorbent dosage, initial adsorbate concentration, pH, temperature, and contact time) affects the quality of the prediction: The more input parameters used for training, the better the performance of the network (Amiri et al. 2013). Furthermore, the choice of output variables is also important for the quality of the prediction. For example, using intensive variables such as adsorption capacity leads to a better prediction result than using extensive variables: Adsorption efficiency/equilibrium concentration (Mendoza-Castillo et al. 2018; Souza et al. 2018). The performance of an ANFIS network is estimated by fitting the experimental data and the predicted data using the correlation coefficient, the determination coefficient, the mean squared error, the sum of squared errors, the average relative error, the mean absolute error, the sum of the absolute error, the absolute average deviation, the root mean square values, etc. (Rezaei et al. 2017; Dolatabadi et al. 2018; Souza et al. 2018).

According to some studies, ANFIS has been found to be a better predictive model for the Nteje clay-Eriochrome black-T system than the artificial neural network and response surface methodology (Onu et al. 2021).

For the layered double hydroxide-graphene oxide-CNTs-Para Nitrophenol systems than general regression neural network and the response surface methodology (Khomeyrani et al. 2021). For tropical soils-Cu(II)/Cd(II)/Pb(II), X and Y faujasite zeolites-methane systems than multiple linear regression (Rezaei et al. 2017; Agbaogun et al. 2022). For activated carbon-Ni(II) system than artificial neural network (Souza et al. 2018).

## 2. MATERIALS AND METHODS

### 2.1. Preparation of composites

#### 2.1.1. Preparation of muscovite mica clay-graphene oxide-maghemite-magnetite composite

A natural sample from the Šaltiškiai industrial exploration site in northern Lithuania contains groups of various minerals, including clay minerals, the predominant minerals being quartz and muscovite (according to XRD, section 3.1.1.), hence this sample is given the following name: Muscovite mica clay. The sample of muscovite mica clay was used without pre-treatment for the preparation of the MSMC-GO-MGH-MG composite.

Graphene oxide was obtained by the Tour method (Marcano et al. 2010). Graphite powder (<20  $\mu\text{m}$  synthetic, Sigma-Aldrich) was mixed with  $\text{H}_2\text{SO}_4$  and  $\text{H}_3\text{PO}_4$  at room temperature under argon flow. Then  $\text{KMnO}_4$  was gradually added to this mixture under constant stirring, 55  $^\circ\text{C}$ , and argon flow. After the mixture turned dark red, it was transferred to a beaker with ice and  $\text{H}_2\text{O}_2$  (30%) was added to remove excess  $\text{MnO}_4^-$  anions. The resulting yellow suspension was centrifuged at 6000 rpm for 10 min. The precipitate was washed in the following order: Milli-Q water (Milli-Q Synthesis A10), concentrated HCl, 1 M HCl, Milli-Q water,  $\text{C}_2\text{H}_5\text{OH}$  (Absolute, Merck),  $\text{C}_6\text{H}_{14}\text{O}$  and Milli-Q water, and then dried under vacuum.

Maghemite-magnetite was obtained by co-precipitation of ferric and ferrous ions (Tayyebi et al. 2015). Aqueous solutions of  $\text{FeCl}_3$  and  $\text{FeCl}_2$  were mixed in a of 2:1 (v/v) ratio at 85  $^\circ\text{C}$  and then a 30% ammonia solution was added. The resulting precipitate was separated by magnetic separation, washed with  $\text{C}_2\text{H}_5\text{OH}$  and Milli-Q water, and then dried at room temperature.

The MSMC-GO-MGH-MG composite was prepared in the following way:

Suspensions of MSMC (4 g in 200 mL Milli-Q water), MGH-MG (2 g in 200 mL Milli-Q water), and GO (0.06 g in 60 mL Milli-Q water) were sonicated at room temperature for 30 min (for MSMC) and 2 h (for MGH-MG and GO). Two samples of the GO suspensions were prepared in this way for further preparation of the MSMC-GO and MGH-MG-GO suspensions.

The suspensions of MSMC-GO and MGH-MG-GO were prepared by mixing the initial suspensions under constant stirring for 30 min and 60  $^\circ\text{C}$  in the first case and under constant stirring for 30 min, sonication, and room temperature in the second case. The suspension MGH-MG-GO was then gradually added to the suspension MSMC-GO. The resulting mixture was kept

under constant stirring in a flow of argon at 60 °C for 1.5 h. The precipitate was removed by magnetic precipitation, washed twice with Milli-Q water and dried in vacuo.

The weight percentage (wt%) of the resulting composite (MSMC-GO-MGH-MG-1 (C-1)) was 65.36% MSMC (4 g), 32.68% MGH-MG (2 g), and 1.96% GO (0.12 g). In addition, another such composite was also prepared by this method (MSMC-GO-MGH-MG-2 (C-2)), but with an increased content of MGH-MG, whose weight percentage was 49.26% MSMC (4 g), 49.26% MGH-MG (4 g), and 1.48% GO (0.12 g). The weight ratio of the components proved to be quite optimal for equally effective adsorption of Cs(I) and Co(II) in the case of C-1 compared to C-2 with a higher content of maghemite-magnetite. In the case of C-2, the adsorption of Cs(I) was 1.7 times lower and that of Co(II) 1.2 times higher (The results of the primary adsorption studies are discussed in more detail in section 3.2.).

### 2.1.2. Preparation of Prussian blue-graphene oxide and magnetite-Prussian blue-graphene oxide composites

Graphene oxide 1 and 2 (GO 1 and GO 2) were obtained by the Hummers method (Hummers and Offeman 1958) by mixing graphite powder and  $\text{NaNO}_3$  with concentrated  $\text{H}_2\text{SO}_4$  under sonication in an ice bath, followed by the stepwise addition of  $\text{KMnO}_4$ , then the excess  $\text{MnO}_4^-$  was removed with  $\text{H}_2\text{O}_2$  (30%) solution. The resulting suspension was filtered and the precipitate was washed with Milli-Q water and  $\text{C}_2\text{H}_5\text{OH}$  and dried at 70 °C in vacuo. The difference between GO 1 and GO 2 lies in the holding time of the mixture after the addition of  $\text{KMnO}_4$ , which was 24 h for GO 1 and 72 h for GO 2.

Magnetite was obtained by mixing solutions of 1 mol/L  $\text{FeSO}_4$ , 2 mol/L  $\text{Fe}_2(\text{SO}_4)_3$ , and 2 mol/L  $\text{H}_2\text{SO}_4$  followed by dropwise addition of 1 mol/L ammonia solution with continuous vigorous stirring in an argon stream and at 90 °C. The magnetite particles were separated with a magnet, then washed with  $\text{C}_3\text{H}_6\text{O}$  and dried.

Prussian blue 1 and 2 (PB 1 and PB 2) were prepared by dropwise addition of  $\text{K}_4[\text{Fe}(\text{CN})_6]$  and  $\text{K}_3[\text{Fe}(\text{CN})_6]$  solutions to 0.02 mol/L  $\text{Fe}_2(\text{SO}_4)_3$  and  $\text{FeSO}_4$  solutions, respectively. The resulting mixture was stirred for 1 h and acidified. Then it was centrifuged (6000 rpm, 10 min) and the resulting precipitate was washed with deionised water to pH~7 and dried.

PBGO 2.1 and PBGO 2.2 were synthesised using GO 2,  $\text{FeSO}_4$  (0.02 mol/L),  $\text{K}_4[\text{Fe}(\text{CN})_6]$  for PBGO 2.1, and  $\text{K}_3[\text{Fe}(\text{CN})_6]$  for PBGO 2.2.

MPBGO 2.3 and MPBGO 3.2 were prepared as follows: Magnetite dispersed in an ultrasonic bath was mixed with a suspension of GO 1 and GO



2 in a ratio of 1:100 for MPBGO 2.3 and MPBGO 3.2, respectively, for 10 min with continuous stirring, acidified to pH 3 with 10% H<sub>2</sub>SO<sub>4</sub>, and FeSO<sub>4</sub> was added gradually. After 1 h, a K<sub>4</sub>[Fe(CN)<sub>6</sub>] solution was added dropwise to the suspensions. The resulting mixtures were stirred in an argon atmosphere for 1 h, then the precipitate was separated with a magnet, washed with water, and dried.

### 2.1.3. Preparation of chitosan-mineral composites

For the preparation of chitosan-mineral composites was used: Chitosan (average molecular weight: 190–310 kDa, ≤75% deacetylation; Sigma-Aldrich), muscovite mica clay, montmorillonite K10 (surface area: 220–270 m<sup>2</sup>/g; Sigma-Aldrich), zeolite Socony Mobil-5 (Acros Organics), cross-linking agents (glutaraldehyde (C<sub>5</sub>H<sub>8</sub>O<sub>2</sub>; 50%, Sigma-Aldrich), epichlorohydrin (C<sub>3</sub>H<sub>5</sub>ClO; ≥99%, Sigma-Aldrich) and sodium tripolyphosphate (Na<sub>5</sub>P<sub>3</sub>O<sub>10</sub>; 85%, Sigma-Aldrich)), and plasticiser – glycerol (C<sub>3</sub>H<sub>8</sub>O<sub>3</sub>; ≥99%, Sigma-Aldrich).

A fine fraction of MSMC with a particle size of 1–0.2 μm was used to prepare the CS-MSMC composite, which was separated from the main sample by wet sieving and column settling, centrifugation and membrane filtration techniques (Lujanienė et al. 2006; Lujanienė et al. 2015). The isolated fraction was dried, ground, and activated with 0.5 M HCl. Then this fraction was added to a 1% CH<sub>3</sub>COOH solution, the resulting suspension was sonicated, then mixed with a 2% chitosan solution in a 1% CH<sub>3</sub>COOH solution and this mixture was then placed in an ultrasonic bath for 30 min. The resulting CS-MSMC gel was precipitated by dropwise addition of a 1 M solution of a mixture of NaOH and C<sub>2</sub>H<sub>5</sub>OH (1:1) to the gel suspension. The gel was washed with C<sub>2</sub>H<sub>5</sub>OH and CH<sub>3</sub>CN solutions. The CS-MSMC gel suspension was left in acetonitrile for several days. Before using CS-MSMC, the gel (composite) was filtered and washed with deionised water to neutral pH.

The CS-MSMC-GLUT composite was prepared by incubating the resulting CS-MSMC gel in an aqueous solution of glutaraldehyde (2.5% w/v) for 24 h, then washing with deionised water and drying.

The CS-MSMC-ECH composite was prepared by dropwise addition of the prepared 1% (40 mM) solution of epichlorohydrin to the CS-MSMC gel with constant stirring for 3 h and 50 °C. The resulting composite was filtered, washed with deionised water, and dried at 50 °C.

The CS-MSMC-STP composite was prepared by gradually adding dropwise a suspension of CS-MSMC to a solution of sodium tripolyphosphate

(pH 8.2) with constant stirring for 4 h and 30 °C. The resulting composite was filtered, washed with deionised water, and dried at room temperature.

The CS-Mt-GLY was synthesised according to the technology used for the preparation of a CS-MSMC composite, in which a plasticiser (glycerol) was first added at a concentration of 1 wt% to a chitosan-CH<sub>3</sub>COOH solution before mixing with montmorillonite in a 1% CH<sub>3</sub>COOH solution.

The CS-Zeo composite was prepared as follows: The ZSM-5 powder was washed with deionised water and heated for 2 h at 105 °C. Then the dried powder was added to the prepared 2% solution of chitosan in 1% CH<sub>3</sub>COOH solution for 2 h with constant stirring. The resulting composite was filtered, washed with deionised water, and dried for 12 h at 60 °C.

## 2.2. Characterisation

X-ray diffraction analyses were performed using the SmartLab X-ray diffractometer (Rigaku, Japan) and the D8 Advance X-ray diffractometer (Bruker AXS, Germany), equipped with an X-ray tube with 9 and 2.4 kW rotating Cu anode, respectively. Measurements were performed using Bragg-Brentano geometry with a graphite monochromator on the diffracted beam in the case of the SmartLab X-ray diffractometer and a V groove Ge monochromator in the case of the D8 Advance X-ray diffractometer and a step-scan mode with a step size of 0.02 ° in a 2 $\theta$ -scale and a counting time of 1s per step. Measurements were made in a 2 $\theta$  range of 5–75 °. Phase identification was performed by the PDXL software package (Rigaku) and the ICDD powder diffraction database PDF4+ (2021 release). Mineral content was estimated using the Reference Intensity Ratio (RIR) method. Fourier transform infrared spectroscopy was performed by the Alpha spectrometer (Bruker Inc., Germany) equipped with an ATR platinum diamond accessory and a room temperature detector RT-DLATGS (spectral resolution was set to 4 cm<sup>-1</sup>). Also, the Vertex 70v vacuum spectrometer (Bruker Inc., Germany) with a KBr pellet for sample preparation (the spectral resolution was set to 2 cm<sup>-1</sup>). The RAM II system (Bruker Inc., Germany) (180° backscattering configuration) with a 1064 nm laser was used to record Raman spectra. X-ray photoelectron spectroscopy was performed using an ESCALAB MKII spectrometer (VG Scientific, UK) equipped with an Al K $\alpha$  X-ray source (1486.6 eV). Mössbauer spectroscopy measurements were performed at room temperature by the Mössbauer spectrometer (Wissenschaftliche Elektronik GmbH, Germany) in transmission geometry by the <sup>57</sup>Co (Rh) source. The morphology of the resulting composites and the original materials was investigated by a dual-beam system scanning electron microscope Helios

NanoLab 650 (FEI, Netherlands) (equipped with a field emission electron gun and a focused Ga-ion beam source of 30 keV) and a transmission electron microscope Tecnai G2 F20 X-TWIN (FEI, Netherlands) (with an accelerating voltage of 200 kV; TEM Images were taken with a Gatan Orius CCD camera in brightfield mode).

### 2.3. Batch experiments

Laboratory batch experiments were used to study the adsorption of Cs(I) and Co(II) on the MSMC-GO-MGH-MG composite. Adsorption of Cs(I) on PBGO and MPBGO composites. Adsorption of Cs(I), Co(II), and Eu(III) on chitosan-mineral composites.

A series of experiments were carried out depending on the initial concentration, pH, and contact time:

For the MSMC-GO-MGH-MG, the investigated range of initial concentrations of Cs(I) and Co(II) were 394–12630 and 100–3200 mg/L, respectively. The pH range of Cs(I) and Co(II) was 1–10 and 1–6, respectively. The range of contact time of Cs(I) and Co(II) was 5–240 min.

For the PBGO and MPBGO composites, the investigated range of initial concentrations of Cs(I) was 50–800 mg/L. The pH range of Cs(I) was 3–9.5. The range of contact time of Cs(I) was 5–1440 min.

For the chitosan-mineral composites, the investigated range of initial concentrations of Cs(I), Co(II), and Eu(III) were 50–5000, 50–3000, and 0.01–30 mg/L, respectively. The pH range of Cs(I), Co(II), and Eu(III) was 3–9, 3–7, and 3–7, respectively. The range of contact time of Cs(I), Co(II) and Eu(III) was 5–1440 min.

Furthermore, additional tests were performed for the systems MSMC-GO-MGH-MG-Cs(I)/Co(II) depending on the mass of the adsorbent (0.01–0.16 g) and the temperature (25–75 °C).

In addition to the variable parameters listed above, the other parameters were constant during the tests:

For the composite MSMC-GO-MGH-MG the initial concentration for Cs(I) of 3158 mg/L and Co(II) of 800 mg/L. The pH for Cs(I) of 7 and Co(II) of 5. The contact time is 1440 and 60 min for the temperature effect only. The mass of the adsorbent is 0.01 g. The temperature is 20±1 °C.

For the PBGO and MPBGO composites, the initial Cs(I) concentration is 200 mg/L (in the case of the pH effect) and 100 mg/L (in the case of the contact time effect). The pH value is 7. The contact time is 1440 min. The mass of the adsorbent is 0.01 and 0.005 g (only to test the effect of the initial concentration). The temperature is 25 °C.

For the chitosan-mineral composites, the initial concentration is Cs(I) 3000 mg/L, Co(II) 3000 mg/L (in the case of the pH effect) and 1000 mg/L (in the case of the contact time effect), and Eu(III) 20 mg/L. The pH for Cs(I) is 7, Co(II) 5, and Eu(III) 5. The contact time is 1440 min. The mass of the adsorbent is 0.01 g. The temperature is 25 °C.

Additionally, primary adsorption studies for MSMC, GO, MGH-MG, MSMC-GO-MGH-MG-1, and -2 for caesium and cobalt ions were performed under the following conditions: The initial ion concentration of 50 mg/L, the pH(Cs(I))=7, pH(Co(II))=5, the mass of the adsorbent of 0.01 g, the temperature of 20±1 °C, and the contact time of 1440 min.

The experimental solutions were prepared from stock solutions using standard dilution methods. In turn, the stock solutions were prepared from Milli-Q water and analytical grade CsCl, Co(NO<sub>3</sub>)<sub>2</sub>·6H<sub>2</sub>O (only in the case of the MSMC-GO-MGH-MG tests), CoCl<sub>2</sub>, and EuCl<sub>3</sub>, which were pre-weighed on a high-precision analytical balance (Mettler Toledo AT201). Adsorption tests were performed in 15 mL polypropylene centrifuge tubes (CLEARLine) with a working volume of 10 mL and a shaking speed of 150–200 rpm. The CsCl, Co(NO<sub>3</sub>)<sub>2</sub>·6H<sub>2</sub>O/CoCl<sub>2</sub>, and EuCl<sub>3</sub> solutions were traced with <sup>137</sup>Cs, <sup>60</sup>Co, and <sup>152</sup>Eu, respectively. The initial pH of the solutions was adjusted by HCl and NaOH and monitored by a pH meter of InoLab pH Level 1 (WTW, Germany) with SenTix 41 pH electrode (WTW, Germany) calibrated with standard buffers DIN 19266. After the adsorption tests, the adsorbents were separated from the solution by centrifugation at 20000xg for 15 min or by a magnet. Subsequently, the activity concentrations of Cs, Co, and Eu in the solution were measured by gamma spectrometry using high purity germanium (HPGe) detectors (GEM40P4-76, resolution 1.9 keV/1.33 MeV and efficiency 42%; and the coaxial well GWL-120-15-LB-AWT detector, resolution 2.25 keV/1.33 MeV).

The adsorption capacity of the adsorbents was calculated by Eq. (1):

$$Q_e = \frac{(C_i - C_e)}{W} \times V \quad (1)$$

where  $Q_e$  (mg/g) is the amount of ion adsorbed at equilibrium,  $C_i$  (mg/L) is the initial concentration of the ion,  $C_e$  (mg/L) is the equilibrium concentration of the ion,  $V$  (L) is the working volume,  $W$  (g) is the mass of the adsorbent.

## 2.4. Adsorption isotherms, kinetics, and thermodynamics

Linear Langmuir (Eq. 2) and Freundlich (Eq. 3) and non-linear Langmuir (Eq. 4) and Freundlich (Eq. 5) isotherms used to describe equilibrium in the composite-Cs(I)/Co(II)/Eu(III) systems. From the Langmuir isotherm it follows that the monolayer adsorption of adsorbates takes place on a homogeneous adsorbent surface where the active adsorption sites have the same affinity for the adsorbate. Furthermore, the adsorbates do not interact with each other after adsorption. In contrast, it follows from the Freundlich isotherm that the multilayer adsorption of the adsorbate takes place on a heterogeneous surface and that there is interaction between the adsorbates after adsorption (Inyinbor et al. 2016; Mohseni-Bandpei et al. 2020; Esmaeili and Tamjidi 2020).

$$\frac{C_e}{Q_e} = \frac{1}{K_L Q_m} + \frac{C_e}{Q_m} \quad (2)$$

$$\log Q_e = \log K_F + \frac{1}{n} \log C_e \quad (3)$$

$$Q_e = \frac{K_L Q_m C_e}{(1 + K_L C_e)} \quad (4)$$

$$Q_e = K_F C_e^{1/n} \quad (5)$$

Where  $K_L$  (L/mg) and  $K_F$  [(mg/g)(L/mg)] are the constant coefficients for the Langmuir and Freundlich isotherms;  $Q_m$  (mg/g) is the theoretical maximum adsorption capacity;  $1/n$  is the Freundlich intensity parameter. If the value of  $1/n < 1$ , the adsorption process is favourable (Al-Senani and Al-Fawzan 2018). For the linear forms of the Langmuir and Freundlich isotherms, these parameters were determined and calculated from the slope and intercept of the linear plot.

Using the Langmuir isotherm, the separation factor  $R_L$  (Eq. 6) was calculated, according to which the adsorption process is favourable at  $0 < R_L < 1$ , unfavourable at  $R_L > 1$ , linear at  $R_L = 1$ , and irreversible at  $R_L = 0$ .

$$R_L = \frac{1}{(1 + K_L C_i)} \quad (6)$$

Linear and non-linear pseudo-first-order kinetic models (Eqs. 7 and 8) and linear and non-linear pseudo-second-order kinetic models (Eqs. 9 and 10) were used to estimate the reaction rate and determine the nature of the adsorption process (physical, chemical or mixed) (Inyinbor et al. 2016; Mohseni-Bandpei et al. 2020; Esmaeili and Tamjidi 2020).

$$\ln(Q_e - Q_t) = \ln Q_e - K_1 t \quad (7)$$

$$Q_t = Q_e(1 - e^{-K_1 t}) \quad (8)$$

$$\frac{t}{Q_t} = \frac{1}{K_2 Q_e^2} + \frac{1}{Q_e} \quad (9)$$

$$Q_t = \frac{Q_e^2 K_2 t}{(1 + K_2 Q_e t)} \quad (10)$$

Where  $Q_t$  (mg/g) is the amount of adsorbed adsorbate per unit mass of adsorbent (mg/g) at time  $t$  (min);  $K_1$  ( $\text{min}^{-1}$ ) and  $K_2$  (g/mg.min) are the rate constants for pseudo-first-order and pseudo-second-order, respectively. For the linear forms of the pseudo-first- and pseudo-second-order kinetic models, these parameters were determined and calculated from the slope and intercept of the linear plot.

To explain the spontaneity and the nature of the interaction of the adsorbate with the adsorbent, the main thermodynamic parameters were used: Gibbs free energy change ( $\Delta G^\circ$ ), enthalpy change ( $\Delta H^\circ$ ), and entropy change ( $\Delta S^\circ$ ) calculated using Eqs. (11), (12), and (13) (Inyinbor et al. 2016; Esmaeili and Tamjidi 2020):

$$K_c = \frac{Q_e}{C_e} \quad (11)$$

$$\Delta G^\circ = -RT \ln K_c \quad (12)$$

$$\ln K_c = -\frac{\Delta H^\circ}{RT} + \frac{\Delta S^\circ}{RT} \quad (13)$$

where  $K_c$  (L/mg) is the adsorption equilibrium constant;  $R$  (8.314 J/mol K) is the universal gas constant,  $T$  (K) is the absolute temperature. The parameters  $\Delta H^\circ$  and  $\Delta S^\circ$  were calculated from the intercept and slope of the linear plot of  $\ln K_c$  versus  $1/T$  (Fig. 7).

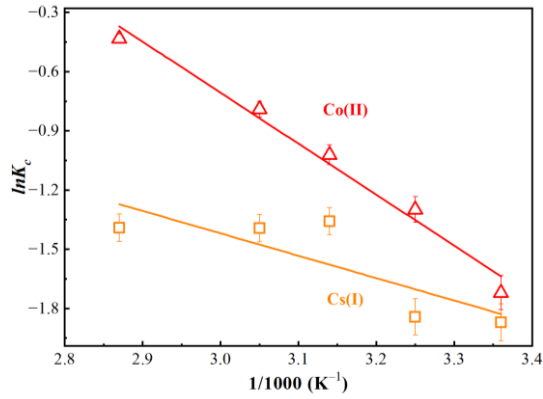


**Fig. 7.** Plots of  $\ln K_c$  as a function of  $1/T$  relating to the adsorption of Cs and Co ions on MSMC-GO-MGH-MG at different temperatures.

### 2.5. ANFIS development

The ANFIS multilayer architecture for the systems MSMC-GO-MGH-MG-Cs(I)/Co(II) (Fig. 8a), and PBGO-Cs(I), MPBGO-Cs(I), and chitosan-mineral-Cs(I)/Co(II)/Eu(III) (Fig. 8b) was implemented in MATLAB R2021a (Fuzzy Logic Toolbox (Sugeno-type)).

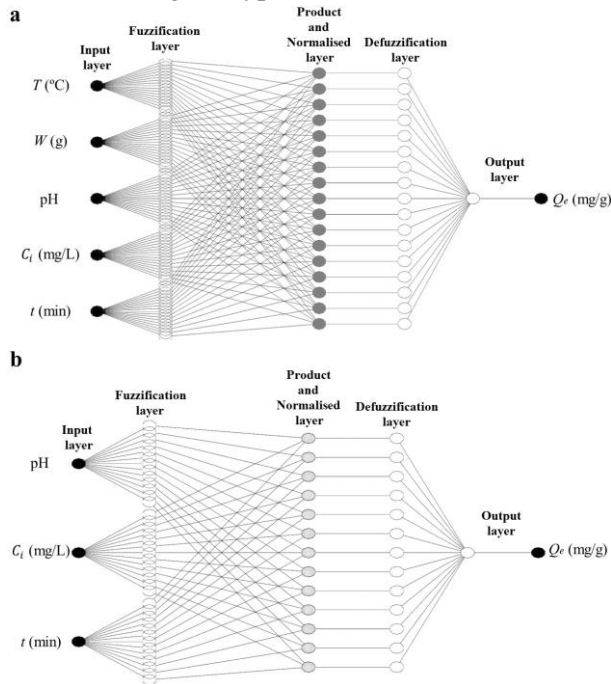


**Fig. 8.** ANFIS architecture for MSMC-GO-MGH-MG-Cs(I)/Co(II) (a) and PBGO-Cs(I), MPBGO-Cs(I), and chitosan-mineral-Cs(I)/Co(II)/Eu(III) (b).

The first layer represents the input variables: Temperature ( $T$  (°C)), mass of adsorbent ( $W$  (g)), pH, initial ion concentration ( $C_i$  (mg/L)), and contact time ( $t$  (min)). The second layer is the fuzzification layer, where the input variables are converted into fuzzy variables. The third layer is the product and normalised layer, which contains the Sugeno if-then type fuzzy rules. The fourth layer is the defuzzification layer, in which the variables from the third layer are converted into crisp output variables. The fifth and final layer is the generated fuzzy output variable (adsorption capacity ( $Q_e$  (mg/g)) from the sum of the values of the previous layer (Sada and Ikpeseni 2021). Neural network training was performed on 21 (MSMC-GO-MGH-MG-Cs(I)/Co(II)), 18 (PBGO 2.2-Cs(I), MPBGO 2.3-Cs(I), MPBGO 3.2-Cs(I), and chitosan-mineral-Cs(I)), 17 (chitosan-mineral-Co(II)), and 16 (PBGO 2.1-Cs(I) and chitosan-mineral-Eu(III)) datasets. Using Gaussian functions (Gausesm2) with subtractive clustering (Table 2), a hybrid method to optimise the modelling (Souza et al. 2018), an error tolerance of 0, and epochs (number of training cycles) of 100 iterations.

**Table 2.** Parameters for ANFIS training.

Adsorbates	Subtractive clustering				Rules
	Range of influence	Reject ratio	Squash factor	Accept ratio	
<b>MSMC-GO-MGH-MG</b>					
Cs(I)	0.5	0.15	0.1	0.5	17
Co(II)	0.1	0.15	1.25	0.5	19
<b>PBGO 2.1</b>					
Cs(I)	0.2	0.15	1.25	0.5	12
<b>PBGO 2.2</b>					
Cs(I)	0.2	0.15	1.25	0.5	12
<b>MPBGO 2.3</b>					
Cs(I)	0.2	0.15	1.25	0.5	12
<b>MPBGO 3.2</b>					
Cs(I)	0.5	0.15	1.25	0.5	6
<b>CS-MSMC</b>					
Cs(I)	0.5	0.15	1.25	0.5	9
Co(II)	0.9	0.15	1.25	0.5	3
Eu(III)	0.5	0.15	1.25	0.5	7
<b>CS-MSMC-GLUT</b>					
Cs(I)	0.5	0.15	1.25	0.5	6
Co(II)	0.5	0.15	1.25	0.5	6
Eu(III)	0.7	0.15	1.25	0.5	4
<b>CS-MSMC-ECH</b>					



Cs(I)	0.5	0.15	1.25	0.5	8
Co(II)	0.5	0.15	1.25	0.5	6
Eu(III)	0.5	0.15	1.25	0.5	6
<b>CS-MSMC-STP</b>					
Cs(I)	0.2	0.15	1.25	0.5	13
Co(II)	0.9	0.15	1.25	0.5	3
Eu(III)	0.7	0.15	1.25	0.5	4
<b>CS-Mt-GLY</b>					
Cs(I)	0.9	0.15	1.25	0.5	4
Co(II)	0.5	0.15	1.25	0.5	6
Eu(III)	0.7	0.15	1.25	0.5	5
<b>CS-Zeo</b>					
Cs(I)	0.2	0.15	1.25	0.5	13
Co(II)	0.3	0.15	1.25	0.5	9
Eu(III)	1	0.15	1.25	0.5	3

Tests of the network were performed on 12 (PBG0 2.1 and 2.2-Cs(I) and MPBG0 2.3 and 3.2-Cs(I)), 10 (MSMC-GO-MGH-MG-Cs(I)/Co(II)), and 5 (chitosan-mineral-Cs(I)/Co(II)/Eu(III)) datasets. In addition, the training and testing data were randomly selected and the input and output variables were normalised from 0 to 1 by Eq. (14) before entering the network. To evaluate the performance and generalisation ability of the network, error analysis was performed using the coefficient of correlation (R) (Eq. 15), the mean squared error (MSE) (Eq. 16), the sum of squared errors (SSE) (Eq. 17), and the average relative error (ARE) (Eq. 18).

$$X_{norm} = \frac{X - X^{\downarrow}}{X^{\uparrow} - X^{\downarrow}} \quad (14)$$

$$R = \frac{\sum_{i=1}^N [(X_{\psi,i} - X_{\psi,av})(X_{\omega,i} - X_{\omega,av})]}{\sum_{i=1}^N [(X_{\psi,i} - X_{\psi,av})^2] \sum_{i=1}^N (X_{\omega,i} - X_{\omega,av})} \quad (15)$$

$$MSE = \frac{1}{N} \sum_{i=1}^N (X_{\psi,i} - X_{\omega,i})^2 \quad (16)$$

$$SSE = \sqrt{\frac{\sum_{i=1}^N (X_{\omega,i} - X_{\psi,i})^2}{N}} \quad (17)$$

$$ARE = \frac{100}{N} \sum_{i=1}^N \left| \frac{X_{\psi,i} - X_{\omega,i}}{X_{\omega,i}} \right| \% \quad (18)$$

Where  $X_{norm}$  is the normalised value,  $X^\downarrow$  and  $X^\uparrow$  are the minimum and maximum values, respectively, and  $\vec{x}$  is a vector of values.  $N$  is the number of experimental points,  $X_{\omega,i}$  is the experimental output,  $X_{\psi,i}$  is the predicted output,  $X_{\psi,av}$  and  $X_{\omega,av}$  are the average of the predicted output and the average of the experimental output, respectively.

### 3. RESULTS AND DISCUSSION

#### 3.1. Material characterisation

##### 3.1.1. XRD

The results of XRD analysis of natural untreated muscovite mica clay, maghemite-magnetite, graphene oxide, and MSMC-GO-MGH-MG-1 and -2 composites are shown in Figs. 9a and b. The following phases were identified in MSMC: Quartz (34.5%; (ICDD # 00-046-1045)), muscovite (23.36%; (ICDD # 01-089-7536)), dolomite (18.2%; (ICDD # 04-012-1195)), clinocllore (9.5%; (ICDD # 04-013-2805)), calcite (12.4%; (ICDD # 01-083-4602)), kaolinite (1.1%; (ICDD # 01-074-1784)), and montmorillonite (0.94%; (ICDD # 00-013-0135)). In the XRD pattern of MGH-MG, the diffraction peaks shown are at  $2\theta=18.43, 30.19, 35.57, 43.27, 53.66, 57.19, 62.79,$  and  $74.15^\circ$  are associated with the *crystallographic planes* (111), (220), (311), (400), (442), (511), (440), and (533) of both MGH ((ICDD # 00-039-1346) and MG (ICDD # 01-084-9337)) (Compeán-Jasso et al. 2008; Esmaeili and Tamjidi 2020). In the XRD pattern of MSMC-GO-MGH-MG-1 and -2 composites, the observed diffraction peaks correspond to muscovite mica clay and maghemite-magnetite, but the characteristic peak of graphene oxide at  $2\theta=10.6^\circ$  was not detected, apparently due to the delamination of graphene oxide layers by the introduction of MSMC layers (Ye et al. 2019). In addition, the percentage of phases in the MSMC-GO-MGH-MG-1 composite was as follows: Muscovite (29.68%), maghemite-magnetite (28.5%), quartz (18.3%), dolomite (8%), clinocllore (3.8%), calcite (10.2%), kaolinite (1.0%), and montmorillonite (0.32%). While in MSMC-GO-MGH-MG-2 composite: Maghemite-magnetite (64.2%), muscovite (12.7%), quartz (8%), dolomite (2.8%), clinocllore (8.03%), calcite (3.47%), and kaolinite (0.8%). The composite MSMC-GO-MGH-MG-1 is dominated by the phases muscovite and maghemite-magnetite, while the composite MSMC-GO-MGH-MG-2 is dominated by the phase maghemite-magnetite. The comparison of the percentages of the phases muscovite and maghemite-magnetite between the composites shows that the content of maghemite-magnetite in the composite MSMC-GO-MGH-MG-2 is 2.3 times higher than in the composite MSMC-GO-MGH-MG-1 and the content of muscovite is 2.2 times lower.

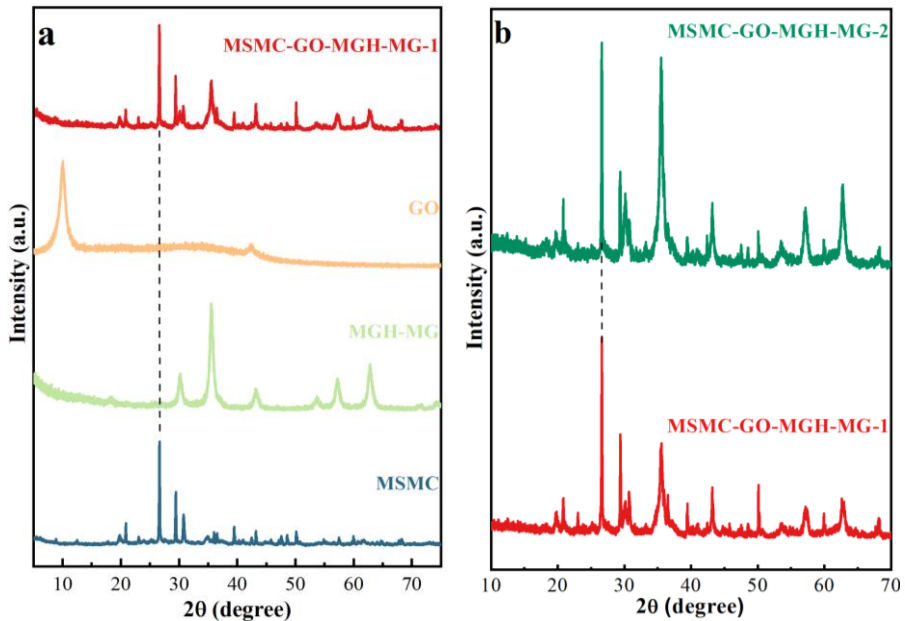


**Fig. 9.** XRD pattern of MSMC, MGH-MG, GO, MSMC-GO-MGH-MG-1 (a), MSMC-GO-MGH-MG-1, and -2 (b).

The XRD patterns of magnetite-Prussian blue-graphene oxide 3.2 and graphene oxide are shown in Fig. 10. The detected diffraction peaks in MPBGO 3.2 at  $2\theta=17.4, 24.7, 35.6, 39.6, 53.7,$  and  $57.2^\circ$  correspond to the face-centred cubic lattice of Prussian blue (ICDD # 01-074-9174), whose particle size was 10 nm. The values at  $2\theta=30.2, 35.6, 43.3, 53.7, 57.2,$  and  $63.0^\circ$  belong to magnetite (ICDD # 01-084-9337) (Thammawong et al. 2013; Shiba et al. 2019) and the particle size was 8 nm. The characteristic peak of graphene oxide at  $2\theta=9.8^\circ$  in the XRD pattern of GO 2 is not observed in MPBGO 3.2. Perhaps this is due to the overlapping of the GO sheets with particles of magnetite and Prussian blue. It should also be noted that the location of the characteristic peak of GO 2 and GO, which are used for MSMC-GO-MGH-MG composites, in the range of low  $2\theta$  values indicates a high degree of their oxidation (Krishnamoorthy et al. 2013).

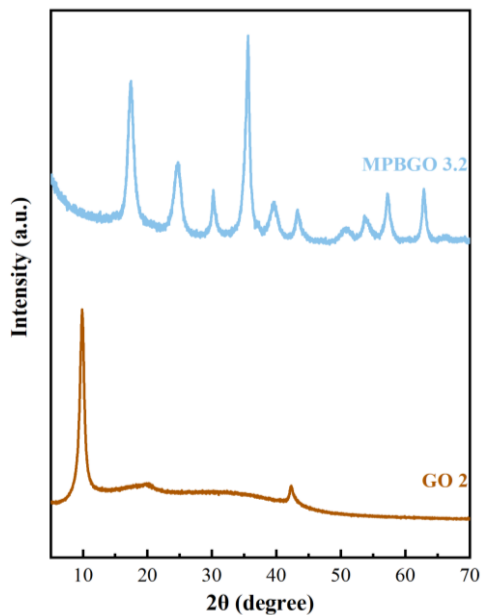


**Fig. 10.** XRD pattern of MPBGO 3.2 and GO 2.

The XRD patterns of MSMC, Mt, Zeo, CS-MSMC, CS-MSMC-STP, CS-MSMC-GLUT, CS-MSMC-ECH, CS-Mt-GLY, and C-Zeo are shown in Figs. 11a, b, c, and d. Diffraction peaks corresponding to the following minerals were found in the XRD pattern of acid-activated MSMC with a fraction of 1–0.2  $\mu\text{m}$ : Quartz (34.0%; (ICDD # 00-046-1045)), muscovite (18.3%; (ICDD # 01-089-7536)), calcite (13.3%; (ICDD # 01-083-4602)), dolomite (10.3%; (ICDD # 04-012-1195)), montmorillonite (7.9%; (ICDD # 00-013-0135)), and kaolinite (7.4%; (ICDD # 01-074-1784)). Unlike untreated MSMC, no diffraction peaks consistent with clinocllore were found in acid-activated MSMC, possibly due to its removal from the composition by the acid treatment. Diffraction peaks of MSMC are observed in CS-MSMC composites. Moreover, new diffraction peaks appear in the CS-MSMC composite at  $2\theta=7.42$ ,  $10.18$ ,  $11.82$ , and  $15.86^\circ$ , and the peak at  $2\theta=23.96^\circ$  disappears. In the XRD patterns of CS-MSMC-GLUT, CS-MSMC-ECH, and CS-MSMC-STP, the intensity of the  $\sim 20^\circ$  diffraction peaks increased significantly in the region of the characteristic chitosan peak at  $2\theta=20^\circ$  (Luo et al. 2015). For the composites CS-MSMC-ECH and CS-MSMC-STP, the peak disappears at  $2\theta=8.90^\circ$ . In the XRD pattern of the latter, many diffraction peaks disappear and/or their intensity is significantly reduced. In all CS-MSMC composites, the intensity of the peaks at  $2\theta=29.42$  and  $30.74^\circ$  has decreased significantly. In CS-Mt-GLY, the characteristic peaks of

montmorillonite are overlaid by chitosan, whose broad peak is at  $2\theta=20^\circ$ . The XRD pattern of CS-Zeo shows a characteristic chitosan peak and some peaks of Zeo. The observed changes in the XRD pattern of the composites thus seem to indicate the location of the chitosan between the mineral layers and/or on their surface (Luo et al. 2015; Biswas et al. 2021; Abukhadra et al. 2021).

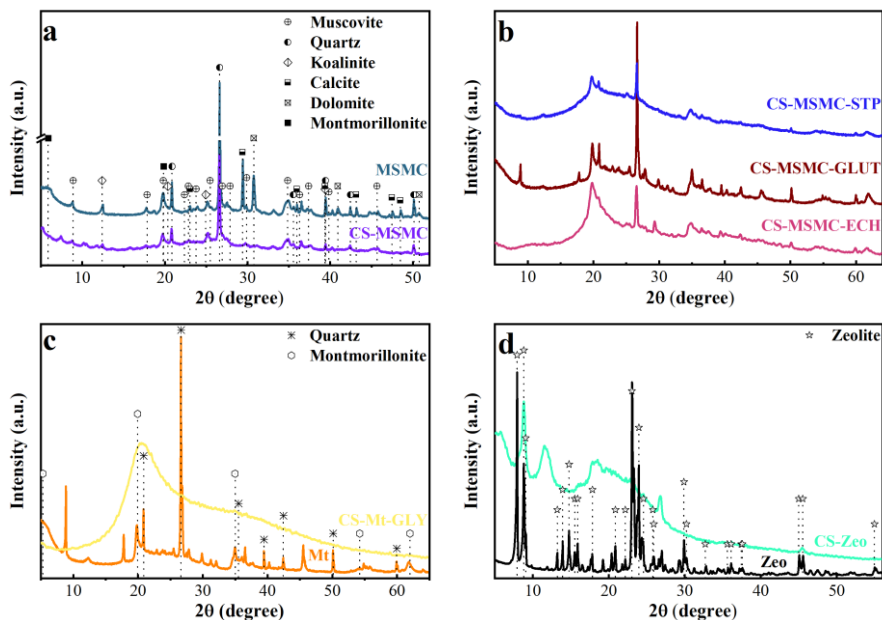


**Fig. 11.** XRD pattern of MSMC, CS-MSMC, CS-MSMC-STP, CS-MSMC-GLUT, and CS-MSMC-ECH composites (a, b), Mt and CS-Mt-GLY (c), Zeo and CS-Zeo (d).

### 3.1.2. ATR-FTIR and FTIR

The ATR-FTIR and FTIR results provide information on the functional groups of natural muscovite mica clay, montmorillonite and zeolite minerals, chitosan, graphene oxide, maghemite-magnetite, magnetite, Prussian blue, and composites based on them. In the ATR-FTIR spectra (Figs. 12a and 13) of the untreated and acid-activated fine fraction of MSMC, a noticeable band at  $989\text{ cm}^{-1}$  is associated with Si–O, and the bands at  $415\text{--}454$ ,  $512$ , and  $795\text{ cm}^{-1}$  are attributed to Si–O–Si, Si–O–Al, and O–Si–O, respectively (Damayanti 2010). The band at  $915\text{ cm}^{-1}$  corresponds to Al–O(H)–Al bending (Mookherjee and Redfern 2002). The peaks at  $710$ ,  $872$ , and  $1423\text{ cm}^{-1}$  indicate the presence of calcite and dolomite phases in the composition (Launer and Arkles 2013). In the spectrum of MGH-MG (Fig. 12a), the band at  $540\text{ cm}^{-1}$  is associated with the stretching vibration of Fe–O (Belachew and Bekele 2019). The signals at  $983$ ,  $1047$ ,  $1731$ , and  $1622\text{ cm}^{-1}$  in the graphene

oxide spectrum (Fig. 12a) can be assigned to the C–O, C–OH, C=O, and C=C stretching vibrations, respectively (Xu et al. 2019). In the MSMC-GO-MGH-MG spectrum of the composite (here and in the subsequent characterisation results this is MSMC-GO-MGH-MG-1) bands of MSMC were identified, but not MGH-MG and GO, apparently due to the overlap of their bands by MSMC bands. However, the observed upshift by 2–4  $\text{cm}^{-1}$  of the characteristic MSMC bands in the composite from the initial 415, 512, 795, 872, 915, and 989  $\text{cm}^{-1}$  indicates that MGH-MG and GO have affected the MSMC structure. Furthermore, a broad band in the 3000–3500  $\text{cm}^{-1}$  region can be assigned to the O–H stretching vibrations in all spectra in Fig. 12a. After adsorption of caesium ions (Fig. 12b), band shifts from 417, 514, and 915  $\text{cm}^{-1}$  to 419, 512, and 913  $\text{cm}^{-1}$  were found in the spectrum of the composite, assigned to Si–O–Si, Al–O–Si/Fe–O or Fe–O–Si/Fe–O–Al, and Al–OH–Al, respectively. In the case of cobalt ion adsorption (Fig. 12c), the observed shifts are associated with Si–O–Si (from 417 to 415  $\text{cm}^{-1}$ ) and Si–O or C–O/C–OH (from 1002 to 998  $\text{cm}^{-1}$ ). In addition, in the wavenumber region at 1423  $\text{cm}^{-1}$  attributed to calcite, broad bands appear at 1349 and 1418  $\text{cm}^{-1}$  that can be attributed to  $\text{Ca}(\text{NO}_3)_2$ , the formation of which is due to the high affinity of calcite for  $\text{NO}_3$  groups (Hofmann et al. 2016) in the cobalt stock solution. The observed changes in the spectra of the composite after adsorption of the ions could thus indicate their interaction with the aforementioned groups (Lingamdinne et al. 2017).

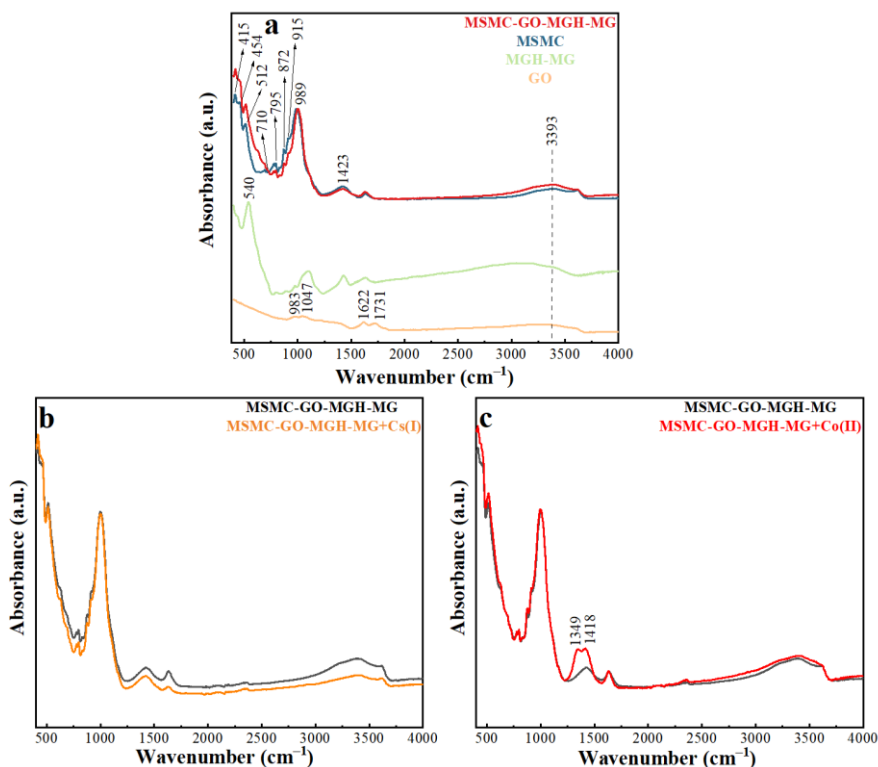


**Fig. 12.** The ATR-FTIR spectra of MSMC, GO, MGH-MG, MSMC-GO-MGH-MG (a), and MSMC-GO-MGH-MG composite after adsorption of Cs(I) (b) and Co(II) (c).

In the chitosan spectrum of ATR-FTIR (Fig. 13), the bands at 1023 and 1058 cm<sup>-1</sup> are associated with C–O stretching, and the bands at 1151 and 1261 cm<sup>-1</sup> correspond to asymmetric C–O–C stretching and the hydroxyl groups present in the chitosan, respectively. A band at 892 cm<sup>-1</sup> attributed to the CH bending out of the plane of the monosaccharide ring. The presence of bands at 1320 and 1651 cm<sup>-1</sup> confirms the C–N stretching of amide III and the C=O stretching of amide I of the residual N-acetyl groups, respectively, but no band was found corresponding to the N–H bending of the amide II, usually located at ~1550 cm<sup>-1</sup>. It is possible that this band overlaps with other bands of chitosan. The signals at 1374 and 1418 cm<sup>-1</sup> confirm the symmetric CH<sub>3</sub> deformations and CH<sub>2</sub> bending, respectively. The band at 1589 cm<sup>-1</sup> can be attributed to the N–H bending of the primary amine, and the bands at 2868 and 2920 cm<sup>-1</sup> to the asymmetric and symmetric C–H stretching, respectively. The bands at 3292 and 3350 cm<sup>-1</sup> are attributed to the N–H and O–H stretching vibrations, respectively (Queiroz et al. 2015). In the spectrum of the mineral montmorillonite (Fig. 13), the bands at 451, 523, 694, and 1025 cm<sup>-1</sup> indicate



the presence of the following silicates: Si–O–Si, Si–O–Al, Si–O–Mg, and Si–O, respectively. In addition, the bands at 798 and 930  $\text{cm}^{-1}$  are attributed to the  $\text{Fe}^{3+}$ –OH–Mg and Al–O(H)–Al bending, and the bands at 1632 and 3622  $\text{cm}^{-1}$  are associated with O–H bending and O–H stretching vibrations, respectively (Alabarse et al. 2011; Caccamo et al. 2020). In the spectrum of the zeolite mineral (Fig. 13), the bands at 432 and 546  $\text{cm}^{-1}$  can be associated with the Si–O bending vibration and the double five rings of the tetrahedral structure of the  $\text{SiO}_4$  and  $\text{AlO}_4$  units, respectively. The presence of a signal at 798  $\text{cm}^{-1}$  indicates the symmetric stretching of the internal tetrahedral, while the signal at 1075  $\text{cm}^{-1}$  is attributed to the internal bonds between the  $\text{SiO}_4$  and  $\text{AlO}_4$  tetrahedra. Furthermore, the band at 1225  $\text{cm}^{-1}$  indicates external vibrations between  $\text{SiO}_4$  and  $\text{AlO}_4$  tetrahedra. The absorption band at 1637  $\text{cm}^{-1}$  is attributed to the O–H bending of the zeolite (Narayanan et al. 2016; Aloulou et al. 2017; Amani et al. 2019).

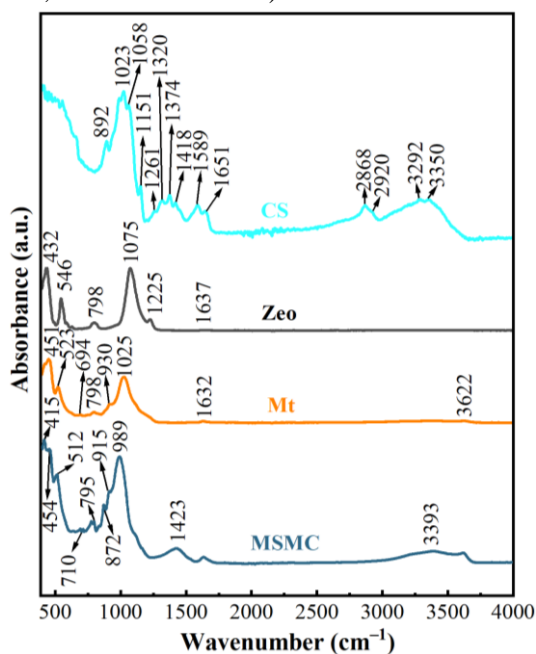


**Fig. 13.** The ATR-FTIR spectra of MSMC, Mt, Zeo, and CS.

ATR-FTIR spectra of chitosan-mineral composites before and after adsorption of caesium, cobalt, and europium ions are shown in Fig. 14. In the CS-MSMC spectra of the composites, bands of MSMC were found in the range of 419–797  $\text{cm}^{-1}$ . However, in the case of the CS-MSMC-ECH and CS-MSMC-STP composites, the intensity of the bands assigned to O–Si–O and calcite/dolomite decreased significantly in their spectra. The band at  $\sim 900 \text{ cm}^{-1}$  can be assigned to both the CH bending of chitosan and the

calcite/dolomite/Al–O(H)–Al bending of MSMC. The absorption band at  $\sim 1000\text{ cm}^{-1}$  can be attributed to both C–O stretching and Si–O. Moreover, characteristic bands of chitosan attributed to hydroxyl groups, C=O stretching of amide I, C–N stretching of amide III,  $\text{CH}_2$  bending, symmetric  $\text{CH}_3$  deformations, and N–H bending of primary amine are found in the spectra of these composites in the range of  $1256\text{--}1641\text{ cm}^{-1}$ . Compared to the original chitosan bands, these show significant changes in intensity and shifts. Also, the signal at  $1151\text{ cm}^{-1}$  (C–O–C stretching) present in the original spectrum of chitosan disappears in the case of CS-MSMC and CS-MSMC-GLUT and is slightly shifted to a smaller wavenumber in the case of CS-MSMC-ECH and CS-MSMC-STP. Moreover, the bands at  $\sim 2880$  (asymmetric C–H stretching) and  $\sim 2930\text{ cm}^{-1}$  (symmetric C–H stretching) in the spectra of CS-MSMC, CS-MSMC-GLUT, and CS-MSMC-ECH in the first case and CS-MSMC-GLUT, CS-MSMC-ECH, and CS-MSMC-STP in the second case shift significantly to a higher wavenumber. In the spectrum of CS-MSMC-STP, the band at  $\sim 2880\text{ cm}^{-1}$  does not shift, but its intensity decreases. In the spectrum of CS-MSMC, the band at  $\sim 2930\text{ cm}^{-1}$  disappears and a band with low intensity appears instead. The signal at  $\sim 3280\text{ cm}^{-1}$  in the CS-MSMC spectrum of the composites can be attributed to the O–H stretching vibrations, while the signal related to the N–H stretching of chitosan disappears in the spectra of the composites.

In the spectrum of CS-Mt-GLY, bands with shifts and altered intensity compared to the original bands of the mineral montmorillonite were identified at  $479$  (Si–O–Si),  $548$  (Si–O–Al),  $818$  (Si–O–Mg),  $851$  ( $\text{Fe}^{3+}$ –OH–Mg), and  $924$  (Al–O(H)–Al bending)  $\text{cm}^{-1}$ . The band at  $1029\text{ cm}^{-1}$  can be assigned to both the C–O stretching of CS and the Si–O of Mt. The chitosan band at  $1151\text{ cm}^{-1}$  (C–O–C stretching) is present in the spectrum of the composite without shifts, while the band assigned to CH bending shifts from  $892$  to  $994\text{ cm}^{-1}$ . In the wavenumber range of  $1200\text{--}3700\text{ cm}^{-1}$  changes in the intensity and shifts of the characteristic chitosan signals are observed. In addition, two small bands were found at  $1207$  and  $1236\text{ cm}^{-1}$  and the band assigned to N–H stretching disappeared in the spectrum of the composite.

In the CS-Zeo spectrum of the composite, the bands at  $438$  and  $535\text{ cm}^{-1}$  can be attributed to the Si–O bending vibrations and the double five rings of the tetrahedral structure of the  $\text{SiO}_4$  and  $\text{AlO}_4$  units of the zeolite, respectively. The bands at  $798$  and  $1225\text{ cm}^{-1}$ , which are related to the symmetrical stretching of the internal tetrahedra and the external vibrations between the tetrahedra, respectively, were not found in the spectrum of the composite. Instead, in the region of the band at  $798\text{ cm}^{-1}$ , two new bands are observed at  $777$  and  $796\text{ cm}^{-1}$ , and in the region of the band at  $1225\text{ cm}^{-1}$ , the observed

bands are at 1203 and 1228  $\text{cm}^{-1}$ . These changes seem to indicate the integration of chitosan into the framework of the zeolite. The band at 1033  $\text{cm}^{-1}$  can be attributed to both C–O stretching and internal bonding between the  $\text{SiO}_4$  and  $\text{AlO}_4$  tetrahedra. Small shoulder peaks at 864, 903, 934, and 971  $\text{cm}^{-1}$  are observed in this band. In the wavenumber range of 1300–3700  $\text{cm}^{-1}$ , changes in intensity and shifts in the characteristic bands of chitosan are observed. In addition, the band attributed to the hydroxyl groups of chitosan has disappeared and two new bands are observed at 1500 and 1709  $\text{cm}^{-1}$ .

Thus, the bands of chitosan and minerals observed in the spectra of chitosan-mineral composites and the associated changes compared to the original bands indicate an interaction between these materials, possibly due to the formation of hydrogen bonds between the –OH groups of minerals and the –OH or –NH<sub>2</sub> groups of chitosan, or electrostatic attraction, since minerals have a negative charge while chitosan is positive (DeLuca and DeLuca 1997; Tan et al. 2008; Sides et al. 2009; Paluszkiwicz et al. 2011; Brigatti et al. 2013; Pereira et al. 2017; Laaraibi et al. 2018; Siddiqui et al. 2019). In addition, changes in the characteristic bands of chitosan in the case of CS-MSMC-GLUT, CS-MSMC-ECH, CS-MSMC-STP, and CS-Mt-GLY may also indicate interaction with cross-linking agents or a plasticiser (Li et al. 2013, 2015; Loutfy et al. 2016; Chen et al. 2020; Smith et al. 2021).

After adsorption of caesium, cobalt, and europium ions, the spectra of the CS-MSMC composite show shifts for all bands except those assigned to Si–O–Al and O–Si–O, and the C–N stretching of the amide III only in the case of adsorption of cobalt. In the CS-MSMC-GLUT spectrum, no shifts were observed only for the bands assigned to Si–O–Si and Si–O–Al after the adsorption of caesium and after the adsorption of cobalt in the case of Si–O–Si and europium in the case of Si–O–Al. Furthermore, after adsorption of all three ions, there were no changes in the shifts associated with the C–H stretching of CS, the calcite/dolomite phase and Al–O(H)–Al of MSMC. After ion adsorption, the CS-MSMC-ECH spectra showed shifts and changes in the intensity of the bands associated with Si–O–Si, Si–O–Al (only after cobalt adsorption), C–H stretching, CH<sub>2</sub> bending, CH<sub>3</sub> symmetrical deformations (only after cobalt adsorption), C–O–C stretching, C–N stretching of amide III (only after caesium and cobalt adsorption), N–H bending, and C=O stretching of amide I. In addition, after adsorption of caesium and europium, there were also changes in the bands associated with the calcite/dolomite phase, Al–O(H)–Al, and the hydroxyl groups. In the spectra of the composite CS-MSMC-STP, shifts of many bands were also detected after the adsorption of ions, except for the bands assigned to the C–O–C stretching and CH<sub>3</sub> symmetrical deformations after the adsorption of caesium, and to the C–N

stretching of the amide III after the adsorption of cobalt. A new band at  $\sim 1248\text{ cm}^{-1}$  was also found in the spectra, close to the band at  $1318\text{ cm}^{-1}$  assigned to the hydroxyl groups of the chitosan. This probably indicates that caesium, cobalt, and europium ions form complexes with the hydroxyl groups of the chitosan (Cadogan et al. 2014).

Changes in the spectra of CS-Mt-GLY after ion adsorption were found for the bands assigned to Si–O–Si, Al–O(H)–Al, Si–O/C–O stretching (only after cobalt adsorption), hydroxyl groups (only after cobalt adsorption), C–N stretching of the amide III (only after adsorption of caesium and cobalt), CH<sub>3</sub> symmetrical deformations, CH<sub>2</sub> bending, N–H bending, and C=O stretching of the amide I (only after adsorption of cobalt and europium). Additionally, after adsorption of caesium, cobalt, and europium, a new band appears at  $\sim 1540\text{ cm}^{-1}$  in the spectra, adjacent to the band at  $\sim 1580\text{ cm}^{-1}$  (N–H bending of CS). The intensity of this band has decreased significantly compared to the original band. This could indicate the formation of a complex between the adsorbed ions and the amino group of chitosan (Wang et al. 2014, 2019; Cadogan et al. 2014).

In the spectra of CS-Zeo, shifts and changes in intensity are observed after ion adsorption for many bands, except for the band assigned to the CH<sub>3</sub> symmetric deformations and only after caesium adsorption. Moreover, the shifts in the bands related to the symmetric stretching of the internal tetrahedra and the external vibrations between the tetrahedra possibly indicate the position of the ions after adsorption within or at the surface of the zeolite framework.

Thus, numerous changes in the bands indicate the interaction of the ions with many functional groups of the composites, and in particular, the changes were associated in most cases with the groups –OH and –NH<sub>2</sub> of chitosan, Si–O–Si, Si–O, and Al–O(H)–Al of minerals.

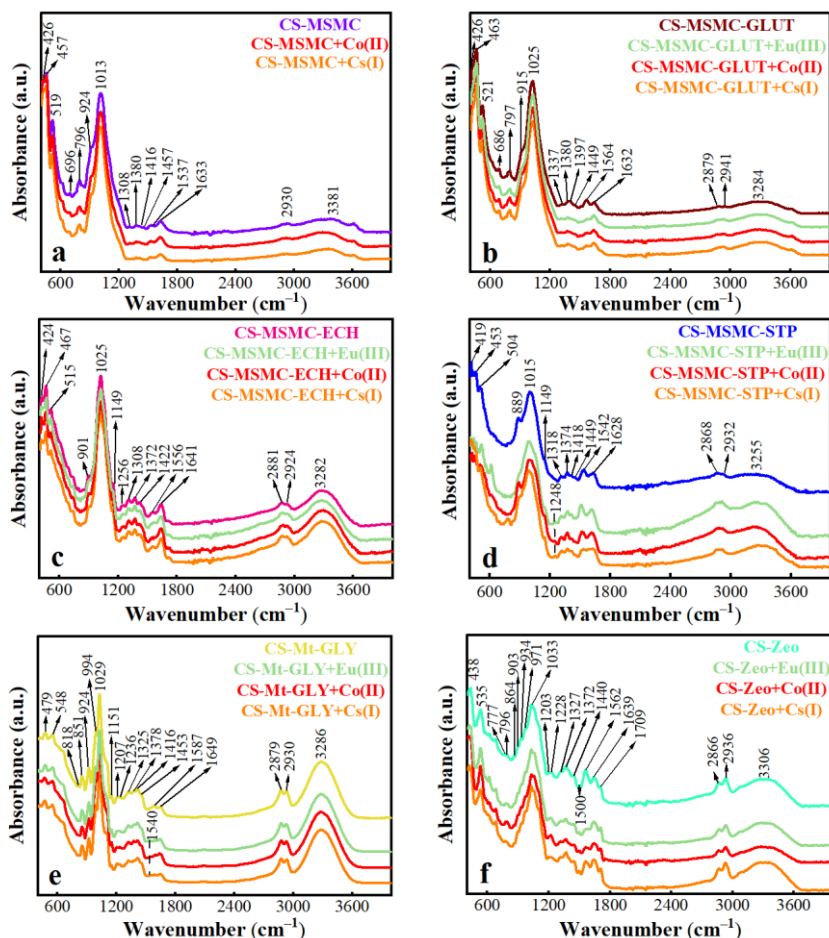


**Fig. 14.** The ATR-FTIR spectra of chitosan-mineral composites before and after adsorption of Cs(I), Co(II), and Eu(III).

The FTIR spectra of GO (1 and 2), magnetite, PB (1 and 2), PBGO (2.1 and 2.2), and MPBGO (2.3 and 3.2) are shown in Fig. 15. In the spectra of graphene oxide 1 and 2, the bands at 1740 and 1420  $\text{cm}^{-1}$  can be attributed to C=O stretching vibrations and the bands at 1229, 1622, and 1054  $\text{cm}^{-1}$  can be attributed to C–O–C, C=C, and C–O stretching vibrations, respectively (Ullah et al. 2020). The intensity of these bands is higher in GO 2 than GO 1, indicating a high degree of oxidation of the obtained GO 2. In the spectrum of magnetite, the band at 583  $\text{cm}^{-1}$  is associated with the Fe–O stretching vibration. In the spectra of PB 1 and PB 2, the bands at 2078 and 498  $\text{cm}^{-1}$  can be attributed to the CN and Fe<sup>2+</sup>–CN–Fe<sup>3+</sup> stretching vibrations, respectively (Jang et al. 2015; Khalil 2015). In addition, all spectra show a broad band in the range of 3560–3200  $\text{cm}^{-1}$  corresponding to the O–H stretching vibrations.

Characteristic bands of Prussian blue and magnetite-Prussian blue are observed in the spectra of PBGO and MPBGO composites, respectively. However, the low intensity or absence of characteristic graphene oxide bands in the spectra of MPBGO and PBGO composites could be related to the reduction of graphene oxide and/or its suppression by the magnetite-Prussian blue and Prussian blue particles, respectively (Azhar et al. 2019). Additionally, in the spectrum of MPBGO 2.3, the bands attributed to the CN and Fe–O stretching vibrations are shifted towards small wavenumbers, with a significant decrease in intensity. The band attributed to the  $\text{Fe}^{2+}\text{-CN-Fe}^{3+}$  stretching vibration was not found. This indicates a difference in the structure of MPBGO 2.3 compared to MPBGO 3.2.

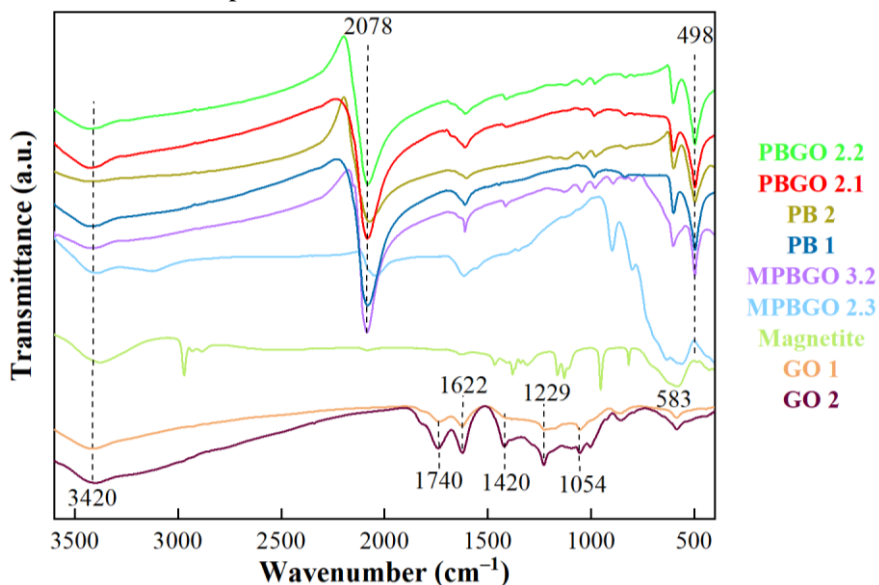


**Fig. 15.** The FTIR spectra of GO, magnetite, PB, PBGO, and MPBGO composites.

### 3.1.3. Raman spectroscopy

In the spectra of Prussian blue 2, PBGO (2.1), and MPBGO (2.3 and 3.2) (Fig. 16), the signals at 271, 533, 2092, 2153, and 2126  $\text{cm}^{-1}$  are  $\text{Fe}^{2+}\text{-CN-Fe}^{3+}$  and CN, respectively (Jang et al. 2015; Moretti and Gervais 2018). The intensity of these signals is much lower in the spectra of MPBGO 2.3 and PBGO 2.1 compared to MPBGO 3.2 and Prussian blue 2. In the spectrum of graphene oxide 2, two signals at 1344 and 1599  $\text{cm}^{-1}$  belong to the D and G bands. The D band is formed by structural defects caused by the addition of oxygen-containing functional groups to the basal plane of disordered carbon, and the G band characterises the stretching vibrations of carbon atoms during

sp<sup>2</sup>-hybridisation (Sabzevari et al. 2018). D and G bands were found in the spectra of the composites containing GO, and the intensity ratio of the D and G bands ( $I_D/I_G$ ) increased compared to graphene oxide 2 (0.76) in the following order: 0.83, 0.86, and 1.36 for MPBGO 3.2, PBGO 2.1, and MPBGO 2.3, respectively. An increase in  $I_D/I_G$  implies an increase in the defect density of GO and a reduction of graphene oxide to reduced graphene oxide (Jang et al. 2015). Consequently, the amount of oxygen-containing functional groups decreases (López-Díaz et al. 2017), indicating the high degree of decoration of the graphene oxide 2 surface with magnetite-Prussian blue or Prussian blue particles.

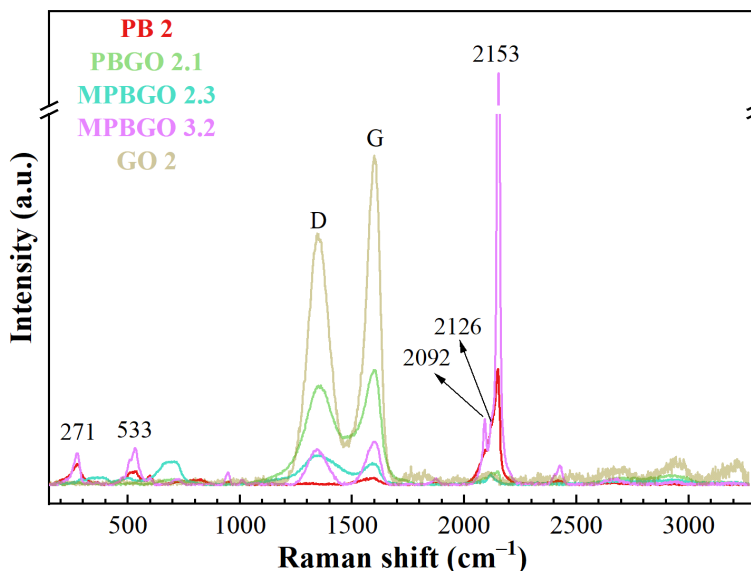


**Fig. 16.** The Raman spectrum of GO, PB, PBGO, and MPBGO composites.

### 3.1.4. XPS

The XPS analysis was used to investigate the bonding interaction and chemical composition of the MSMC-GO-MGH-MG composite before and after ion adsorption. The wide-scale XPS spectrum (Fig. 17a) contains peaks in different regions such as 75.24, 103.20, 284.62, 293.71, 347.62, 531.48, and 710.03 eV for Al2p, Si2p, C1s, K2p, Ca2p, O1s, and Fe2p, respectively. After adsorption, peaks at 725.87 and 780.44 eV were found in the spectrum of the composite, which can be assigned to Cs3d and Co2p, respectively. After deconvolution of the Cs3d spectrum (Fig. 17b), two peaks were identified at 726.5 and 723.7 eV, corresponding to Cs3d<sub>5</sub> and Fe2p<sub>1/2</sub>, respectively (Wu et al. 2012; Zheng et al. 2017; Chen et al. 2021). The Co2p spectrum is deconvoluted into two distinct peaks (Co2p<sub>3/2</sub> and Co2p<sub>1/2</sub>) and two weak

satellites (Fig. 17c). The Co2p<sub>3/2</sub> spin-orbit duplet can be deconvoluted into two peaks at 780.2 and 783.5 eV, corresponding to the Co<sup>3+</sup> and Co<sup>2+</sup> configurations, respectively (Smyrnioti and Ioannides 2017; Yin et al. 2018).

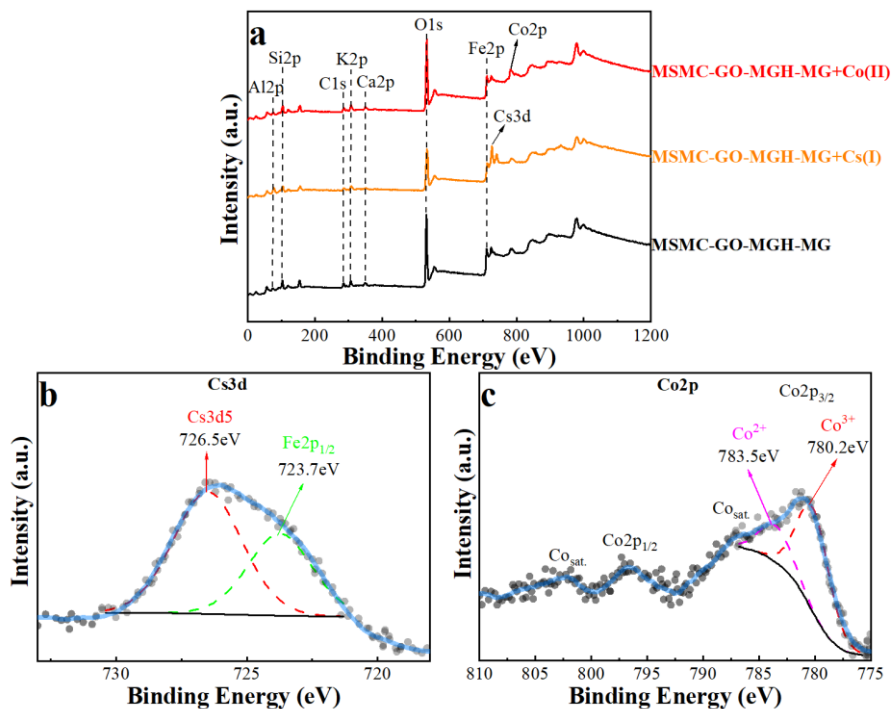


**Fig. 17.** The wide-scale XPS spectrum (a), the deconvoluted XPS spectrum of Cs3d (b) and Co2p (c).

The deconvoluted O1s spectrum (Fig. 18a) of the composite contains peaks representing differently functionalised oxygen: C–OH/C–O–C (532.2 eV), C=O (531.1 eV), and metal oxides (Fe<sub>2</sub>O<sub>3</sub>, Si–O, Al–O (529.5 eV)). The spectrum of the C1s of composite (Fig. 18b) is deconvoluted into four main peaks with binding energies of 288.3, 286.1, 284.7, and 283.5 eV, corresponding to the carbon in the carboxylic acid group, the carbonyl carbon, the C–O in hydroxyl and epoxide, and the sp<sup>2</sup> carbon, respectively (Narayanan et al. 2020; Cai and Larese-Casanova 2020; Bian et al. 2022). The spectrum of the Al2p of the composite (Fig. 19a) shows two peaks at 75.8 and 74.4 eV. The binding energy of the first peak is related to Al<sup>3+</sup> in Al–OH, and the second peak is related to octahedrally coordinated aluminium in the MSMC layers. The Si2p spectrum (Fig. 19b) of the composite contains two peaks at 103.3 and 101.3 eV, attributed to SiO<sub>2</sub> and Si–O–Si – silicon from tetrahedral layers (Narayanan et al. 2020). Figs. 20a and b show the high-resolution spectra of Ca2p and K2p, in which the peaks at binding energies of



350.4 and 347.3 eV are assigned to Ca2p<sub>1/2</sub> and Ca2p<sub>3/2</sub>, respectively, and 296.3 and 293.6 eV to K2p<sub>1/2</sub> and K2p<sub>3/2</sub>, respectively. (Ma et al. 2020; Guo et al. 2022). In the Fe2p spectrum of the composite (Fig. 21a), two distinct peaks of Fe2p<sub>1/2</sub> and Fe2p<sub>3/2</sub> can be distinguished. After deconvolution of Fe2p<sub>3/2</sub>, two peaks with binding energies of 712.0 and 709.8 eV were found, corresponding to Fe<sup>3+</sup> and Fe<sup>2+</sup>, respectively (Wu et al. 2012; Liu et al. 2018a).

After adsorption of Cs(I), the composite spectrum was found to change in the binding energy of the characteristic peaks of Fe2p, Ca2p, K2p, O1s, C1s, Si2p, and Al2p. The binding energy increases by 0.31 and 0.07 eV for Fe2p and O1s, respectively, and in the case of Ca2p, K2p, C1s, Si2p, and Al2p, the binding energy decreases by 0.43, 0.3, 1.18, 0.69, and 0.31 eV, respectively (Table 3). An increase in the binding energy of Fe2p could indicate the interaction of Cs(I) with Fe atoms (Zheng et al. 2017). A decrease in binding energy for K2p could indicate incomplete cation exchange of K<sup>+</sup> for Cs<sup>+</sup> occurring in the FES regions of the muscovite (Fuller et al. 2014). The cation exchange was incomplete because the characteristic K2p peak did not completely disappear and not all potassium ions were replaced by caesium, as found for example by Huo et al. (2021) in the adsorption of caesium ions by Prussian blue analogues anchored on 3D reduced graphene oxide aerogel. Changes in the binding energy in the deconvoluted spectra of Al2p and Si2p (Figs. 19c and d) were detected only for Al–OH and Si–O–Si, respectively, which could indicate an interaction of the ions with Al–OH and Si–O–Si. What also indicate the results of ATR-FTIR. The area of the characteristic peak of Ca2p in the spectrum of the composite (Fig. 20c) decreased ninefold compared to the initial peak before adsorption, and the binding energy also decreased, indicating that it is not an interaction of caesium ions with Ca atoms, but the leaching of calcium from the calcite and dolomite phases of the MSMC during adsorption (Bouchelaghem 2010). Similar changes were found in the spectra of ATR-FTIR, where the intensity of the band at 1423 cm<sup>-1</sup> referred to calcite and dolomite decreases. However, after adsorption of cobalt ions, a characteristic Ca2p peak can be observed with minimal changes in binding energy and peak area. The presence of this peak is apparently due to the formation of Ca(NO<sub>3</sub>)<sub>2</sub> due to the high affinity of calcite for the NO<sub>3</sub> group present in the cobalt stock solution (Demri and Muster 1995; Hofmann et al. 2016). This is confirmed by the results of ATR-FTIR, where new bands at 1349 and 1418 cm<sup>-1</sup> were seen in the spectrum of the composite after cobalt adsorption instead of the calcite bands, which attribute to Ca(NO<sub>3</sub>)<sub>2</sub>. The area of the characteristic peaks of O1s and C1s in the composite spectrum after caesium adsorption decreased 8- and 33-fold, respectively, compared to the initial peaks, while the binding energy increased slightly in the former case

and decreased significantly in the latter. Moreover, some peaks assigned to O=C–O, C=O, and C–O groups were not detected in the deconvoluted spectrum of the C1s of the composite after Cs(I) adsorption (Fig. 18d). These changes could indicate that all functional groups of graphene oxide are involved in the adsorption of caesium ions, while the adsorption centres are almost completely filled. The change in the O1s peak could also indicate the interaction of metal oxides with caesium ions (Zheng et al. 2017, Huo et al. 2021).

After adsorption of Co(II), the binding energy of the characteristic peaks of the composite spectrum of Ca2p, K2p, O1s, C1s, Si2p, and Al2p was found to decrease by 0.11, 0.34, 0.39, 0.26, 0.42, and 0.21 eV, respectively, and to increase by 0.01 eV in the case of Fe2p (Table 3). In the deconvoluted spectrum of Fe2p, changes in binding energy were detected only for the peak related to Fe<sup>3+</sup> (Fig. 21c), possibly indicating the interaction of Co<sup>2+</sup> with Fe<sup>3+</sup>. The change in the binding energy of the characteristic peaks of Ca2p and K2p (Figs. 20e and f) indicates the formation of Ca(NO<sub>3</sub>)<sub>2</sub> in the first case and possibly ion exchange with potassium on PS in the second case. In the deconvoluted spectrum of Al2p (Fig. 19e), a new peak was found that can be associated with the Co–Al bond, possibly as a result of complexation between cobalt and Al–OH (Penke et al. 2017; Woodward et al. 2018). The spectrum of Si2p also changes (Fig. 19f). After deconvolution, no peak associated with Si–O–Si was found, and the binding energy of the SiO<sub>2</sub> peak increased, which could be due to the complete filling of the Si–O–Si adsorption sites and interaction with SiO<sub>2</sub> (Woodward et al. 2018). The interaction of cobalt with functional groups of graphene oxide and metal oxides is indicated by changes in the binding energy of the peaks in the deconvoluted spectra of O1s and C1s (Figs. 18e and f). Moreover, cobalt oxide may have formed after adsorption, as evidenced by the presence of two satellites near two spin-orbit doublets in the Co2p spectrum (Fig. 17c) (Smyrnioti and Ioannides 2017) and an increase in the binding energy of the metal oxide peak in the O1s spectrum.

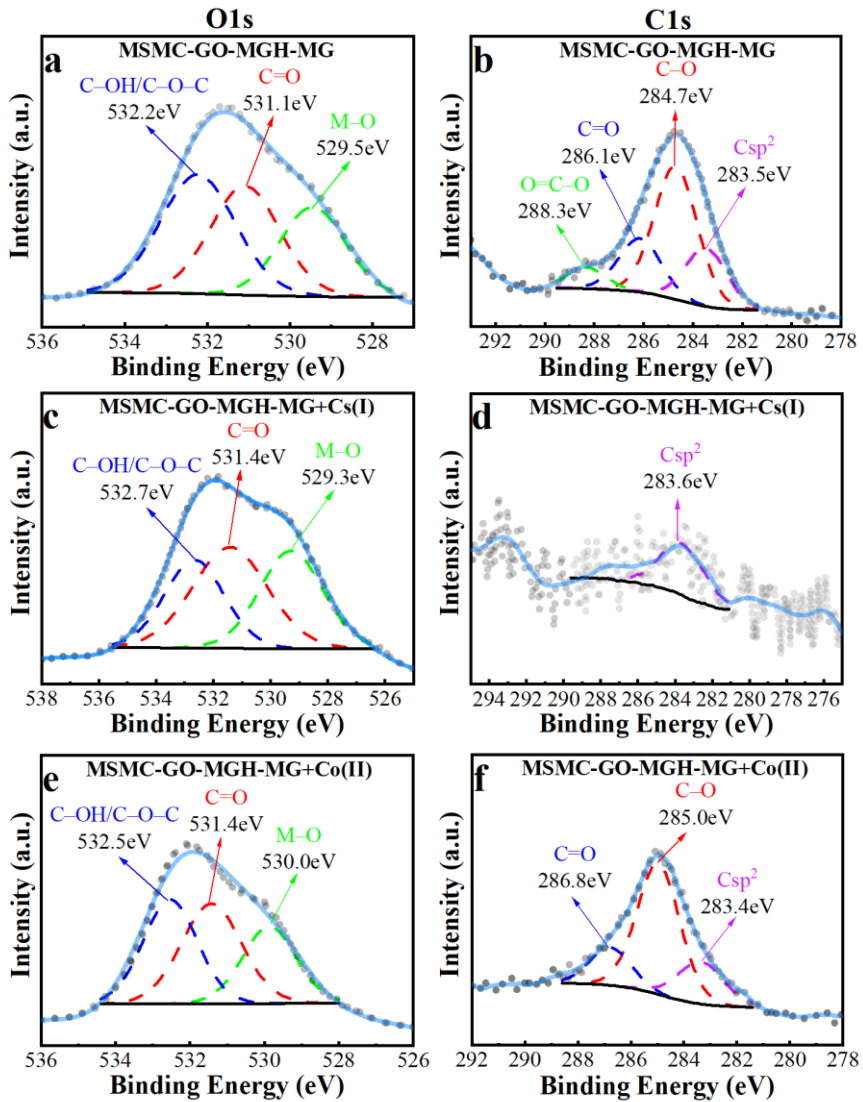


**Fig. 18.** The deconvoluted XPS spectra of O1s and C1s before (a, b) and after adsorption of Cs(I) (c, d) and Co(II) (e, f).

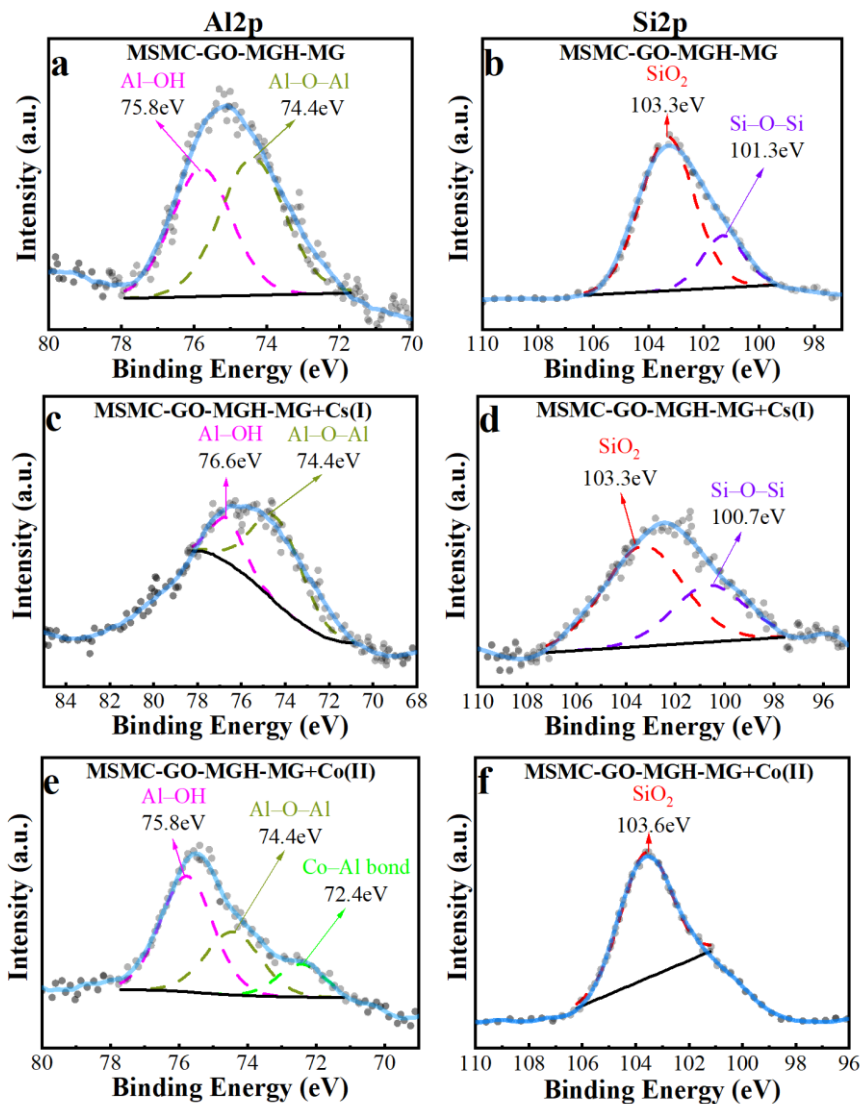


**Fig. 19.** The deconvoluted XPS spectra of Al<sub>2</sub>p and Si<sub>2</sub>p before (a, b) and after adsorption of Cs(I) (c, d) and Co(II) (e, f).

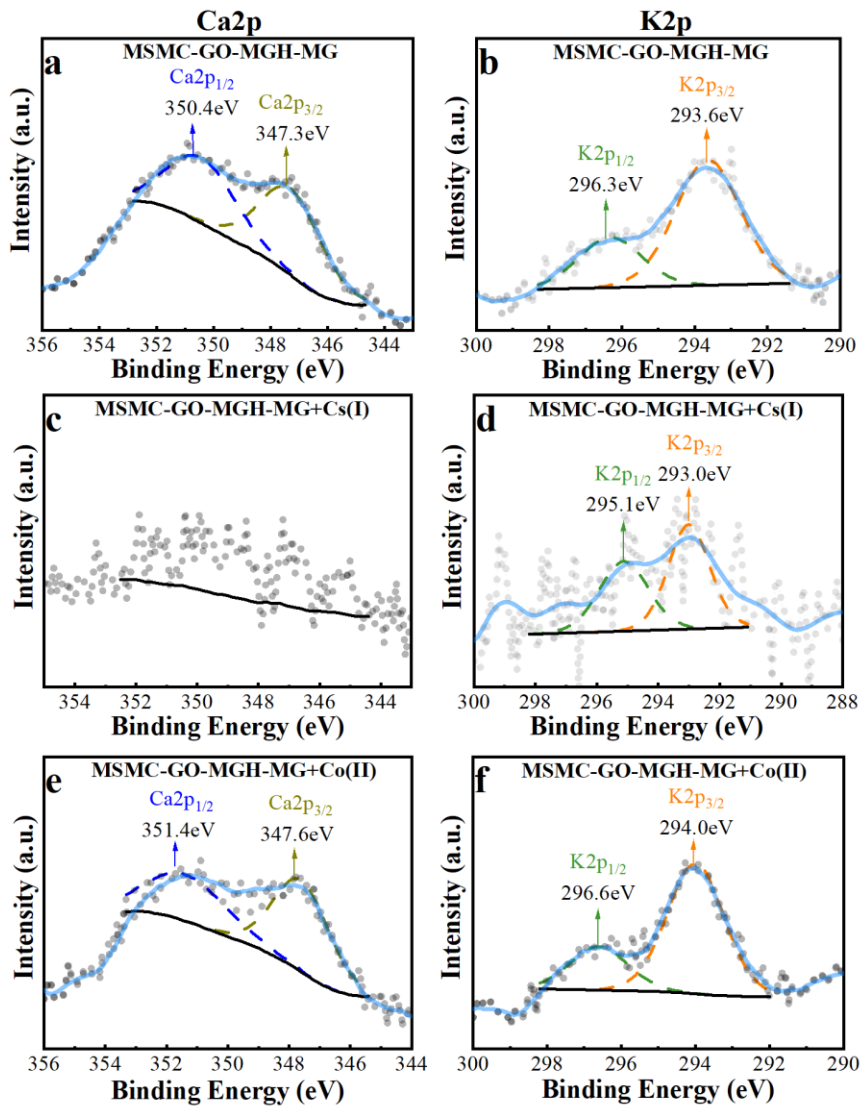


**Fig. 20.** The deconvoluted XPS spectra of Ca<sub>2p</sub> and K<sub>2p</sub> before (a, b) and after adsorption of Cs(I) (c, d) and Co(II) (e, f).

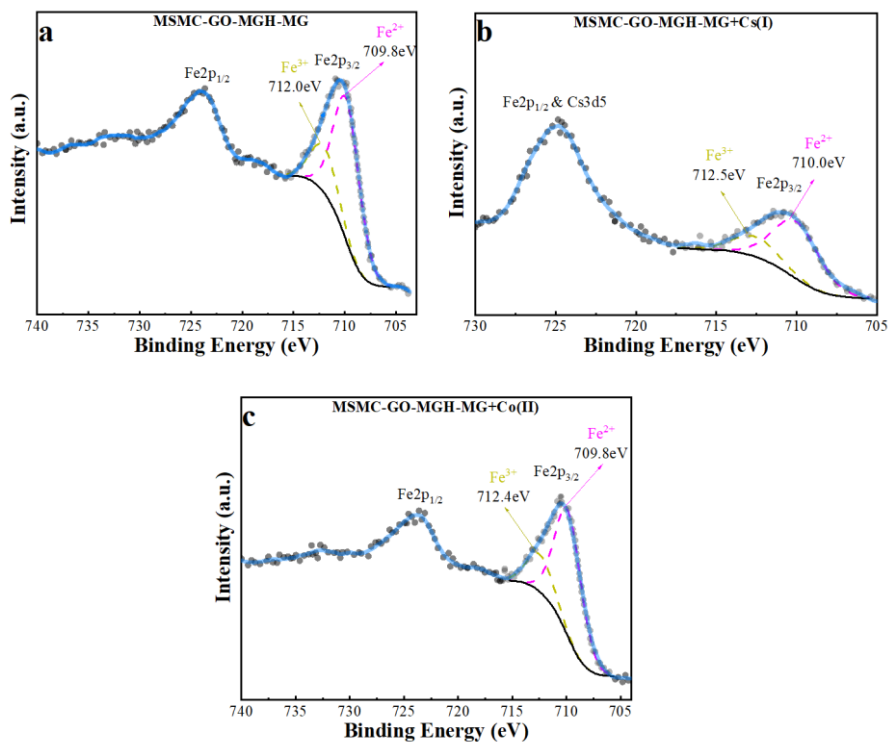


**Fig. 21.** The deconvoluted XPS spectrum of Fe2p before (a) and after adsorption of Cs(I) (b) and Co(II) (c).

**Table 3.** The binding energy of the characteristic peaks in the composite spectrum before and after ion adsorption.

Peaks	Samples		
	MSMC-GO-MGH-MG	MSMC-GO-MGH-MG+Cs(I)	MSMC-GO-MGH-MG+Co(II)
Fe2p	710.03	710.34	710.02
Ca2p	347.62	347.19	347.73
K2p	293.71	293.41	294.05
O1s	531.48	531.55	531.87
C1s	284.62	283.44	284.88
Si2p	103.20	102.51	103.62
Al2p	75.24	74.93	75.45
Cs3d	-	725.87	-
Co2p	-	-	780.44

Thus, caesium and cobalt ions were successfully adsorbed, as evidenced by the appearance of new characteristic peaks in the spectrum of the composite after adsorption, assigned to Cs3d and Co2p. Moreover, these ions interact with a variety of functional groups of the composite, which is confirmed by changes in the characteristic peaks in the spectrum of the composite after adsorption.

### 3.1.5. Mössbauer spectroscopy

The results of Mössbauer spectroscopy for MGH-MG, MSMC-GO-MGH-MG, PBGO, and MPBGO composites are shown in Fig. 22 and Table 4.

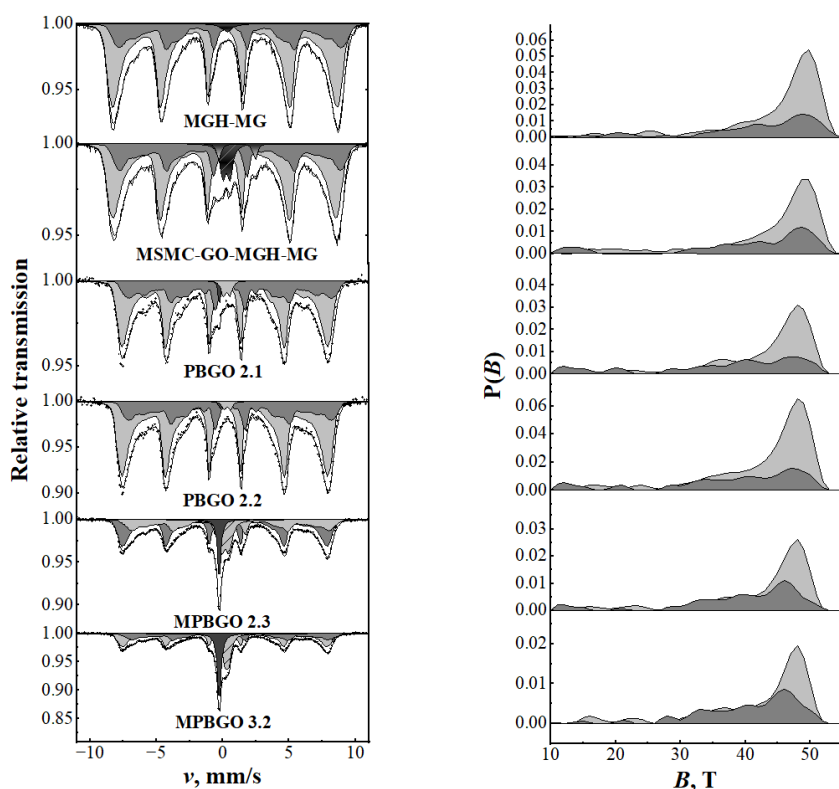


**Fig. 22.** Mössbauer spectra of MGH-MG, MSMC-GO-MGH-MG, PBGO, and MPBGO composites.

In the spectra of PBGO and MPBGO, two additional subspectra, singlet, and doublet, which are clearly distinguished were assigned to the Prussian blue sites with high spin HS  $\text{Fe}^{3+}$  and low spin LS  $\text{Fe}^{2+}$  based on the isomer shift values. In addition, the contribution of superparamagnetic magnetite to

the doublet is possible. Most of the spectrum is covered by two distributions P(B) hyperfine field distributions, which have different isomer shifts. The first distribution (A) with an isomer shift  $\delta=0.26\text{--}0.28$  mm/s for MGH-MG and MSMC-GO-MGH-MG and with an isomer shift  $\delta=0.26\text{--}0.27$  mm/s for MPBGO composites, can be related to the A sublattice of magnetite or maghemite in the first case and to the A sublattice of magnetite in the second case. The second distribution B with a value of  $\delta=0.65$  (MGH-MG and MSMC-GO-MGH-MG) and  $0.68\text{--}0.69$  (MPBGO) mm/s is attributed to the B sublattice of magnetite. The relative area of B corresponds to  $\text{Fe}^{2+}/(\text{Fe}^{2+}+\text{Fe}^{3+})=0.15$  in maghemite-magnetite (MGH-MG and MSMC-GO-MGH-MG) and  $\text{Fe}^{2+}/(\text{Fe}^{2+}+\text{Fe}^{3+})=0.15\text{--}0.20$  in magnetite (MPBGO). The average hyperfine fields are  $\sim 11\text{--}15\%$  in the case of MGH-MG and MSMC-GO-MGH-MG and  $\sim 11\text{--}20\%$  in the case of MPBGO, which is lower than that of bulk magnetite ( $B_0(\text{A})=49.3$  and  $B_0(\text{B})=46$  T). This is due to collective excitations and superparamagnetic relaxation of the magnetic moment of small magnetic nanoparticles with size  $\sim 14\text{--}15$  (MGH-MG and MSMC-GO-MGH-MG) and  $\sim 13$  nm (MPBGO). The size is determined by the relationship between the hyperfine field and the volume of the nanoparticles according to Eq. (19) (Thomas and Johnson 1986):

$$B = B_0 \left( 1 - \frac{kT}{2KV} \right) \quad (19)$$

where  $k$  is the Boltzmann constant,  $T$  is the temperature,  $K$  is the magnetic anisotropy of the magnetite, and  $V$  is the volume of the nanoparticle.

Furthermore, two additional doublets in the spectrum of MSMC-GO-MGH-MG are attributed to the  $\text{Fe}^{3+}$  and  $\text{Fe}^{2+}$  of the MSMC component, due to their different isomeric shift and values of quadrupole splitting.



**Table 4.** Parameters of the fit to Mössbauer spectra: Isomer shift  $\delta$ , quadrupole splitting (shift)  $\Delta(2\epsilon)$ , average hyperfine field  $\langle B \rangle$ , and relative area  $A$ .

Samples	$A$ , %	$\delta$ , mm/s	$\Delta(2\epsilon)$ , mm/s	$\langle B \rangle$ , T	Subspectrum
MGH-MG	70	0.28±0.01	-0.01±0.01	43.40	Mag. A (Fe <sup>3+</sup> )
	29	0.65	-0.02	40.90	Mag. B (Fe <sup>2+</sup> +Fe <sup>3+</sup> )
	1	0.42±0.09	-	-	Superparam.
MSMC-GO-MGH-MG	63	0.26±0.01	-0.02±0.01	42.40	Mag. A (Fe <sup>3+</sup> )
	30	0.65	-0.02	39.30	Mag. B (Fe <sup>2+</sup> +Fe <sup>3+</sup> )
	5	0.39±0.01	0.49±0.02	-	Fe <sup>3+</sup>
	2	1.12±0.02	2.49±0.04	-	Fe <sup>2+</sup>
PBG0 2.1	1	-0.14±0.01	-	-	PB LS Fe <sup>2+</sup>
	3	0.41±0.03	0.48±0.04	-	PB HS Fe <sup>3+</sup> + superpar. Fe <sup>3+</sup>
PBG0 2.2	1	-0.03±0.05	-	-	PB LS Fe <sup>2+</sup>
	1	0.46±0.04	0.48±0.06	-	PB HS Fe <sup>3+</sup> + superpar. Fe <sup>3+</sup>
MPBGO 2.3	48	0.27±0.01	-0.01±0.01	43.0	Mag. A (Fe <sup>3+</sup> )
	30	0.69±0.01	0	39.6	Mag. B (Fe <sup>2+</sup> +Fe <sup>3+</sup> )
	8	-0.15±0.01	-	-	PB LS Fe <sup>2+</sup>
	14	0.32±0.01	0.55±0.01	-	PB HS Fe <sup>3+</sup> + superpar. Fe <sup>3+</sup>
MPBGO 3.2	40	0.26±0.01	0.00±0.01	42.5	Mag. A (Fe <sup>3+</sup> )
	26	0.68±0.01	0	40.8	Mag. B (Fe <sup>2+</sup> +Fe <sup>3+</sup> )
	17	-0.15±0.01	-	-	PB LS Fe <sup>2+</sup>
	17	0.42±0.01	0.30±0.01	-	PB HS Fe <sup>3+</sup> + superpar. Fe <sup>3+</sup>

### 3.1.6. SEM and TEM

SEM and TEM images of composites and original components can be seen in Figs. 23 and 24. The muscovite mica clay and montmorillonite mineral have a layered structure with a rough surface, while the zeolite mineral consists of sphere-like fragments corresponding to the zeolite Socony Mobil-5 (Reza Safaei et al. 2012). Magnetic particles are spherical-granular agglomerates, while graphene oxide has a layered structure with curved edges.

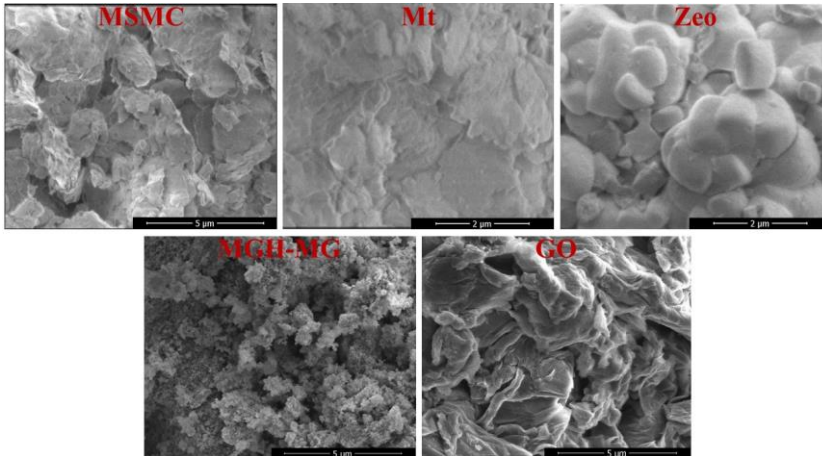


**Fig. 23.** The SEM images of MSMC, Mt, Zeo, MGH-MG, and GO.

The composite MSMC-GO-MGH-MG has a layered structure in which graphene oxide sheets and muscovite mica clay layers overlap each other, and maghemite-magnetite particles are distributed fairly evenly on the surface of the composite and between the layers. There are also irregularly shaped pores on the surface of this composite, some of which are created by the distribution of the magnetic particles. The MPBGO composites consist of sheets of graphene oxide with magnetite and Prussian blue particles distributed on their surface. In the case of MPBGO 2.3, the Prussian blue particles have a non-cubic shape with rounded edges, while the Prussian blue particles in MPBGO 3.2 have a well-defined cubic structure with a size of 5 to 20 nm. It can also be noted that the graphene oxide sheets in the MPBGO 3.2 composite are better decorated with magnetite-Prussian blue particles than in the case of MPBGO 2.3. In the composites CS-MSMC and CS-Mt-GLY, chitosan layers overlap with muscovite mica clay/montmorillonite layers. The CS-Zeo composite consists of zeolite fragments integrated into the surface of chitosan. The surface of chitosan-mineral composites is folded.

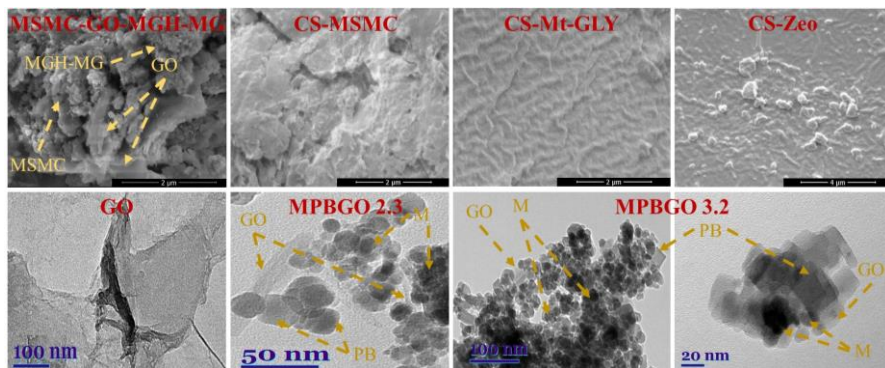


**Fig. 24.** The SEM images of MSMC-GO-MGH-MG, CS-MSMC, CS-Mt-GLY, and CS-Zeo composites, and the TEM images of GO and MPBGO composites.

### 3.2. Primary adsorption studies for MSMC-GO-MGH-MG composites and for original components

According to the primary results of the adsorption studies (Fig. 25), the adsorption of caesium ions on composite C-2 was lower by a factor of 1.7 and the adsorption of cobalt ions was higher by a factor of 1.2 than on composite C-1. Furthermore, according to XRD, the content of muscovite and maghemite-magnetite phases was the same in composite C-1, while it was 2.2 and 2.3 times lower and higher, respectively, in composite C-2 compared to composite C-1. These results indicate that muscovite plays a dominant role in the adsorption of caesium ions, while maghemite-magnetite plays a dominant role in the adsorption of cobalt ions, which is consistent with literature data (Fan et al. 2014; Tayyebi et al. 2015; Zheng et al. 2017). Moreover, the adsorption of caesium on the C-1 composite is on average 1.4 times lower than on MSMC and GO, but 52 times higher than on MGH-MG, while in terms of cobalt adsorption it was non-inferior to MSMC and GO, and 8.8 times higher than on MGH-MG. For the C-2 composite, the adsorption of caesium ions was significantly lower compared to MSMC and GO, and 8.8 times higher only compared to MGH-MG. For cobalt ions, the adsorption on C-2 was higher compared to all original components. Thus, the same content of muscovite and maghemite-magnetite phases in composite C-1 is optimal for equally efficient adsorption of the studied ions, and the difference in adsorption capacity compared to the originals MSMC and GO was insignificant, and only in the case of MGH-MG, whose adsorption capacity is significantly inferior to composite C-1. Therefore, composite C-1 was selected for further adsorption

studies and will be referred to as MSMC-GO-MGH-MG in the following sections.

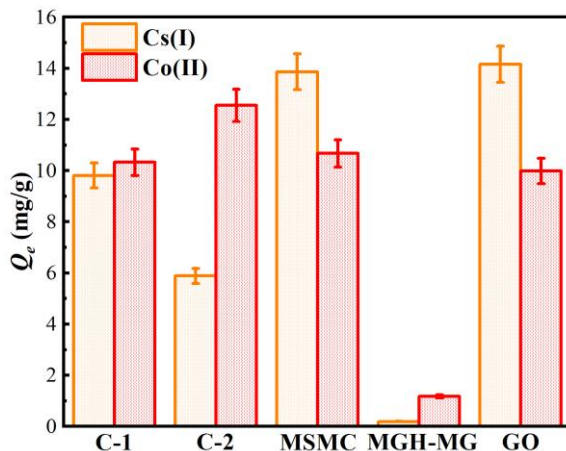


**Fig. 25.** Adsorption of caesium and cobalt ions on composites, MSMC, GO, and MGH-MG.

### 3.3. Adsorption studies

#### 3.3.1. Effect of initial concentration

With increasing initial ion concentration, the adsorption capacity of the composites increases (Fig. 26). For the composite MSMC-GO-MGH-MG saturation was not reached for Cs(I) and Co(II). For the PBGO 2.1, PBGO 2.2, and MPBGO 3.2 composites, saturation for Cs(I) was reached at 400 mg/L, and for MPBGO 2.3 at 200 mg/L. For the chitosan-mineral composites, saturation for Cs(I) and Co(II) was reached at 2000 mg/L, and only in the case of CS-Zeo, saturation for Co(II) was reached at 1000 mg/L, and for Eu(III), saturation was reached at 20 mg/L for all chitosan-mineral composites. The maximum experimental adsorption capacity for MSMC-GO-MGH-MG, PBGO 2.1, PBGO 2.2, MPBGO 2.3, MPBGO 3.2, CS-MSMC, CS-MSMC-GLUT, CS-MSMC-ECH, CS-MSMC-STP, CS-Mt-GLY, and CS-Zeo with respect to Cs(I) was 2286, 678, 644, 216, 774, 1123, 1035, 1152, 818, 1139, and 919 mg/g, respectively. With respect to Co(II) for MSMC-GO-MGH-MG, CS-MSMC, CS-MSMC-GLUT, CS-MSMC-ECH, CS-MSMC-STP, CS-Mt-GLY, and CS-Zeo was 652, 560, 487, 619, 458, 557, and 275 mg/g, respectively. With respect to Eu(III) for CS-MSMC, CS-MSMC-GLUT, CS-MSMC-ECH, CS-MSMC-STP, CS-Mt-GLY, and CS-Zeo was 8.10, 7.99, 7.42, 7.89, 6.27, and 9.89 mg/g, respectively.

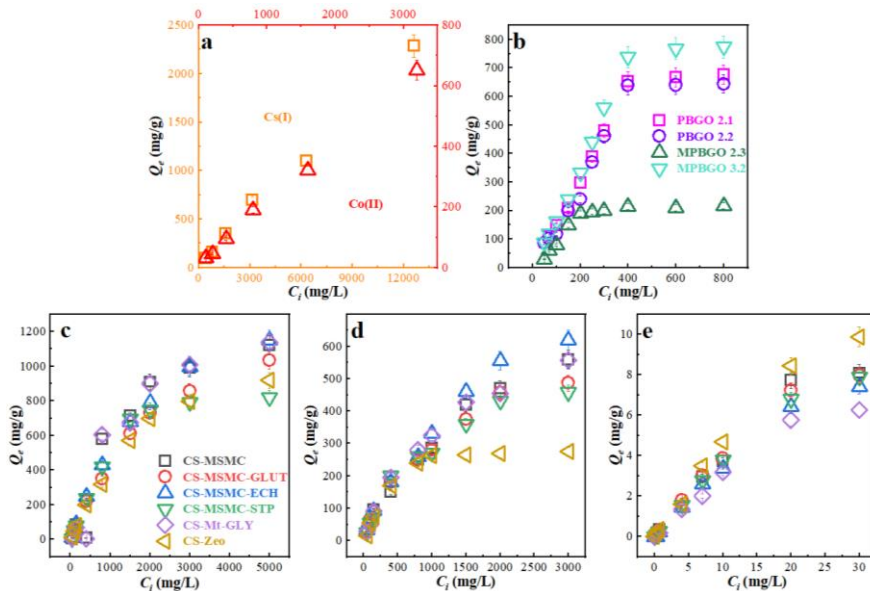


**Fig. 26.** The effect of initial concentration of Cs(I) and Co(II) for MSMC-GO-MGH-MG composite (a), Cs(I) for PBGO and MPBGO composites (b), Cs(I) (c), Co(II) (d), and Eu(III) (e) for chitosan-mineral composites.

The composite MSMC-GO-MGH-MG thus has a sufficiently high adsorption capacity, which is due to a large number of different functional groups due to the complexity of the matrix. The lack of saturation at high ion concentrations, in turn, could indicate that not all adsorption sites are occupied yet. The comparison of adsorption capacity values for PBGO and MPBGO composites showed that the MPBGO 3.2 composite had the highest adsorption capacity and the MPBGO 2.3 composite had the lowest, while the PBGO composites were only slightly inferior to the adsorption capacity of the MPBGO 3.2 composite. The higher Cs(I) adsorption on MPBGO 3.2 compared to MPBGO 2.3 is due to structural and chemical differences detected by FTIR, Raman spectroscopy, and TEM. These changes may be related to the use of different approaches in the synthesis. For MPBGO composites, the use of ferrous sulphate resulted in greater binding strength and affinity for graphene oxide due to the high electronegativity and smaller hydration radius of ferrous cations compared to ferric cations (Ching et al. 2020). The high oxidation degree of graphene oxide 2 compared to graphene oxide 1 provided a larger number of adsorption sites for ferrous cations and consequently a better coating of graphene oxide 2 sheets. Additionally, ferrous cations on the surface of graphene oxide 2 were oxidised to ferric cations, which in turn created better conditions for the formation of Prussian blue

particles (Jang et al. 2015). The high degree of decoration of graphene oxide 2 sheets (Figs. 16 and 24) with magnetite-Prussian blue or Prussian blue particles and the resulting larger number of potential adsorption sites for caesium determine the high adsorption capacity of MPBGO 3.2, PBGO 2.1, and PBGO 2.2 composites. Furthermore, free oxygen-containing functional groups not occupied by magnetite-Prussian blue or Prussian blue particles may have contributed to such high adsorption of caesium, as the low  $I_D/I_G$  values in the MPBGO 3.2 and PBGO 2.1 composites indicate a greater number of oxygen-containing functional groups compared to MPBGO 2.3. Among the chitosan-mineral composites, the composites CS-MSMC, CS-MSMC-ECH, and CS-Mt-GLY have the highest adsorption capacity for Cs(I) and Co(II). The composites CS-MSMC-STP and CS-Zeo have the lowest adsorption capacity for Cs(I) and Co(II), respectively. For the adsorption of Eu(III), the CS-Zeo composite had the highest adsorption capacity, while the CS-Mt-GLY composite had the lowest. From the results obtained, it can be assumed that the number of available  $-NH_2$  groups plays an important role in the adsorption of caesium and cobalt, and it follows that the  $-NH_2$  groups are more responsible for the adsorption of these ions. Since the use of GLUT and STP (cross-linking via  $-NH_2$  groups) led to a decrease in the adsorption of ions on the composites CS-MSMC-GLUT and CS-MSMC-STP compared to the composite without cross-linker – CS-MSMC. The use of ECH (cross-linking via  $-OH$  groups), on the other hand, slightly increased the adsorption capacity of the CS-MSMC-ECH composite. The importance of amino groups in adsorption is also noted by Hastuti et al. (2016) and Yu et al. (2021). It is noteworthy that the composite CS-Mt-GLY has a rather high adsorption capacity for Cs(I) and Co(II). Although glycerol may reduce the content of potential adsorption sites due to its interaction with chitosan via the  $-NH_2$  and  $-OH$  groups. However, Ekayem et al. (2021) found that when the composition is optimally loaded with glycerol, the adsorption capacity of the adsorbent can, on the contrary, be increased. Therefore, it can be assumed that such a high adsorption index is due to the synergistic effect of the presence of glycerol in the composition, montmorillonite, and free functional groups of chitosan. As for Eu(III), the type of minerals used could be the main factor affecting adsorption. Since a better result was obtained when zeolite was used than when muscovite mica clay or montmorillonite was used. On the other hand, for the adsorption of Cs(I) and Co(II), the use of muscovite mica clay or montmorillonite is better than that of zeolite in a synergistic effect.

### 3.3.2. Effect of pH

In a wide pH range from 1 to 12, Cs(I) is mainly in the form of  $\text{Cs}^+$  (Awual et al. 2016). At  $\text{pH} < 8$ , the predominant ionic form of Co(II) is  $\text{Co}^{2+}$ , while at  $\text{pH} > 8$  it is  $\text{Co}(\text{OH})^+$ ,  $\text{Co}(\text{OH})_2$ , and  $\text{Co}(\text{OH})_3^-$  (Mnasri-Ghnimi and Frini-Srasra 2019). Eu(III) is mainly present as  $\text{Eu}^{3+}$  at  $\text{pH} < 5$ , while the following species dominate at  $\text{pH} > 5$ :  $\text{Eu}(\text{OH})_2^+$  and  $\text{Eu}(\text{OH})_3^+$  (Plancque et al. 2003). Cs(I) adsorption on the composite MSMC-GO-MGH-MG (Fig. 27a) was quite stable over the pH range from 1 to 10. The adsorption of Co(II) on this composite (Fig. 27a) increased over the pH range from 1 to 5 and reached a maximum at pH of 5. At  $\text{pH} > 5$ , adsorption decreased slightly. The Cs(I) adsorption on the composites PBGO 2.1, PBGO 2.2, MPBGO 2.3, MPBGO 3.2, CS-MSMC, CS-MSMC-GLUT, CS-MSMC-ECH, CS-MSMC-STP, and CS-Mt-GLY (Figs. 27b and c) increases over the pH range from 3 to 7, reaching a maximum at  $\text{pH} = 7$ , and at  $\text{pH} > 7$  the adsorption decreases. In the case of the composite CS-Zeo, Cs(I) adsorption reaches a maximum at  $\text{pH} = 8$  and decreases thereafter (Fig. 27c). With increasing pH, the adsorption of Co(II) on the composites CS-MSMC-GLUT, CS-MSMC-ECH, CS-Mt-GLY and CS-MSMC, CS-MSMC-STP, CS-Zeo reaches a maximum at  $\text{pH} = 5$  and 6, respectively, and thereafter the adsorption decreases (Fig. 27d). The adsorption of Eu(III) (Fig. 27e) on CS-MSMC, CS-MSMC-ECH, and CS-MSMC-STP reaches a maximum at  $\text{pH} = 5$  and on CS-MSMC-GLUT at  $\text{pH} = 6$ , after which the adsorption decreases and only for the composites CS-Zeo and CS-Mt-GLY the adsorption of Eu(III) was constantly high after pH of 5 and 6, respectively.

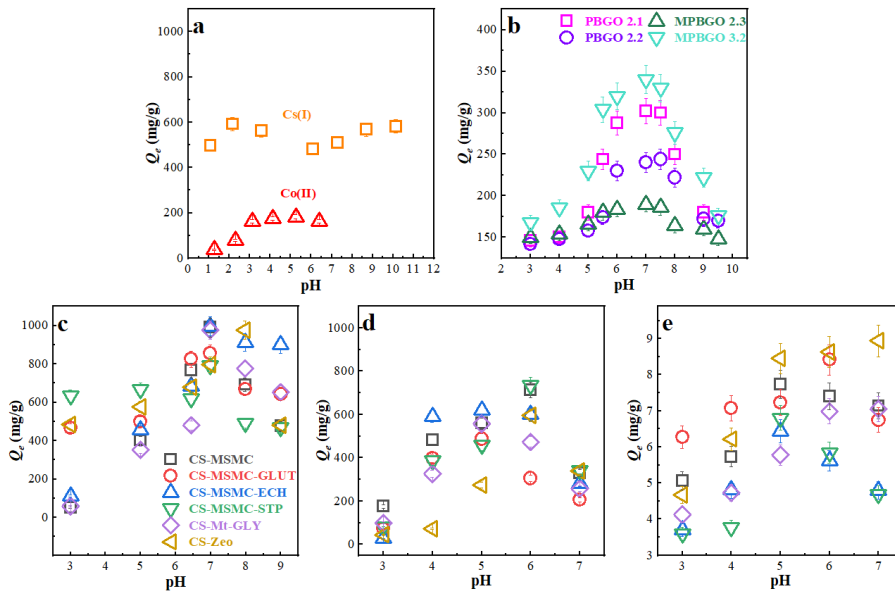


**Fig. 27.** Effect of pH on adsorption of Cs(I) and Co(II) for MSMC-GO-MGH-MG composite (a), Cs(I) for PBGO and MPBGO composites (b), Cs(I) (c), Co(II) (d), and Eu(III) (e) for chitosan-mineral composites.

Thus, the stable adsorption of Cs(I) on the composite MSMC-GO-MGH-MG possibly indicates an ion exchange mechanism (Lujanienė et al. 2010; Zhang et al. 2020a). In other cases, the increase in adsorption capacity with increasing pH is apparently due to the fact that the amount of  $H^+$  and  $H_3O^+$  in the medium decreases with increasing pH, resulting in less competition for adsorption sites between  $H^+/H_3O^+$  and the cations studied ( $Cs^+$ ,  $Co^{2+}$ , and  $Eu^{3+}$ ), and that the negative charge of the composites also increases, resulting in an electrostatic attraction between the deprotonated surface of the composites and  $Cs^+$ ,  $Co^{2+}$ , and  $Eu^{3+}$ , which promotes adsorption. Furthermore, adsorption of cations in an acidic medium occurs despite electrostatic repulsion, possibly by ion exchange or complexation. The low adsorption of Cs(I) under alkaline conditions on the composites is possibly due to the binding of caesium ions to the surrounding  $OH^-$  and in the case of PBGO and MPBGO composites also to the destruction of the structure of PB and MPB, respectively, as a result of the interaction of the surrounding hydroxide ions with iron ions. In the case of chitosan-mineral composites with the destruction of the silicate structure of minerals. The low adsorption of Co(II) and Eu(III) on the composites at  $pH > 5/6$  is probably due to the predominant precipitation rather than the adsorption process. However, in the case of CS-Zeo and CS-Mt-GLY, both adsorption and precipitation processes may occur for Eu(III)



(Cadogan et al. 2014; Awual et al. 2016; Zhang et al. 2017, 2021; Mnasri-Ghnimi and Frini-Srasra 2019; Seema 2020; Khan et al. 2021; Yushin et al. 2022; Feng et al. 2022).

### 3.3.3. Effect of contact time

The results of the kinetic studies, presented in Fig. 28, show that the adsorption of Cs(I) and Co(II) on the MSMC-GO-MGH-MG composite increases sharply over 30 and 50 min, respectively, of Cs(I) on the PBGO and MPBGO composites over 60 min, and during the same time Cs(I), Co(II), and Eu(III) on the chitosan-mineral composites. Thereafter, the adsorption slows down and reaches the equilibrium state for 40 and 60 min in the case of adsorption of Cs(I) and Co(II), respectively, on the MSMC-GO-MGH-MG composite. For 240 min in the case of adsorption of Cs(I) on PBGO and MPBGO composites and in the case of adsorption of Cs(I), Co(II), and Eu(III) on chitosan-mineral composites. The sharp increase in ion adsorption can be explained by the large number of available adsorption sites on the surface of the composites in the early contact time. The slowdown of adsorption probably indicates that all adsorption sites on the surface are filled and the ions move into the pores and/or into the layers of the composite. After all adsorption sites are filled, equilibrium is reached (Esmaili and Tamjidi 2020; Feng et al. 2022).

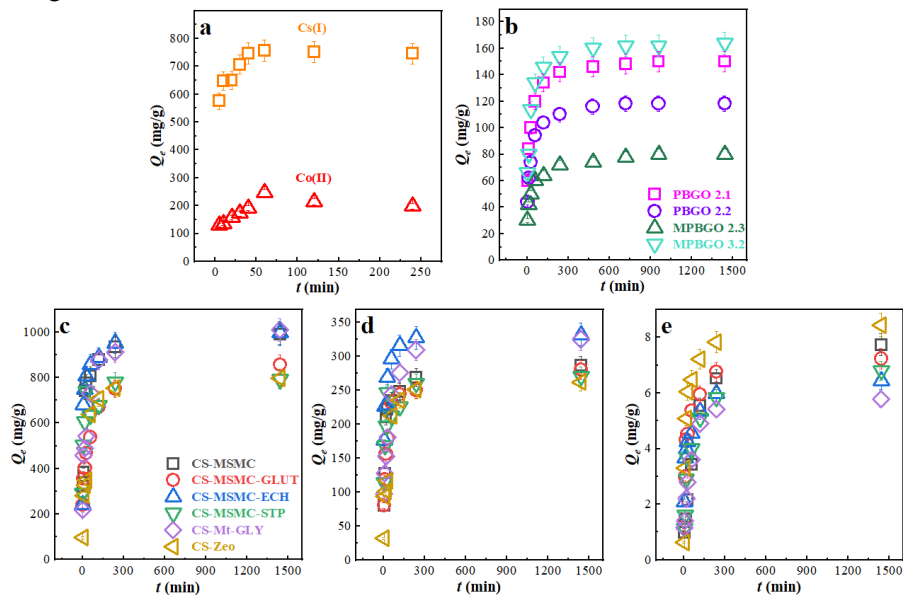


**Fig. 28.** Effect of contact time on adsorption of Cs(I) and Co(II) for MSMC-GO-MGH-MG composite (a), Cs(I) for PBGO and MPBGO composites (b), Cs(I) (c), Co(II) (d), and Eu(III) (e) for chitosan-mineral composites.

### 3.3.4. Effect of the mass of the adsorbent and thermodynamic study

The results on the effect of mass of adsorbent and the temperature on the adsorption of Cs(I) and Co(II) on the MSMC-GO-MGH-MG composite are shown in Fig. 29. With an increase in the mass of the adsorbent in the range of 0.01–0.16 g, the adsorption capacity of the composite decreases from 537 to 60 mg/g for caesium ions and from 154 to 26 mg/g for cobalt ions. The decrease in the adsorption capacity of the composite is possibly related to its agglomeration and aggregation. With increasing temperature, the adsorption capacity of the composite for caesium ions increases in the range of 25 to 45 °C, and after adsorption of caesium it was consistently high in the range of 45 to 75 °C. For cobalt ions, a linear increase in adsorption capacity is observed with an increase in temperature from 25 to 75 °C (Egbosiuba et al 2020; Esmaeili and Tamjidi 2020).

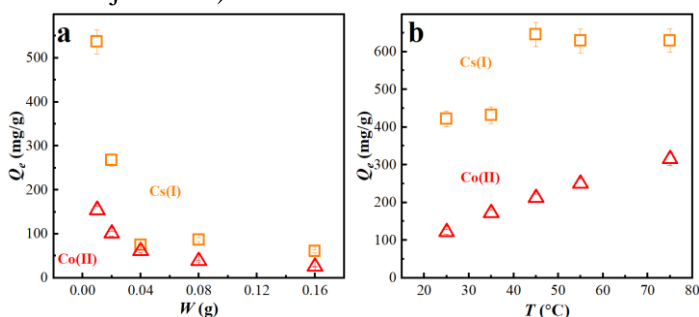


**Fig. 29.** Effect of the mass of the adsorbent (a) and the temperature (b) on the adsorption of Cs(I) and Co(II) on MSMC-GO-MGH-MG composite.

From the thermodynamic parameters presented in Table 5, it appears that the adsorption of cobalt was spontaneous, since the positive  $\Delta G^\circ$  values obtained decrease with increasing temperature, whereas these positive values do not decrease in the case of caesium, indicating non-spontaneous adsorption. Positive  $\Delta H^\circ$  values indicate the endothermic nature of the physical adsorption of the ions on the MSMC-GO-MGH-MG composite, and positive  $\Delta S^\circ$  values indicate an increase in the randomness of the adsorption of the caesium and cobalt ions on the composite (Egbosiuba et al 2020; Esmaeili and Tamjidi 2020).

**Table 5.** Thermodynamic parameters of adsorption of Cs(I) and Co(II) on MSMC-GO-MGH-MG composite.

$T$ (K)	$\Delta G^\circ$ (kJ/mol)	$\Delta H^\circ$ (kJ/mol)	$\Delta S^\circ$ (J/mol K)
Cs(I)			
298	4.635	9.514	16.754
308	4.719		
318	3.593		
328	3.798		
348	4.025		
Co(II)			
298	4.263	21.801	59.567
308	3.326		
318	2.701		
328	2.157		
348	1.251		

### 3.4. Adsorption isotherms and kinetics

The results of the linear and non-linear Langmuir and Freundlich isotherms are shown in Figs. 30–34 and Tables 6–8. According to the obtained  $R^2$  values, the linear Freundlich isotherm fits the obtained experimental data for the systems MSMC-GO-MGH-MG-Cs(I)/Co(II) better than the Langmuir isotherm. Based on the assumption of the Freundlich isotherm, it follows that the adsorption of caesium and cobalt ions occurred in multilayer on the heterogeneous surface of the composite. According to the  $K_F$  values, the affinity of the composite for cobalt is 1.4 times greater than for caesium. The resulting  $1/n$  values for the ions were below unity, indicating favourable adsorption (Al-Senani and Al-Fawzan 2018; Esmaeili and Tamjidi 2020; Mohseni-Bandpei et al. 2020; Achour et al. 2021).

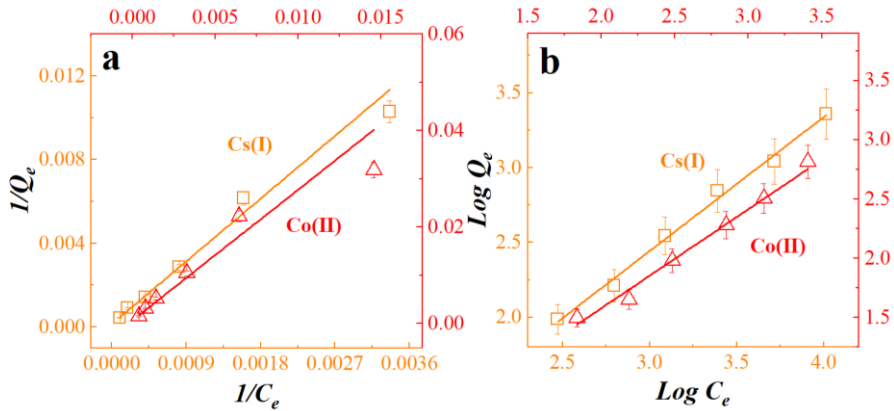


**Fig. 30.** The linear Langmuir (a) and Freundlich (b) isotherms for MSMC-GO-MGH-MG-Cs(I)/Co(II) systems.

**Table 6.** The parameters of the isotherms for MSMC-GO-MGH-MG composite.

Isotherms	Langmuir				Freundlich		
	$R^2$	$Q_m$	$K_L$	$R_L$	$R^2$	$K_F$	$1/n$
Cs(I)	0.982	2650	1.23E-04	0.392	0.993	0.570	0.895
Co(II)	0.926	373	0.001	0.202	0.987	0.705	0.859

The data obtained for PBGO-Cs(I), MPBGO-Cs(I), and chitosan-mineral-Cs(I)/Co(II)/Eu(III) systems are in better agreement with the non-linear Langmuir isotherm than with the non-linear Freundlich isotherm, as shown by the values of  $R^2$ . According to the assumption of the Langmuir non-linear isotherm, the adsorption of caesium on PBGO and MPBGO composites and the adsorption of caesium, cobalt, and europium on chitosan-mineral composites is a monolayer occurring on the homogeneous surface of the composites. Furthermore, the adsorption process is favourable as the obtained  $R_L$  values for these systems were greater than 0 but less than 1 (Mohseni-Bandpei et al. 2020; Achour et al. 2021).

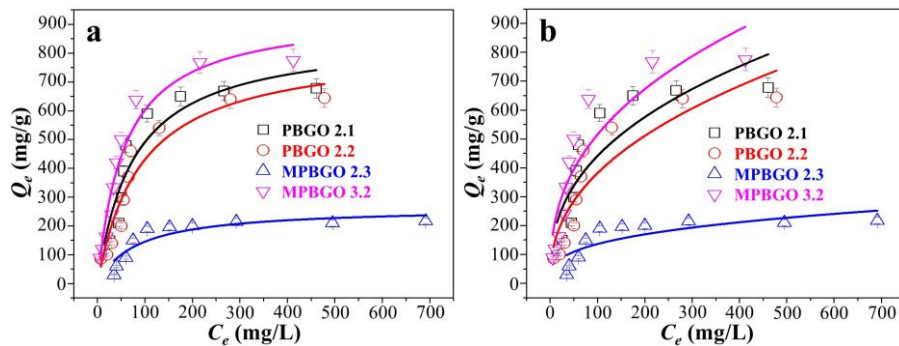


**Fig. 31.** The non-linear Langmuir (a) and Freundlich (b) isotherms for PBGO-Cs(I) and MPBGO-Cs(I) systems.

**Table 7.** The parameters of the isotherms for PBGO and MPBGO composites.

Isotherms	Langmuir				Freundlich		
	$R^2$	$Q_m$	$K_L$	$R_L$	$R^2$	$K_F$	$1/n$
PBGO 2.1	0.886	863	0.013	0.088	0.754	75	0.384
PBGO 2.2	0.912	826	0.011	0.102	0.813	55	0.42
MPBGO 2.3	0.813	265	0.012	0.094	0.622	32	0.318
MPBGO 3.2	0.959	943	0.018	0.065	0.827	88	0.385

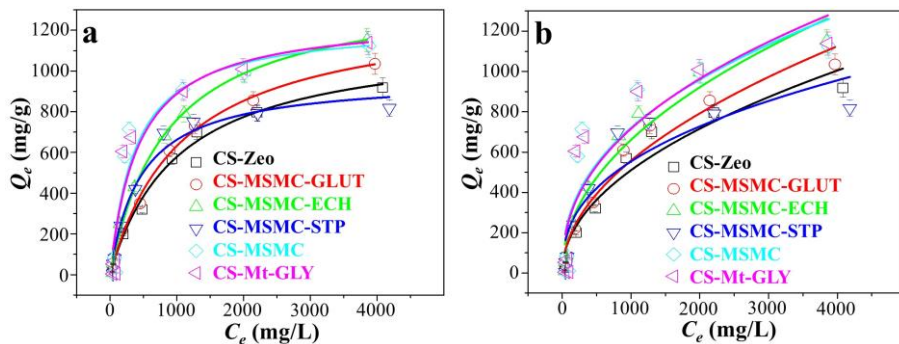


**Fig. 32.** The non-linear Langmuir (a) and Freundlich (b) isotherms for chitosan-mineral-Cs(I) systems.

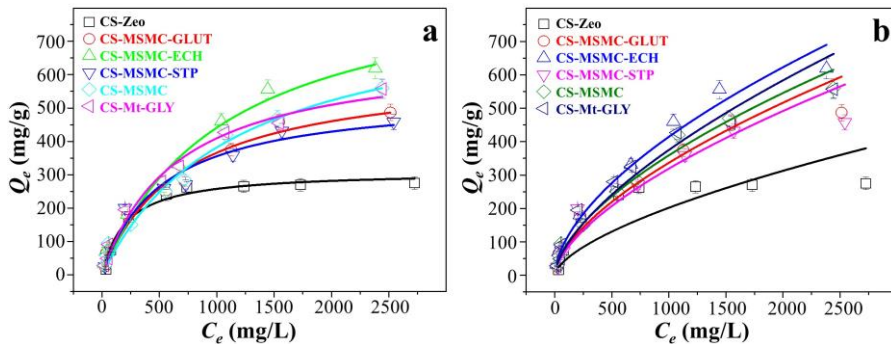


**Fig. 33.** The non-linear Langmuir (a) and Freundlich (b) isotherms for chitosan-mineral-Co(II) systems.

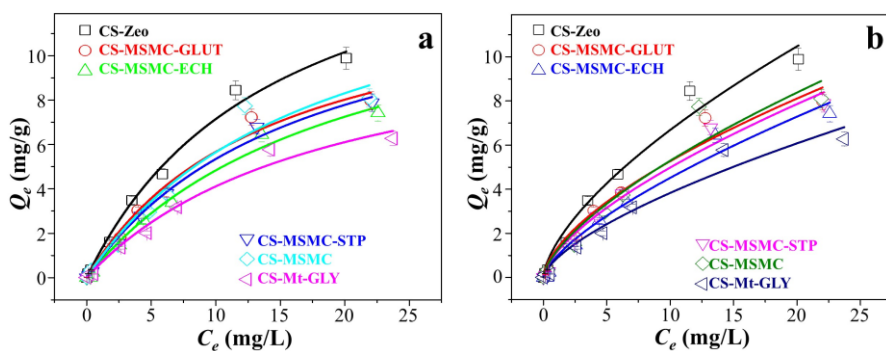


**Fig. 34.** The non-linear Langmuir (a) and Freundlich (b) isotherms for chitosan-mineral-Eu(III) systems.

**Table 8.** The parameters of the isotherms for chitosan-mineral composites.

Isotherms	Langmuir				Freundlich		
	Parameters	$R^2$	$Q_m$	$K_L$	$R_L$	$R^2$	$K_F$
Cs(I)							
CS-MSMC	0.910	1234	0.003	0.070	0.791	42	0.413
CS-MSMC-GLUT	0.995	1314	9.26E-04	0.178	0.955	17	0.506
CS-MSMC-ECH	0.996	1408	0.001	0.146	0.948	24	0.480
CS-MSMC-STP	0.973	968	0.002	0.085	0.834	36	0.394
CS-Mt-GLY	0.902	1268	0.002	0.079	0.795	37	0.429
CS-Zeo	0.993	1170	9.78E-04	0.170	0.942	17	0.489
Co(II)							
CS-MSMC	0.977	827	8.58E-04	0.280	0.956	5.54	0.604
CS-MSMC-GLUT	0.968	621	0.001	0.188	0.895	4.72	0.618
CS-MSMC-ECH	0.974	916	9.30E-04	0.264	0.961	7.16	0.587
CS-MSMC-STP	0.969	542	0.002	0.149	0.918	4.31	0.623
CS-Mt-GLY	0.984	675	0.002	0.178	0.929	4.59	0.638
CS-Zeo	0.978	311	0.005	0.064	0.719	2.60	0.630
Eu(III)							
CS-MSMC	0.960	16	0.056	0.373	0.938	1.15	0.663
CS-MSMC-GLUT	0.986	14	0.071	0.321	0.966	1.26	0.622
CS-MSMC-ECH	0.989	15	0.050	0.400	0.973	0.920	0.691
CS-MSMC-STP	0.993	14	0.060	0.359	0.977	1.10	0.657
CS-Mt-GLY	0.981	12	0.053	0.386	0.961	0.827	0.666
CS-Zeo	0.991	18	0.068	0.328	0.975	1.50	0.648

The obtained values of maximum theoretical adsorption capacity ( $Q_m$ ) were compared with those reported in other studies (Tables 9–11). The comparative results showed that the composites obtained can be promising adsorbents for caesium and cobalt, as the adsorption capacity is higher than that of other adsorbents. However, as far as the adsorption of europium is concerned, the chitosan-mineral composites are on average 1.4 times inferior to the other adsorbents in adsorption capacity. Also, in the case of MPBGO 2.3, its adsorption capacity for caesium was 2 times lower than that of the

Prussian blue analogues synthesised by ionic liquid-assisted strategy (PBIL-BF4).

**Table 9.** Comparison of  $Q_m$  of different adsorbents for Cs(I).

<b>Adsorbents</b>	<b><math>Q_m</math></b>	<b>Refs.</b>
Bio-based lignin microspheres	44	(Goyal et al. 2020)
Copper hexacyanoferrates	70	(Zhuang et al. 2022)
Nano-Fe/Cu-zeolite	78	(Eljamal et al. 2019)
Magnetic zeolite	5	(Falyouna et al. 2020)
Bentonite-chitosan hybrid beads	57	(Wang et al. 2019)
Bentonite	49	
Porous magnetic chitosan hydrogel beads	7	
Montmorillonite	73	(Zheng et al. 2017)
Oxidised bamboo charcoal	55	(Khandaker et al. 2018)
Prussian blue analogues synthesised by ionic liquid-assisted strategy (PBIL-BF4)	549	(Chen et al. 2022)
Prussian blue graphene oxide-chitosan	48	(Rethinasabapathy et al. 2019)
MSMC-GO-MGH-MG	2286*	This work
PBGO 2.1	863	
PBGO 2.2	826	
MPBGO 2.3	265	
MPBGO 3.2	943	
CS-MSMC	1234	
CS-MSMC-GLUT	1314	
CS-MSMC-ECH	1408	
CS-MSMC-STP	968	
CS-Mt-GLY	1268	
CS-Zeo	1170	

\*The maximum experimental adsorption capacity is used



**Table 10.** Comparison of  $Q_m$  of different adsorbents for Co(II).

Adsorbents	$Q_m$	Refs.
Chitosan-activated carbon/UiO-66 MOFs	45	(Motaghi et al. 2022)
Magnetic cyanoethyl chitosan beads	17	(Zhang et al. 2020c)
Magnetic graphene oxide/chitosan	10	(Zhuang and Wang 2019)
Chitosan–montmorillonite	150	(Wang et al. 2014)
Magnetic cobalt ion-imprinted polymer	84	(Adibmehr and Faghihian 2020)
MSMC-GO-MGH-MG	652*	This work
CS-MSMC	827	
CS-MSMC-GLUT	621	
CS-MSMC-ECH	916	
CS-MSMC-STP	542	
CS-Mt-GLY	675	
CS-Zeo	311	

\*The maximum experimental adsorption capacity is used

**Table 11.** Comparison of  $Q_m$  of different adsorbents for Eu(III).

Adsorbents	$Q_m$	Refs.
Chitosan nanoparticles	115	(Cadogan et al. 2014)
NKF-6 zeolite	24	(Khan et al. 2021)
<i>Saccharomyces cerevisiae</i> -glutaraldehyde-chitosan	19	(Arunraj et al. 2019)
Graphene oxide	68	(Ma et al. 2019)
MnO <sub>2</sub> /graphene oxide	84	
CS-MSMC	16	This work
CS-MSMC-GLUT	14	
CS-MSMC-ECH	15	
CS-MSMC-STP	14	
CS-Mt-GLY	12	
CS-Zeo	18	

The results of the linear and non-linear kinetic models presented in Figs. 35–39 and Tables 12–14 show that the adsorption of Cs(I) and Co(II) on MSMC-GO-MGH-MG, of Cs(I) on PBGO and MPBGO composites, and of Cs(I), Co(II), and Eu(III) on chitosan-mineral composites is better described by the pseudo-second-order kinetic model than by the pseudo-first-order kinetic model, as indicated by the obtained  $R^2$  values. Moreover, the calculated equilibrium adsorption capacity values ( $Q_{e\ Theoretical}$ ) are close to the experimental

values ( $Q_{e\text{ Exp}}$ ). However, the systems CS-MSMC-ECH-Cs(I), CS-MSMC-STP-Cs(I), and CS-Zeo-Co(II) are in better agreement with the pseudo-first-order kinetic model. From the assumption of the pseudo-second-order model, it follows that the predominant mechanism of adsorption in the systems studied that fit this model is chemisorption. In contrast, it follows from the assumption of the pseudo-first-order model that the predominant mechanism of adsorption in the systems CS-MSMC-ECH-Cs(I), CS-MSMC-STP-Cs(I), and CS-Zeo-Co(II) is physisorption (Cadogan et al. 2014; Kaveeshwar et al. 2018; Achour et al. 2021; Al-Musawi et al. 2021; Zhang et al. 2022).

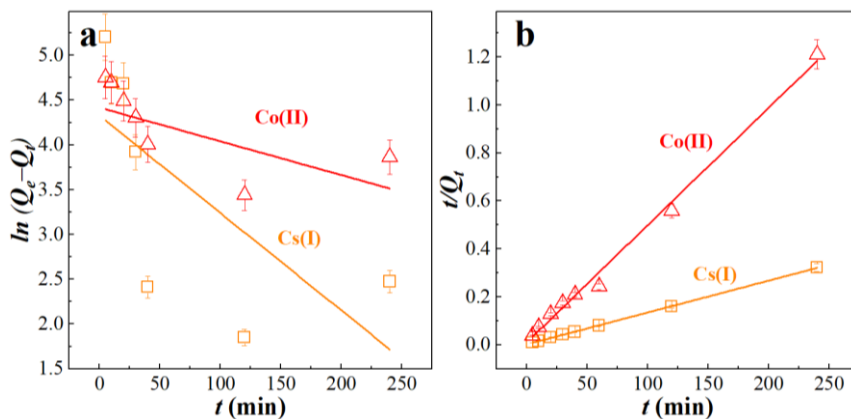


**Fig. 35.** Adsorption kinetics of Cs(I) and Co(II) on MSMC-GO-MGH-MG composite according to the linear form of the model pseudo-first-order (a) and pseudo-second-order (b).

**Table 12.** The parameters of the kinetic models for MSMC-GO-MGH-MG composite.

Models	Pseudo-first-order				Pseudo-second-order		
	$R^2$	$K_1$	$Q_{e\text{ Theo}}$	$Q_{e\text{ Exp}}$	$R^2$	$K_2$	$Q_{e\text{ Theo}}$
Cs(I)	0.247	-4.17E-05	76	758	0.999	0.001	769
Co(II)	0.394	-1.25E-05	88	246	0.993	0.002	250

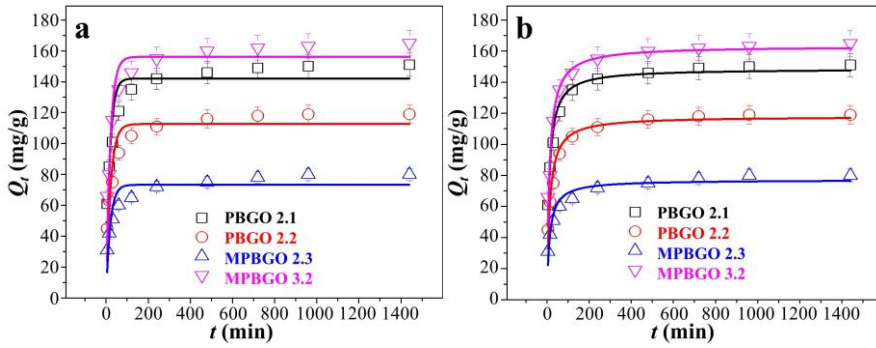


**Fig. 36.** Adsorption kinetics of Cs(I) on PBGO and MPBGO composites according to the non-linear form of the model pseudo-first-order (a) and pseudo-second-order (b).

**Table 13.** The parameters of the kinetic models for PBGO and MPBGO composites.

Models	Pseudo-first-order				Pseudo-second-order		
	$R^2$	$K_1$	$Q_e$ <i>Theo</i>	$Q_e$ <i>Exp</i>	$R^2$	$K_2$	$Q_e$ <i>Theo</i>
PBGO 2.1	0.820	0.057	142	151	0.960	6.40E-04	149
PBGO 2.2	0.839	0.048	113	119	0.959	6.70E-04	118
MPBGO 2.3	0.771	0.052	73	80	0.930	1.10E-03	77
MPBGO 3.2	0.858	0.051	156	165	0.959	5.20E-04	163

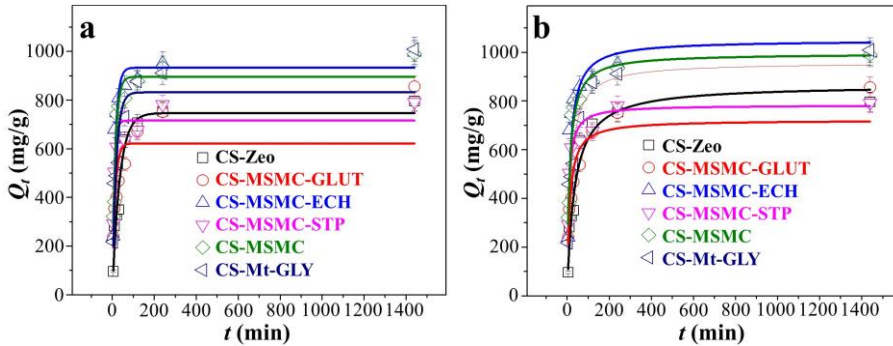


**Fig. 37.** Adsorption kinetics of Cs(I) on chitosan-mineral composites according to the non-linear form of the model pseudo-first-order (a) and pseudo-second-order (b).

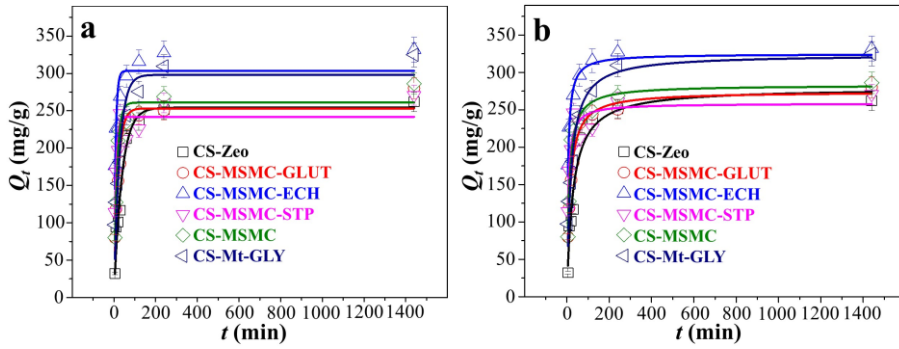


**Fig. 38.** Adsorption kinetics of Co(II) on chitosan-mineral composites according to the non-linear form of the model pseudo-first-order (a) and pseudo-second-order (b).

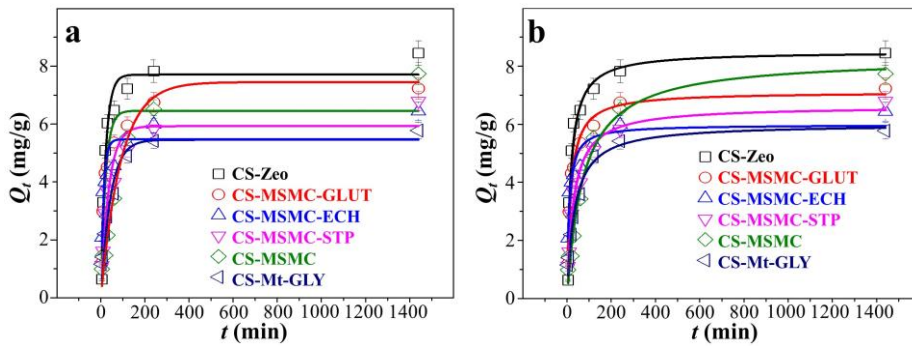


**Fig. 39.** Adsorption kinetics of Eu(III) on chitosan-mineral composites according to the non-linear form of the model pseudo-first-order (a) and pseudo-second-order (b).

**Table 14.** The parameters of the kinetic models for chitosan-mineral composites.

Models	Pseudo-first-order				Pseudo-second-order		
Parameters	$R^2$	$K_1$	$Q_e$ <i>Theo</i>	$Q_e$ <i>Exp</i>	$R^2$	$K_2$	$Q_e$ <i>Theo</i>
Cs(I)							
CS-MSMC	0.924	0.070	896	990	0.937	8.40E-05	995
CS-MSMC-GLUT	0.761	0.075	622	856	0.911	1.20E-04	722
CS-MSMC-ECH	0.930	0.071	933	996	0.901	7.00E-05	1049
CS-MSMC-STP	0.947	0.109	716	791	0.929	1.80E-04	783
CS-Mt-GLY	0.892	0.054	832	1009	0.956	6.30E-05	959
CS-Zeo	0.943	0.029	747	797	0.946	3.35E-04	866
Co(II)							
CS-MSMC	0.947	0.071	261	286	0.961	3.42E-04	283
CS-MSMC-GLUT	0.929	0.051	253	280	0.987	2.62E-04	274
CS-MSMC-ECH	0.679	0.130	303	332	0.919	6.10E-04	325
CS-MSMC-STP	0.816	0.115	242	271	0.865	6.74E-04	259
CS-Mt-GLY	0.877	0.038	298	325	0.961	1.64E-04	324
CS-Zeo	0.957	0.027	254	262	0.951	1.25E-04	279
Eu(III)							
CS-MSMC	0.973	0.011	7.45	7.74	0.978	0.002	8.30
CS-MSMC-GLUT	0.915	0.047	6.46	7.23	0.973	0.009	7.11
CS-MSMC-ECH	0.731	0.080	5.47	6.44	0.901	0.018	5.98
CS-MSMC-STP	0.906	0.028	5.93	6.80	0.977	0.005	6.63
CS-Mt-GLY	0.957	0.023	5.46	5.78	0.985	0.005	6.01
CS-Zeo	0.933	0.047	7.71	8.45	0.940	0.007	8.51

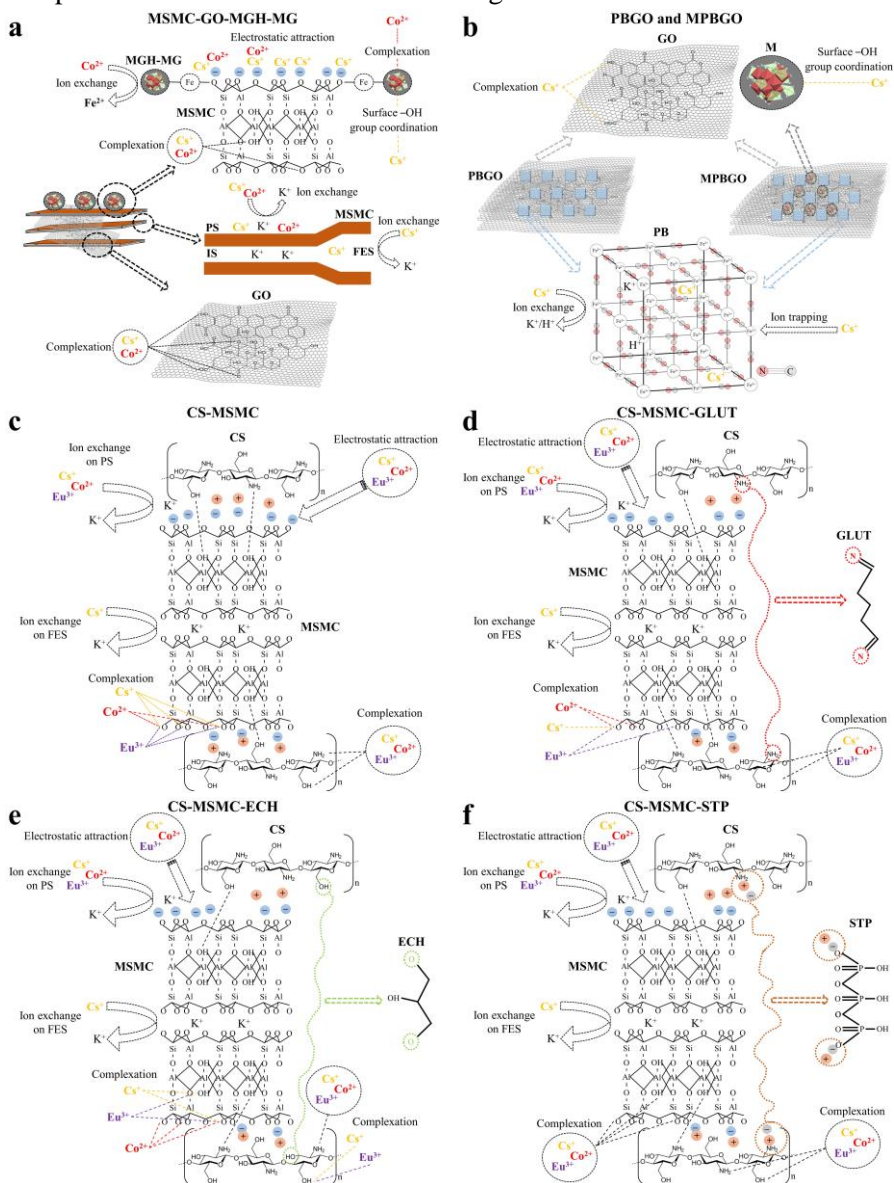
### 3.5. The suggested adsorption mechanism

The pH effect results indicate physical adsorption (electrostatic attraction) for the systems MSMC-GO-MGH-MG-Co(II), PBGO-Cs(I), MPBGO-Cs(I), and chitosan-mineral-Cs(I)/Co(II)/Eu(III), while chemical adsorption (ion exchange) is present in the case of the system MSMC-GO-MGH-MG-Cs(I). The thermodynamic results for the systems MSMC-GO-MGH-MG-Cs(I)/Co(II) indicate the physical nature of adsorption. The kinetic modelling results indicate chemical adsorption for the systems MSMC-GO-MGH-MG-Cs(I)/Co(II), PBGO-Cs(I), MPBGO-Cs(I), and chitosan-mineral-Cs(I)/Co(II)/Eu(III) and physical adsorption only in the case of CS-MSMC-ECH-Cs(I), CS-MSMC-STP-Cs(I), and CS-Zeo-Co(II). Moreover, the obtained ATR-FTIR results after adsorption indicate a possible interaction of Cs(I) and Co(II) with the following groups of the MSMC-GO-MGH-MG composite: Si–O–Si, Al–O–Si/Fe–O, Fe–O–Si/Fe–O–Al, Al–OH–Al and Si–O–Si, Si–O, C–O/C–OH, respectively. Also Cs(I), Co(II), and Eu(III), in most cases with –OH, –NH<sub>2</sub>, Si–O–Si, Si–O, and Al–O(H)–Al groups chitosan-mineral composites. Additionally, XPS results after ion adsorption on the MSMC-GO-MGH-MG composite indicate possible interactions of caesium with Fe<sup>2+</sup>, Fe<sup>3+</sup>, metal oxides, Al–OH, Si–O–Si, C–OH/C–O–C, C–O, C=O, and O=C–O. Cobalt ions with Fe<sup>3+</sup>, metal oxides, Si–O–Si, SiO<sub>2</sub>, C–OH/C–O–C, C–O, C=O, and O=C–O. Furthermore, these results indicate ion exchange with K<sup>+</sup> probably on PS and FES of muscovite, in the case of caesium and in the case of cobalt only on PS. After adsorption of cobalt, a Co–Al bond was also detected, possibly formed as a result of complexation with Al–OH (Ogwada and Sparks 1986; Fan et al. 2014; Penke et al. 2017; Woodward et al. 2018).

In addition to our results, Eljamal et al. (2019) and Falyouna et al. (2020), in a study on the adsorption of caesium on iron-based nanoparticles-zeolite and magnetic zeolite, respectively found that the main adsorption mechanism is ion exchange, and Falyouna et al. (2020) also found that caesium forms chemical bonds with silicate and aluminium oxide groups of zeolite. Zhang et al. (2021) found that caesium interacts with the chitosan-vermiculite composite through the formation of coordination bonds between caesium and –OH groups of vermiculite and –NH<sub>2</sub> groups of chitosan. The mechanism of caesium adsorption on this composite is ion exchange, ligand complexation, and electrostatic attraction. Wang et al. (2019), when adsorbing caesium on a magnetic bentonite-chitosan composite, also found that caesium interacts with the –NH<sub>2</sub> groups of the chitosan component of the composite by forming a complex. On the bentonite component, ion exchange takes place. Fuller et al.

(2014) found that caesium adsorbs on FES, PS, and THS (Type II sites) of micaceous aquifer sediment. The authors of Ishizaki et al. (2013) found that the adsorption of caesium on “insoluble” Prussian blue occurs via proton exchange using the hydrophilic crystal lattice sites. In the work of Takahashi et al. (2018), adsorption of caesium on Prussian blue analogues occurs mainly by ion exchange with  $K^+$  as well as by proton exchange in the range of low  $K^+$  incorporation. Yang et al. (2014) suggested that the adsorption of caesium on Prussian blue and magnetic Prussian blue/graphene oxide encapsulated in calcium alginate microbeads occurs by chemisorption ( $K^+/H^+$  exchange) and physisorption (ion trapping). Huo et al. (2021) found that the adsorption of caesium onto Prussian blue analogues anchored on 3D-reduced graphene oxide aerogel occurs by complexation interaction between caesium and the residual oxygen-containing functional groups in the graphene oxide edges ( $-COOH$  and  $-OH$ ), ion exchange with  $K^+$ , and ion trapping on the Prussian blue analogues part of the adsorbent. Zheng et al. (2017) found that adsorption of caesium onto magnetite as part of the MMT/ $Fe_3O_4$  composite occurs due to surface hydroxyl group coordination. Efimova et al. (2021) found that the adsorption of  $^{137}Cs$  and  $^{60}Co$  on  $\alpha-Fe_2O_3$  and  $Fe_3O_4$  occurs by ion exchange. The adsorption of cobalt on palygorskite and graphene oxide-magnetite occurs by ion exchange and inner-sphere complexation, and on the organo-modification of montmorillonite by outer-sphere complexation (He et al. 2011; Tayyebi et al. 2015; Soliman et al. 2019). The adsorption of cobalt on chitosan-montmorillonite and magnetic cyanoethyl-chitosan beads is chemical in nature. In the case of magnetic cyanoethyl-chitosan beads, it was also found that the  $-NH_2$  groups of chitosan are involved in the adsorption (Wang et al. 2014; Zhang et al. 2020c). In the work of Cadogan et al. (2014) on the adsorption of europium on chitosan nanoparticles, it was found that the interaction of europium with the adsorbent occurs through the formation of a complex with  $-OH$  and  $-NH_2$  groups. The adsorption of europium on *Saccharomyces cerevisiae* immobilised in glutaraldehyde cross-linked chitosan occurs by inner-sphere complexation (Arunraj et al. 2019). The authors of the work Kowal-Fouchard et al. (2004) and Khan et al. (2021) found that the adsorption of europium on montmorillonite and zeolite, respectively, occurs by complexation in both the outer- and inner-sphere. The adsorption of europium on phlogopite and muscovite is controlled by ion exchange or outer-sphere complexation. The adsorption process occurs at the planar and interlayer sites in phlogopite and only at the planar sites in muscovite (Rauret et al. 1999; Bradbury and Baeyens 2000; Fan et al. 2014; Pan et al. 2017; Wu et al. 2021).

Thus, based on experimental and literary data, it can be assumed that the adsorption mechanism is mixed and includes ion exchange, complexation, and electrostatic attraction for the systems MSMC-GO-MGH-MG-Cs(I)/Co(II) and chitosan-mineral-Cs(I)/Co(II)/Eu(III), while for the systems PBGO-Cs(I) and MPBGO-Cs(I) the adsorption mechanism includes complexation, ion exchange, and ion trapping. Schematic representations of the suggested adsorption mechanisms can be found in Fig. 40.





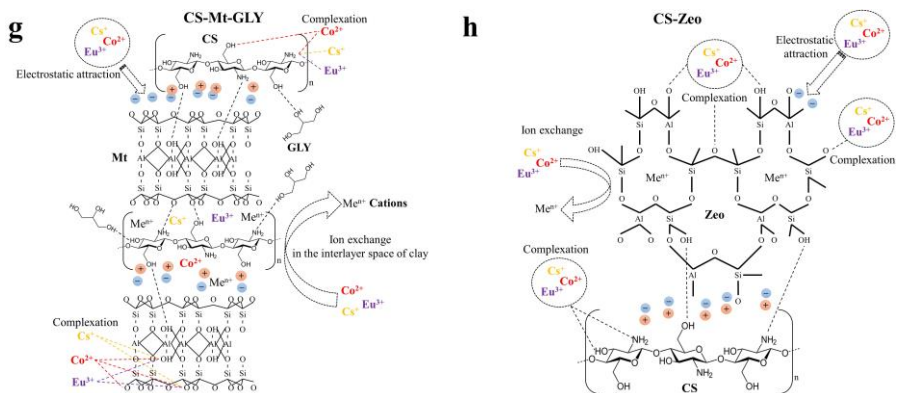


**Fig. 40.** Suggested mechanism of adsorption of ions on MSMC-GO-MGH-MG (a), PBGO and MPBGO (b), CS-MSMC (c), CS-MSMC-GLUT (d), CS-MSMC-ECH (e), CS-MSMC-STP (f), CS-Mt-GLY (g), and CS-Zeo (h) composites.

### 3.6. ANFIS

The results of the comparison of experimental and predicted data (total and testing) by ANFIS as well as error analysis are shown in Figs. 41–49. The very high values of the correlation coefficient close to one and the low values of MSE, SSE, and ARE for the total data of the systems MSMC-GO-MGH-MG-Cs(I)/Co(II), PBGO-Cs(I), MPBGO-Cs(I), and chitosan-mineral-Cs(I)/Co(II)/Eu(III) indicate a good agreement between the predicted and experimental data. For the testing data of these systems, high and very high correlation values and low MSE, SSE, and ARE values indicate that ANFIS has good generalisation ability (Souza et al. 2018; Onu et al. 2021).

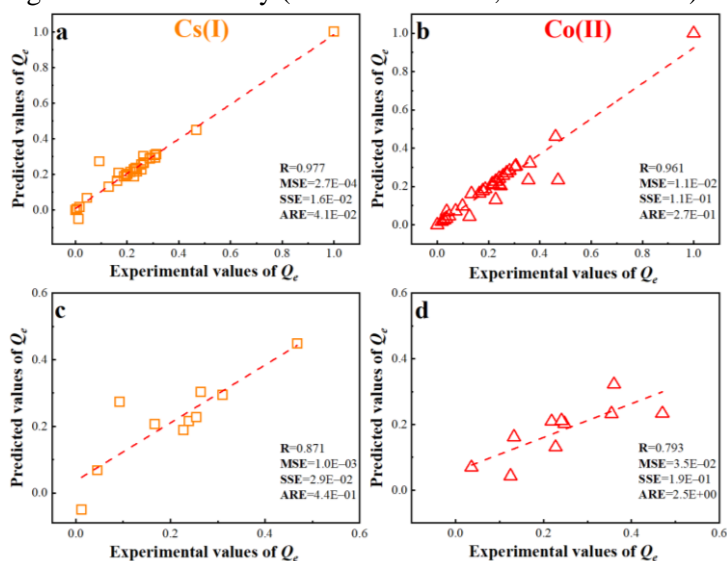


**Fig. 41.** Comparative plots of experimental data with ANFIS predicted data for MSMC-GO-MGH-MG composite: Total data (a and b) and testing data (c and d).

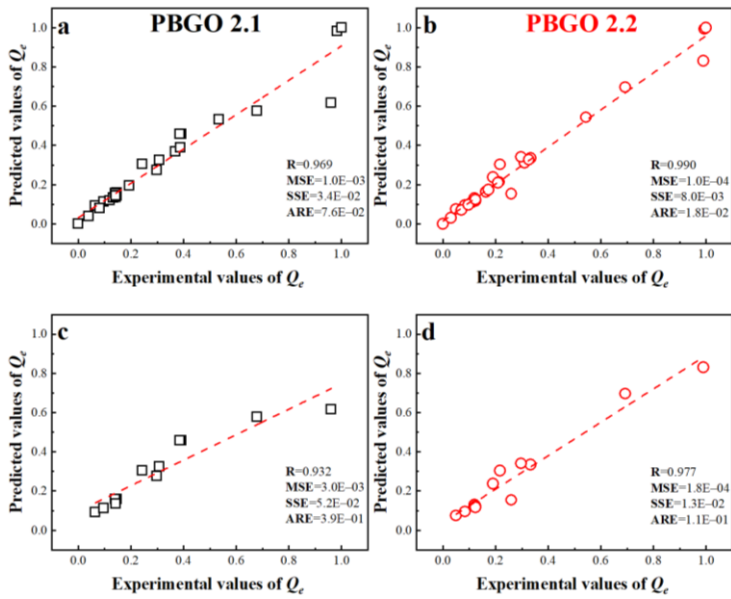


**Fig. 42.** Comparative plots of experimental data with ANFIS predicted data for PBGO composites: Total data (a and b) and testing data (c and d).

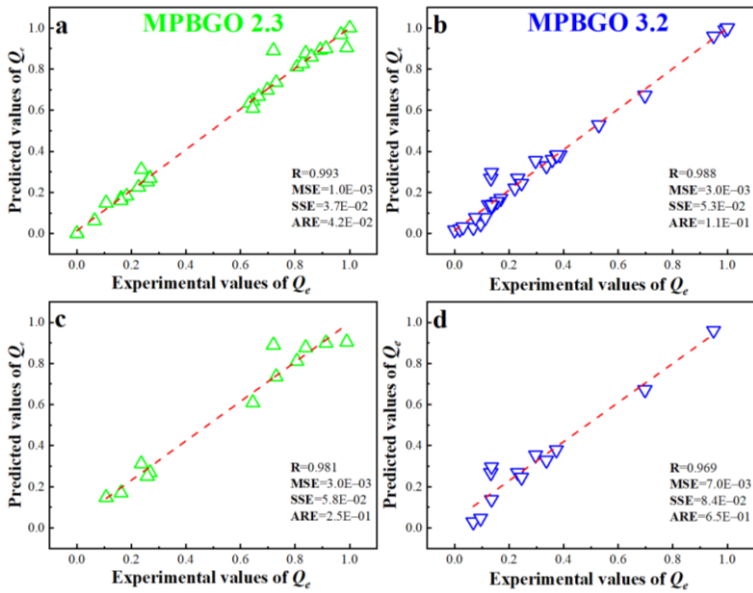


**Fig. 43.** Comparative plots of experimental data with ANFIS predicted data for MPBGO composites: Total data (a and b) and testing data (c and d).

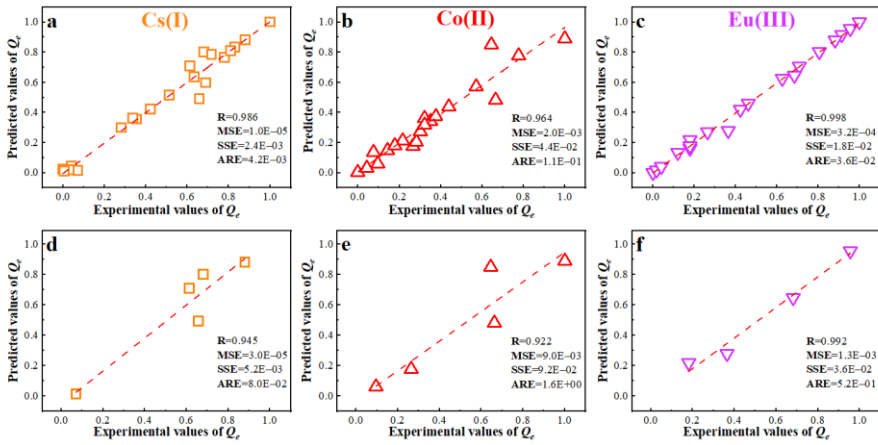


**Fig. 44.** Comparative plots of experimental data with ANFIS predicted data for CS-MSMC composite: Total data (a–c) and testing data (d–f).

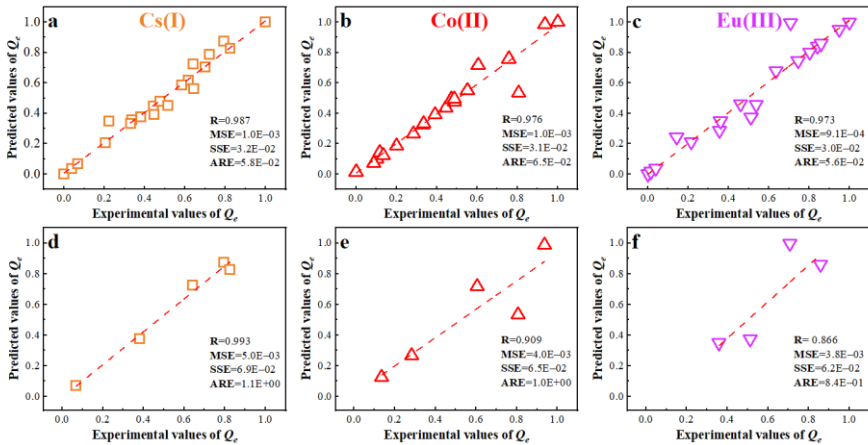


**Fig. 45.** Comparative plots of experimental data with ANFIS predicted data for CS-MSMC-GLUT composite: Total data (a–c) and testing data (d–f).

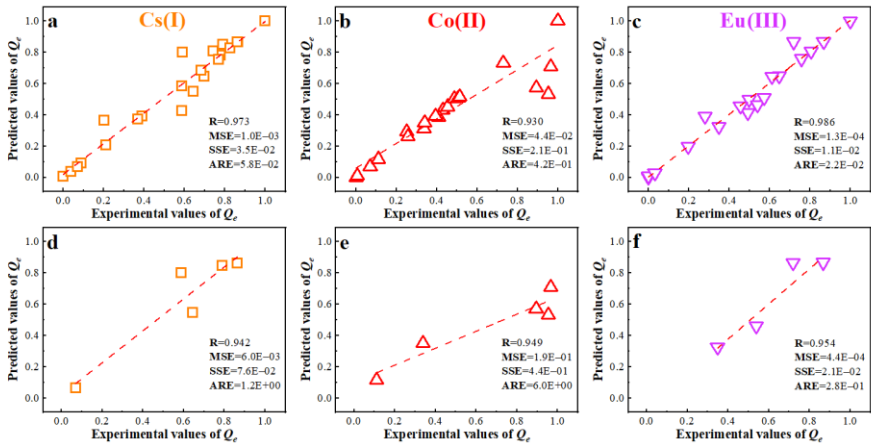


**Fig. 46.** Comparative plots of experimental data with ANFIS predicted data for CS-MSMC-ECH composite: Total data (a–c) and testing data (d–f).

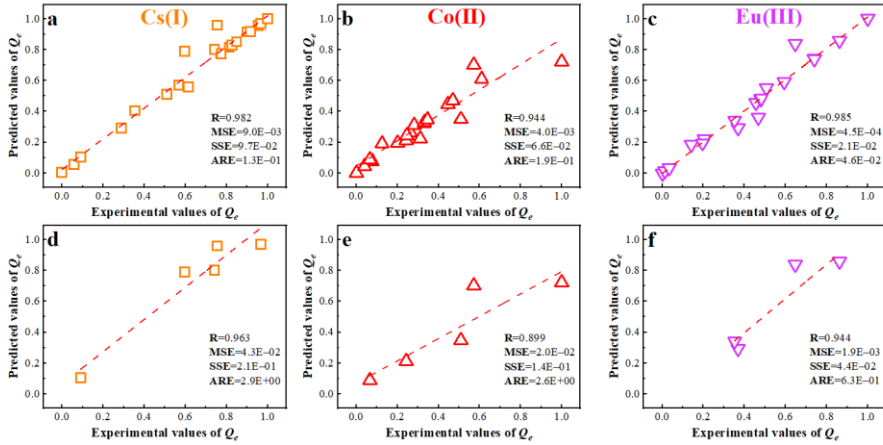


**Fig. 47.** Comparative plots of experimental data with ANFIS predicted data for CS-MSMC-STP composite: Total data (a–c) and testing data (d–f).

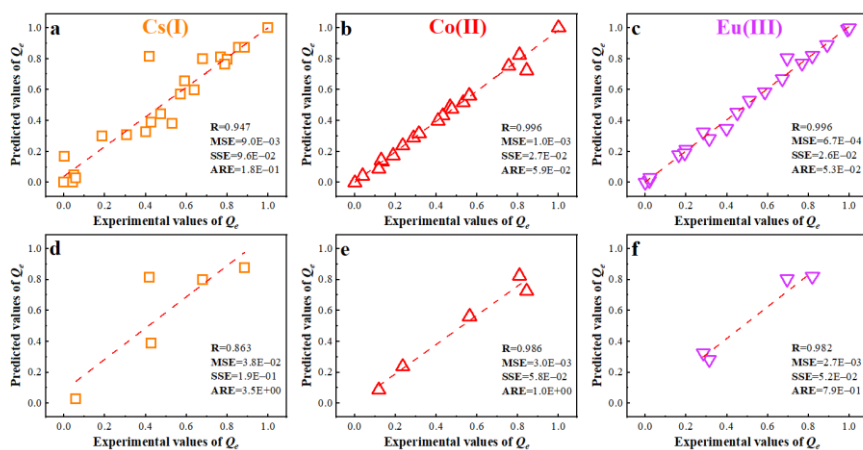


**Fig. 48.** Comparative plots of experimental data with ANFIS predicted data for CS-Mt-GLY composite: Total data (a–c) and testing data (d–f).

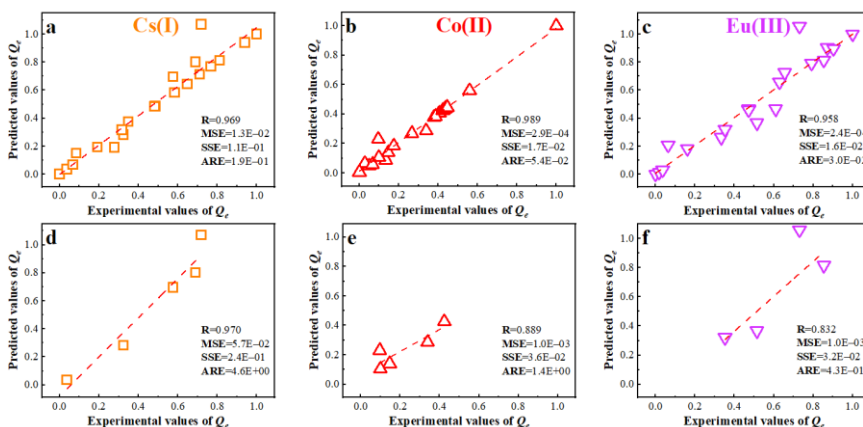


**Fig. 49.** Comparative plots of experimental data with ANFIS predicted data for CS-Zeo composite: Total data (a–c) and testing data (d–f).

The results of 3D surface modelling (Figs. 50–59) show that caesium adsorption on MSMC-GO-MGH-MG, PBGO 2.1, PBGO 2.2, MPBGO 2.3, MPBGO 3.2, CS-MSMC, CS-MSMC-GLUT, CS-MSMC-ECH, CS-MSMC-STP, CS-Mt-GLY, and CS-Zeo composites. Cobalt on MSMC-GO-MGH-MG, CS-MSMC, CS-MSMC-GLUT, CS-MSMC-ECH, CS-MSMC-STP, CS-Mt-GLY, and CS-Zeo composites. Europium on CS-MSMC, CS-MSMC-GLUT, CS-MSMC-ECH, CS-MSMC-STP, CS-Mt-GLY, and CS-Zeo composites. Has a complex and non-linear behaviour depending on the parameters studied, in the case of MSMC-GO-MGH-MG – pH, initial concentration, contact time, mass of adsorbent, and temperature. In the case

of PBGO, MPBGO, and chitosan-mineral composites – pH, initial concentration, and contact time.

### Cs(I)

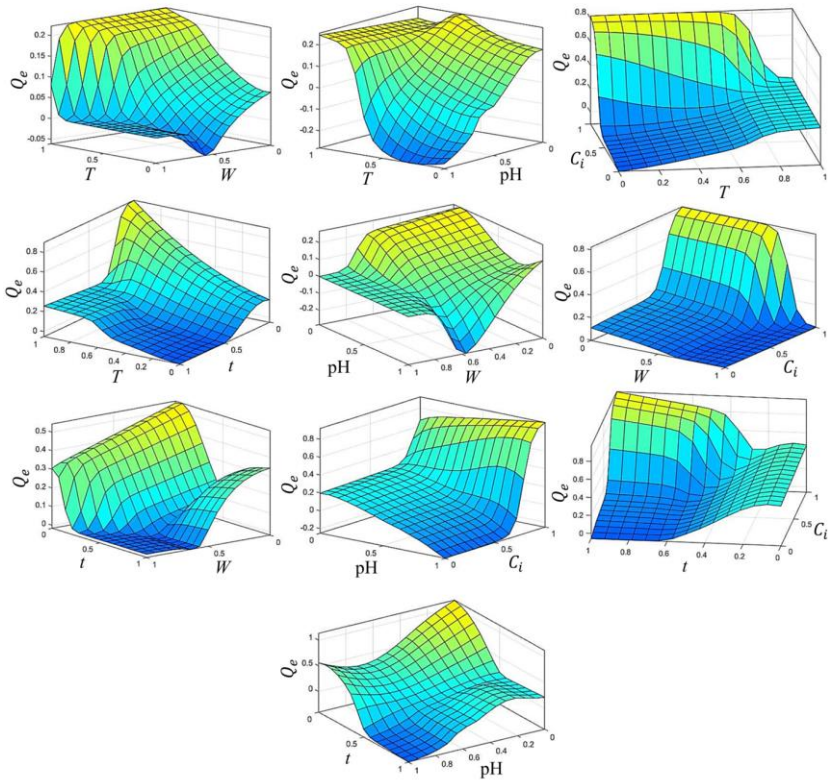


**Fig. 50.** Input-output surfaces of the ANFIS model for the MSMC-GO-MGH-MG composite.

# Co(II)

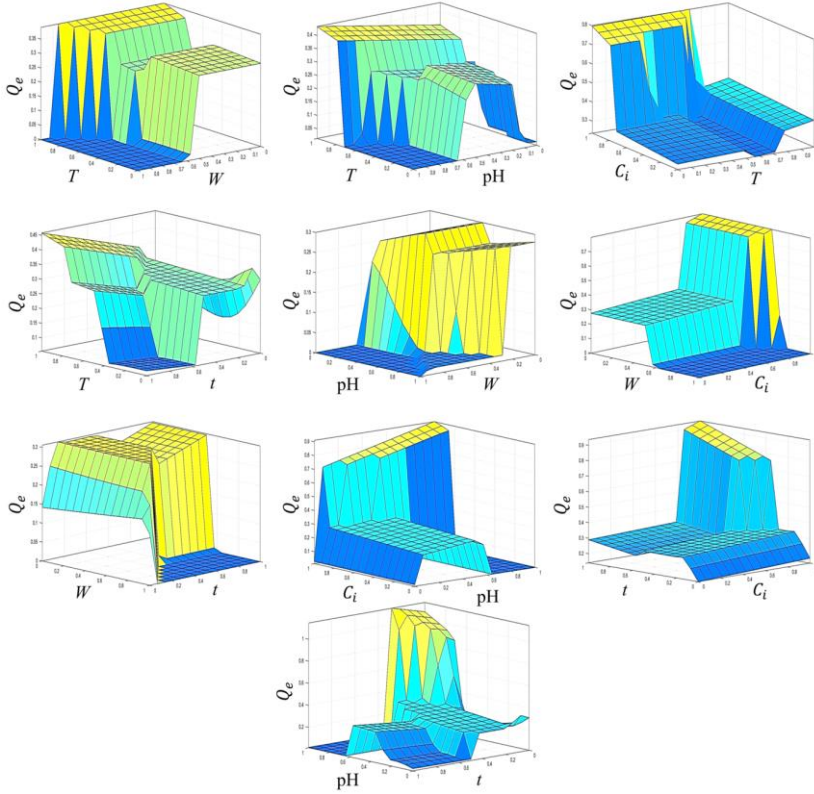


**Fig. 51.** Input-output surfaces of the ANFIS model for the MSMC-GO-MGH-MG composite.



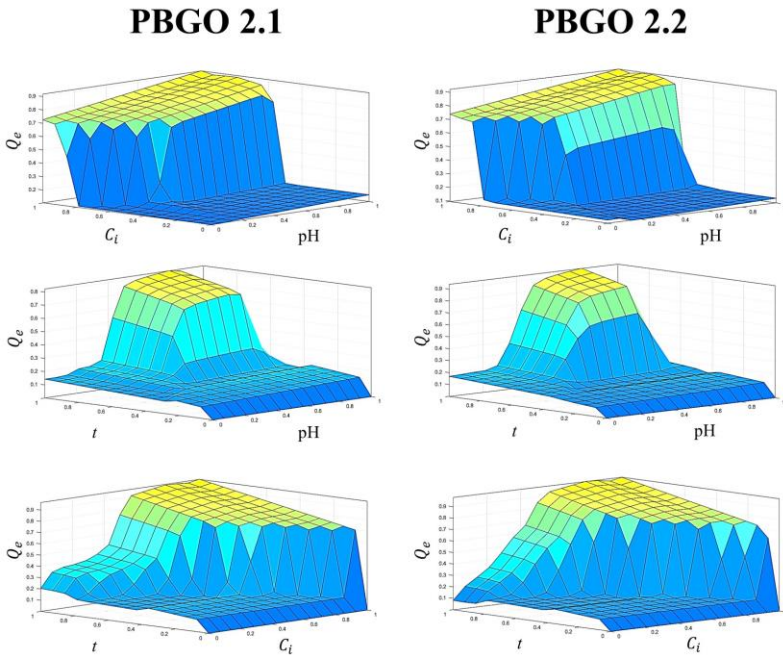


**Fig. 52.** Input-output surfaces of the ANFIS model for the PBGO composites.

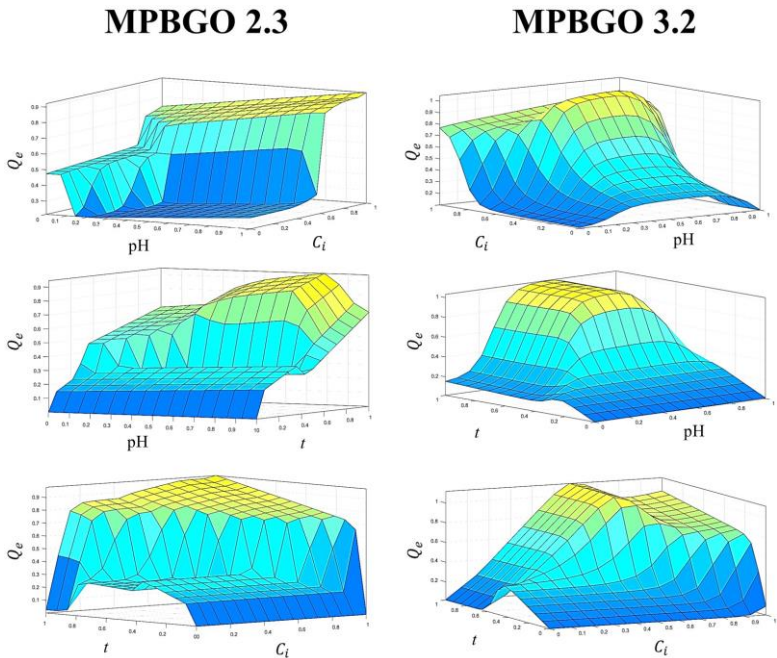


**Fig. 53.** Input-output surfaces of the ANFIS model for the MPBGO composites.

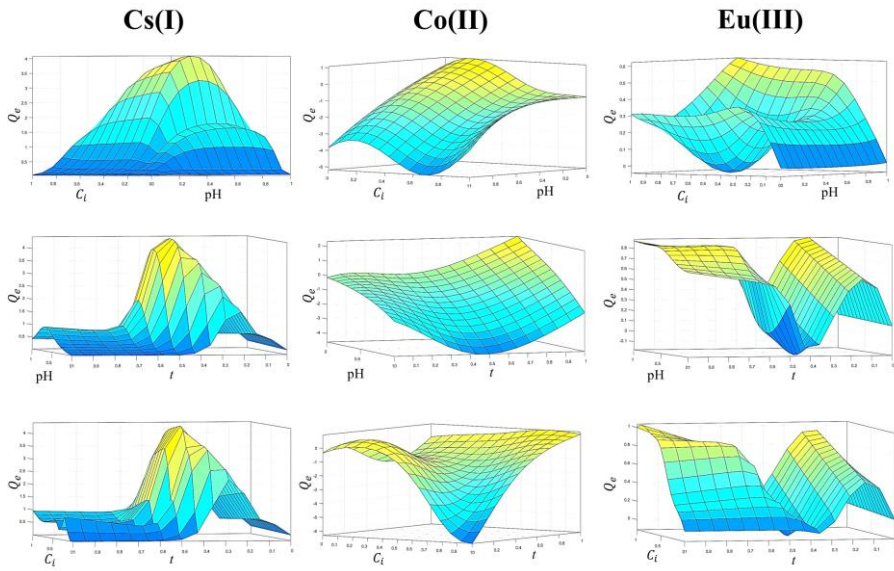


**Fig. 54.** Input-output surfaces of the ANFIS model for the CS-MSMC composite.

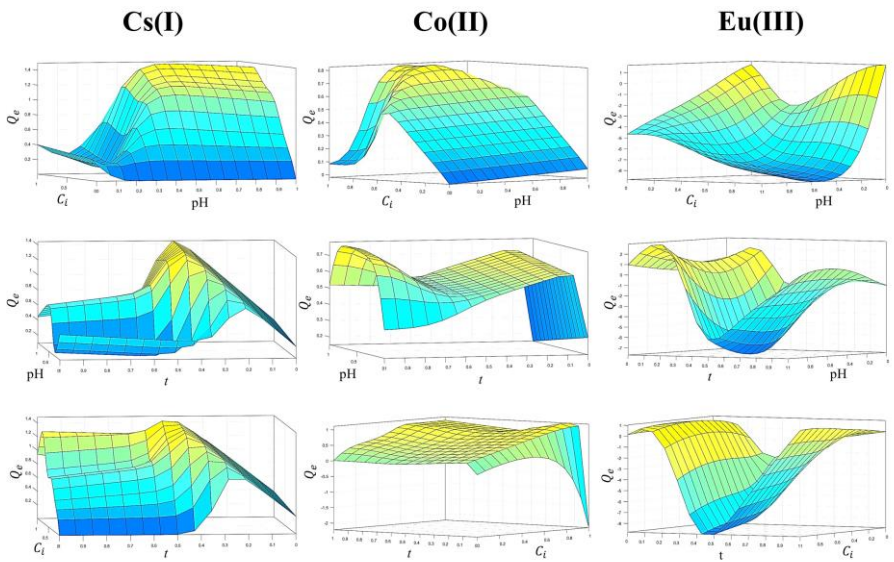


**Fig. 55.** Input-output surfaces of the ANFIS model for the CS-MSMC-GLUT composite.

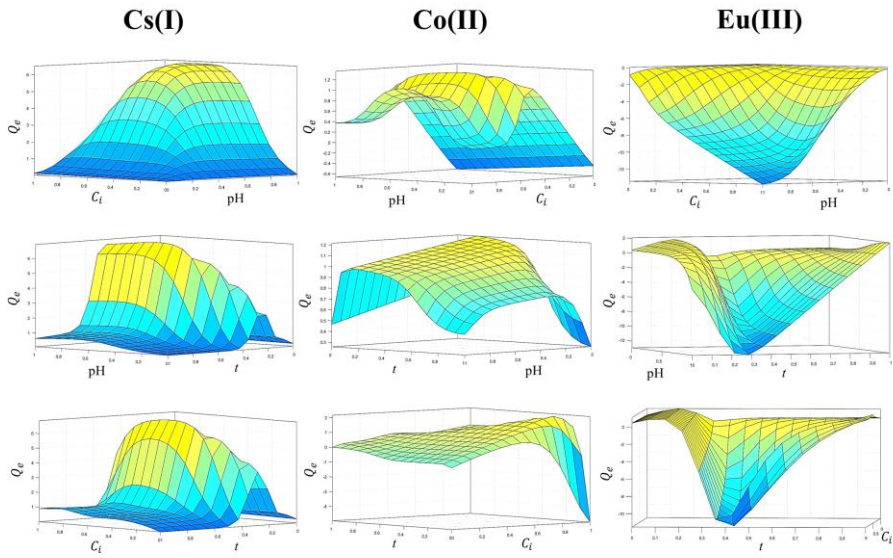


**Fig. 56.** Input-output surfaces of the ANFIS model for the CS-MSMC-ECH composite.

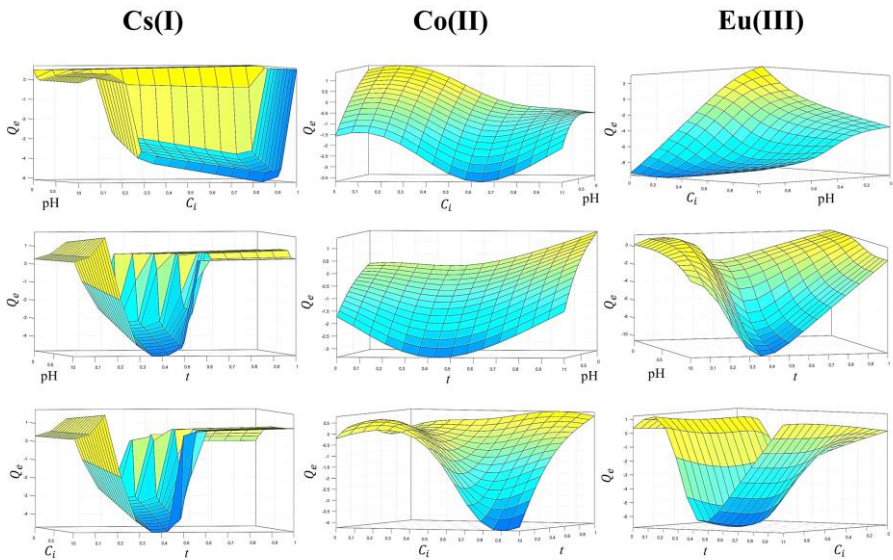


**Fig. 57.** Input-output surfaces of the ANFIS model for the CS-MSMC-STP composite.



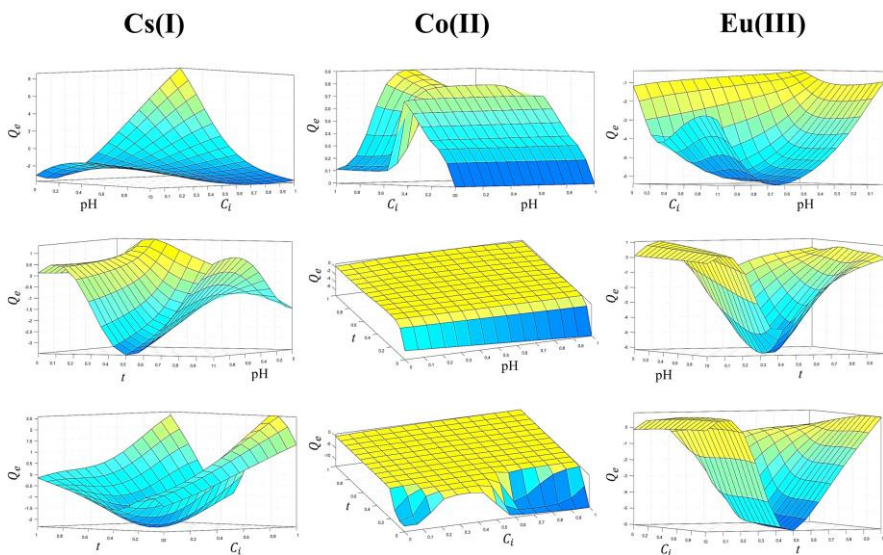


**Fig. 58.** Input-output surfaces of the ANFIS model for the CS-Mt-GLY composite.

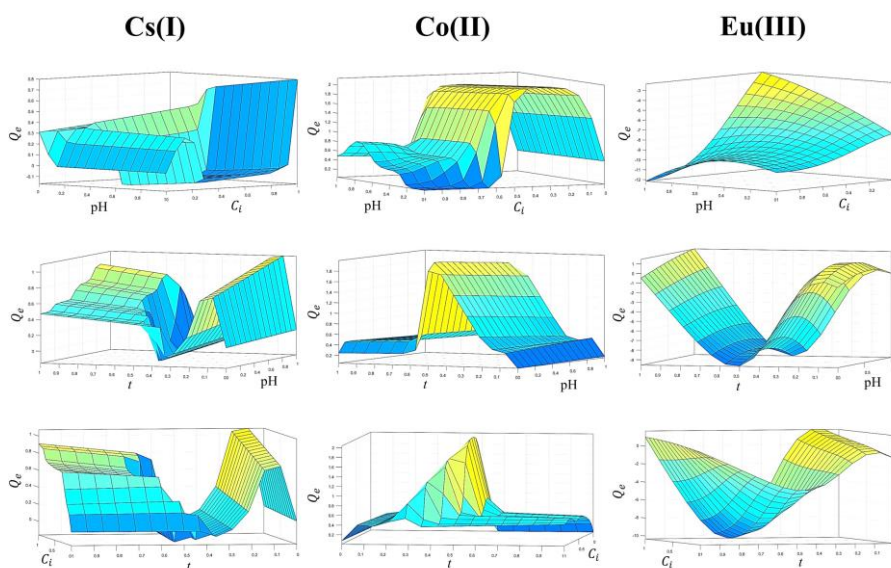


**Fig. 59.** Input-output surfaces of the ANFIS model for the CS-Zeo composite.

ANFIS thus allows one to work with small datasets and has good performance and generalisation ability. The obtained prediction data are close to the experimental data and according to the 3D surface modelling, the behaviour of the adsorbate on the adsorbents is complex and non-linear.

Furthermore, the trained ANFIS can be used to predict the adsorption capacity of composites for ions as a function of pH, initial concentration, contact time, mass of adsorbent, and temperature.

## CONCLUSIONS

1. It was found that the composite MSMC-GO-MGH-MG-1 adsorbs caesium and cobalt ions equally effectively compared to the composite MSMC-GO-MGH-MG-2. Furthermore, the muscovite phase is more responsible for the adsorption of caesium ions, while the maghemite-magnetite phase is more responsible for the adsorption of cobalt ions.

2. The composite MSMC-GO-MGH-MG has a sufficiently high adsorption capacity for caesium (2286 mg/g) and cobalt (652 mg/g) ions. Composites based on graphene oxide 2 (PBGO 2.1 (678 mg/g), PBGO 2.2 (644 mg/g), and MPBGO 3.2 (774 mg/g)) absorb caesium better than composite based on graphene oxide 1 (MPBGO 2.3 (216 mg/g)). For caesium and cobalt ions, the composites CS-MSMC (1123 and 560 mg/g), CS-MSMC-ECH (1152 and 619 mg/g), and CS-Mt-GLY (1139 and 557 mg/g) showed the highest adsorption capacity, for europium ions CS-Zeo (9.89 mg/g).

3. Depending on the pH, the adsorption of caesium ions on all composites, with the exception of the composite MSMC-GO-MGH-MG, reached a maximum at pH 7–8. In the case of the composite MSMC-GO-MGH-MG, adsorption was stable over a pH range of 1–10. The adsorption of cobalt and europium on the composites reached a maximum at pH 5–6. Furthermore, the adsorption of europium on the composites CS-Zeo and CS-Mt-GLY was consistently high from pH of 5 and 6, respectively.

4. The equilibrium state at MSMC-GO-MGH-MG was reached for 40 and 60 min for caesium and cobalt ions, respectively, and for 240 min, equilibrium was reached in PBGO-Cs(I), MPBGO-Cs(I), and chitosan-mineral-Cs(I)/Co(II)/Eu(III) systems.

5. According to the results of the effects of the mass of the adsorbent, the maximum adsorption capacity for caesium and cobalt ions was achieved at a MSMC-GO-MGH-MG composite mass of 0.01 g. Thermodynamic studies showed that the adsorption of caesium and cobalt on the MSMC-GO-MGH-MG composite is physical in nature, non-spontaneous and spontaneous endothermic, respectively.

6. The Freundlich isotherm fits better the data for the systems MSMC-GO-MGH-MG-Cs(I)/Co(II), while the Langmuir isotherm fits better the data for the systems PBGO-Cs(I), MPBGO-Cs(I), and chitosan-mineral-Cs(I)/Co(II)/Eu(III). The pseudo-second-order kinetic model fits the data better for most systems, except for the systems CS-MSMC-ECH-Cs(I), CS-MSMC-STP-Cs(I), and CS-Zeo-Co(II), whose data fit the pseudo-first-order kinetic model better.

7. Based on experimental and literary data, the suggested mechanism for the adsorption of caesium and cobalt on MSMC-GO-MGH-MG and of caesium, cobalt, and europium on chitosan-mineral composites is ion exchange, complexation, and electrostatic attraction. The mechanism of caesium adsorption on PBGO and MPBGO composites is complexation, ion exchange, and ion trapping.

8. ANFIS trained on small datasets has good performance and generalisation ability and can be used to predict the adsorption capacity of composite materials. According to 3D surface modelling, the adsorption behaviour of ions on composite materials was complex and non-linear.

## SANTRAUKA

### ĮVADAS

Žmogaus sukeltos katastrofos, tokios kaip Černobylio ir Fukušimos-Daiči branduolinės elektrinės ir branduolinių ginklų bandymai, lėmė aplinkos taršą antropogeniniais radionuklidais (RN). Be to, šiuo metu galimas pavojus, susijęs su antropogeninių RN patekimu į aplinką, gali kilti dėl radioaktyviųjų atliekų kiekio padidėjimo dėl aktyvaus branduolinės energijos naudojimo ir dėl problemų, susijusių su laidojimu, pavyzdžiui, didelio radioaktyvumo radioaktyviųjų atliekų. Aktyvus branduolinės energijos, kaip ekologiško energijos šaltinio, naudojimas, ypač energetikos krizių akivaizdoje, susijęs su tuo, kad daugeliu atveju ji yra konkurencingesnė nei, pavyzdžiui, saulės ir vėjo energija (Jalali-Rad et al. 2004; Zhang et al. 2019; Masoudi et al. 2019; Zhidkin et al. 2020; Liu et al. 2022; Nian et al. 2022; Tong et al. 2023). Tarp RN vieni iš labiausiai paplitusių teršalų yra  $^{137}\text{Cs}$ ,  $^{60}\text{Co}$ ,  $^{152}\text{Eu}$  ir  $^{154}\text{Eu}$ .  $^{137}\text{Cs}$  susidaro dalijantis uranui.  $^{60}\text{Co}$  susidaro, kai metalinės branduolinių reaktorių konstrukcijos apšvitinamos neutronų spinduliuote.  $^{152}\text{Eu}$  ir  $^{154}\text{Eu}$  susidaro iš  $^{151}\text{Eu}$  ir  $^{153}\text{Eu}$  absorbuojant neutronus.  $^{137}\text{Cs}$ ,  $^{60}\text{Co}$ ,  $^{152}\text{Eu}$  ir  $^{154}\text{Eu}$  pusėjimo trukmė yra atitinkamai 30,17, 5,27, 13,5 ir 8,6 metų. Šie RN yra vieni iš toksiškų teršalų, kurie taip pat yra kancerogeniniai (IAEA 1963; Directive 1966; Carter et al. 1993; Jalali-Rad et al. 2004; Peterson et al. 2007; Fazal-ur-Rehman and Akram 2017; Vanhoudt et al. 2018; Garty et al. 2020; Wang et al. 2022; Tong et al. 2023; Xiong et al. 2023). Neradioaktyviųjų kobalto ir europio formų antropogeninio koncentracijų padidėjimas aplinkoje rezultatas – aktyvus jų naudojimas pramonėje. Pavyzdžiui, kobaltas naudojamas elektronikos, kasybos, lydinių, katalizatorių, pigmentų, sodininkystės ir plieno pramonėje, o europis – elektronikos pramonėje, pavyzdžiui, liuminescencinėse lempose, šviesos dioduose, nešiojamuosiuose belaidžiuose prietaisuose, išmaniuosiuose telefonuose, optiniuose pluoštuose ir plokščiuose ekranuose. Kalbant apie neradioaktyvųjį cezį, jo komercinis naudojimas yra ribotas dėl didelio reaktyvumo ir jis daugiausia naudojamas kaip likutinių dujų priemaišų surinktuvas vakuuminiuose vamzdžiuose, cezio jodidas ir fluoridas scintiliaciniuose skaitikliuose (ATSDR 2004; Rim et al. 2013; Liang et al. 2014; Ramos et al. 2016; Rzetala 2016; Yang et al. 2016c; Henriques et al. 2021; Montes de Oca-Palma et al. 2021). Skirtingai nei radioaktyviosios cezio, kobalto ir europio formos, neradioaktyviosios formos yra mažiau toksiškos, tačiau jų per didelis poveikis turi neigiamą poveikį aplinkai ir žmonių sveikatai (Domingo 1989; ATSDR 2004, 2023; Ramos et al. 2016; Leysens et al. 2017; Henriques et al. 2021).



Siekiant apsaugoti aplinką nuo taršos RN ir metalais poveikio, taikomi įvairūs šalinimo metodai, tokie kaip jonų mainai, adsorbicija, ekstrakcija tirpikliais, koaguliacija, atvirkštinė osmozė ir elektrodinis nusodinimas (Ca and Cox 2004; Bruggeman and Maes 2010; Newsome et al. 2015; Yu et al. 2019). Be to, adsorbicija pasirodė esanti perspektyviausias RN ir metalų šalinimo metodas dėl didelio efektyvumo, nedidelių sąnaudų ir paprastumo (Li et al. 2014; Yang et al. 2016b; Wang et al. 2020).

Šiuo metu vis daugiau dėmesio skiriama labai veiksmingų, aplinkai nekenksmingų adsorbentų, kurių pagrindą sudaro natūralios medžiagos dėl jų mažo toksiškumo, gamybai. Šios medžiagos yra, pavyzdžiui, silikatiniai mineralai (bentonitas, montmorilonitas, vermikulitas, illitas, muskovitas, biotitas, ceolitai, flogopitas ir t. t.), alginatas ir chitozanas (Macht et al. 2011; Uddin 2017; Ohkubo et al. 2018; Hong et al. 2019; Brix et al. 2019; Falyouna et al. 2020; Wu et al. 2020; Liu et al. 2021, 2023; Sutirman et al. 2021; Biswas et al. 2021; Gendy et al. 2021; Latrille and Bildstein 2022; Novikau and Lujaniene 2022; Ewis et al. 2022). Taip pat labai paklausios yra pigios medžiagos, tokios kaip magnetitas, maghemitas, feritai, Berlyno mėlis, ir kelių atomų sluoksnių storio nanomedžiagos, pavyzdžiui, polimerų nanolapai, grafeno oksidas, sluoksniuotieji dvigubi hidroksidai ir kt, dėl jų labai reaktyvių sričių ir didelio savitojo paviršiaus ploto (Yong et al. 2014; Modi et al. 2015; Jang et al. 2015; Liu et al. 2021, 2023; Novikau and Lujaniene 2022; Wani et al. 2022; Wang et al. 2023). Silikatiniai mineralai, chitozanas, magnetitas, maghemitas, Berlyno mėlis ir grafeno oksidas yra perspektyvūs RN ir metalų adsorbentai. Jie dažnai modifikuojami, derinami tarpusavyje arba su kitais potencialiais adsorbentais, siekiant padidinti naudojimo efektyvumą ir sumažinti šių medžiagų trūkumus (Romanchuk et al. 2013; Jang et al. 2015; Jang and Lee 2016, 2018; Thakur et al. 2016; Xu et al. 2016, 2019; Kuzenkova et al. 2020; Boulanger et al. 2020, 2022; Biswas et al. 2021; Abukhadra et al. 2021).

Turimi cezio jonų adsorbicijos tyrimai buvo atlikti su šiais adsorbentais: biotitas (Mukai et al. 2018), amoniu padengtu montmorilonito- $\text{Fe}_3\text{O}_4$  kompozitu (Zheng et al. 2017), magnetiniu Berlyno mėlu (Yang et al. 2016a), muskovitu (Cornell 1993; McKinley et al. 2004; Kwong-Moses et al. 2020), magnetinio Berlyno mėlio šerdies/apvalkalo nanodalelėmis (Chang et al. 2016), viskozės pluoštai padengti chitozanu su įmobilizuotais Berlyno mėlynojo dalelėmis (Dechojarassri et al. 2017), geležies pagrindo ceolito nanodalelės (Eljamal et al. 2019), Berlyno mėlio analogai, įtvirtinti ant 3D redukuoto grafeno oksido aerogelio (Huo et al. 2021), nanostruktūrizuotas chitozanas/molekulinis sietas-4A (Goyal et al. 2020), pluoštinis chitozanas, modifikuotas metalų heksacianoferatais (Zhuang et al. 2022), magnetinis

Berlyno mėlis/grafeno oksidas (Yang et al. 2014), montmorilonito-Berlyno mėlio hibridas (Alamudy and Cho 2018), magnetinis ceolitas (Falyouna et al. 2020), chitozanu dengtas porėtas vermikulitas su mažu išsiplėtimu (Zhang et al. 2021) ir magnetinis bentonitas-chitozanas (Wang et al. 2019).

Tyrimai su kobalto jonai: grafeno oksido-magnetito (Tayyebi et al. 2015), magnetinio chitozано/aktyviosios anglies@UiO-66 (Motaghi et al. 2022), chitozanas su įterpta maleino rūgštimi (Zhuang et al. 2018), magnetinių cianoetil chitozано granulių (Zhang et al. 2020c), magnetinio grafeno oksido/chitozано (Zhuang and Wang 2019), chitozано (Khan et al. 2022) ir chitozано-montmorilonito kompozitai (Wang et al. 2014).

Tyrimai su europio jonais (pastaba: adsorbcijos tyrimuose jie naudojami kaip trivalentinių aktinidų analogas (Shao et al. 2009; Kapnisti et al. 2018; Zheng et al. 2020)) ant: muskovitas (Pan et al. 2017; Wu et al. 2021), magnetiniu amidoksimu funkcionalizuotu MCM-41 (Liu et al. 2022), flogopitas (Wu et al. 2021), granitas (Li et al. 2019), natrio dodecilsulfatu modifikuotu molibdeno disulfidu (Wang et al. 2020), grafeno oksidas dekoruotas magnetitu (Li et al. 2014), NKF-6 ceolitas (Khan et al. 2021), ceolitas Socony Mobil-5 (Shao et al. 2009), magnetito nanodalelės (Carvalho et al. 2016), titanato nanovamzdeliai (Zheng et al. 2020), sintetinis maghemitas (Xu et al. 2016), chitozanas (Cadogan et al. 2014) ir *Saccharomyces cerevisiae*, imobilizuotas glutaraldehidu susietame chitozane (Arunraj et al. 2019).

Nors atlikta daug Cs(I), Co(II) ir Eu(III) adsorbcijos ant įvairių adsorbentų tyrimų, Cs(I) ir Co(II) adsorbcijos ant MSMC-GO-MGH-MG kompozito tyrimų nerasta, o taip pat Cs(I), Co(II) ir Eu(III) ant CS-MSMC, CS-MSMC-GLUT, CS-MSMC-ECH, CS-MSMC-STP, CS-Mt-GLY ir CS-Zeo kompozitų nerasta. Be to, turimi šių kompozitų analogai, pavyzdžiui, chitozано-montmoriljonito/bentonito/kaolinito, pasižymi gera adsorbcijos talpa ir geru efektyvumu įvairiems dažikliams ir sunkiesiems metalams (Biswas et al. 2021), o naujausiame Esmaeili and Tamjidi (2020) darbe gautas montmoriljonito-grafeno oksido-magnetito kompozitas, palyginus su originaliu montmoriljonitu ir magnetito-montmoriljonitu, pasižymėjo dideliu šešiavalenčio chromo šalinimo efektyvumu. Nors jau yra atlikta darbų apie cezio adsorbciją ant magnetinio-Berlyno mėlio ir magnetinio-Berlyno mėlio grafeno oksido, šiame darbe pateikiama informacija apie naujų metodų taikymą sintetinant šiuos kompozitus, siekiant padidinti jų adsorbcinį pajėgumą.

Šiuo metu adsorbcijos tyrimuose aktyviai naudojamas mašininis mokymasis. Jis leidžia prognozuoti adsorbcijos talpą arba adsorbentų efektyvumą kaip įvairių sąlygų (pH, kontakto laiko, pradinės koncentracijos

ir kt.) funkcija, o tai savo ruožtu naudinga vėliau planuojant eksperimentus, taupant laiką ir reagentų sąnaudas. Dažniausiai taikomi modeliavimo metodai yra atsako paviršiaus metodologija, dirbtinis neuroninis tinklas, neuronų bendrasis regresijos tinklas ir adaptyvioji „neuro-fuzzy“ išvadų sistema, iš kurių geriausias prognozavimo rezultatas gaunamas taikant ANFIS. ANFIS yra galingas įrankis netiesiniams pokyčiams sudėtingose sistemose, tokiose kaip adsorbentas-adsorbatas, aprašyti; tai daugiapakopis tinklas, kurio principas – analizuoti pagal „fuzzy if-then“ taisyklių rinkinį ir sukurti numatytas įvesties-išvesties poras. ANFIS apjungia dirbtinių neuronų tinklų metodus ir „fuzzy“ logiką (Amiri et al. 2013; Rezaei et al. 2017; Mendoza-Castillo et al. 2018; Dolatabadi et al. 2018; Souza et al. 2018; Sadeghizadeh et al. 2019; Foroutan et al. 2020; Khomeyrani et al. 2021; Onu et al. 2021). Anksčiau ANFIS buvo naudojamas šioms sistemoms: tropinių dirvožemių-Cu(II)/Cd(II)/Pb(II) (Agbaogun et al. 2022), funkcionalizuoto bentonito-Pb(II)/As(V) (Lingamdinne et al. 2023), stručio kaulų pelenų-Pb(II) (Amiri et al. 2013), X ir Y faujasito ceolitai-metanas (Rezaei et al. 2017), aktyvinta anglis-Ni(II) (Souza et al. 2018), hidroksiapatitas/chitozanas-Pb(II) (Sadeghizadeh et al. 2019), chitozanas/molis/Fe<sub>3</sub>O<sub>4</sub>-Cr(VI) (Foroutan et al. 2020) ir Nteje molis-eriochromo juodasis-T (Onu et al. 2021). Tačiau nerasta darbų apie ANFIS taikymą sistemoms MSMC-GO-MGH-MG-Cs(I)/Co(II), chitozanas-mineralas-Cs(I)/Co(II)/Eu(III), PBGO-Cs(I) ir MPBGO-Cs(I).

## PAGRINDINIS TIKSLAS IR UŽDAVINIAI

Šio darbo tikslas – įvertinti muskovito žėručio molio-grafeno oksido-magemito-magnetito kompozito adsorbicijos savybes cezio ir kobalto jonams, Berlyno mėlio-grafeno oksido ir magnetito-Berlyno mėlio-grafeno oksido kompozitų adsorbicijos savybes ceziui ir chitozano-mineralinių kompozitų adsorbicijos savybes ceziui, kobaltui ir europiui, bei sukurti ANFIS modelį naudojant gautus eksperimentinių duomenų rinkinius. Tyrimo tikslams pasiekti buvo suformuluoti šie uždaviniai:

1. Susintetinti MSMC-GO-MGH-MG, PBGO, MPBGO, CS-MSMC, CS-MSMC-GLUT, CS-MSMC-ECH, CS-MSMC-STP, CS-Mt-GLY ir CS-Zeo kompozitus.
2. Apibūdinti gautus kompozitus.
3. Ištirti jonų adsorbiciją ant kompozitų atliekant – laboratorinius eksperimentus.
4. Išanalizuoti jonų adsorbicijos ant kompozitų elgseną naudojant adsorbicijos izotermas, kinetiką ir termodinamiką.
5. Ištirti jonų adsorbicijos ant kompozitų mechanizmą.

6. Pritaikyti ANFIS modelį kompozitų adsorbcijos gebai prognozuoti.

## NAUJUMAS

Kiek šiuo metu žinoma, kompozitas MSMC-GO-MGH-MG pirmą kartą buvo panaudotas cezio ir kobalto adsorbcijos tyrimams, o kompozitai CS-MSMC, CS-MSMC-GLUT, CS-MSMC-ECH, CS-MSMC-STP, CS-Mt-GLY ir CS-Zeo – ceziui, kobaltui ir europiui. Buvo sukurti ir panaudoti nauji PBGO ir MPBGO kompozitų, kaip cezio adsorbentų, sintezės būdai. Be to, sukurtas ANFIS modelis ir pirmą kartą pritaikytas sistemoms MSMC-GO-MGH-MG-Cs(I)/Co(II), PBGO-Cs(I), MPBGO-Cs(I) ir chitozano-mineralo-Cs(I)/Co(II)/Eu(III).

## GINAMIEJI TEIGINIAI

1. Kompozitas MSMC-GO-MGH-MG pasižymi dideliu Cs(I) ir Co(II) adsorbcijos pajėgumu. Siūlomas Cs(I) ir Co(II) adsorbcijos mechanizmas yra jonų mainai, kompleksavimas ir elektrostatinė trauka.

2. Kompozitai PBGO 2.1, PBGO 2.2 ir MPBGO 3.2 geriau adsorbuoja Cs(I) nei MPBGO 2.3. Siūlomas Cs(I) adsorbcijos mechanizmas yra kompleksacija, jonų mainai ir jonų pagava.

3. Chitozano-mineralų kompozitų kompozitai CS-MSMC, CS-MSMC-ECH ir CS-Mt-GLY turi didžiausią Cs(I) ir Co(II) adsorbcijos gebą, o kompozitas CS-Zeo – Eu(III) adsorbcijos gebą.

4. ANFIS pasižymi geru našumu ir apibendrinamuoju gebėjimu prognozuoti kompozitų adsorbcinį pajėgumą.

## AUTORIAUS INDĖLIS

Darbo autorius susintetino MSMC-GO-MGH-MG kompozitus, suplanavo ir atliko cezio bei kobalto adsorbcijos tyrimus laboratoriniuose eksperimentuose. Dalyvavo sintetinant chitozano-mineralų kompozitus, atliko adsorbcijos tyrimus, analizavo ir interpretavo rezultatus, kūrė grafines iliustracijas, rašė rankraščius bei pristatė rezultatus mokslinėse konferencijose.

## 4. EKSPERMENTO METODIKA

### 4.1. Kompozitų paruošimas

#### 4.1.1. Muskovito žėručio molio-grafeno oksido-magemito-magnetito kompozito paruošimas

Gamtiniame mėginyje iš Šaltiškių pramoninės žvalgyto vietos Šiaurės Lietuvoje yra įvairių mineralų, tame tarpe molio mineralų grupių, kur vyraujantys mineralai yra kvarcas ir muskovitas (pagal XRD), todėl šiam mėginiui suteiktas toks pavadinimas: muskovitinis žėručio molis. Muskovito žėručio molio mėginys buvo naudojamas be pirminio apdoravimo MSMC-GO-MGH-MG kompozitui ruošti. Grafeno oksidas gautas „Tour“ metodu (Marcano et al. 2010). Maghemitas-magnetitas gautas nusodinant divalenčius ir trivalenčius geležies jonus (Tayyebi et al. 2015). MSMC-GO-MGH-MG kompozitas buvo paruoštas sumaišant MSMC (4 g 200 ml Milli-Q vandens), MGH-MG (2 g 200 ml Milli-Q vandens) ir GO (0,06 g 60 ml Milli-Q vandens) suspensijas. Gauta kompozito (MSMC-GO-MGH-MG-1 (C-1)) masės procentinė dalis (masės %) buvo 65,36% MSMC (4 g), 32,68% MGH-MG (2 g) ir 1,96% GO (0,12 g). Be to, šiuo metodu buvo pagamintas ir kitas kompozitas (MSMC-GO-MGH-MG-2 (C-2)), tačiau su didesniu MGH-MG kiekiu, kurio masės procentinė dalis buvo 49,26% MSMC (4 g), 49,26% MGH-MG (4 g) ir 1,48% GO (0,12 g).

#### 4.1.2. Berlyno mėlio-grafeno oksido ir magnetito-Berlyno mėlio-grafeno oksido kompozitų paruošimas

Grafeno oksidas 1 ir 2 (GO 1 ir GO 2) buvo gauti „Hummers“ metodu (Hummers and Offeman 1958). Skirtumas tarp GO 1 ir GO 2 yra mišinio išlaikymo laikas po  $\text{KMnO}_4$  pridėjimo, kuris GO 1 atveju buvo 24 val., o GO 2 atveju – 72 val. Magnetitas gautas sumaišius 1 mol/l  $\text{FeSO}_4$ , 2 mol/l  $\text{Fe}_2(\text{SO}_4)_3$  ir 2 mol/l  $\text{H}_2\text{SO}_4$  tirpalus, po to lašinant 1 mol/l amoniako tirpalą. Magnetito dalelės buvo atskirtos magnetu, po to nuplautos  $\text{C}_3\text{H}_6\text{O}$  ir išdžiovintos.

Berlyno mėlis 1 ir 2 (PB 1 ir PB 2) buvo paruošti į 0,02 mol/l  $\text{Fe}_2(\text{SO}_4)_3$  ir  $\text{FeSO}_4$  tirpalus lašinant  $\text{K}_4[\text{Fe}(\text{CN})_6]$  ir  $\text{K}_3[\text{Fe}(\text{CN})_6]$  tirpalus. Gautos nuosėdos nuplautos dejonizuotu vandeniu iki  $\text{pH} \sim 7$  ir išdžiovintos. PBGO 2.1 ir PBGO 2.2 susintetinti naudojant GO 2,  $\text{FeSO}_4$  (0,02 mol/l),  $\text{K}_4[\text{Fe}(\text{CN})_6]$  PBGO 2.1 ir  $\text{K}_3[\text{Fe}(\text{CN})_6]$  PBGO 2.2. MPBGO 2.3 ir MPBGO 3.2 paruošti taip: magnetitas, disperguotas ultragarso vonioje, maišomas su GO 1 ir GO 2

suspensija santykiu 1:100 atitinkamai MPBGO 2.3 ir MPBGO 3.2 10 min. nuolat maišant, parūgštintas iki pH=3 su 10% H<sub>2</sub>SO<sub>4</sub> ir palaispniui pridėta FeSO<sub>4</sub>. Po 1 val. į suspensijas buvo lašinamas K<sub>4</sub>[Fe(CN)<sub>6</sub>] tirpalas. Gauti mišiniai buvo maišomi argono atmosferoje 1 val., tada nuosėdos atskirtos magnetu, nuplautos vandeniu ir išdžiovintos.

#### 4.1.3. Chitozano-mineralų kompozitų paruošimas

CS-MSMC kompozitui ruošti naudota smulkioji MSMC frakcija, kurios dalelių dydis 1–0,2 μm, kuri nuo pagrindinio mėginio buvo atskirta drėgnučiu sijojimu ir nusodinimu kolonėlėmis, centrifugavimo ir membraninio filtravimo metodais (Lujanienė et al. 2006; Lujanienė et al. 2015). Išskirta frakcija buvo aktyvuota 0,5 M HCl. Tada ši frakcija 1% CH<sub>3</sub>COOH tirpale buvo sumaišyta su 2% chitozano tirpalu 1% CH<sub>3</sub>COOH tirpale. Gautas CS-MSMC gelis nusodintas į gelio suspensiją lašinant 1 M NaOH ir C<sub>2</sub>H<sub>5</sub>OH mišinio tirpalą (1:1). Gelis nuplautas C<sub>2</sub>H<sub>5</sub>OH ir CH<sub>3</sub>CN tirpalais. CS-MSMC gelio suspensija palikta CH<sub>3</sub>CN keletą dienų. Prieš naudojant CS-MSMC, gelis (kompozitas) filtruojamas ir plaunamas dejonizuotu vandeniu iki neutralaus pH.

CS-MSMC-GLUT, CS-MSMC-ECH ir CS-MSMC-STP kompozitai paruošti sumaišius gautą CS-MSMC gelį su glutaraldehido (2,5% w/v) vandeniniu tirpalu, 1% (40 mM) epichlorhidrino tirpalu ir natrio tripolifosfato tirpalu (pH 8,2). CS-Mt-GLY buvo susintetintas pagal CS-MSMC kompozito paruošimo technologiją, kai į chitozano-CH<sub>3</sub>COOH tirpalą pirmiausia įdėta 1% masės plastifikatoriaus (glicerolio) ir tik po to jis sumaišytas su montmorilonitu 1% CH<sub>3</sub>COOH tirpale. CS-Zeo kompozitas paruoštas sumaišius ZSM-5 miltelius su 2% chitozano tirpalu 1% CH<sub>3</sub>COOH tirpale.

#### 4.2. Apibūdinimas

Kompozitų ir jų pirminių komponentų bandiniai charakterizuojami XRD, ATR-FTIR, FTIR, Ramano, XPS, Mösbauerio spektroskopijos, SEM ir TEM metodais.

#### 4.3. Sorbcijos eksperimentai

Laboratoriniais sorbcijos eksperimentais tiriama Cs(I) ir Co(II) adsorbicija ant MSMC-GO-MGH-MG kompozito. Cs(I) adsorbicija ant PBGO ir MPBGO kompozitų. Cs(I), Co(II) ir Eu(III) adsorbicija ant chitozano-mineralų kompozitų.

Buvo atlikti keli eksperimentai, priklausomai nuo pradinės koncentracijos, pH ir kontakto laiko:

MSMC-GO-MGH-MG pradinės Cs(I) ir Co(II) koncentracijos atitinkamai 394–12630 ir 100–3200 mg/l. Cs(I) ir Co(II) pH intervalas atitinkamai 1–10 ir 1–6. Cs(I) ir Co(II) kontakto trukmė buvo 5–240 min.

PBGO ir MPBGO kompozitams tirta pradinė Cs(I) koncentracija 50–800 mg/l. Cs(I) pH intervalas 3–9,5. Cs(I) kontakto laiko intervalas buvo 5–1440 min.

Tiriant chitozano-mineralų kompozitus, Cs(I), Co(II) ir Eu(III) pradinės koncentracijos atitinkamai 50–5000, 50–3000 ir 0,01–30 mg/l. Cs(I), Co(II) ir Eu(III) pH intervalas atitinkamai 3–9, 3–7 ir 3–7. Cs(I), Co(II) ir Eu(III) kontakto laiko intervalas 5–1440 min.

Taip pat atlikti papildomi MSMC-GO-MGH-MG-Cs(I)/Co(II) sistemų bandymai, priklausomai nuo adsorbento masės (0,01–0,16 g) ir temperatūros (25–75 °C).

Be pirmiau išvardytų kintamųjų parametru, kiti parametrai bandymų metu buvo pastovūs:

MSMC-GO-MGH-MG pradinė Cs(I) koncentracija yra 3158 mg/l, o Co(II) – 800 mg/l. Cs(I) pH – 7, o Co(II) – 5. Kontakto trukmė 1440 ir 60 min. tik dėl temperatūros poveikio. Adsorbento masė – 0,01 g. Temperatūra –  $20 \pm 1$  °C.

PBGO ir MPBGO kompozitų pradinė Cs(I) koncentracija yra 200 mg/l (pH poveikio atveju) ir 100 mg/l (kontakto laiko poveikio atveju). pH vertė yra 7. Kontakto trukmė – 1440 min. Adsorbento masė yra 0,01 ir 0,005 g (tik pradinės koncentracijos poveikiui patikrinti). Temperatūra – 25 °C.

Chitozano-mineralų kompozitų pradinė koncentracija yra tokia: Cs(I) – 3000 mg/l, Co(II) – 3000 mg/l (pH poveikio atveju) ir 1000 mg/l (kontakto laiko poveikio atveju), o Eu(III) – 20 mg/l. Cs(I) pH yra 7, Co(II) – 5, o Eu(III) – 5. Kontakto laikas – 1440 min. Adsorbento masė – 0,01 g. Temperatūra – 25 °C.

Pirminiai MSMC, GO, MGH-MG, MSMC-GO-MGH-MG-1 ir -2 cezio ir kobalto jonų adsorbicijos tyrimai buvo atlikti tokiomis sąlygomis: pradinė jonų koncentracija – 50 mg/l, pH(Cs(I))=7, pH(Co(II))=5, adsorbento masė – 0,01 g, temperatūra –  $20 \pm 1$  °C, kontakto trukmė – 1440 min.

Pradiniai tirpalai paruošti iš Milli-Q vandens ir analitinės klasės CsCl, Co(NO<sub>3</sub>)<sub>2</sub>·6H<sub>2</sub>O (tik MSMC-GO-MGH-MG tyrimų atveju), CoCl<sub>2</sub> ir EuCl<sub>3</sub>. Adsorbicijos bandymai atliekami 15 ml polipropileno centrifuginiuose mėgintuvėliuose (CLEARLine), kurių darbinis tūris 10 ml, o kratymo greitis – 150–200 aps/min. Eksperimentuose naudojami CsCl, Co(NO<sub>3</sub>)<sub>2</sub>·6H<sub>2</sub>O/CoCl<sub>2</sub> ir EuCl<sub>3</sub> tirpalai ir <sup>137</sup>Cs, <sup>60</sup>Co ir <sup>152</sup>Eu žymekliai.

Pradinis tirpalų pH buvo koreguojamas HCl ir NaOH. Po adsorbcijos bandymų adsorbentai atskirti nuo tirpalo 15 min. centrifuguojant 20000 G greičiu arba magnetu. Vėliau Cs, Co ir Eu aktyvumo koncentracijos tirpale matuojamos gama spektrometrijos metodu, naudojant HPGe detektorius.

#### 4.4. Adsorbcijos izotermos, kinetika ir termodinamika

Tiesinės ir netiesinės Langmuiro ir Freundlichio izotermos, naudojamos kompozito-Cs(I)/Co(II)/Eu(III) sistemų pusiausvyrai aprašyti. Reakcijos greičiui įvertinti ir adsorbcijos proceso pobūdžiui (fizikiniam, cheminiam ar mišriam) nustatyti naudojami tiesiniai ir netiesiniai pseudo-pirmosios eilės kinetiniai modeliai, bei pseudo-antrosios eilės kinetiniai modeliai. Adsorbato ir adsorbento sąveikos su adsorbentu spontaniškumui ir pobūdžiui paaiškinti naudojami pagrindiniai termodinaminiai parametrai: Gibso laisvosios energijos pokytis ( $\Delta G^\circ$ ), entalpijos pokytis ( $\Delta H^\circ$ ) ir entropijos pokytis ( $\Delta S^\circ$ ) (Inyinbor et al. 2016; Mohseni-Bandpei et al. 2020; Esmaeili and Tamjidi 2020).

#### 4.5. ANFIS taikymas

Daugiasluoksniė ANFIS architektūra kompozitinėms-Cs(I)/Co(II)/Eu(III) sistemoms buvo įgyvendinta MATLAB R2021a (Fuzzy Logic Toolbox (Sugeno tipo)). Neuroninio tinklo mokymas atliktas 21 (MSMC-GO-MGH-MG-Cs(I)/Co(II)), 18 (PBGO 2.2-Cs(I), MPBGO 2.3-Cs(I), MPBGO 3.2-Cs(I) ir chitozano-mineralo-Cs(I)), 17 (chitozano-mineralo-Co(II) ir 16 (PBGO 2.1-Cs(I) ir chitozano-mineralo-Eu(III)) duomenų rinkinių. Gauso funkcijų (Gaussmf2) panaudojimas su subtraciniu klasterizavimu, hibridinio modeliavimo optimizavimo metodu (Souza et al. 2018), paklaidos tolerancija 0 ir epochų 100 iteracijų. Tinklo testavimas atliktas su 12 (PBGO 2.1 ir 2.2-Cs(I) ir MPBGO 2.3 ir 3.2-Cs(I)), 10 (MSMC-GO-MGH-MG-Cs(I)/Co(II)) ir 5 (chitozano-mineralo-Cs(I)/Co(II)/Eu(III)) duomenų rinkiniais. Be to, mokymo ir testavimo duomenys parinkti atsitiktinai, o įvesties ir išvesties kintamieji prieš įvedant į tinklą normalizuoti nuo 0 iki 1. Siekiant įvertinti tinklo našumą ir apibendrinimo gebėjimą, klaidų analizė atlikta naudojant koreliacijos koeficientą (R), vidutinę kvadratinę paklaidą (MSE), kvadratinių paklaidų sumą (SSE) ir vidutinę santykinę paklaidą (ARE).



## 5. TYRIMO REZULTATAI IR JŲ APTARIMAS

### 5.1. Medžiagos apibūdinimas

#### 5.1.1. XRD

XRD analizės rezultatai rodo, kad MSMC-GO-MGH-MG-1 ir -2 kompozituose yra šios fazės: kvarcas (ICDD # 00-046-1045), muskovitas (ICDD # 01-089-7536), maghemitas-magnetitas ((ICDD # 00-039-1346)-(ICDD # 01-084-9337)), dolomitas (ICDD # 04-012-1195), klinochloras (ICDD # 04-013-2805), kalcitas (ICDD # 01-083-4602), kaolinitas (ICDD # 01-074-1784) ir montmorilonitas (ICDD # 00-013-0135). Grafeno oksidui būdinga smailė ties  $2\theta=10,6^\circ$  nebuvo aptikta, matyt, dėl grafeno oksido sluoksnių atsiskyrimo įvedus MSMC sluoksnius (Ye et al. 2019). Be to, kompozite MSMC-GO-MGH-MG-1 dominuoja muskovito ir MGH-MG fazės, o kompozite MSMC-GO-MGH-MG-2 – MGH-MG fazė. Palyginus muskovito ir MGH-MG fazių procentinę dalį tarp kompozitų, matyti, kad kompozite MSMC-GO-MGH-MG-2 MGH-MG kiekis yra 2,3 karto didesnis nei kompozite MSMC-GO-MGH-MG-1, o muskovito kiekis yra 2,2 karto mažesnis. MPBGO 3.2 kompozite rasta 10 nm dydžio Berlyno mėlynojo dalelių (ICDD # 01-074-9174) ir 8 nm dydžio magnetito dalelių (ICDD # 01-084-9337). Nebuvo aptikta grafeno oksidui būdingos smailės ties  $2\theta=9,8^\circ$ , galbūt dėl GO lakštų persidengimo su magnetito ir Berlyno mėlynumo dalelėmis. GO 2 (MPBGO 3.2 atveju) ir GO (MSMC-GO-MGH-MG-1 ir -2 atveju) būdingos smailės išsidėstymas mažų  $2\theta$  kampo verčių intervale rodo aukštą jų oksidacijos laipsnį (Krishnamoorthy et al. 2013). Chitozano-mineralų kompozitų XRD spektruose pastebėta, kad pirminių komponentų difrakcinės smailės, lyginant su pirminėmis sudedamųjų dalių XRD spektais, turi nemažai pakitimų. Iš to galima priėti prie išvados, kad esami pokyčiai rodo chitozano išsidėstymą tarp mineralinių sluoksnių ir (arba) jų paviršiuje (Luo et al. 2015; Biswas et al. 2021; Abukhadra et al. 2021).

#### 5.1.2. ATR-FTIR ir FTIR

Kompozito MSMC-GO-MGH-MG spektre (čia ir tolesniuose apibūdinimo rezultatuose tai MSMC-GO-MGH-MG-1) identifikuotos MSMC juostos, bet ne MGH-MG ir GO, matyt, dėl to, kad jų juostos sutampa su MSMC juostomis. Tačiau pastebėtas charakteringų MSMC juostų pasislinkimas  $2-4\text{ cm}^{-1}$ , palyginti su pradinėmis 415, 512, 795, 872, 915 ir  $989\text{ cm}^{-1}$  juostomis, rodo, kad MGH-MG ir GO paveikė MSMC struktūrą. Po

Cs(I) ir Co(II) adsorbcijos pastebėti kompozito spektrų pokyčiai gali rodyti jų sąveiką atitinkamai su Si–O–Si, Al–O–Si/Fe–O, Fe–O–Si/Fe–O–Al, Al–OH–Al ir Si–O–Si, Si–O, C–O/C–OH. Pastebėti chitozano-mineralų kompozitų juostų pokyčiai, lyginant su pradinėmis juostomis, priskirtomis chitozanui ir mineralams, rodo, kad jie gali sąveikauti per vandenilinį ryšį arba elektrostatinę trauką (DeLuca and DeLuca 1997; Tan et al. 2008; Sides et al. 2009; Paluszkiewicz et al. 2011; Brigatti et al. 2013; Pereira et al. 2017; Laaraibi et al. 2018; Siddiqui et al. 2019). Be to, chitozanui būdingų juostų pokyčiai CS-MSMC-GLUT, CS-MSMC-ECH, CS-MSMC-STP ir CS-Mt-GLY atveju taip pat gali rodyti sąveiką su skersinio ryšio medžiagomis arba plastifikatoriumi (Li et al. 2013, 2015; Loutfy et al. 2016; Chen et al. 2020; Smith et al. 2021). Po Cs(I), Co(II) ir Eu(III) adsorbcijos pastebėti gausūs kompozitų būdingų juostų pokyčiai rodo galimą jų sąveiką, daugeliu atveju su kompozitų –OH, –NH<sub>2</sub>, Si–O–Si, Si–O ir Al–O(H)–Al grupėmis. PBGO ir MPBGO kompozitų, bei jų pirminių komponentų FTIR rezultatai rodo, kad GO 2 yra labiau oksiduotas nei GO 1. Kompozituose rasta atitinkamų PB arba M ir PB juostų. Tačiau mažas grafeno oksido juostų intensyvumas arba jų nebuvimas kompozitų spektruose gali būti susijęs su grafeno oksido redukcija ir (arba) jo slopinimu magnetito-Berlyno mėlio arba Berlyno mėlio dalelėmis (Azhar et al. 2019). Be to, pastebėti skirtumai tarp MPBGO 2.3 ir 3.2 spektrų rodo jų struktūrinius skirtumus.

### 5.1.3. Ramano spektroskopija

Ramano spektroskopija parodė, kad PBGO ir MPBGO kompozitų spektruose D ir G juostų intensyvumo santykis ( $I_D/I_G$ ) padidėjo, palyginus su grafeno oksidu 2.  $I_D/I_G$  padidėjimas reiškia GO defektų tankio padidėjimą ir grafeno oksido sumažėjimą iki redukuoto grafeno oksido (Jang et al. 2015). Todėl mažėja deguonies turinčių funkcinių grupių kiekis (López-Díaz et al. 2017), o tai rodo didelį grafeno oksido 2 paviršiaus modifikavimo laipsnį magnetito-Berlyno mėlynojo arba Berlyno mėlio dalelėmis.

### 5.1.4. XPS

Remiantis XPS analizės rezultatais, MSMC-GO-MGH-MG kompozito plačiame spektre yra smailės, priskiriamos Al2p, Si2p, C1s, K2p, Ca2p, O1s ir Fe2p, o po jonų adsorbcijos – smailės, priskiriamos Cs3d ir Co2p. Kompozito charakteringuose spektruose pastebėti smailės jungimosi energijų ir intensyvumo pokyčiai rodo Cs(I) sąveiką su Fe<sup>2+</sup>, Fe<sup>3+</sup>, metalų oksidais, Al–OH, Si–O–Si, C–OH/C–O–C, C–O, C=O ir O=C–O. Co(II) su Fe<sup>3+</sup>, metalų

oksidais, Si–O–Si, SiO<sub>2</sub>, C–OH/C–O–C, C–O, C=O ir O=C–O. Be to, jonų mainai su K<sup>+</sup> tikriausiai vyksta muskovito PS ir FES, Cs(I) atveju ir Co(II) atveju tik PS. Po Co(II) adsorbcijos aptikta Co–Al jungtis, matomai susidariusi dėl kompleksacijos su Al–OH (Ogwada and Sparks 1986; Fan et al. 2014; Penke et al. 2017; Woodward et al. 2018).

#### 5.1.5. Mösbauerio spektroskopija

Mösbauerio spektroskopijos rezultatai rodo, kad MSMC-GO-MGH-MG kompozito sudėtyje yra magemito-magnetito fazė, o PBGO ir MPBGO kompozituose – atitinkamai Berlyno mėlio ir magnetito-Berlyno mėlio fazės. Magnetinių dalelių dydis MSMC-GO-MGH-MG kompozite yra ~14–15 nm, o MPBGO kompozite – ~13 nm.

#### 5.1.6. SEM ir TEM

Pagal SEM vaizdus matyti, kad kompozitas MSMC-GO-MGH-MG turi sluoksniuotą struktūrą, kurioje grafeno oksido lakštai ir muskovito žėručio molio sluoksniai dengia vienas kitą, o magemito-magnetito dalelės gana tolygiai pasiskirsčiusios kompozito paviršiuje ir tarp sluoksnių. Kompozituose CS-MSMC ir CS-Mt-GLY chitozono sluoksniai persidengia su muskovito žėručio molio ir montmorilonito sluoksniais. Kompozitą CS-Zeo sudaro ceolito fragmentai, integruoti į chitozono paviršių. Chitozono-mineralų kompozitų paviršius yra sulankstytas. Pagal TEM vaizdus MPBGO kompozitai sudaryti iš grafeno oksido lakštų, kurių paviršiuje pasiskirsčiusios magnetito ir Berlyno mėlio dalelės. MPBGO 2.3 atveju Berlyno mėlynojo dalelės yra ne kūgio formos su užapvalintais kraštais, o MPBGO 3.2 atveju Berlyno mėlynojo dalelės yra aiškiai apibrėžtos kubinės struktūros, o jų dydis yra nuo 5 iki 20 nm. Be to, MPBGO 3.2 kompozito grafeno oksido lakštai yra geriau padengti magnetito-Berlyno mėlynojo dalelėmis nei MPBGO 2.3 atveju.

## 5.2. MSMC-GO-MGH-MG kompozitų ir originalių komponentų pirminės adsorbcijos tyrimai

Remiantis XRD ir pirminės adsorbcijos tyrimų rezultatais, nustatyta, kad vienodas muskovito (labiau atsakingo už Cs(I) adsorbciją) ir magemito-magnetito (labiau atsakingo už Co(II) adsorbciją) fazių kiekis kompozite MSMC-GO-MGH-MG-1 yra optimalus vienodai veiksmingai tiriamų jonų adsorbcijai, palyginus su kompozitu MSMC-GO-MGH-MG-2, o adsorbcijos gebos skirtumas, lyginant su originaliaisiais MSMC ir GO, yra nereikšmingas tik MGH-MG atveju, kurio adsorbcijos geba yra gerokai mažesnė nei kompozito MSMC-GO-MGH-MG-1. Todėl tolesniems adsorbcijos tyrimams pasirinktas kompozitas MSMC-GO-MGH-MG-1.

## 5.3. Adsorbcijos tyrimai, izotermos, kinetika ir siūlomas adsorbcijos mechanizmas

Nustatyta, kad MSMC-GO-MGH-MG kompozitas nepasiekė soties Cs(I) ir Co(II) atžvilgiu (Pav. 60a), o pusiausvyros būseną pasiekia atitinkamai per 40 ir 60 min. (Pav. 61a). Didžiausia eksperimentinė MSMC-GO-MGH-MG kompozito adsorbcijos talpa 2286 ir 652 mg/g atitinkamai Cs(I) ir Co(II) jonams. Tokius didelius adsorbcijos greičius lemia didelis skirtingų funkcinių grupių skaičius dėl kompozitinės matricos sudėtingumo. Be to, Cs(I) adsorbcija ant kompozito nepriklausė nuo pH, o tai rodo, kad vyksta jonų mainų procesai (Lujanienė et al. 2010; Zhang et al. 2020a). Kita vertus, kobalto adsorbcija didėjant pH didėja ir pasiekia maksimumą esant pH=5 (Pav. 62a). Didėjant MSMC-GO-MGH-MG kompozito masei (Pav. 63a), jo Cs(I) ir Co(II) adsorbcinė geba mažėja, greičiausiai dėl jo aglomeracijos ir agregacijos, o geriausias rezultatas pasiektas esant 0,01 g kompozito kiekiui. Kylant temperatūrai (Pav. 63b), Cs(I) adsorbcija didėja iki 45 °C, o vėliau ji buvo nuolat aukšta. Co(I) adsorbcija didėja tiesiškai su temperatūra. Teigiamos  $\Delta G^\circ$  vertės, kurios mažėja Co(II) adsorbcijai didėjant temperatūrai ir nemažėja Cs(I) adsorbcijai, rodo savaiminį Co(II) adsorbcijos procesą ir nesavaiminį Cs(I) adsorbcijos procesą. Tiek Cs(I), tiek Co(II) atveju teigiamos  $\Delta H^\circ$  vertės rodo fizikinės adsorbcijos endoterminį pobūdį, o teigiamos  $\Delta S^\circ$  vertės – didėjančią adsorbcijos atsitiktinumą. Pagal gautas  $R^2$  vertes tiesinė Freundlichio izoterma ( $R^2$  0,987–0,993) ir tiesinis pseudo-antrosios eilės kinetinis modelis ( $R^2$  0,993–0,999) geriau atitinka gautus duomenis nei tiesinė Langmuiro izoterma ( $R^2$  0,926–0,982) ir tiesinis pseudo-pirmosios eilės kinetinis modelis ( $R^2$  0,247–0,394). Iš Freundlichio izotermos prielaidos matyti, kad Cs(I) ir Co(II) daugiasluoksnė adsorbcija vyksta ant heterogeninio

kompozito paviršiaus, o iš pseudo-antrosios eilės kinetinio modelio pastebėta, kad chemisorbcija yra dominuojantis adsorbcijos procesas. Be to, pagal  $K_F$  (Freundlichio izotermos konstantos) reikšmės kompozito giminingumas Co(II) yra 1,4 karto didesnis nei Cs(I), o  $1/n$  (Freundlichio intensyvumo parametro) reikšmės, kurios yra mažesnės už vienetą, rodo palankią jonų adsorbciją (Al-Senani and Al-Fawzan 2018; Esmaeili and Tamjidi 2020; Mohseni-Bandpei et al. 2020; Achour et al. 2021). Siūlomas Cs(I) ir Co(II) adsorbcijos ant MSMC-GO-MGH-MG kompozito mechanizmas yra jonų mainai, kompleksavimas ir elektrostatinė trauka.

Kompozitų PBGO 2.1, PBGO 2.2 ir MPBGO 3.2 prisotinimas Cs(I) buvo pasiektas esant 400 mg/l, o MPBGO 2.3 atveju – 200 mg/l (Pav. 60b). Visiems kompozitams pusiausvyros būseną pasiekta per 240 min. (Pav. 61b). Didžiausia eksperimentinė PBGO 2.1, PBGO 2.2, MPBGO 2.3 ir MPBGO 3.2 kompozitų adsorbcijos talpa buvo atitinkamai 678, 644, 216 ir 774 mg/g. Didelę PBGO 2.1, PBGO 2.2 ir MPBGO 3.2 kompozitų adsorbcijos talpą galima paaiškinti dideliu grafeno oksido 2 lakštų padengimo Berlyno mėlio arba magnetito-Berlyno mėlio dalelių laipsniu. Kadangi GO 2 aukšto oksidacijos laipsnio grafeno oksidas suteikia daugiau vietų geležies katijonams adsorbuoti, lyginant su GO 1, todėl GO 2 lakštai geriau padengiami. Be to, laisvos deguonies turinčios funkcinės grupės, neužimtos magnetito-Berlyno mėlio arba Berlyno mėlio dalelių, galėjo turėti įtakos tokiai didelei Cs(I) adsorbcijai, nes mažos  $I_D/I_G$  vertės MPBGO 3.2 ir PBGO 2.1 kompozituose rodo didesnę deguonies turinčių funkcinų grupių skaičių, lyginant su MPBGO 2.3. Optimalus Cs(I) adsorbcijos ant šių kompozitų pH yra 7 (Pav. 62b). Netiesinė Langmuiro izoterma ( $R^2$  0,886–0,959) geriau atitinka gautus duomenis nei netiesinė Freundlichio izoterma ( $R^2$  0,622–0,827). Iš Langmuiro izotermos prielaidos matyti, kad Cs(I) vienasluoksni adsorbcija vyksta ant homogeninio kompozitų paviršiaus. Be to, gautos  $R_L$  (atskyrimo faktoriaus) vertės buvo mažesnės už 1, bet didesnės už 0, o tai rodo palankią adsorbciją (Mohseni-Bandpei et al. 2020). Nelinijinis pseudo-antrosios eilės kinetinis modelis ( $R^2$  0,930–0,960) geriau koreliuoja su eksperimentiniais duomenimis nei nelinijinis pseudo-pirmosios eilės kinetinis modelis ( $R^2$  0,771–0,858), o tai rodo, kad ant kompozitų dominuoja Cs(I) cheminė adsorbcija. Siūlomas Cs(I) adsorbcijos ant PBGO ir MPBGO kompozitų mechanizmas yra kompleksavimas, jonų mainai ir jonų pagava.

Cs(I) ir Co(II) chitozano-mineralinių kompozitų prisotinimas pasiektas, kai pradinė koncentracija buvo 2000 mg/l, o Co(II) – tik su CS-Zeo esant 1000 mg/l pradinei koncentracijai. Eu(III) įsotinimas pasiektas 20 mg/l visose chitozano-mineralų kompozicijose (Pav. 60c, d ir e). Chitozano-mineralų-

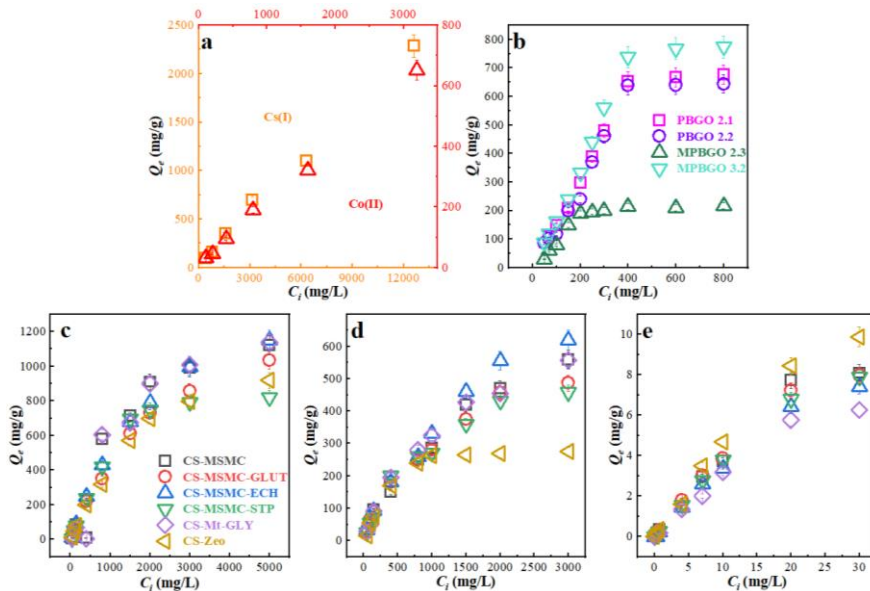
Cs(I)/Co(II)/Eu(III) sistemose pusiausvyra pasiekta per 240 min. (Pav. 61c, d ir e). Didžiausia eksperimentinė adsorbcijos talpa buvo:

Cs(I): 1123 (CS-MSMC), 1035 (CS-MSMC-GLUT), 1152 (CS-MSMC-ECH), 818 (CS-MSMC-STP), 1139 (CS-Mt-GLY) ir 919 (CS-Zeo) mg/g.

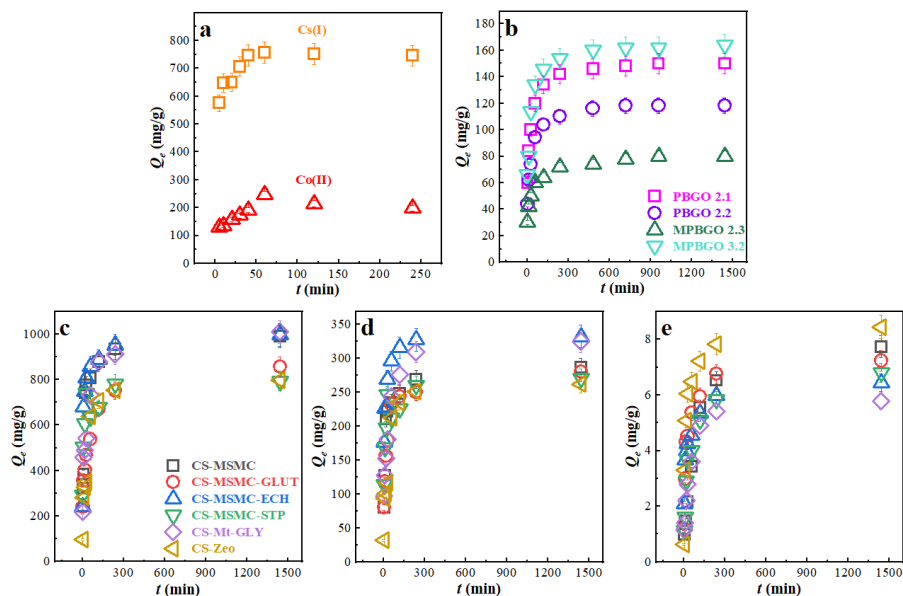
Co(II): 560 (CS-MSMC), 487 (CS-MSMC-GLUT), 619 (CS-MSMC-ECH), 458 (CS-MSMC-STP), 557 (CS-Mt-GLY) ir 275 (CS-Zeo) mg/g.

Eu(III): 8,10 (CS-MSMC), 7,99 (CS-MSMC-GLUT), 7,42 (CS-MSMC-ECH), 7,89 (CS-MSMC-STP), 6,27 (CS-Mt-GLY) ir 9,89 (CS-Zeo) mg/g.

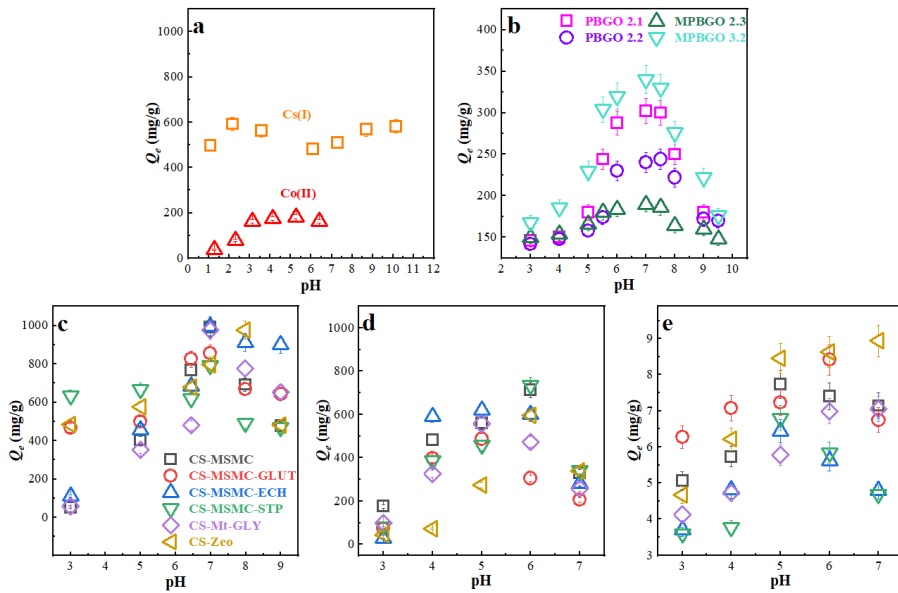
Kompozitai CS-MSMC, CS-MSMC-ECH ir CS-Mt-GLY turi didžiausią Cs(I) ir Co(II) adsorbcijos gebą, o Eu(III) – kompozitas CS-Zeo. Gauti rezultatai rodo, kad naudojant MSMC ir Mt su chitozanu sinergetinio poveikio būdu gaunamas geriausias Cs(I) ir Co(II) adsorbcijos rezultatas, kai chitozано –NH<sub>2</sub> grupės, manoma, yra labiau atsakingos už šių jonų adsorbciją. Eu(III) adsorbcijos atveju galimas dominuojantis veiksnys yra naudotų mineralų tipas. Didelę CS-Mt-GLY kompozito Cs(I) ir Co(II) adsorbcijos gebą, matyt, lemia chitozано laisvųjų funkcinių grupių, panaudoto montmorilonito ir glicerolio sinergetinis poveikis. Didėjant pH (Pav. 62c, d ir e), Cs(I) adsorbcijos maksimumas buvo pasiektas esant 7–8 pH, o Co(II) ir Eu(III) – esant 5–6 pH. Be to, Eu(III) adsorbcija ant CS-Zeo ir CS-Mt-GLY buvo didelė, esant pradiniam pH atitinkamai 5 ir 6. Nelinijinė Langmuiro izoterma ( $R^2$  0,902–0,996) geriau atitinka gautus duomenis nei nelinijinė Freundlichio izoterma ( $R^2$  0,719–0,977). Tai rodo, kad Cs(I), Co(II) ir Eu(III) vienasluoksnė adsorbcija vyksta ant homogeniško chitozано-mineralų kompozitų paviršiaus. Remiantis gautomis  $R_L$  vertėmis, adsorbcija buvo palanki. Daugeliu atvejų vyraujantis adsorbcijos mechanizmas yra chemisorbcija, tai rodo geriausias tirtų sistemų duomenų atitikimas netiesiniam pseudo-antrosios eilės kinetiniam modeliui ( $R^2$  0,865–0,987). Tačiau CS-MSMC-ECH/CS-MSMC-STP-Cs(I) ir CS-Zeo-Co(II) atveju vyraujantis mechanizmas yra fizikosorbcija, tai rodo geresnis gautų duomenų atitikimas pseudo-pirmosios eilės kinetiniam modeliui ( $R^2$  0,930–0,957). Siūlomas Cs(I), Co(II) ir Eu(III) adsorbcijos ant chitozано-mineralų kompozitų mechanizmas yra jonų mainai, kompleksavimas ir elektrostatinė trauka.



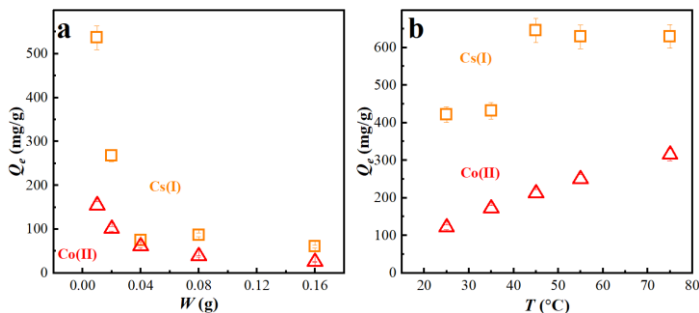
**Pav. 60.** Cs(I) ir Co(II) pradinės koncentracijos poveikis MSMC-GO-MGH-MG kompozitui (a), Cs(I) – PBGO ir MPBGO kompozitams (b), Cs(I) (c), Co(II) (d) ir Eu(III) (e) – chitozano-mineraliniams kompozitams.



**Pav. 61.** Kontakto laiko poveikis Cs(I) ir Co(II) adsorbacijai MSMC-GO-MGH-MG kompozito (a), Cs(I) PBGO ir MPBGO kompozituose (b), Cs(I) (c), Co(II) (d) ir Eu(III) (e) chitozano-mineraliniuose kompozituose.



**Pav. 62.** pH poveikis Cs(I) ir Co(II) adsorbacijai MSMC-GO-MGH-MG kompozito (a), Cs(I) PBGO ir MPBGO kompozituose (b), Cs(I) (c), Co(II) (d) ir Eu(III) (e) chitozano-mineraliniuose kompozituose.



**Pav. 63.** Adsorbento masės (a) ir temperatūros (b) poveikis Cs(I) ir Co(II) adsorbacijai ant MSMC-GO-MGH-MG kompozito.

Palyginus su kitais tirtais kompozitais nustatyta, kad MSMC-GO-MGH-MG ir chitozano-mineraliniai kompozitai turi didžiausią Cs(I) ir Co(II) adsorbacijos gebą, o PBGO 2.1, PBGO 2.2 ir MPBGO 3.2 – Cs(I). Todėl šie kompozitai gali būti perspektyvūs šių jonų adsorbentai.



#### 5.4. ANFIS

Gautos labai didelės koreliacijos vertės ir mažos MSE, SSE ir ARE vertės, lyginant eksperimentines ir prognozuojamas adsorbcinės talpos vertes (visi duomenys), rodo gerą eksperimentinių ir prognozuojamų verčių atitikimą, taigi ir gerą ANFIS veikimą. Bandomųjų duomenų atveju didelės ir labai didelės koreliacijos vertės ir mažos MSE, SSE ir ARE vertės parodo, kad ANFIS turi gerą apibendrinimo gebėjimą (Souza et al. 2018; Onu et al. 2021). 3D paviršiaus modeliavimo rezultatai atskleidė, kad adsorbato elgsena ant adsorbentų yra sudėtinga ir netiesinė, priklausomai nuo tiriamų veiksnių.

## IŠVADOS

1. Nustatyta, kad kompozitas MSMC-GO-MGH-MG-1 adsorbuoja cezio ir kobalto jonus vienodai efektyviai, palyginus su kompozitu MSMC-GO-MGH-MG-2. Be to, muskovito fazė yra labiau atsakinga už cezio jonų adsorbciją, o magemito-magnetito fazė – už kobalto jonų adsorbciją.

2. Kompozitas MSMC-GO-MGH-MG turi didelę cezio (2286 mg/g) ir kobalto (652 mg/g) jonų adsorbcijos talpą. Grafeno oksido 2 pagrindu sukurti kompozitai (PBGO 2.1 (678 mg/g), PBGO 2.2 (644 mg/g) ir MPBGO 3.2 (774 mg/g)) cezių absorbuoja geriau nei grafeno oksido 1 pagrindu sukurtas kompozitai (MPBGO 2.3 (216 mg/g)). Didžiausią cezio ir kobalto jonų adsorbcijos gebą turėjo kompozitai CS-MSMC (1123 ir 560 mg/g), CS-MSMC-ECH (1152 ir 619 mg/g) ir CS-Mt-GLY (1139 ir 557 mg/g), europio jonų – CS-Zeo (9,89 mg/g).

3. Priklausomai nuo pH, cezio jonų adsorbcija ant visų kompozitų, išskyrus kompozitą MSMC-GO-MGH-MG, pasiekė maksimumą esant pH 7–8. Kompozito MSMC-GO-MGH-MG atveju adsorbcija buvo stabili pH intervale nuo 1 iki 10. Kobalto ir europio adsorbcija ant kompozitų pasiekė maksimumą esant pH 5–6. Be to, europio adsorbcija ant kompozitų CS-Zeo ir CS-Mt-GLY buvo pastoviai didelė atitinkamai nuo pH 5 ir 6.

4. MSMC-GO-MGH-MG pusiausvyros būsena cezio ir kobalto jonams buvo pasiekta atitinkamai per 40 ir 60 min., o PBGO-Cs(I), MPBGO-Cs(I) ir chitozano-mineralo-Cs(I)/Co(II)/Eu(III) sistemose pusiausvyra pasiekta per 240 min.

5. Remiantis adsorbento masės poveikio rezultatais, didžiausia cezio ir kobalto jonų adsorbcijos talpa pasiekta, kai MSMC-GO-MGH-MG kompozito masė buvo 0,01 g. Termodinaminiai tyrimai parodė, kad cezio ir kobalto adsorbcija ant MSMC-GO-MGH-MG kompozito yra fizikinės prigimties, atitinkamai nesavaiminė ir savaiminė endoterminė.

6. Freundlich'o izoterma geriau atitinka MSMC-GO-MGH-MG-Cs(I)/Co(II) sistemų duomenis, o Langmuir'o izoterma geriau atitinka PBGO-Cs(I), MPBGO-Cs(I) ir chitozano-mineralų-Cs(I)/Co(II)/Eu(III) sistemų duomenis. Daugumos sistemų duomenis geriau atitinka pseudo-antrosios eilės kinetinis modelis, išskyrus sistemas CS-MSMC-ECH-Cs(I), CS-MSMC-STP-Cs(I) ir CS-Zeo-Co(II), kurių duomenys geriau atitinka pseudo-pirmosios eilės kinetinį modelį.

7. Remiantis eksperimentiniais ir literatūriniais duomenimis, siūlomas cezio ir kobalto adsorbcijos ant MSMC-GO-MGH-MG bei cezio, kobalto ir europio adsorbcijos ant chitozano-mineralų kompozitų mechanizmas yra jonų mainai, kompleksavimas ir elektrostatinė trauka. Cezio adsorbcijos ant PBGO

ir MPBGO kompozitų mechanizmas yra kompleksacija, jonų mainai ir jonų pagava.

8. ANFIS, analizė naudojant nedidelius duomenų rinkinius, pasižymi geru našumu ir apibendrinamuoju gebėjimu, todėl gali būti taikoma kompozitinių medžiagų adsorbcijos gebai prognozuoti. Remiantis 3D paviršiaus modeliavimo duomenimis, jonų adsorbcijos elgsena ant kompozitinių medžiagų buvo sudėtinga ir netiesinė.

## REFERENCES

- Abdelmonem IM, Allam EA, Gizawy MA, et al (2023) Adsorption of  $^{60}\text{Co}(\text{II})$  and  $^{152+154}\text{Eu}(\text{III})$  radionuclides by a sustainable nanobentonite@sodium alginate@oleylamine nanocomposite. *Int J Biol Macromol* 229:344–353. <https://doi.org/10.1016/j.ijbiomac.2022.12.288>
- Abukhadra MR, Mostafa M, Jumah MNB, et al (2021) Insight into the Adsorption Properties of Chitosan/Zeolite-A Hybrid Structure for Effective Decontamination of Toxic Cd (II) and As (V) Ions from the Aqueous Environments. *J Polym Environ* 30:295–307. <https://doi.org/10.1007/S10924-021-02197-0>
- Achour S, Amokrane S, Chegrouche S, et al (2021) Adsorption Mechanism Study of Radionuclide  $^{60}\text{Co}$  by Purified and  $\alpha\text{-Fe}_2\text{O}_3$ -Supported Bentonite from Radioactive Solution. *Arab J Sci Eng* 47:5629–5645. <https://doi.org/10.1007/S13369-021-05570-2>
- Adam C, Garnier-Laplace J, Roussel-Debet S (2010) Radionuclide fact sheet: Cobalt and the environment. Institut de radioprotection et de sûreté nucléaire.
- Adibmehr Z, Faghihian H (2020) Preparation of highly selective magnetic cobalt ion-imprinted polymer based on functionalized SBA-15 for removal  $\text{Co}^{2+}$  from aqueous solutions. *J Environ Heal Sci Eng* 17:1213–1225. <https://doi.org/10.1007/S40201-019-00439-X>
- Agbaogun BK, Olu-Owolabi BI, Buddenbaum H, Fischer K (2022) Adaptive neuro-fuzzy inference system (ANFIS) and multiple linear regression (MLR) modelling of Cu, Cd, and Pb adsorption onto tropical soils. *Environ Sci Pollut Res* 30:31085–31101. <https://doi.org/10.1007/s11356-022-24296-8>
- Ahman B, Ahman G (1994) Radiocesium in Swedish reindeer after the Chernobyl fallout: seasonal variations and long-term decline. *Health Phys* 66:503–512. <https://doi.org/10.1097/00004032-199405000-00002>
- Ajala OJ, Tijani JO, Bankole MT, Abdulkareem AS (2022) A critical review on graphene oxide nanostructured material: Properties, Synthesis, characterization and application in water and wastewater treatment. *Environ Nanotechnology, Monit Manag* 18:100673. <https://doi.org/10.1016/j.enmm.2022.100673>
- Al-Musawi TJ, Mengelizadeh N, Al Rawi O, Balarak D (2021) Capacity and Modeling of Acid Blue 113 Dye Adsorption onto Chitosan Magnetized by  $\text{Fe}_2\text{O}_3$  Nanoparticles. *J Polym Environ* 30:344–359. <https://doi.org/10.1007/S10924-021-02200-8>

Al-Senani GM, Al-Fawzan FF (2018) Study on Adsorption of Cu and Ba from Aqueous Solutions Using Nanoparticles of *Origanum (OR)* and *Lavandula (LV)*. Bioinorg Chem Appl. <https://doi.org/10.1155/2018/3936178>

Alabarse FG, Conceição RV, Balzaretto NM, et al (2011) In-situ FTIR analyses of bentonite under high-pressure. Appl Clay Sci 51:202–208. <https://doi.org/10.1016/J.CLAY.2010.11.017>

Alamudy HA, Cho K (2018) Selective adsorption of cesium from an aqueous solution by a montmorillonite-prussian blue hybrid. Chem Eng J 349:595–602. <https://doi.org/10.1016/j.cej.2018.05.137>

Alexander GA (2015) Radiation decontamination, 2nd edn. Elsevier Inc.

Aloulou H, Bouhamed H, Ghorbel A, et al (2017) Elaboration and characterization of ceramic microfiltration membranes from natural zeolite: Application to the treatment of cuttlefish effluents. Desalin Water Treat 95:9–17. <https://doi.org/10.5004/dwt.2017.21348>

Amani S, Garmarudi AB, Rahmani N, Khanmohammadi M (2019) The  $\beta$ -cyclodextrin-modified nanosized ZSM-5 zeolite as a carrier for curcumin. RSC Adv 9:32348–32356. <https://doi.org/10.1039/C9RA04739E>

Amiri MJ, Abedi-Koupai J, Eslamian SS, et al (2013) Modeling Pb (II) adsorption from aqueous solution by ostrich bone ash using adaptive neural-based fuzzy inference system. J Environ Sci and Health, Part A 48:543–558. <https://doi.org/10.1080/10934529.2013.730451>

Arunraj B, Talasila S, Rajesh V, Rajesh N (2019) Removal of Europium from aqueous solution using *Saccharomyces cerevisiae* immobilized in glutaraldehyde cross-linked chitosan. Sep Sci Technol 54:1620–1631. <https://doi.org/10.1080/01496395.2018.1556303>

ATSDR (Agency for Toxic Substances and Disease Registry) (2004) Toxicological Profile for Cesium. U.S. Department of Health and Human Services, Public Health Service, Atlanta, USA.

ATSDR (Agency for Toxic Substances and Disease Registry) (2023) Toxicological Profile for Cobalt. U.S. Department of Health and Human Services, Public Health Service, Atlanta, USA.

Australian Mining (2023a) Fears rising over lost radioactive capsule [internet database] available via <https://www.australianmining.com.au/news/further-fears-over-lost-radioactive-capsule/>. Accessed January 31, 2023; Published on 2023 January.

Australian Mining (2023b) “An extraordinary result”: Radioactive tablet found though questions remain [internet database] available via <https://www.australianmining.com.au/news/radioactive-tablet-found-though-questions-remain/>. Accessed February 14, 2023; Published on 2023 February.

Awual MR, Yaita T, Miyazaki Y, et al (2016) A Reliable Hybrid Adsorbent for Efficient Radioactive Cesium Accumulation from Contaminated Wastewater. *Sci Rep* 6:19937.

<https://doi.org/10.1038/srep19937>

Azhar A, Yamauchi Y, Allah AE, et al (2019) Nanoporous Iron Oxide/Carbon Composites through In-Situ Deposition of Prussian Blue Nanoparticles on Graphene Oxide Nanosheets and Subsequent Thermal Treatment for Supercapacitor Applications. *Nanomater* 9:776.

<https://doi.org/10.3390/NANO9050776>

Balonov M, Alexakhin R, Bouville A, Liljinzin JO (2006) Report from the Techa River Dosimetry review Workshop held on 8–10 December 2003 at the State Research Centre Institute of Biophysics, Moscow, Russia. *Health Phys* 90:97–113. <https://doi.org/10.1097/01.HP.0000175628.64637.8c>

Balonov MI, Bruk GY, Golikov VY, et al (2007) Assessment of current exposure of the population living in the Techa River basin from radioactive releases of the Mayak facility. *Health Phys* 92:134–147.

<https://doi.org/10.1097/01.HP.0000237599.92479.09>

Belachew N, Bekele G (2019) Synergy of Magnetite Intercalated Bentonite for Enhanced Adsorption of Congo Red Dye. *Silicon* 12:603–612.

<https://doi.org/10.1007/S12633-019-00152-2>

Bhattacharyya KG, Gupta SS (2008) Adsorption of a few heavy metals on natural and modified kaolinite and montmorillonite: A review. *Adv Colloid Interface Sci* 140:114–131. <https://doi.org/10.1016/J.CIS.2007.12.008>

Bian J, Wang A, Sun Y, Zhu Q (2022) Adsorption of nitrate from water by core-shell chitosan wrinkled microspheres @LDH composite: Electrostatic interaction, hydrogen bonding and surface complexation. *Appl Clay Sci* 225:106550. <https://doi.org/10.1016/J.CLAY.2022.106550>

Biswas S, Fatema J, Debnath T, Rashid TU (2021) Chitosan–Clay Composites for Wastewater Treatment: A State-of-the-Art Review. *ACS EST Water* 1:1055–1085. <https://doi.org/10.1021/ACSESTWATER.0C00207>

Bolsunovsky A, Melgunov M, Chuguevskii A, et al (2017) Unique diversity of radioactive particles found in the Yenisei River floodplain. *Sci Rep* 7:11132. <https://doi.org/10.1038/S41598-017-11557-7>

Bouchelaghem F (2010) A numerical and analytical study on calcite dissolution and gypsum precipitation. *Appl Math Model* 34:467–480.

<https://doi.org/10.1016/J.APM.2009.06.004>

Boulanger N, Kuzenkova AS, Iakunkov A, et al (2020) Enhanced Sorption of Radionuclides by Defect-Rich Graphene Oxide. *ACS Appl Mater Interfaces* 12:45122–45135. <https://doi.org/10.1021/acsami.0c11122>

Boulanger N, Kuzenkova AS, Iakunkov A, et al (2022) High Surface Area “3D Graphene Oxide” for Enhanced Sorption of Radionuclides. *Adv Mater Interfaces* 9:2200510. <https://doi.org/10.1002/ADMI.202200510>

Bradbury MH, Baeyens B (2000) A generalised sorption model for the concentration dependent uptake of caesium by argillaceous rocks. *J Contam Hydrol* 42:141–163. [https://doi.org/10.1016/S0169-7722\(99\)00094-7](https://doi.org/10.1016/S0169-7722(99)00094-7)

Brigatti MF, Galán E, Theng BKG (2013) Structure and Mineralogy of Clay Minerals. In: *Developments in Clay Science*. Elsevier Inc.

Brisebois PP, Siaj M (2020) Harvesting graphene oxide-years 1859 to 2019: A review of its structure, synthesis, properties and exfoliation. *J Mater Chem C* 8:1517–1547. <https://doi.org/10.1039/c9tc03251g>

Brix K, Hein C, Haben A, Kautenburger R (2019) Adsorption of caesium on raw Ca-bentonite in high saline solutions: Influence of concentration, mineral composition, other radionuclides and modelling. *Appl Clay Sci* 182:105275. <https://doi.org/10.1016/J.CLAY.2019.105275>

Bruggeman C, Maes N (2010) Uptake of Uranium(VI) by pyrite under boom clay conditions: Influence of dissolved organic carbon. *Environ Sci Technol* 44:4210–4216. <https://doi.org/10.1021/es100919p>

Buddemeier BR, Dillon MB (2009) Key response planning factors for the aftermath of nuclear terrorism (No. LLNL-TR-410067). Lawrence Livermore National Lab, Livermore, United States.

Ca DV, Cox JA (2004) Solid Phase Extraction of Cesium from Aqueous Solution Using Sol-Gel Encapsulated Cobalt Hexacyanoferrate. *Microchim Acta* 147:31–37. <https://doi.org/10.1007/S00604-004-0224-4>

Caccamo MT, Mavilia G, Mavilia L, et al (2020) Self-Assembly Processes in Hydrated Montmorillonite by FTIR Investigations. *Materials* 13:1100. <https://doi.org/10.3390/MA13051100>

Cadogan EI, Lee CH, Popuri SR, Lin HY (2014) Efficiencies of chitosan nanoparticles and crab shell particles in europium uptake from aqueous solutions through biosorption: Synthesis and characterization. *Int Biodeterior Biodegradation* 95:232–240. <https://doi.org/10.1016/J.IBIBOD.2014.06.003>

Cai N, Larese-Casanova P (2020) Facile Synthesis and Reuse of Magnetic Black Carbon Magnetite (BC-Mag) for Fast Carbamazepine Removal from Water. *Nanomater* 10:213. <https://doi.org/10.3390/NANO10020213>

Carter MW, Burns P, Munslow-Davies L (1993) Radiotoxicity hazard classification: the basis and development of a new list. Technical Memorandum 38, Australian Government Publishing Service, Canberra, Australia.

Carvalho RS, Daniel-Da-Silva AL, Trindade T (2016) Uptake of Europium(III) from Water using Magnetite Nanoparticles. *Part Part Syst Charact* 33:150–157. <https://doi.org/10.1002/PPSC.201500170>

Chang L, Chang S, Chen W, et al (2016) Facile one-pot synthesis of magnetic Prussian blue core/shell nanoparticles for radioactive cesium removal. *RSC Adv* 6:96223–96228. <https://doi.org/10.1039/C6RA17525B>

Chen S, Brown L, Levendorf M, et al (2011) Oxidation Resistance of Graphene-Coated Cu and Cu/Ni Alloy. *ACS Nano* 5:1321–1327. <https://doi.org/10.1021/NN103028D>

Chen P, Xie F, Tang F, McNally T (2020) Glycerol plasticisation of chitosan/carboxymethyl cellulose composites: Role of interactions in determining structure and properties. *Int J Biol Macromol* 163:683–693. <https://doi.org/10.1016/J.IJBIOMAC.2020.07.004>

Chen H, Li R, Guo A, Xia Y (2021) Highly fluorescent CsPbBr<sub>3</sub>/TiO<sub>2</sub> core/shell perovskite nanocrystals with excellent stability. *SN Appl Sci* 3:654. <https://doi.org/10.1007/s42452-021-04648-8>

Chen S, Dong Y, Wang H, et al (2022) Highly efficient and selective cesium recovery from natural brine resources using mesoporous Prussian blue analogs synthesized by ionic liquid-assisted strategy. *Resour Conserv Recycl* 186:106542. <https://doi.org/10.1016/J.RESCONREC.2022.106542>

Ching K, Lian B, Leslie G, et al (2020) Metal-cation-modified graphene oxide membranes for water permeation. *Carbon* 170:646–657. <https://doi.org/10.1016/J.CARBON.2020.08.059>

Cho DW, Jeon BH, Chon CM, et al (2012) A novel chitosan/clay/magnetite composite for adsorption of Cu(II) and As(V). *Chem Eng J* 200–202:654–662. <https://doi.org/10.1016/J.CEJ.2012.06.126>

Christensen GC, Romanov GN, Strand P, et al (1997) Radioactive contamination in the environment of the nuclear enterprise ‘Mayak’ PA. Results from the joint Russian-Norwegian field work in 1994. *Sci Total Environ* 202:237–248. [https://doi.org/10.1016/S0048-9697\(97\)00119-8](https://doi.org/10.1016/S0048-9697(97)00119-8)

Cochran TB, Arkin WM, Norris RS (1989) *Nuclear Weapons Databook: Volume IV – Soviet Nuclear Weapons*, 1st edn. Harper & Row, New York.

Compeán-Jasso ME, Ruiz F, Martínez JR, Herrera-Gómez A (2008) Magnetic properties of magnetite nanoparticles synthesized by forced hydrolysis. *Mater Lett* 62:4248–4250. <https://doi.org/10.1016/J.MATLET.2008.06.053>

Cornell RM (1993) Adsorption of cesium on minerals: A review. *J Radioanal Nucl Chem* 171:483–500. <https://doi.org/10.1007/BF02219872>



Damayanti NP (2010) Preparation of Superhydrophobic PET fabric from Al<sub>2</sub>O<sub>3</sub>–SiO<sub>2</sub> hybrid: geometrical approach to create high contact angle surface from low contact angle materials. *J Sol-Gel Sci Technol* 56:47–52. <https://doi.org/10.1007/s10971-010-2271-0>

Dechojarassri D, Asaina S, Omote S, et al (2017) Adsorption and desorption behaviors of cesium on rayon fibers coated with chitosan immobilized with Prussian blue. *Int J Biol Macromol* 104:1509–1516. <https://doi.org/10.1016/J.IJBIOMAC.2017.03.056>

DeLuca TH, DeLuca DK (1997) Composting for Feedlot Manure Management and Soil Quality. *J Prod Agric* 10:235–241. <https://doi.org/10.2134/JPA1997.0235>

Demri B, Muster D (1995) XPS study of some calcium compounds. *J Mater Process Technol* 55:311–314. [https://doi.org/10.1016/0924-0136\(95\)02023-3](https://doi.org/10.1016/0924-0136(95)02023-3)

Directive (1966) Council Directive 66/45/Euratom of 27 October 1966 amending the Directives laying down the basic standards for the protection of the health of workers and the general public against the dangers arising from ionising radiations (OJ 216 26.11.1966, p. 265, ELI: <http://data.europa.eu/eli/dir/1966/45/oj>).

Dolatabadi M, Mehrabpour M, Esfandyari M, et al (2018) Modeling of simultaneous adsorption of dye and metal ion by sawdust from aqueous solution using of ANN and ANFIS. *Chemom Intell Lab Syst* 181:72–78. <https://doi.org/10.1016/J.CHEMOLAB.2018.07.012>

Domingo JL (1989) Cobalt in the environment and its toxicological implications. In: *Reviews of Environmental Contamination and Toxicology*. Springer.

Doumic LI, Salierno G, Ramos C, et al (2016) “Soluble”: Vs. “insoluble” Prussian blue based catalysts: Influence on Fenton-type treatment. *RSC Adv* 6:46625–46633. <https://doi.org/10.1039/c6ra06618f>

Dubey V, Kain V (2018) Synthesis of magnetite by coprecipitation and sintering and its characterization. *Mater Manuf Process* 33:835–839. <https://doi.org/10.1080/10426914.2017.1401720>

Efimova NV., Krasnopyorova AP, Yuhno GD, et al (2021) Uptake of Radionuclides <sup>60</sup>Co, <sup>137</sup>Cs, and <sup>90</sup>Sr with α-Fe<sub>2</sub>O<sub>3</sub> and Fe<sub>3</sub>O<sub>4</sub> Particles from Aqueous Environment. *Mater* 14:2899. <https://doi.org/10.3390/MA14112899>

Egboseiuba TC, Abdulkareem AS, Kovo AS, et al (2020) Ultrasonic enhanced adsorption of methylene blue onto the optimized surface area of activated carbon: Adsorption isotherm, kinetics and thermodynamics. *Chem Eng Res Des* 153:315–336. <https://doi.org/10.1016/J.CHERD.2019.10.016>

Ekrayem NA, Alhwaige AA, Elhrari W, Amer M (2021) Removal of lead (II) ions from water using chitosan/polyester crosslinked spheres derived from chitosan and glycerol-based polyester. *J Environ Chem Eng* 9:106628. <https://doi.org/10.1016/j.jece.2021.106628>

Eljamal O, Shubair T, Tahara A, et al (2019) Iron based nanoparticles-zeolite composites for the removal of cesium from aqueous solutions. *J Mol Liq* 277:613–623. <https://doi.org/10.1016/J.MOLLIQ.2018.12.115>

El-Naggar MR, Ibrahim HA, El-Kamash AM (2014) Sorptive Removal of Cesium and Cobalt Ions in a Fixed bed Column Using Lewatit S100 Cation Exchange Resin. *Arab J Nucl Sci Appl* 47:77–93.

EPA (US Environmental Protection Agency) (2022a) Radionuclide Basics: Cobalt-60 [internet database] available via <https://www.epa.gov/radiation/radionuclide-basics-cobalt-60>. Accessed January 16, 2023; Updated 2022 July.

EPA (US Environmental Protection Agency) (2022b) R Radionuclide Basics: Cesium-137 [internet database] available via <https://www.epa.gov/radiation/radionuclide-basics-cesium-137>. Accessed January 19, 2023; Updated 2022 July.

Esmaeili H, Tamjidi S (2020) Ultrasonic-assisted synthesis of natural clay/Fe<sub>3</sub>O<sub>4</sub>/graphene oxide for enhance removal of Cr (VI) from aqueous media. *Environ Sci Pollut Res* 27:31652–31664. <https://doi.org/10.1007/S11356-020-09448-Y>

Ewis D, Ba-Abbad MM, Benamor A, El-Naas MH (2022) Adsorption of organic water pollutants by clays and clay minerals composites: A comprehensive review. *Appl Clay Sci* 229:106686. <https://doi.org/10.1016/J.CLAY.2022.106686>

Falyouna O, Eljamal O, Maamoun I, et al (2020) Magnetic zeolite synthesis for efficient removal of cesium in a lab-scale continuous treatment system. *J Colloid Interface Sci* 571:66–79. <https://doi.org/10.1016/J.JCIS.2020.03.028>

Fan QH, Tanaka M, Tanaka K, et al (2014) An EXAFS study on the effects of natural organic matter and the expandability of clay minerals on cesium adsorption and mobility. *Geochim Cosmochim Acta* 135:49–65. <https://doi.org/10.1016/J.GCA.2014.02.049>

Farrokhpay S, Ndlovu B, Bradshaw D (2016) Behaviour of swelling clays versus non-swelling clays in flotation. *Miner Eng* 96–97:59–66. <https://doi.org/10.1016/j.mineng.2016.04.011>

Fazal-ur-Rehman M, Akram S (2017) Half-Life and Decay Law of Actinide Elements. Chem Sci J 8:000151.

(<https://www.readcube.com/articles/10.4172%2F2150-3494.1000151>)

<https://doi.org/10.4172/2150-3494.1000151>

Feng S, Cao X, Zheng W, et al (2022) In-situ formed Prussian blue nanoparticles supported by porous biochar as highly efficient removal of cesium ions. J Environ Chem Eng 10:107972.

<https://doi.org/10.1016/J.JECE.2022.107972>

Foerstendorf H, Jordan N, Heim K (2014) Probing the surface speciation of uranium (VI) on iron (hydr)oxides by *in situ* ATR FT-IR spectroscopy. J Colloid Interface Sci 416:133–138. <https://doi.org/10.1016/j.jcis.2013.10.054>

Foroutan R, Peighambaroust SJ, Mohammadi R, et al (2020) Influence of chitosan and magnetic iron nanoparticles on chromium adsorption behavior of natural clay: Adaptive neuro-fuzzy inference modeling. Int J Biol Macromol 151:355–365. <https://doi.org/10.1016/J.IJBIOMAC.2020.02.202>

Fuller AJ, Shaw S, Peacock CL, et al (2014) Ionic strength and pH dependent multi-site sorption of Cs onto a micaceous aquifer sediment. Appl Geochemistry 40:32–42.

<https://doi.org/10.1016/J.APGEOCHEM.2013.10.017>

Garty G, Xu Y, Johnson GW, et al (2020) VADER: a variable dose-rate external <sup>137</sup>Cs irradiator for internal emitter and low dose rate studies. Sci Reports 10:19899. <https://doi.org/10.1038/s41598-020-76941-2>

Gendy EA, Oyekunle DT, Ali J, et al (2021) High-performance removal of radionuclides by porous organic frameworks from the aquatic environment: A review. J Environ Radioact 238–239:106710.

<https://doi.org/10.1016/J.JENVRAD.2021.106710>

Goyal N, Gao P, Wang Z, et al (2020) Nanostructured chitosan/molecular sieve-4A an emergent material for the synergistic adsorption of radioactive major pollutants cesium and strontium. J Hazard Mater 392:122494.

<https://doi.org/10.1016/J.JHAZMAT.2020.122494>

Gui CX, Wang QQ, Hao SM, et al (2014) Sandwichlike magnesium silicate/reduced graphene oxide nanocomposite for enhanced Pb<sup>2+</sup> and methylene blue adsorption. ACS Appl Mater Interfaces 6:14653–14659.

<https://doi.org/10.1021/am503997e>

Guo F, Li D, Fein JB, et al (2022) Roles of hydrogen bond and ion bridge in adsorption of two bisphenols onto montmorillonite: an experimental and DFT study. Appl Clay Sci 217:106406.

<https://doi.org/10.1016/J.CLAY.2022.106406>

Hastuti B, Masykur A, Hadi S (2016) Modification of chitosan by swelling and crosslinking using epichlorohydrin as heavy metal Cr (VI) adsorbent in batik industry wastes. *OP Conf Ser: Mater Sci Eng* 107:012020. <https://doi.org/10.1088/1757-899X/107/1/012020>

He M, Zhu Y, Yang Y, et al (2011) Adsorption of cobalt(II) ions from aqueous solutions by palygorskite. *Appl Clay Sci* 54:292–296. <https://doi.org/10.1016/j.clay.2011.09.013>

Henriques B, Morais T, Cardoso CED, et al (2021) Can the recycling of europium from contaminated waters be achieved through living macroalgae? Study on accumulation and toxicological impacts under realistic concentrations. *Sci Total Environ* 786:147176. <https://doi.org/10.1016/j.scitotenv.2021.147176>

Hofmann S, Voitchovsky K, Spijker P, et al (2016) Visualising the molecular alteration of the calcite (104) – water interface by sodium nitrate. *Sci Reports* 6:21576. <https://doi.org/10.1038/srep21576>

Hong M, Yu L, Wang Y, et al (2019) Heavy metal adsorption with zeolites: The role of hierarchical pore architecture. *Chem Eng J* 359:363–372. <https://doi.org/10.1016/J.CEJ.2018.11.087>

Hoor YQ, Au PI, Mubarak NM, et al (2020) Surface force arising from Adsorbed graphene oxide in kaolinite suspensions. *Colloids Surfaces A Physicochem Eng Asp* 592:124592. <https://doi.org/10.1016/J.COLSURFA.2020.124592>

Hoshi M, Yamamoto M, Kawamura H, et al (1994) Fallout radioactivity in soil and food samples in the Ukraine: measurements of iodine, plutonium, cesium, and strontium isotopes. *Health Phys* 67:187–191. <https://doi.org/10.1097/00004032-199408000-00012>

Hove K, Pedersen O, Garmo TH, et al (1990) Fungi: a major source of radiocesium contamination of grazing ruminants in Norway. *Health Phys* 59:189–192. <https://doi.org/10.1097/00004032-199008000-00004>

Hu QH, Weng JQ, Wang JS (2010) Sources of anthropogenic radionuclides in the environment: a review. *J Environ Radioact* 101:426–437. <https://doi.org/10.1016/J.JENVRAD.2008.08.004>

Hu Z, Qin S, Huang Z, et al (2017) Recyclable graphene oxide-covalently encapsulated magnetic composite for highly efficient Pb(II) removal. *J Environ Chem Eng* 5:4630–4638. <https://doi.org/10.1016/J.JECE.2017.09.003>

Hummers WS, Offeman RE (1958) Preparation of Graphitic Oxide. *J Am Chem Soc* 80:1339. <https://doi.org/10.1021/ja01539a017>

Huo J, Yu G, Wang J (2021) Selective adsorption of cesium (I) from water by Prussian blue analogues anchored on 3D reduced graphene oxide aerogel. *Sci Total Environ* 761:143286.

<https://doi.org/10.1016/J.SCITOTENV.2020.143286>

IAEA (International Atomic Energy Agency) (1963) A Basic Toxicity Classification of Radionuclides. Technical Reports, № 15, Vienna, Austria.

IAEA (International Atomic Energy Agency) (1998) Radiological Characterization of Shut Down Nuclear Reactors for Decommissioning Purposes. Technical Reports, № 389, Vienna, Austria.

IAEA (International Atomic Energy Agency) (2006) Environmental Consequences of the Chernobyl Accident and Their Remediation: Twenty Years of Experience. Report of the Chernobyl Forum Expert Group 'Environment'. Assessment Reports, № 8, Vienna, Austria.

IAEA (International Atomic Energy Agency) (2011) Radioactive Particles in the Environment: Sources, Particle Characterization and Analytical Techniques. IAEA-TECDOC-1663, Vienna, Austria.

Inyinbor AA, Adekola FA, Olatunji GA (2016) Kinetics, isotherms and thermodynamic modeling of liquid phase adsorption of Rhodamine B dye onto *Raphia hookerie* fruit epicarp. *Water Resour Ind* 15:14–27.

<https://doi.org/10.1016/J.WRI.2016.06.001>

Ishizaki M, Akiba S, Ohtani A, et al (2013) Proton-exchange mechanism of specific Cs<sup>+</sup> adsorption *via* lattice defect sites of Prussian blue filled with coordination and crystallization water molecules. *Dalt Trans* 42:16049–16055. <https://doi.org/10.1039/C3DT51637G>

Iwahara A, Delgado JU, Poledna R, et al (2009) Primary radioactivity standardization and gamma intensities determination of <sup>124</sup>Sb. *Nucl Instruments Methods Phys Res Sect A Accel Spectrometers, Detect Assoc Equip* 602:450–456. <https://doi.org/10.1016/J.NIMA.2009.01.021>

Jalali-Rad R, Ghafourian H, Asef Y, et al (2004) Biosorption of cesium by native and chemically modified biomass of marine algae: introduce the new biosorbents for biotechnology applications. *J Hazard Mater* 116:125–134.

<https://doi.org/10.1016/J.JHAZMAT.2004.08.022>

Jang JSR (1992) Self-Learning Fuzzy Controllers Based on Temporal Back Propagation. *IEEE Trans Neural Networks* 3:714–723.

<https://doi.org/10.1109/72.159060>

Jang SC, Haldorai Y, Lee GW, et al (2015) Porous three-dimensional graphene foam/Prussian blue composite for efficient removal of radioactive <sup>137</sup>Cs. *Sci Reports* 5:17510. <https://doi.org/10.1038/srep17510>

Jang J, Lee DS (2016) Magnetic Prussian Blue Nanocomposites for Effective Cesium Removal from Aqueous Solution. *Ind Eng Chem Res* 55:3852–3860. <https://doi.org/10.1021/acs.iecr.6b00112>

Jang J, Lee DS (2018) Magnetite nanoparticles supported on organically modified montmorillonite for adsorptive removal of iodide from aqueous solution: Optimization using response surface methodology. *Sci Total Environ* 615:549–557. <https://doi.org/10.1016/j.scitotenv.2017.09.324>

Jolivet JP, Chanéac C, Tronc E (2004) Iron oxide chemistry. From molecular clusters to extended solid networks. *Chem Commun* 4:481–483. <https://doi.org/10.1039/B304532N>

Józwiak T, Filipkowska U, Szymczyk P, et al (2017) Effect of ionic and covalent crosslinking agents on properties of chitosan beads and sorption effectiveness of Reactive Black 5 dye. *React Funct Polym* 114:58–74. <https://doi.org/10.1016/j.reactfunctpolym.2017.03.007>

Kapnisti MG, Noli FG, Papastergiadis ES, Pavlidou EG (2018) Exploration of the parameters affecting the europium removal from aqueous solutions by novel synthesized titanium phosphates. *J Environ Chem Eng* 6:3408–3417. <https://doi.org/10.1016/J.JECE.2018.05.010>

Kaveeshwar AR, Ponnusamy SK, Revellame ED, et al (2018) Pecan shell based activated carbon for removal of iron(II) from fracking wastewater: Adsorption kinetics, isotherm and thermodynamic studies. *Process Saf Environ Prot* 114:107–122. <https://doi.org/10.1016/J.PSEP.2017.12.007>

Khalil MI (2015) Co-precipitation in aqueous solution synthesis of magnetite nanoparticles using iron(III) salts as precursors. *Arab J Chem* 8:279–284. <https://doi.org/10.1016/J.ARABJC.2015.02.008>

Khan S, Anjum R, Bilal M (2021) Revealing chemical speciation behaviors in aqueous solutions for uranium (VI) and europium (III) adsorption on zeolite. *Environ Technol Innov* 22:101503. <https://doi.org/10.1016/J.ETI.2021.101503>

Khan N, Khan I, Zada N, et al (2022) Utilization of cross-linked chitosan for cobalt adsorption and its reutilization as a photocatalyst for the photodegradation of methyl violet dye in aqueous medium. *Appl Water Sci* 12:107. <https://doi.org/10.1007/s13201-022-01633-3>

Khandaker S, Toyohara Y, Kamida S, Kuba T (2018) Adsorptive removal of cesium from aqueous solution using oxidized bamboo charcoal. *Water Resour Ind* 19:35–46. <https://doi.org/10.1016/J.WRI.2018.01.001>

Khomeyrani SFN, Azqhandi MHA, Ghalami-Choobar, B (2021) Rapid and efficient ultrasonic assisted adsorption of PNP onto LDH-GO-CNTs: ANFIS, GRNN and RSM modeling, optimization, isotherm, kinetic, and thermodynamic study. *J Mol Liq* 333:115917.

<https://doi.org/10.1016/J.MOLLIQ.2021.115917>

Kobayashi T, Nagai H, Chino M, Kawamura H (2013) Source term estimation of atmospheric release due to the Fukushima Dai-ichi Nuclear Power Plant accident by atmospheric and oceanic dispersion simulations. *J Nucl Sci and Technol* 50:255–264.

<https://doi.org/10.1080/00223131.2013.772449>

Kowal-Fouchard A, Drot R, Simoni E, et al (2004) Structural identification of europium(III) adsorption complexes on montmorillonite. *New J Chem* 28:864–869. <https://doi.org/10.1039/b400306c>

Krishnamoorthy K, Veerapandian M, Yun K, Kim SJ (2013) The chemical and structural analysis of graphene oxide with different degrees of oxidation. *Carbon* 53:38–49. <https://doi.org/10.1016/j.carbon.2012.10.013>

Kropatcheva M, Chuguevsky A, Melgunov M (2012) Distribution of  $^{152}\text{Eu}$  and  $^{154}\text{Eu}$  in the “alluvial soil-rhizosphere-plant roots” system. *J Environ Radioact* 106:58–64. <https://doi.org/10.1016/J.JENVRAD.2011.10.021>

Kryuchkova M, Fakhrullin R (2018) Kaolin Alleviates Graphene Oxide Toxicity. *Environ Sci Technol Lett* 5:295–300.

<https://doi.org/10.1021/acs.estlett.8b00135>

Kusmono, Abdurrahim I (2019) Water sorption, antimicrobial activity, and thermal and mechanical properties of chitosan/clay/glycerol nanocomposite films. *Heliyon* 5:e02342.

<https://doi.org/10.1016/j.heliyon.2019.e02342>

Kuzenkova AS, Romanchuk AY, Trigub AL, et al (2020) New insights into the mechanism of graphene oxide and radionuclide interaction. *Carbon* 158:291–302. <https://doi.org/10.1016/J.CARBON.2019.10.003>

Kwong-Moses DS, Elliott WC, Wampler JM, et al (2020) Sorption and desorption of radiocesium by muscovite separated from the Georgia kaolin. *J Environ Radioact* 211:106074. <https://doi.org/10.1016/j.jenvrad.2019.106074>

Laaraibi A, Moughaoui F, Damiri F, et al (2018) Chitosan-Clay Based (CS-NaBNT) Biodegradable Nanocomposite Films for Potential Utility in Food and Environment. In: *Chitin-Chitosan - Myriad Functionalities in Science and Technology*. IntechOpen.

Latrille C, Bildstein O (2022) Cs selectivity and adsorption reversibility on Ca-illite and Ca-vermiculite. *Chemosphere* 288:132582.

<https://doi.org/10.1016/J.CHEMOSPHERE.2021.132582>

Launer PJ, Arkles B (2013) Infrared Analysis of Organosilicon Compounds: Spectra-Structure Relationships. In: *Silicon Compounds: Silanes and Silicones*, Barry Arkles, Gerald Larson (eds). Gelest Inc.

Lee SJ, Jeong JR, Shin SC, et al (2004) Synthesis and characterization of superparamagnetic maghemite nanoparticles prepared by coprecipitation technique. *J Magn Mater* 282:147–150.

<https://doi.org/10.1016/j.jmmm.2004.04.035>

Leyssens L, Vinck B, Van Der Straeten C, et al (2017) Cobalt toxicity in humans—A review of the potential sources and systemic health effects. *Toxicology* 387:43–56. <https://doi.org/10.1016/j.tox.2017.05.015>

Li H, Zhang L, Christy AG (2011) The Correlation Between Raman Spectra and the Mineral Composition of Muscovite and Phengite. In: *Ultrahigh-Pressure Metamorphism: 25 Years After The Discovery Of Coesite And Diamond*. Elsevier Inc.

Li B, Shan CL, Zhou Q, et al (2013) Synthesis, Characterization, and Antibacterial Activity of Cross-Linked Chitosan-Glutaraldehyde. *Mar Drugs* 11:1534–1552. <https://doi.org/10.3390/MD11051534>

Li Y, Sheng G, Sheng J (2014) Magnetite decorated graphene oxide for the highly efficient immobilization of Eu(III) from aqueous solution. *J Mol Liq* 199:474–480. <https://doi.org/10.1016/J.MOLLIQ.2014.08.009>

Li C, Cui J, Wang F, et al (2015) Adsorption removal of Congo red by epichlorohydrin-modified cross-linked chitosan adsorbent. *Desalination Water Treat* 57:14060–14066.

<https://doi.org/10.1080/19443994.2015.1060904>

Li H, He B, Li P, et al (2019) Adsorption behaviors of Eu(III) on granite: batch, electron probe micro-analysis and modeling studies. *Environ Earth Sci* 78:249. <https://doi.org/10.1007/S12665-019-8170-Y>

Li W, Zuo Y, Wang L, et al (2022) Abundance, spatial variation, and sources of rare earth elements in soils around ion-adsorbed rare earth mining areas. *Environ Pollut* 313:120099.

<https://doi.org/10.1016/J.ENVPOL.2022.120099>

Liang T, Li K, Wang L (2014) State of rare earth elements in different environmental components in mining areas of China. *Environ Monit Assess* 186:1499–1513. <https://doi.org/10.1007/s10661-013-3469-8>

Lin X, Jia J, Champness NR, et al (2008) Metal-organic framework materials for hydrogen storage. In: *Solid-State Hydrogen Storage: Materials and Chemistry*. Woodhead Publishing.



Lingamdinne LP, Choi YL, Kim IS, et al (2017) Preparation and characterization of porous reduced graphene oxide based inverse spinel nickel ferrite nanocomposite for adsorption removal of radionuclides. *J Hazard Mater* 326:145–156. <https://doi.org/10.1016/J.JHAZMAT.2016.12.035>

Lingamdinne LP, Amelirad O, Koduru JR, et al (2023) Functionalized bentonite for removal of Pb(II) and As(V) from surface water: Predicting capability and mechanism using artificial neural network. *J Water Process Eng* 51:103386. <https://doi.org/10.1016/j.jwpe.2022.103386>

Linnik VG, Brown JE, Dowdall M, et al (2006) Patterns and inventories of radioactive contamination of island sites of the Yenisey River, Russia. *J Environ Radioact* 87:188–208. <https://doi.org/10.1016/J.JENVRAD.2005.11.011>

Liu CH, Chuang YH, Chen TY, et al (2015) Mechanism of Arsenic Adsorption on Magnetite Nanoparticles from Water: Thermodynamic and Spectroscopic Studies. *Environ Sci Technol* 49:7726–7734. <https://doi.org/10.1021/acs.est.5b00381>

Liu D, Wu C, Yan M, Wang J (2018a) Correlating the microstructure, growth mechanism and magnetic properties of FeSiAl soft magnetic composites fabricated via HNO<sub>3</sub> oxidation. *Acta Mater* 146:294–303. <https://doi.org/10.1016/J.ACTAMAT.2018.01.001>

Liu H, Xie S, Liao J, et al (2018b) Novel graphene oxide/bentonite composite for uranium(VI) adsorption from aqueous solution. *J Radioanal Nucl Chem* 317:1349–1360. <https://doi.org/10.1007/S10967-018-5992-0>

Liu Y, Pang H, Wang X, et al (2021) Zeolitic imidazolate framework-based nanomaterials for the capture of heavy metal ions and radionuclides: A review. *Chem Eng J* 406:127139. <https://doi.org/10.1016/J.CEJ.2020.127139>

Liu F, Huang W, Wang S, Hu B (2022) Investigation of adsorption properties and mechanism of uranium(VI) and europium(III) on magnetic amidoxime-functionalized MCM-41. *Appl Surf Sci* 594:153376. <https://doi.org/10.1016/J.APSUSC.2022.153376>

Liu H, Fu T, Sarwar MT, Yang H (2023) Recent progress in radionuclides adsorption by bentonite-based materials as ideal adsorbents and buffer/backfill materials. *Appl Clay Sci* 232:106796. <https://doi.org/10.1016/J.CLAY.2022.106796>

Lizardi-Mendoza J, Monal WMA, Valencia FMG (2016) Chemical Characteristics and Functional Properties of Chitosan. In: *Chitosan in the Preservation of Agricultural Commodities*. Elsevier Inc.

López-Díaz D, López Holgado M, García-Fierro JL, Velázquez MM (2017) Evolution of the Raman Spectrum with the Chemical Composition of Graphene Oxide. *J Phys Chem C* 121:20489–20497.

<https://doi.org/10.1021/acs.jpcc.7b06236>

Loutfy SA, El-Din HMA, Elberry MH, et al (2016) Synthesis, characterization and cytotoxic evaluation of chitosan nanoparticles: *in vitro* liver cancer model. *Adv Nat Sci Nanosci Nanotechnol* 7:035008.

<https://doi.org/10.1088/2043-6262/7/3/035008>

Lu S, Sun Y, Chen C (2019) Adsorption of radionuclides on carbon-based nanomaterials. In: *Interface Science and Technology*, 1st edn. Elsevier Ltd.

Lujanienė G, Jokšas K, Šilobritienė B, Morkuniene R (2006) Physical and chemical characteristics of <sup>137</sup>Cs in the Baltic Sea. *Radioact Environ* 8:165–179. [https://doi.org/10.1016/S1569-4860\(05\)08011-3](https://doi.org/10.1016/S1569-4860(05)08011-3)

Lujanienė G, Beneš P, Štamberg K, et al (2010) Effect of natural clay components on sorption of Cs, Pu and Am by the clay. *J Radioanal Nucl Chem* 286:353–359. <https://doi.org/10.1007/s10967-010-0726-y>

Lujanienė G, Štamberg K, Pakštas V, et al (2015) Study of Pu sorption behavior in natural clay. *J Radioanal Nucl Chem* 304:53–59.

<https://doi.org/10.1007/s10967-014-3585-0>

Lujanienė G, Novikau R, Joel EF, et al (2022) Preparation of Graphene Oxide-Maghemite-Chitosan Composites for the Adsorption of Europium Ions from Aqueous Solutions. *Molecules* 27:8035.

<https://doi.org/10.3390/molecules27228035>

Luo J, Han G, Xie M, et al (2015) Quaternized chitosan/montmorillonite nanocomposite resin and its adsorption behavior. *Iran Polym J* 24:531–539.

<https://doi.org/10.1007/s13726-015-0343-2>

Ma J, Yang M, Yu F, Zheng J (2015) Water-enhanced Removal of Ciprofloxacin from Water by Porous Graphene Hydrogel. *Sci Reports* 5:13578. <https://doi.org/10.1038/srep13578>

Ma J, Zhao Q, Zhou L, et al (2019) Mutual effects of U(VI) and Eu(III) immobilization on interpenetrating 3-dimensional MnO<sub>2</sub>/graphene oxide composites. *Sci Total Environ* 695:133696.

<https://doi.org/10.1016/J.SCITOTENV.2019.133696>

Ma S-wei, Zhang G, Li H, et al (2020) Catalytic fast pyrolysis of walnut shell with K/AC catalyst for the production of phenolic-rich bio-oil. *Biomass Convers Biorefinery* 12:2451–2462.

<https://doi.org/10.1007/S13399-020-00799-7>

Macht F, Eusterhues K, Pronk GJ, Totsche KU (2011) Specific surface area of clay minerals: Comparison between atomic force microscopy measurements and bulk-gas (N<sub>2</sub>) and -liquid (EGME) adsorption methods. *Appl Clay Sci* 53:20–26. <https://doi.org/10.1016/J.CLAY.2011.04.006>

Makarchuk OV, Dontsova TA, Astrelin IM (2016) Magnetic Nanocomposites as Efficient Sorption Materials for Removing Dyes from Aqueous Solutions. *Nanoscale Res Lett* 11:161. <https://doi.org/10.1186/s11671-016-1364-2>

Marcano DC, Kosynkin DV, Berlin JM, et al (2010) Improved synthesis of graphene oxide. *ACS Nano* 4:4806–4814. <https://doi.org/10.1021/nn1006368>

Masoudi P, Le Coz M, Cazala C, Saito K (2019) Spatial properties of soil analyses and airborne measurements for reconnaissance of soil contamination by <sup>137</sup>Cs after Fukushima nuclear accident in 2011. *J Environ Radioact* 202:74–84. <https://doi.org/10.1016/J.JENVRAD.2018.11.014>

Massaro M, Cavallaro G, Lazzara G, Riela S (2020) Covalently modified nanoclays: synthesis, properties and applications. In: *Clay Nanoparticles*. MNT.

Maxbauer DP, Feinberg JM, Fox DL (2016) Magnetic mineral assemblages in soils and paleosols as the basis for paleoprecipitation proxies: A review of magnetic methods and challenges. *Earth-Science Rev* 155:28–48. <https://doi.org/10.1016/j.earscirev.2016.01.014>

McHaffie DR, Khuntia D, Suh JH, et al (2012) Stereotactic Irradiation: Linear Accelerator and Gamma Knife. In: *Clinical Radiation Oncology 3rd edn*. W.B. Saunders.

McKinley JP, Zachara JM, Heald SM, et al (2004) Microscale Distribution of Cesium Sorbed to Biotite and Muscovite. *Environ Sci Technol* 38:1017–1023. <https://doi.org/10.1021/es034569m>

Mendoza-Castillo DI, Reynel-Ávila HE, Sánchez-Ruiz FJ, et al (2018) Insights and pitfalls of artificial neural network modeling of competitive multi-metallic adsorption data. *J Mol Liq* 251:15–27. <https://doi.org/10.1016/J.MOLLIQ.2017.12.030>

Meredith WJ, Massey JB (1977) Teletherapy sources. In: *Fundamental Physics of Radiology 3rd edn*. Butterworth-Heinemann.

Mnasri-Ghnimi S, Frini-Srasra N (2019) Removal of heavy metals from aqueous solutions by adsorption using single and mixed pillared clays. *Appl Clay Sci* 179:105151. <https://doi.org/10.1016/j.clay.2019.105151>

Modi MK, Pattanaik P, Dash N, Subramanian S (2015) Sorption of radionuclides. *Int J Pharm Sci Rev Res* 34:122–130.

Mohseni-Bandpei A, Eslami A, Kazemian H, et al (2020) A high density 3-aminopropyltriethoxysilane grafted pumice-derived silica aerogel as an efficient adsorbent for ibuprofen: Characterization and optimization of the adsorption data using response surface methodology. *Environ Technol Innov* 18:100642. <https://doi.org/10.1016/J.ETI.2020.100642>

Montes-Navajas P, Asenjo NG, Santamaría R, et al (2013) Surface area measurement of graphene oxide in aqueous solutions. *Langmuir* 29:13443–13448. <https://doi.org/10.1021/la4029904>

Montes de Oca-Palma R, Solache-Ríos M, Jiménez-Reyes M, et al (2021) Adsorption of cobalt by using inorganic components of sediment samples from water bodies. *Int J Sediment Res* 36:524–531. <https://doi.org/10.1016/j.ijsrc.2020.11.003>

Mookherjee M, Redfern SAT (2002) A high-temperature Fourier transform infrared study of the interlayer and Si–O-stretching region in phengite-2M<sub>1</sub>. *Clay Miner* 37:323–336. <https://doi.org/10.1180/0009855023720036>

Moretti G, Gervais C (2018) Raman spectroscopy of the photosensitive pigment Prussian blue. *J Raman Spectrosc* 49:1198–1204. <https://doi.org/10.1002/jrs.5366>

Moskowitz BM, Jackson M, Chandler V (2015) Geophysical Properties of the Near-Surface Earth: Magnetic Properties. In: *Treatise on Geophysics*, 2nd edn. Elsevier Inc.

Motaghi H, Arabkhani P, Parvinnia M, Asfaram A (2022) Simultaneous adsorption of cobalt ions, azo dye, and imidacloprid pesticide on the magnetic chitosan/activated carbon@UiO-66 bio-nanocomposite: Optimization, mechanisms, regeneration, and application. *Sep Purif Technol* 284:120258. <https://doi.org/10.1016/J.SEPPUR.2021.120258>

Mukai H, Tamura K, Kikuchi R, et al (2018) Cesium desorption behavior of weathered biotite in Fukushima considering the actual radioactive contamination level of soils. *J Environ Radioact* 190–191:81–88. <https://doi.org/10.1016/J.JENVRAD.2018.05.006>

Narayanan S, Vijaya JJ, Sivasanker S, et al (2016) Hierarchical ZSM-5 catalytic performance evaluated in the selective oxidation of styrene to benzaldehyde using TBHP. *J Porous Mater* 23:741–752. <https://doi.org/10.1007/s10934-016-0129-8>

Narayanan DP, Gopalakrishnan A, Yaakob Z, et al (2020) A facile synthesis of clay – graphene oxide nanocomposite catalysts for solvent free multicomponent Biginelli reaction. *Arab J Chem* 13:318–334. <https://doi.org/10.1016/J.ARABJC.2017.04.011>

Newsome L, Morris K, Trivedi D, et al (2015) Biostimulation by Glycerol Phosphate to Precipitate Recalcitrant Uranium(IV) Phosphate. *Environ Sci Technol* 49:11070–11078.

<https://doi.org/10.1021/acs.est.5b02042>

Nguyen MN, Yaqub M, Kim S, Lee W (2021) Optimization of cesium adsorption by Prussian blue using experiments and gene expression modeling. *J Water Process Eng* 41:102084. <https://doi.org/10.1016/j.jwpe.2021.102084>

Nian V, Mignacca B, Locatelli G (2022) Policies toward net-zero: Benchmarking the economic competitiveness of nuclear against wind and solar energy. *Appl Energy* 320:119275.

<https://doi.org/10.1016/j.apenergy.2022.119275>

Niese S, Gleisberg B (1996) Determination of radioisotopes of Ce, Eu, Pu, Am and Cm in low-level wastes from power reactors using low-level measuring techniques. *Appl Radiat Isot* 47:1113–1114.

[https://doi.org/10.1016/S0969-8043\(96\)00115-7](https://doi.org/10.1016/S0969-8043(96)00115-7)

Novikov AP, Kalmykov SN, Utsunomiya S, et al (2006) Colloid transport of plutonium in the far-field of the Mayak Production Association, Russia. *Science* 314:638–641. <https://doi.org/10.1126/science.1131307>

Novikau R, Lujaniene G (2022) Adsorption behaviour of pollutants: Heavy metals, radionuclides, organic pollutants, on clays and their minerals (raw, modified and treated): A review. *J Environ Manage* 309:114685.

<https://doi.org/10.1016/J.JENVMAN.2022.114685>

Obeid L, Bée A, Talbot D, et al (2013) Chitosan/maghemite composite: A magsorbent for the adsorption of methyl orange. *J Colloid Interface Sci* 410:52–58. <https://doi.org/10.1016/j.jcis.2013.07.057>

Ogwada RA, Sparks DL (1986) Kinetics of Ion Exchange on Clay Minerals and Soil: I. Evaluation of Methods. *Soil Sci Soc Am J* 50:1158–1162. <https://doi.org/10.2136/SSSAJ1986.03615995005000050013X>

Ohkubo T, Okamoto T, Kawamura K, et al (2018) New Insights into the Cs Adsorption on Montmorillonite Clay from <sup>133</sup>Cs Solid-State NMR and Density Functional Theory Calculations. *J Phys Chem A* 122:9326–9337.

<https://doi.org/10.1021/acs.jpca.8b07276>

Omar H, Arida H, Daifullah A (2009) Adsorption of <sup>60</sup>Co radionuclides from aqueous solution by raw and modified bentonite. *Appl Clay Sci* 44:21–26. <https://doi.org/10.1016/j.clay.2008.12.013>

Onu CE, Nwabanne JT, Ohale PE, Asadu CO (2021) Comparative analysis of RSM, ANN and ANFIS and the mechanistic modeling in eriochrome black-T dye adsorption using modified clay. *South African J Chem Eng* 36:24–42. <https://doi.org/10.1016/J.SAJCE.2020.12.003>

Paluszkiewicz C, Stodolak E, Hasik M, Blazewicz M (2011) FT-IR study of montmorillonite–chitosan nanocomposite materials. *Spectrochim Acta Part A Mol Biomol Spectrosc* 79:784–788.

<https://doi.org/10.1016/J.SAA.2010.08.053>

Pan D, Fan F, Wang Y, et al (2017) Retention of Eu(III) in muscovite environment: Batch and spectroscopic studies. *Chem Eng J* 330:559–565.

<https://doi.org/10.1016/J.CEJ.2017.07.184>

Penke YK, Anantharaman G, Ramkumar J, Kar KK (2017) Aluminum Substituted Cobalt Ferrite (Co–Al–Fe) Nano Adsorbent for Arsenic Adsorption in Aqueous Systems and Detailed Redox Behavior Study with XPS. *ACS Appl Mater Interfaces* 9:11587–11598.

<https://doi.org/10.1021/acsami.6b16414>

Pereira FAR, Sousa KS, Cavalcanti GRS, et al (2017) Green biosorbents based on chitosan-montmorillonite beads for anionic dye removal. *J Environ Chem Eng* 5:3309–3318. <https://doi.org/10.1016/J.JECE.2017.06.032>

Petcharoen K, Sirivat A (2012) Synthesis and characterization of magnetite nanoparticles via the chemical co-precipitation method. *Mater Sci Eng B* 177:421–427. <https://doi.org/10.1016/j.mseb.2012.01.003>

Peterson J, MacDonell M, Haroun L, et al (2007) Radiological and chemical fact sheets to support health risk analyses for contaminated areas. *Argonne National Laboratory Environmental Science Division* 133:40–41.

Plancque G, Moulin V, Toulhoat P, Moulin C (2003) Europium speciation by time-resolved laser-induced fluorescence. *Anal Chim Acta* 478:11–22. [https://doi.org/10.1016/S0003-2670\(02\)01486-1](https://doi.org/10.1016/S0003-2670(02)01486-1)

Priyadarshi R, Kumar B, Negi YS (2018) Chitosan film incorporated with citric acid and glycerol as an active packaging material for extension of green chilli shelf life. *Carbohydr Polym* 195:329–338.

<https://doi.org/10.1016/j.carbpol.2018.04.089>

Qiu HJ, Liu L, Wang Y (2016) Template-directed fabrication of 3D graphene-based composite and their electrochemical energy-related applications. *Sci Bull* 61:443–450.

<https://doi.org/10.1007/S11434-016-1024-Z>

Queiroz MF, Melo KRT, Sabry DA, et al (2015) Does the Use of Chitosan Contribute to Oxalate Kidney Stone Formation? *Mar Drugs* 13:141–158. <https://doi.org/10.3390/MD13010141>

Ramos SJ, Dinali GS, Oliveira C, et al (2016) Rare Earth Elements in the Soil Environment. *Curr Pollut Reports* 2:28–50.

<https://doi.org/10.1007/s40726-016-0026-4>

Rauret G, López-Sánchez JF, Sahuquillo A, et al (1999) Improvement of the BCR three step sequential extraction procedure prior to the certification of new sediment and soil reference materials. *J Environ Monit* 1:57–61. <https://doi.org/10.1039/A807854H>

Ravindra A, Kulkarni DB, Sharma R, et al (2022) Activity measurement of mixed complex radionuclide like  $^{152}\text{Eu}$  with different methods. *Appl Radiat Isot* 185:110228. <https://doi.org/10.1016/J.APRADISO.2022.110228>

Rim KT, Koo KH, Park JS (2013) Toxicological Evaluations of Rare Earths and Their Health Impacts to Workers: A Literature Review. *Saf Health Work* 4:12–26. <https://doi.org/10.5491/SHAW.2013.4.1.12>

Rzetalma MA (2016) Cobalt and vanadium in bottom sediments of anthropogenic lakes in the Silesian Upland (southern Poland). *International Multidisciplinary Scientific GeoConference: SGEM: Surveying Geology & Mining Ecology and Management*, November 16–18, 2016, Hamilton, New Zealand, 169–176.

Rethinasabapathy M, Kang SM, Lee I, et al (2019) Highly stable Prussian blue nanoparticles containing graphene oxide–chitosan matrix for selective radioactive cesium removal. *Mater Lett* 241:194–197. <https://doi.org/10.1016/J.MATLET.2019.01.070>

Reza Safaei H, Reza Safaei M, Rahmanian V (2012) Film Formation and Anticorrosive Behavior of Zn-ZSM-5 Nano-Sized Zeolite Composite Coatings. *Open Electrochem J* 4:1–8. <https://doi.org/10.2174/1876505x01204010001>

Rezaei H, Rahmati M, Modarress H (2017) Application of ANFIS and MLR models for prediction of methane adsorption on *X* and *Y* faujasite zeolites: effect of cations substitution. *Neural Comput Appl* 28:301–312. <https://doi.org/10.1007/S00521-015-2057-Y>

Romanchuk AY, Slesarev AS, Kalmykov SN, et al (2013) Graphene oxide for effective radionuclide removal. *Phys Chem Chem Phys* 15:2321–2327. <https://doi.org/10.1039/C2CP44593J>

Sabzevari M, Cree DE, Wilson LD (2018) Graphene Oxide-Chitosan Composite Material for Treatment of a Model Dye Effluent. *ACS Omega* 3:13045–13054. <https://doi.org/10.1021/acsomega.8b01871>

Sada SO, Ikpeseni SC (2021) Evaluation of ANN and ANFIS modeling ability in the prediction of AISI 1050 steel machining performance. *Heliyon* 7:e06136. <https://doi.org/10.1016/J.HELIYON.2021.E06136>

Sadeghizadeh A, Ebrahimi F, Heydari M, et al (2019) Adsorptive removal of Pb (II) by means of hydroxyapatite/chitosan nanocomposite hybrid nanoadsorbent: ANFIS modeling and experimental study. *J Environ Manage* 232:342–353. <https://doi.org/10.1016/J.JENVMAN.2018.11.047>

Saheed IO, Oh WD, Suah FBM (2021) Chitosan modifications for adsorption of pollutants – A review. *J Hazard Mater* 408:124889. <https://doi.org/10.1016/J.JHAZMAT.2020.124889>

Sawidis T, Drossos E, Heinrich G, Papastefanou C (1990) Cesium-137 accumulation in higher plants before and after chernobyl. *Environ Int* 16:163–169. [https://doi.org/10.1016/0160-4120\(90\)90156-Z](https://doi.org/10.1016/0160-4120(90)90156-Z)

Seema H (2020) Novel self assembled magnetic Prussian blue graphene based aerogel for highly selective removal of radioactive cesium in water. *Arab J Chem* 13:4417–4424. <https://doi.org/10.1016/J.ARABJC.2019.08.009>

Shao DD, Fan QH, Li JX, et al (2009) Removal of Eu(III) from aqueous solution using ZSM-5 zeolite. *Microporous Mesoporous Mater* 123:1–9. <https://doi.org/10.1016/j.micromeso.2009.03.043>

Shiba F, Mameuda U, Tatejima S, Okawa Y (2019) Synthesis of uniform Prussian blue nanoparticles by a polyol process using a polyethylene glycol aqueous solution. *RSC Adv* 9:34589–34594. <https://doi.org/10.1039/C9RA07080J>

Siddiqui SI, Fatima B, Tara N, et al (2019) Recent advances in remediation of synthetic dyes from wastewaters using sustainable and low-cost adsorbents. In: *The Impact and Prospects of Green Chemistry for Textile Technology*. Woodhead Publishing.

Sides PJ, Faruqui D, Gellman AJ (2009) Dynamics of charging of muscovite mica: measurement and modeling. *Langmuir* 25:1475–1481. <https://doi.org/10.1021/la802752g>

Smith CN, Goshawk JA, Charles K, et al (2003) MEAD (part II)–Predictions of radioactivity concentrations in the Irish Sea. *J Environ Radioact* 68:193–214. [https://doi.org/10.1016/S0265-931X\(03\)00041-9](https://doi.org/10.1016/S0265-931X(03)00041-9)

Smith DR, Escobar AP, Andris MN, et al (2021) Understanding the Molecular-Level Interactions of Glucosamine-Glycerol Assemblies: A Model System for Chitosan Plasticization. *ACS Omega* 6:25227–25234. <https://doi.org/10.1021/acsomega.1c03016>

Smyrnioti M, Ioannides T (2017) Synthesis of Cobalt-Based Nanomaterials from Organic Precursors. In: *Cobalt*, Maaz K (ed). IntechOpen.



Soliman MA, Rashad GM, Mahmoud MR (2019) Organo-modification of montmorillonite for enhancing the adsorption efficiency of cobalt radionuclides from aqueous solutions. *Environ Sci Pollut Res* 26:10398–10413. <https://doi.org/10.1007/S11356-019-04478-7>

Solodov IN, Zotov AV., Khoteev AD, et al (1998) Geochemistry of natural and contaminated subsurface waters in fissured bed rocks of the Lake Karachai area, Southern Urals, Russia. *Appl Geochemistry* 13:921–939. [https://doi.org/10.1016/S0883-2927\(98\)00025-0](https://doi.org/10.1016/S0883-2927(98)00025-0)

Souza PR, Dotto GL, Salau NPG (2018) Artificial neural network (ANN) and adaptive neuro-fuzzy interference system (ANFIS) modelling for nickel adsorption onto agro-wastes and commercial activated carbon. *J Environ Chem Eng* 6:7152–7160. <https://doi.org/10.1016/J.JECE.2018.11.013>

Sun Y, Shao D, Chen C, et al (2013) Highly efficient enrichment of radionuclides on graphene oxide-supported polyaniline. *Environ Sci Technol* 47:9904–9910. <https://doi.org/10.1021/es401174n>

Sutirman ZA, Sanagi MM, Aini WIW (2021) Alginate-based adsorbents for removal of metal ions and radionuclides from aqueous solutions: A review. *Int J Biol Macromol* 174:216–228. <https://doi.org/10.1016/J.IJBIOMAC.2021.01.150>

Taher FA, Kamal FH, Badawy NA, Shrsr AE (2018) Hierarchical magnetic/chitosan/graphene oxide 3D nanostructure as highly effective adsorbent. *Mater Res Bull* 97:361–368. <https://doi.org/10.1016/J.MATERRESBULL.2017.09.023>

Takahashi A, Tanaka H, Minami K, et al (2018) Unveiling Cs-adsorption mechanism of Prussian blue analogs: Cs<sup>+</sup>-percolation via vacancies to complete dehydrated state. *RSC Adv* 8:34808–34816. <https://doi.org/10.1039/C8RA06377J>

Talerko M, Kovalets I, Lev T, et al (2021) Simulation study of radionuclide atmospheric transport after wildland fires in the Chernobyl Exclusion Zone in April 2020. *Atmos Pollut Res* 12:193–204. <https://doi.org/10.1016/j.apr.2021.01.010>

Tan W, Zhang Y, Szeto YS, Liao L (2008) A novel method to prepare chitosan/montmorillonite nanocomposites in the presence of hydroxy-aluminum oligomeric cations. *Compos Sci Technol* 68:2917–2921. <https://doi.org/10.1016/J.COMPSCITECH.2007.10.007>

Tayyebi A, Outokesh M, Moradi S, Doram A (2015) Synthesis and characterization of ultrasound assisted “graphene oxide–magnetite” hybrid, and investigation of its adsorption properties for Sr(II) and Co(II) ions. *Appl Surf Sci* 353:350–362. <https://doi.org/10.1016/J.APSUSC.2015.06.087>

Thakur G, Singh A, Singh I (2016) Chitosan-Montmorillonite Polymer Composites: Formulation and Evaluation of Sustained Release Tablets of Aceclofenac. *Sci Pharm* 84:603-617.

<https://doi.org/10.3390/scipharm84040603>

Thammawong C, Opaprakasit P, Tangboriboonrat P, Sreearunothai P (2013) Prussian blue-coated magnetic nanoparticles for removal of cesium from contaminated environment. *J Nanoparticle Res* 15:1689.

<https://doi.org/10.1007/s11051-013-1689-z>

Thomas MF, Johnson CE (1986) Mössbauer Spectroscopy, Dickson DPE, Berry FJ (eds.). Cambridge University Press.

Tong Q, Liu S, Huo J, et al (2023) Structure and stability analysis of basaltic glasses for immobilizing simulated actinides Nd, Ce and La. *J Non Cryst Solids* 600:122043.

<https://doi.org/10.1016/J.JNONCRY SOL.2022.122043>

Tran HV, Bui LT, Dinh TT, et al (2017) Graphene oxide/Fe<sub>3</sub>O<sub>4</sub>/chitosan nanocomposite: a recoverable and recyclable adsorbent for organic dyes removal. Application to methylene blue. *Mater Res Express* 4:035701.

<https://doi.org/10.1088/2053-1591/AA6096>

Tripathy M, Hota G (2020) Maghemite and Graphene Oxide Embedded Polyacrylonitrile Electrospun Nanofiber Matrix for Remediation of Arsenate Ions. *ACS Appl Polym Mater* 2:604–617.

<https://doi.org/10.1021/acsapm.9b00982>

Uddin MK (2017) A review on the adsorption of heavy metals by clay minerals, with special focus on the past decade. *Chem Eng J* 308:438–462.

<https://doi.org/10.1016/J.CEJ.2016.09.029>

Ullah R, Khan SA, Aladresi AAM, et al (2020) Ovalbumin-mediated synthesis and simultaneous functionalization of graphene with increased protein stability. *Green Chem Lett Rev* 13:60–67.

<https://doi.org/10.1080/17518253.2020.1725150>

UNSCEAR (United Nations Scientific Committee on the Effects of Atomic Radiation) (1993) Sources and effects of ionizing radiation. UNSCEAR 1993 Report to the General Assembly, with Scientific Annexes, New York, United Nations.

UNSCEAR (United Nations Scientific Committee on the Effects of Atomic Radiation) (2000) Sources and effects of ionizing radiation. UNSCEAR 2000 Report to the General Assembly, with Scientific Annexes, New York, United Nations.

UNSCEAR (United Nations Scientific Committee on the Effects of Atomic Radiation) (2008) Sources and effects of ionizing radiation. UNSCEAR 2008 Report to the General Assembly, with Scientific Annexes, New York, United Nations.

UNSCEAR (United Nations Scientific Committee on the Effects of Atomic Radiation) (2013) Sources, effects and risks of ionizing radiation. UNSCEAR 2013 Report to the General Assembly and Scientific Annexes, New York, United Nations.

Van De Voorde M, Van Hecke K, Binnemans K, Cardinaels T (2018) Separation of samarium and europium by solvent extraction with an undiluted quaternary ammonium ionic liquid: towards high-purity medical samarium-153. *RSC Adv* 8:20077–20086. <https://doi.org/10.1039/C8RA03279C>

Vanhoudt N, Van Ginneken P, Nauts R, Van Hees M (2018) Potential of four aquatic plant species to remove  $^{60}\text{Co}$  from contaminated water under changing experimental conditions. *Environ Sci Pollut Res* 25:27187–27195. <https://doi.org/10.1007/S11356-018-2759-7>

Vincent C, Barré Y, Vincent T, et al (2015) Chitin-Prussian blue sponges for Cs(I) recovery: From synthesis to application in the treatment of accidental dumping of metal-bearing solutions. *J Hazard Mater* 287:171–179. <https://doi.org/10.1016/J.JHAZMAT.2015.01.041>

Wang H, Tang H, Liu Z, et al (2014) Removal of cobalt(II) ion from aqueous solution by chitosan–montmorillonite. *J Environ Sci* 26:1879–1884. <https://doi.org/10.1016/J.JES.2014.06.021>

Wang K, Ma H, Pu S, et al (2019) Hybrid porous magnetic bentonite-chitosan beads for selective removal of radioactive cesium in water. *J Hazard Mater* 362:160–169. <https://doi.org/10.1016/J.JHAZMAT.2018.08.067>

Wang J, Yang S, Cheng G, Gu P (2020) The Adsorption of Europium and Uranium on the Sodium Dodecyl Sulfate Modified Molybdenum Disulfide Composites. *J Chem Eng Data* 65:2178–2185. <https://doi.org/10.1021/acs.jced.0c00049>

Wang X, Shi C, Guan J, et al (2022) The development of molecular and nano actinide decorporation agents. *Chinese Chem Lett* 33:3395–3404. <https://doi.org/10.1016/J.CCLET.2022.04.017>

Wang J, Han Q, Wang K, et al (2023) Recent advances in development of functional magnetic adsorbents for selective separation of proteins/peptides. *Talanta* 253:123919. <https://doi.org/10.1016/J.TALANTA.2022.123919>

Wani AA, Shahadat M, Ali SW, et al (2022) Recent advances and future perspectives of polymer-based magnetic nanomaterials for detection and removal of radionuclides: A review. *J Mol Liq* 365:119976.

<https://doi.org/10.1016/J.MOLLIQ.2022.119976>

Wei B, Li Y, Li H, et al (2013) Rare earth elements in human hair from a mining area of China. *Ecotoxicol Environ Saf* 96:118–123.

<https://doi.org/10.1016/J.ECOENV.2013.05.031>

Wei J, Aly Aboud MF, Shakir I, et al (2020) Graphene Oxide-Supported Organo-Montmorillonite Composites for the Removal of Pb(II), Cd(II), and As(V) Contaminants from Water. *ACS Appl Nano Mater* 3:806–813.

<https://doi.org/10.1021/acsanm.9b02311>

Widayat W, Annisa AN (2017) Synthesis and Characterization of ZSM-5 Catalyst at Different Temperatures. *IOP Conf Ser Mater Sci Eng* 214:012032. <https://doi.org/10.1088/1757-899X/214/1/012032>

Woodward GL, Peacock CL, Otero-Fariña A, et al (2018) A universal uptake mechanism for cobalt(II) on soil constituents: Ferrihydrite, kaolinite, humic acid, and organo-mineral composites. *Geochim Cosmochim Acta* 238:270–291. <https://doi.org/10.1016/J.GCA.2018.06.035>

Wu H, Gao G, Zhou X, et al (2012) Control on the formation of Fe<sub>3</sub>O<sub>4</sub> nanoparticles on chemically reduced graphene oxide surfaces. *CrystEngComm* 14:499–504. <https://doi.org/10.1039/C1CE05724C>

Wu H, Lin S, Cheng X, et al (2020) Comparative study of strontium adsorption on muscovite, biotite and phlogopite. *J Environ Radioact* 225:106446. <https://doi.org/10.1016/j.jenvrad.2020.106446>

Wu H, Chen J, Su Z, et al (2021) Insight into the adsorption of europium(III) on muscovite and phlogopite: Effects of pH, electrolytes, humic substances and mica structures. *Chemosphere* 282:131087.

<https://doi.org/10.1016/J.CHEMOSPHERE.2021.131087>

Xiong Y, Li J, Zhao D, et al (2023) High capacity synergistic immobilization of simulated trivalent actinides by zirconia/zircon multiphase ceramics. *Ceram Int* 49:2472-2477.

<https://doi.org/10.1016/J.CERAMINT.2022.09.221>

Xu B, Zhu Y, Liu H, et al (2016) The kinetic and thermodynamic adsorption of Eu(III) on synthetic maghemite. *J Mol Liq* 221:171–178.

<https://doi.org/10.1016/J.MOLLIQ.2016.05.055>

Xu W, Chen Y, Zhang W, Li B (2019) Fabrication of graphene oxide/bentonite composites with excellent adsorption performances for toluidine blue removal from aqueous solution. *Adv Powder Technol* 30:493–501. <https://doi.org/10.1016/J.APT.2018.11.028>

Yamamoto M, Komura K, Sakanoue M, et al (1985) Pu Isotopes,  $^{241}\text{Am}$  and  $^{137}\text{Cs}$  in Soils from the Atomic Bombed Areas in Nagasaki and Hiroshima. *J Radiat Res* 26:211–223. <https://doi.org/10.1269/JRR.26.211>

Yang H, Li H, Zhai J, et al (2014) Magnetic prussian blue/graphene oxide nanocomposites caged in calcium alginate microbeads for elimination of cesium ions from water and soil. *Chem Eng J* 246:10–19. <https://doi.org/10.1016/J.CEJ.2014.02.060>

Yang HM, Jang SC, Hong SB, et al (2016a) Prussian blue-functionalized magnetic nanoclusters for the removal of radioactive cesium from water. *J Alloys Compd* 657:387–393. <https://doi.org/10.1016/J.JALLCOM.2015.10.068>

Yang S, Okada N, Nagatsu M (2016b) The highly effective removal of  $\text{Cs}^+$  by low turbidity chitosan-grafted magnetic bentonite. *J Hazard Mater* 301:8–16. <https://doi.org/10.1016/J.JHAZMAT.2015.08.033>

Yang L, Wang X, Nie H, et al (2016c) Residual levels of rare earth elements in freshwater and marine fish and their health risk assessment from Shandong, China. *Mar Pollut Bull* 107:393–397. <https://doi.org/10.1016/j.marpolbul.2016.03.034>

Yang S, Wu G, Song J, Hu B (2022) Preparation of chitosan-based asymmetric electrodes by co-imprinting technology for simultaneous electro-adsorption of multi-radionuclides. *Sep Purif Technol* 297:121568. <https://doi.org/10.1016/j.seppur.2022.121568>

Yasunari TJ, Stohl A, Hayano RS, et al (2011) Cesium-137 deposition and contamination of Japanese soils due to the Fukushima nuclear accident. *Proc Natl Acad Sci* 108:19530–19534. <https://doi.org/10.1073/pnas.1112058108>

Ye S, Yang Z, Xu J, et al (2019) Clay–graphene oxide liquid crystals and their aerogels: synthesis, characterization and properties. *R Soc Open Sci* 6:181439. <https://doi.org/10.1098/RSOS.181439>

Yin H, Zhu J, Chen J, et al (2018) PEG-templated assembling of  $\text{Co}_3\text{O}_4$  nanosheets with nanoparticles for enhanced sensitive non-enzymatic glucose sensing performance. *J Mater Sci Mater Electron* 29:17305–17313. <https://doi.org/10.1007/S10854-018-9825-2>

Yong SK, Shrivastava M, Srivastava P, et al (2014) Environmental applications of chitosan and its derivatives. In: *Reviews of Environmental Contamination and Toxicology*. Springer New York LLC.

Yu J, Yuan L, Wang S, et al (2019) Phosphonate-decorated covalent organic frameworks for actinide extraction: A breakthrough under highly acidic conditions. *CCS Chem* 1:286–295. <https://doi.org/10.31635/CCSCHEM.019.20190005>

Yu X, Zhang J, Zheng Y (2021) Perchlorate adsorption onto epichlorohydrin crosslinked chitosan hydrogel beads. *Sci Total Environ* 761:143236. <https://doi.org/10.1016/j.scitotenv.2020.143236>

Yuan P, Fan M, Yang D, et al (2009) Montmorillonite-supported magnetite nanoparticles for the removal of hexavalent chromium [Cr(VI)] from aqueous solutions. *J Hazard Mater* 166:821–829. <https://doi.org/10.1016/J.JHAZMAT.2008.11.083>

Yushin N, Zinicovscaia I, Cepoi L, et al (2022) Biosorption and Bioaccumulation Capacity of *Arthrospira platensis* toward Yttrium Ions. *Metals* 12:1465. <https://doi.org/10.3390/met12091465>

Zaichick S, Zaichick V, Karandashev V, Nosenko S (2011) Accumulation of rare earth elements in human bone within the lifespan. *Metallomics* 3:186–194. <https://doi.org/10.1039/C0MT00069H>

Zhang X, Wang X, Chen Z (2017) Radioactive cobalt(II) removal from aqueous solutions using a reusable nanocomposite: Kinetic, isotherms, and mechanistic study. *Int J Environ Res Public Health* 14:1453. <https://doi.org/10.3390/ijerph14121453>

Zhang X, Gu P, Liu Y (2019) Decontamination of radioactive wastewater: State of the art and challenges forward. *Chemosphere* 215:543–553. <https://doi.org/10.1016/J.CHEMOSPHERE.2018.10.029>

Zhang H, Dong Y, He H, et al (2020a) Sorption of cesium on Tamusu clay in synthetic groundwater with high ionic strength. *Radiochim Acta* 108:287–296. <https://doi.org/10.1515/ract-2019-3161>

Zhang J, Lin S, Han M, et al (2020b) Adsorption Properties of Magnetic Magnetite Nanoparticle for Coexistent Cr(VI) and Cu(II) in Mixed Solution. *Water* 12:446. <https://doi.org/10.3390/w12020446>

Zhang Q, Zhuang S, Wang J (2020c) Biosorptive removal of cobalt(II) from aqueous solutions using magnetic cyanoethyl chitosan beads. *J Environ Chem Eng* 8:104531. <https://doi.org/10.1016/J.JECE.2020.104531>

Zhang S, Wang H, Liu J, Bao C (2020d) Measuring the specific surface area of monolayer graphene oxide in water. *Mater Lett* 261:127098. <https://doi.org/10.1016/j.matlet.2019.127098>

Zhang N, Chen S, Hu J, et al (2020e) Robust and recyclable sodium carboxymethyl cellulose–ammonium phosphomolybdate composites for cesium removal from wastewater. *RSC Adv* 10:6139–6145. <https://doi.org/10.1039/C9RA09803H>

Zhang B, Zhang B, Liu X (2021) Chitosan coated - porous low expansion vermiculite for efficient removal of cesium from radioactive wastewater. *Environ Chem Ecotoxicol* 3:182–196. <https://doi.org/10.1016/J.ENCECO.2021.05.001>

Zhang Y, Wang H, Gao K, et al (2022) Efficient removal of Cs(I) from water using a novel Prussian blue and graphene oxide modified PVDF membrane: Preparation, characterization, and mechanism. *Sci Total Environ* 838:156530. <https://doi.org/10.1016/J.SCITOTENV.2022.156530>

Zhao Y, Liu Y, Zhang X, Liao W (2021) Environmental transformation of graphene oxide in the aquatic environment. *Chemosphere* 262:127885. <https://doi.org/10.1016/j.chemosphere.2020.127885>

Zhdanova NN, Redchits TI, Zheltonozhsky VA, et al (2003) Accumulation of radionuclides from radioactive substrata by some micromycetes. *J Environ Radioact* 67:119–130. [https://doi.org/10.1016/S0265-931X\(02\)00164-9](https://doi.org/10.1016/S0265-931X(02)00164-9)

Zheng X, Dou J, Yuan J, et al (2017) Removal of Cs<sup>+</sup> from water and soil by ammonium-pillared montmorillonite/Fe<sub>3</sub>O<sub>4</sub> composite. *J Environ Sci* 56:12–24. <https://doi.org/10.1016/J.JES.2016.08.019>

Zheng M, Ji H, Duan J, et al (2020) Efficient adsorption of europium (III) and uranium (VI) by titanate nanorings: Insights into radioactive metal species. *Environ Sci Ecotechnology* 2:100031. <https://doi.org/10.1016/J.ESE.2020.100031>

Zhidkin AP, Shamshurina EN, Golosov VN, et al (2020) Detailed study of post-Chernobyl Cs-137 redistribution in the soils of a small agricultural catchment (Tula region, Russia). *J Environ Radioact* 223–224:106386. <https://doi.org/10.1016/j.jenvrad.2020.106386>

Zhu R, Chen Q, Zhou Q, et al (2016) Adsorbents based on montmorillonite for contaminant removal from water: A review. *Appl Clay Sci* 123:239–258. <https://doi.org/10.1016/j.clay.2015.12.024>

Zhuang S, Yin Y, Wang J (2018) Removal of cobalt ions from aqueous solution using chitosan grafted with maleic acid by gamma radiation. *Nucl Eng Technol* 50:211–215. <https://doi.org/10.1016/J.NET.2017.11.007>

Zhuang S, Wang J (2019) Removal of cobalt ion from aqueous solution using magnetic graphene oxide/chitosan composite. *Environ Prog Sustain Energy* 38:S32–S41. <https://doi.org/10.1002/ep.12912>

Zhuang S, Zhu K, Hu J, Wang J (2022) Selective and effective adsorption of cesium ions by metal hexacyanoferrates (MHCF, M = Cu, Co, Ni) modified chitosan fibrous biosorbent. *Sci Total Environ* 835:155575. <https://doi.org/10.1016/J.SCITOTENV.2022.155575>

Zibold G, Drissner J, Kaminski S, et al (2001) Time-dependence of the radiocaesium contamination of roe deer: measurement and modelling. *J Environ Radioact* 55:5–27. [https://doi.org/10.1016/S0265-931X\(00\)00184-3](https://doi.org/10.1016/S0265-931X(00)00184-3)

# CURRICULUM VITAE

Raman Novikau

1995-06-25, Pinsk, Republic of Belarus

## Education:

Francisk Skorina Gomel State University, Biological faculty <i>Bachelor of Science in Biology</i>	2013–2017
---	-----------

Francisk Skorina Gomel State University, Biological faculty <i>Magister of Science in Biology</i>	2017–2019
---	-----------

Advanced training course: “highly effective liquid chromatography: theory and practice”	2017
---	------

Center for Physical Sciences and Technology <i>PhD studies</i>	2019–2023
---	-----------

## Professional career:

Institute of Radiobiology of the National Academy of Sciences of Belarus, laboratory endocrinology and biochemistry <i>Junior researcher</i>	2017–2019
---	-----------



## ACKNOWLEDGMENTS/PADĖKA

I am sincerely grateful to my academic supervisor, Dr. Galina Lujanienė, for her help and advice in research activities and for her support and kindness in difficult times. They have undoubtedly played a very important role in the realisation of my goal. Many thanks to Dr. Vidas Pakštas, Dr. Martynas Talaikis, Dr. Kęstutis Mažeika, Dr. Audrius Drabavičius, Dr. Vitalija Jasulaitienė, Dr. Arnas Naujokaitis, Dr. Saulius Tumėnas, and Dr. Martynas Skapas for the characterisation results and help in their interpretation. Once again, I would like to thank Dr. Vidas Pakštas, Dr. Martynas Talaikis, and Dr. Kęstutis Mažeika for your responsiveness and invaluable research assistance. I sincerely thank Dr. Sergej Šemčuk for his advice on adsorption studies, for the synthesis of graphene oxide and Prussian blue composites and their adsorption tests. Thank you to Karolina Karalevičiūtė for the synthesis of chitosan-mineral composites and adsorption tests. I am grateful to all the staff in the Department of Environmental Research and very happy to have found myself in such a cosy and pleasant team. In general, I am very happy to have been among such highly qualified specialists from whom I have learned a lot. Finally, I would like to thank my parents, relatives, and friends for their faith in me and support.

FOR NOTES

FOR NOTES

Vilnius University Press  
9 Saulėtekio Ave., Building III, LT-10222 Vilnius  
Email: [info@leidykla.vu.lt](mailto:info@leidykla.vu.lt), [www.leidykla.vu.lt](http://www.leidykla.vu.lt)  
[bookshop.vu.lt](http://bookshop.vu.lt), [journals.vu.lt](http://journals.vu.lt)  
Print run copies 22